Model independent search for new particles in two-dimensional mass space using events with missing energy, two jets and two leptons with the CMS detector

Von der Fakultät für Mathematik, Informatik und Naturwissenschaften der RWTH Aachen University zur Erlangung des akademischen Grades einer Doktorin der Naturwissenschaften genehmigte Dissertation

vorgelegt von

Diplom-Physikerin

Sarah Beranek

aus Münster

Berichter: Universitätsprofessor Dr. Stefan Schael
Universitätsprofessor Dr. Thomas Hebbeker

Tag der mündlichen Prüfung: 29.06.2017

CERN-THESIS-2017-115
29/06/2017

Abstract

Model independent search for new particles in two-dimensional mass space using events with missing energy, two jets and two leptons with the CMS detector

The discovery of a new particle consistent with the standard model Higgs boson at the Large Hadron Collider in 2012 completed the standard model of particle physics (SM). Despite its remarkable success many questions remain unexplained. Numerous theoretical models, predicting the existence of new heavy particles, provide answers to these unresolved questions and are tested at high energy experiments such as the Compact Muon Solenoid (CMS) detector at the Large Hadron Collider (LHC).

In this thesis a model independent search method for new particles in two-dimensional mass space in events with missing transverse energy is presented using 19.7 fb^{-1} of proton-proton collision data recorded by the CMS detector at a centre of mass energy $\sqrt{s} = 8\,\text{TeV}$ at the LHC. The analysis searches for signatures of pair-produced new heavy particles T′ , which decay further into unknown heavy particles W′ and SM quarks q ($\text{T}'\overline{\text{T}'} \to \text{W}'^{+}\ \text{q}\ \text{W}'^{-}\ \overline{\text{q}}$), in which both W′ bosons decay leptonically, $\text{W}' \to \text{l}\nu$. A mass reconstruction of the $\text{T}'\overline{\text{T}'}$ system is performed using the analytical solution of the kinematical equation system together with constraints from the parton distribution functions leading to an estimate of $\text{M}_{T'}$ and $\text{M}_{W'}$ for each event. The masses of the unknown particles T′ and W′ are unconstrained and reconstructed simultaneously. There are no further assumptions apart from the topology of the decay chain. The mass reconstruction method can be applied to search for any particle decaying with the same topology into the final state mentioned.

For the same event selection, the search method is employed in multiple applications. Initially, as a proof of principle, the top quark and the W boson are observed simultaneously in the two-dimensional mass space in standard model top quark pair decays. A search for a new heavy top quark partner T′ decaying to standard model W bosons and b quarks is performed in the one-dimensional projection, as well as a search for a new heavy neutral gauge boson Z′ , decaying to standard model top pairs, in the invariant mass distribution of the $\text{t}\bar{\text{t}}$ system. In absence of significant excesses over standard model predictions for both observables, 95% confidence level upper limits on the cross section times branching ratio $\sigma \cdot BR$ are calculated and presented. In order to quantify the performance of the model-independent mass reconstruction method results are compared with dedicated searches. Finally a search for pair-produced new heavy top quark partners T′ , decaying into new heavy charged gauge bosons W′ and standard model b quarks, as predicted by a simplified Littlest Higgs model, is carried out in the two-dimensional mass-plane. No significant deviation from standard model predictions is observed. The observed 95% confidence level lower limit on the mass $\text{M}_{T'}$ for a new heavy top-partner T′ is consistent with expectations ranging from 870 GeV and 950 GeV depending on the mass $\text{M}_{W'}$ for a new heavy charged gauge boson W′ . This is the first search performed at the LHC for both a new heavy top quark partner T′ and a new heavy charged gauge boson W′ as predicted by the Littlest Higgs model.

Zusammenfassung

Modellunabhängige Suche nach neuen Teilchen im zwei-dimensionalen Massenraum in Ereignissen mit fehlender Energie, zwei Jets und zwei Leptonen

Die Entdeckung eines mit dem Higgs-Boson des Standardmodells konsistenten Teilchens am Large Hadron Collider im Jahr 2012, komplettierte das Standardmodell der Elementarteilchenphysik (SM). Trotz seines außergewöhnlichen Erfolgs bleiben viele Fragen ungeklärt. Zahlreiche theoretische Modelle, die die Existenz von neuen schweren Elementarteilchen vorhersagen, liefern Antworten auf diese ungeklärten Fragen. Diese Theorien können an Hochenergie-Experimenten wie dem Compact-Muon-Solenoid-Detektor (CMS) am Large Hadron Collider (LHC) getestet werden.

Diese Dissertation präsentiert eine modellunabhängige Suche nach neuen Elementarteilchen im zwei-dimensionalen Massenraum in Ereignissen mit fehlender transversaler Energie. Die analysierten Daten umfassen $19.7\,\mathrm{fb}^{-1}$ der Proton-Proton-Kollisionen, die mit dem CMS Detektor bei einer Schwerpunktsenergie $\sqrt{s} = 8\,\mathrm{TeV}$ am LHC aufgenommen wurden. Die Analyse sucht nach Signaturen von Paar-produzierten neuen schweren Elementarteilchen T' , die ihrerseits in unbekannte schwere Teilchen W' und SM Quarks q zerfallen ($\mathrm{T}'\overline{\mathrm{T}'} \rightarrow \mathrm{W}'^{+}\ \mathrm{q}\ \mathrm{W}'^{-}\ \overline{\mathrm{q}}$). Die W' Bosonen zerfallen dabei leptonisch, $\mathrm{W}' \rightarrow \mathrm{l}\nu$. Die Rekonstruktion der Massen des $\mathrm{T}'\overline{\mathrm{T}'}$ Systems wird unter Verwendung der analytischen Lösung des kinematischen Gleichungssystems zusammen mit Zwangsbedingungen der Partondichtefunktionen errechnet und liefert einen Schätzwert der Massen $\mathrm{M}_{T'}$ und $\mathrm{M}_{W'}$ für jedes Ereignis. Die Massen der unbekannten Teilchen T' und W' sind dabei nicht beschränkt und werden simultan rekonstruiert. Außer der Topologie der Zerfallskette werden keine weiteren Annahmen gemacht. Diese Methode der Massenrekonstruktion kann auf beliebige Suchen nach Teilchen mit derselben Topologie und dem genannten Endzustand angewendet werden.

Die Suchmethode kommt, basierend auf der gleichen Ereignisselektion, bei verschiedenen Anwendungen zum Einsatz. Zunächst wird in einer Machbarkeitsstudie das Top-Quark und das W Boson simultan im zwei-dimensionalen Massenraum in Top-Paar Zerfällen des Standardmodells rekonstruiert. Eine Suche nach neuen schweren Top-Quark Partnern T' , die in SM W Bosonen und b-Quarks zerfallen, wird in einer ein-dimensionalen Projektion durchgeführt. Nach einem neuen schweren Eichboson Z' , das in SM Top-Paare zerfällt, wird in der invarianten Massenverteilung des $\mathrm{t}\bar{\mathrm{t}}$ Systems gesucht. In Abwesenheit von signifikanten Überschüssen im Vergleich zu Standardmodell Vorhersagen für beide Observablen wird eine obere Ausschlussgrenze mit einem Konfidenzniveau von 95% auf das Produkt von Wirkungsquerschnitt und Verzweigungsverhältnis $\sigma \cdot BR$ berechnet und präsentiert. Um die Leistungsfähigkeit der modellunabhängigen Massenrekonstruktionsmethode zu bewerten, werden die Ergebnisse mit dedizierten Suchen verglichen. Letztendlich wird eine Suche nach neuen schweren Paar-produzierten Top-Quark Partnern T', welche in neue schwere geladene Eichboson W' und b-Quarks zerfallen, im zwei-dimensionalen Massenraum durchgeführt. Diese Signatur wird von einem vereinfachten Littlest Higgs Model vorhergesagt. Es wird keine signifikante Abweichung von der Standardmodell Vorhersage gemessen.

Die beobachte untere Ausschlussgrenze mit einem Konfidenzniveau von 95% auf die Masse $M_{T'}$ ist konsistent mit der Erwartung in einem Bereich von 870 GeV bis 950 GeV in Abhängigkeit der Masse $M_{W'}$. Dies ist die erste gleichzeitig durchgeführte Suche am LHC nach neuen schweren Top-Quark Partnern T′ und neuen schweren geladenen Eichbosonen W′ , welche von Littlest Higgs Modellen vorhergesagt werden.

List of publications

CMS Collaboration, "Search in two-dimensional mass space for $T'\overline{T'} \rightarrow W'^{+}\, b\, W'^{-}\, \overline{b}$ in the dilepton final state in proton-proton collisions at $\sqrt{s} = 8$ TeV", CMS Physics Analysis Summary CMS-PAS-B2G-12-025, 2015. http://cms-results.web.cern.ch/cms-results/public-results/preliminary-results/B2G-12-025/

Sarah Beranek for the CMS Collaboration, "Search in two-dimensional mass space for $T'\overline{T'} \rightarrow W'^{+}\, b\, W'^{-}\, \overline{b}$ in the dilepton final state with the CMS detector", in *Proceedings of Science (PoS), 27th International Symposium on Lepton Photon Interactions at High Energies (LP15): Ljubljana, Slovenia, August 17-22, 2015*, vol. LeptonPhoton2015, p. 075, 2015. http://inspirehep.net/record/1500772/files/PoS(LeptonPhoton2015)075.pdf.

Contents

CHAPTER 1

Introduction

The Standard Model of particle physics (SM) encapsulates the basic building blocks of matter and their interactions. Since its development in the 20th century, it has been a tremendously successful theory. The discovery of a new particle [1–3] at the Large Hadron Collider (LHC) with a mass of 125 GeV consistent with the predicted SM Higgs Boson [4–6] completed the SM in 2012. Despite its remarkable accomplishments over the last decades many unresolved questions remain. For instance, explanations for the observed baryon asymmetry in the universe, the nature of dark matter, the accelerating expansion of the universe (dark energy) and an implementation of the neutrino masses are still to be found. In addition to these observations, theoretical issues like the achievement of gauge unification and the extremely large difference between the electroweak and the Planck scale remain unanswered. Numerous theoretical models have been proposed through the years to provide answers to many of the unresolved problems of the SM. Many of these hypothetical solutions, often introducing new heavy particles [7–9], are tested at high energy experiments such as the Compact Muon Solenoid (CMS) detector at the LHC. The nature of the new physics is uncertain and can have a large variety of properties. In addition to dedicated searches, which are optimised for specific models, model-independent analyses with only little theoretical input are also needed. Particularly suited for discoveries, model-independent methods are important to cover a wider range of theoretical predictions and enable global searches.

In this thesis a model independent search method for new heavy particles in events with missing transverse energy in the final state is presented using $19.7\,\mathrm{fb}^{-1}$ of proton-proton (pp) collision data recorded by the CMS detector at a centre of mass energy $\sqrt{s} = 8\,\mathrm{TeV}$

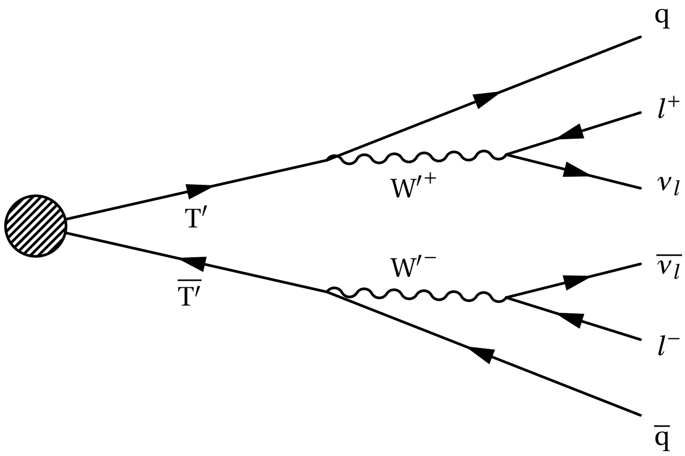

Figure 1.1: Generic decay chain for the presented mass reconstruction method searching simultaneously for a new T′ quark and a new W′ boson.

at the LHC [10, 11]. Many theoretical models predict missing transverse energy (E_T^{miss}) in the final state, but discoveries with E_T^{miss} -related observables are difficult to establish, because new physics typically manifests itself in the tail of rapidly falling distributions.

The presented method searches for two unknown pair produced heavy particles $T'\overline{T'}$, which decay further into unknown heavy particles W′ and SM particles q, whereby the W′ subsequently decays into one observed SM particle f and one undetected invisible particle, measured as E_T^{miss} :

$$pp \to T'\overline{T'} \to W'^+ \, q \; + W'^- \, \overline{q} \, , \qquad W' \to f + E_T^{miss}$$

The two-dimensional mass reconstruction of the $T'\overline{T'}$ system uses the analytic solutions of the kinematical equation system to scan the two-dimensional mass space ($M_{T'}$ vs $M_{W'}$) for the existence of a solution. The measured particle kinematics in each event are smeared according to the CMS detector resolution. The upper limits of the allowed mass space are restricted by the collision energy, therefore probabilities from parton distribution functions (PDF) are used to select the final $M_{T'}$ and $M_{W'}$ per event. The masses of the two unknown particles T′ and W′ are reconstructed simultaneously. There are no constraints on the masses of T′ and W′ and no further assumptions apart from the topology of the decay chain. Although other final states with similar symmetric topologies and E_T^{miss} could be analysed with the presented mass reconstruction method, in this thesis the W′ is assumed to decay leptonically:

$$pp \to T'\overline{T'} \to W'^+ \, q \; + W'^- \, \overline{q} \, , \qquad W' \to l \, + \, \nu_l,$$

where the charged leptons l are either electrons or muons. The SM particles q form highly energetic jets, which are measured. The generic decay chain for the searches under study in this thesis is illustrated in the diagram in figure 1.1.

This is similar to top quark pair decays, which are a first important standard candle measurement to establish the mass reconstruction method. This analysis can search for the existence of any particle decaying with the same topology into a final state with two charged leptons, two jets and $E_{\mathrm{T}}^{\mathrm{miss}}$.

In 1991 Dalitz and Goldstein [12] proposed a geometrical approach using the solvability of the kinematic equation system in one dimension with a matrix element weight to reconstruct dileptonic top decays. This and Kondo's [13, 14] earlier likelihood reconstruction procedure based on dynamical assumptions lead to the numerically based matrix element weighting method (MWT) at the Tevatron [15–18] and later the Analytical MWT (AMWT) at the LHC [19, 20]. In contrast to these methods to reconstruct dileptonic top quark pair decays, the presented analysis aims to remove as much model dependence as possible arising from matrix elements and other dynamical theoretical inputs. More importantly the mass reconstruction method presented in this thesis searches for two unknown particles simultaneously in decays involving two invisible particles.

After a brief description of the theoretical foundation and the experimental setup in chapters 2 and 3, respectively, the data and simulation samples are described in chapter 4. The same event selection is applied for various applications and is presented in chapter 5. The two-dimensional mass reconstruction is explained in chapter 6.
The results using data after the mass reconstruction are presented in chapter 7. The recorded data collected with the CMS detector is examined for compatibility with various theoretical models at the TeV scale using different observables. In order to quantify the performance of the model-independent mass reconstruction method, results are obtained looking into one-dimensional observables. In the one-dimensional projection to the $\mathrm{M}_{T'}$ plane a search for a new heavy vector-like top quark partner T' [9, 21] decaying to SM W bosons and b quarks ($pp \rightarrow \mathrm{T}'\overline{\mathrm{T}'} \rightarrow \mathrm{W}^+ \mathrm{b} + \mathrm{W}^- \overline{\mathrm{b}}$) as well as a search for a new heavy neutral gauge boson Z' [22, 23] decaying to SM top quark pairs in the $\mathrm{M}_{t\bar{t}}$ invariant mass distribution is performed ($pp \rightarrow \mathrm{Z}' \rightarrow t\bar{t} \rightarrow \mathrm{W}^+ \mathrm{b} + \mathrm{W}^- \overline{\mathrm{b}}$) and compared to dedicated searches. The top quark being the heaviest known fundamental particle is the perfect candidate to further study the mechanism of electroweak symmetry breaking. Moreover heavy resonances might manifest themselves as an additional resonant top pair contribution. The simultaneous reconstruction of two unknown particles in the two-dimensional mass phase-space is the main advantage of this search method. It is then used to search for pair-produced new heavy top quark partners T' , decaying into new heavy charged gauge bosons W' and SM b quarks as predicted by Littlest Higgs models [9, 24–27]. Little Higgs models introduce spontaneously broken global symmetries due to a mechanism called "collective symmetry breaking" where the Higgs field appears as a pseudo-Nambu-Goldstone boson. Little Higgs models introduce new heavy gauge bosons and new heavy fermions to cancel the quadratic divergences to the Higgs boson mass arising from the large scale differences be-

tween the electroweak and the Planck scale. To address models with similar particle content and masses a simplified model is used. Simultaneous searches for a new heavy top quark partner and a new heavy gauge boson as predicted by the Littlest Higgs model in this final state have not been performed by LHC experiments so far. The systematic uncertainties in the different observables are presented in chapter 8 and the search results in chapter 9. This thesis is summarised in chapter 10.

CHAPTER 2

Theoretical Foundation

In this chapter a brief overview of the theoretical framework of particle physics relevant to this thesis is given. The description of the SM in section 2.1 covers the empirically determined particle content and the interactions between particles through the fundamental forces. A more detailed and in-depth coverage can be found for example in [28–31]. Limitations of the SM and proposed solutions are described in section 2.2 and 2.3, respectively. In the last section 2.4 the final state of dilepton and $E_{\mathrm{T}}^{\mathrm{miss}}$ events is discussed for a pp collider.

Convention of natural units:
Throughout this thesis natural units are used, setting the velocity of light c and the reduced Planck constant $\hbar$ to unity. Energy, momentum and mass have the same dimension : eV.

2.1 Standard Model of Particle Physics

The SM is a Lorentz-invariant quantum field theory (QFT) based on gauge symmetry groups describing the interactions between the fundamental building blocks of matter. The Dirac and Klein-Gordon equations [32] in the 1920s paved the way for the development of the SM QFT encapsulating the concepts of quantum mechanics and special relativity. The SM Lagrange density (Lagrangian) describes the interaction of the SM particles in terms of quantized fields. The Lagrangian is required to be invariant under various symmetry transformations dictated by nature. Global symmetries like translation in space and time as well as rotations imply via Noether's theorem [33] various conservation laws: momentum, energy and angular momentum. Additionally, the Lagrangian needs to obey local gauge symmetry transformations, which determine the specific properties of the different interactions. The SM describes the strong interaction, represented by the theory of Quantumchromodynamics (QCD), and the weak and the electromagnetic interaction, combined in the Electroweak Theory (EWT). Gravity, as described by Einsteins General Relativity [34], is the only known fundamental force, which is not (yet) described by the SM framework. The SM is a non-Abelian gauge theory built on the following symmetry group:

$$\underbrace{SU(3)_C}_{\substack{\text{Strong}\\\text{Interaction}}} \otimes \underbrace{SU(2)_L \otimes U(1)_Y}_{\substack{\text{Electroweak}\\\text{Interaction}}} \tag{2.1}$$

where C denotes colour, Y Hypercharge and L denotes Left-Handedness[1]. The SM Lagrangian must be renormalisable. In the perturbative framework, infinities arising from loops can be reabsorbed by re-definition of physical parameters to obtain physical observables. The energy scale (renormalisation scale) introduced by the renormalisation mechanism is arbitrary. The SM Lagrangian is the most general one consistent with all the requirements mentioned before:

$$\mathscr{L}_{\text{SM}} = \mathscr{L}_{\text{QCD}} + \mathscr{L}_{\text{EWT}} + \mathscr{L}_{\text{Higgs}} + \mathscr{L}_{\text{Yukawa}} \tag{2.2}$$

In the following, the components of the symmetry group and the SM Lagrangian will be described.

Table 2.1: Gauge bosons of the SM and their properties [35].

Particle	Symbol	Mass [GeV]	Electric Charge [e]	Spin	Interaction
photon	γ	0	0	1	electromagnetic
8 gluons	g	0	0	1	strong
W bosons	$W^\pm$	80.385 ± 0.015	1/-1	1	weak
Z boson	Z	91.1876 ± 0.0021	0	1	weak
Higgs boson	H^0	125.09 ± 0.24	0	0	Higgs mechanism

The building blocks of matter are spin-1/2-particles (fermions) and the forces between them are mediated by spin-1-gauge bosons. The strong force is mediated by massless gluons, the weak force by the massive $W^\pm$ and Z bosons and the electromagnetic force by massless photons. The properties of the gauge bosons are summarised in table 2.1, where the Higgs boson originates from the electroweak symmetry breaking mechanism, which is necessary to explain the observation of massive particles, as described in subsection 2.1.3. Each fundamental interaction couples to a corresponding charge and only particles coupling to that

[1] Simplified explanation: "Left-handed" means that the direction of the particle's spin and motion are opposite. Right-handed means that the direction of spin and momentum are the same.

Table 2.2: Fermions of the SM and their properties [35]. Gen. stands for Generation. The top quark mass is measured directly. The lighter quark masses are determined indirectly using QCD perturbation theory in the $\overline{MS}$ renormalisation scheme [35].

	Gen.	Particle	Symbol	Mass [MeV]	Electric Charge [e]
Leptons	1	electron	e^-	$0.511 \pm (1.1 \cdot 10^{-8})$	-1
		electron neutrino	ν_e	$< 2 \cdot 10^{-6}$	0
	2	muon	μ^-	$105.66 \pm (3.5 \cdot 10^{-6})$	-1
		muon neutrino	ν_μ	$< 2 \cdot 10^{-6}$	0
	3	tau	τ^-	1776.86 ± 0.12	-1
		tau neutrino	ν_τ	$< 2 \cdot 10^{-6}$	0
Quarks	1	up	u	$2.3^{+0.7}_{-0.5}$	$+2/3$
		down	d	$4.8^{+0.5}_{-0.3}$	$-1/3$
	2	charm	c	$(1.275 \pm 0.025) \cdot 10^3$	$+2/3$
		strange	s	95 ± 5	$-1/3$
	3	top	t	$(173.21 \pm 0.51 \pm 0.71) \cdot 10^3$	$+2/3$
		bottom	b	$(4.18 \pm 0.03) \cdot 10^3$	$-1/3$

charge are affected by the corresponding interaction. Fermions are divided into leptons and quarks, where quarks take part in the strong interaction and leptons do not. All of them participate in the electroweak interaction. Both are sorted into three generations with increasing masses. A summary of the properties of the fermions can be found in table 2.2.

Fermions are classified by their quantum numbers. Each generation of leptons consists of one electrically charged (-1 e) and one neutral lepton[2]. The charged leptons (e, μ, τ) interact via the weak and the electromagnetic force. The neutral leptons (neutrinos ν) interact only via the weak force and are therefore hard to detect in experiments. Apart from their electric charge (q), leptons are further sorted according to different quantum numbers: the lepton flavour number ($L_{e/\mu/\tau}$) and the weak isospin (I_3).

For each charged fermion particle there exists an anti-particle with reversed signs of all quantum numbers. [3]

Each generation of quarks consists of one “up-type” quark with an electrical charge of +2/3e and one “down-type” quark with an electrical charge of -1/3e. Apart from their elec-

[2] The elementary charge is a constant of nature e $\approx 1.602 \cdot 10^{-19}$ C

[3] In the SM framework, neutrinos are massless Dirac particles, which have anti-particles. However, the possibility, for neutrinos to be their own anti-particles (Majorana particles), is still under investigation.

tric charge (q) quarks are classified by different flavour numbers: the baryon number (B), strangeness (S), charmness (C'), bottomness (B') and topness (T).

Additionally, (anti-)quarks carry (anti-)colour charge which can have one out of three values ((anti-)red, (anti-)green, (anti-)blue). Quarks are therefore the only elementary particles influenced by all three forces. The conservation of colour charge results in colour-neutral bound states of quarks, the hadrons. For example the mesons are composed of one quark and one antiquark and the baryons are made out of three quarks.

Since particles from the second and the third generations quickly decay to first generation particles, matter in the universe is made out of first generation fermions only: electrons e, up quarks u and down quarks d (in proton and neutron baryons).

2.1.1 Quantum Chromodynamics

The strong interaction of particles is described by the theory of QCD, which was developed in the 1960s and 1970s [36–42] based on the Yang-Mills-theory [43]. It is a non-Abelian gauge theory based on the $SU(3)_C$ symmetry group, whose charge is called colour C. The gauge-invariant Lagrangian of QCD is defined as[4]:

$$\mathscr{L}_{\text{QCD}} = \underbrace{\sum_{j=1}^{n_f} \overline{q}_j (i D_\mu \gamma^\mu - m_j) q_j}_{\text{Quarks}} - \underbrace{\frac{1}{4} \sum_{a=1}^{8} G^a_{\mu\nu} G^{\mu\nu}_a}_{\text{Gluons}}, \tag{2.3}$$

where n_f is equal to the 6 quark flavours, γ^μ denotes the Dirac matrices, the six quark fields q_j with their corresponding masses m_j are defined by the quark field spinors $q_j = (q^1_j, q^2_j, q^3_j)$ (1,2,3 are the three colour states: red, green, blue). The gauge bosons mediating the strong interaction of coloured quarks are the massless gluons, which carry both colour and anti-colour leading to eight coloured gluons in total. The eight gluon fields G^a_μ correspond to the eight massless gluons. The covariant derivative is defined:

$$D_\mu = \partial_\mu - i g_s T_a G^a_\mu, \tag{2.4}$$

where T_a are the eight generators of the $SU(3)_C$ symmetry group and $g_s = \sqrt{4\pi\alpha_s}$ is the gauge coupling parameter with the coupling constant α_s. The field strength tensor $G^a_{\mu\nu}$ based on the gluon fields G^a_μ and the structure constant f_{ABC} of the SU(3) symmetry group can be written as:

$$G^a_{\mu\nu} = \partial_\mu G^a_\nu - \partial_\nu G^a_\mu - g_s f_{ABC} G^b_\mu G^c_\nu \tag{2.5}$$

[4] In this thesis the Einstein summation convention is used, where a summation over upper and lower indices is implied.

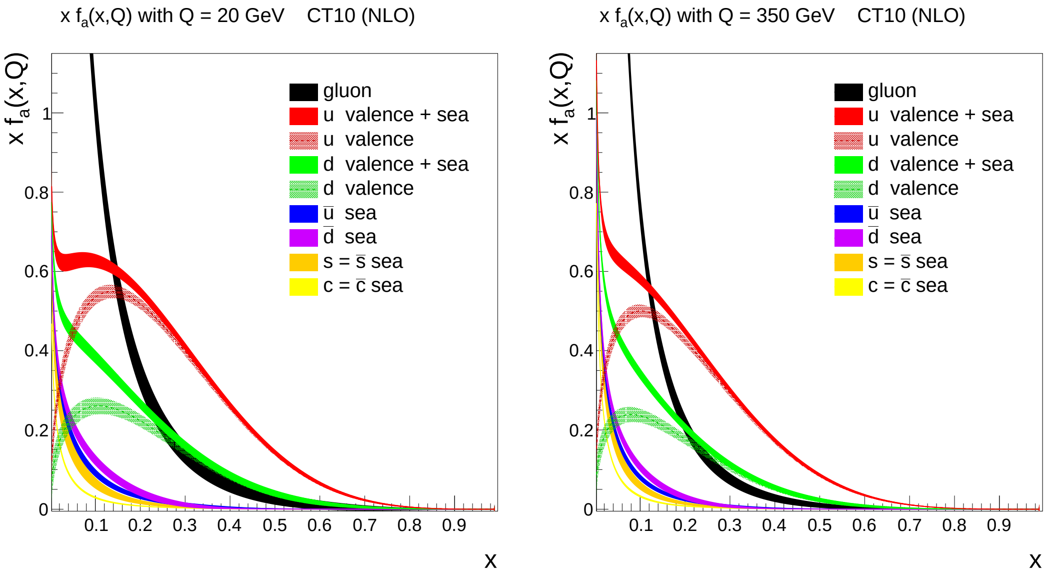

Figure 2.1: Parton distribution functions $x \cdot f_a(x,Q)$ for partons in the proton, at a hard scale Q = 20 GeV (left) and 350 GeV (right) as a function of x as calculated with the CT10 PDF set [44] using LHAPDF libraries [45–48].

The last term of the field strength tensor $G^a_{\mu\nu}$ appears due to the non-Abelian nature of the $SU(3)$ symmetry group. The gluon fields, carrying colour charge themselves, have therefore the ability to self-interact. The self-interaction of the gluons leads to special properties of the strong interaction. Firstly, at decreasing distances (increasing energies) the strong coupling constant converges to zero, where the interaction of the quarks and gluons is similar to that of free particles. This feature is called asymptotic freedom. Secondly, at increasing distances (decreasing energies) the strong force on a quark in the colour field becomes stronger until it is energetically favourable to produce new quark-antiquark pairs instead of compensating the colour imbalance with gluon exchange. Therefore free colour charged quarks cannot be observed. This feature is known as confinement. Instead colour-neutral hadrons are formed as mentioned above, a process known as hadronization.

Hard scattering phenomena involving hadrons in the initial state depend on a precise knowledge of the hadron structure, because the actual interactions in hadron colliders occur between the constituents of the hadron, the partons (identified with gluons and quarks) [49]. A formulation by Feynman in 1969 [50] to describe deep inelastic scattering led to the parton model, which describes hadronic collisions at high energies. Each hadron carrying a momentum $\vec{P}$ is composed of partons, moving collinearly with the hadron and carrying a momentum fraction $\vec{p} = x\vec{P}$. The momentum distributions of the partons $f_a(x,Q)$, the **Parton Distribution Functions** (PDFs), are defined as the probability density to have a parton of flavour a with a certain longitudinal momentum fraction x scattered at the momentum transfer Q [49]. PDFs cannot be obtained by perturbative QCD calculations and are measured experimentally for a range of x and Q values. A set of perturbative differential equations describes the evolution of the PDFs at a renormalisation scale[5] μ, the renormalisation group equation DGLAP (Dokshitzer-Gribov-Lipatov-Altarelli-Parisi) [51–53]. They can be used to extrapolate to different Q^2 [29, 30, 35, 49].

PDFs are obtained at Leading-Order (LO) and Next-to-Leading-Order (NLO) accuracy by global fits to experimental data from deep inelastic scattering, Drell-Yan ($Z/\gamma^* \to ll$) and jet production covering numerous x and Q values by various collaborations, e.g. the CTEQ (The Coordinated Theoretical-Experimental Project on QCD) [44], NNPDF (Neural Network PDF) [54] and MSTW (Martin-Stirling-Thorne-Watt) [55] collaborations. The behaviour of the PDFs of the proton as a function of x, at a hard scale Q = 20 GeV and also 350 GeV ($\approx \mathrm{M}_{t\bar{t}}$) is shown in figure 2.1 for the CT10 PDF set [44]. At small momentum fractions up to x≈0.2 the gluon dominates the proton structure, whereas at higher momentum fractions the valence quarks (up and down quarks) dominate the distributions.

2.1.2 Electroweak Theory

The electromagnetic interaction is fully described by the theory of Quantum Electrodynamics (QED) developed in the late 1940s [56–59]. QED describes the interaction of electrically charged particles through the exchange of photons. QED is an Abelian gauge theory introducing a massless gauge field A to establish local gauge invariance under the $U(1)_q$ symmetry group of electric charge q.

Early attempts by Fermi in the 1930 to describe beta decays [60], evolved into the formulation of the weak interaction in the 1950s [61, 62] as an effective quantum field theory, Quantum Flavour Dynamics (QFD), based on the $SU(2)_I$ symmetry group of the weak isospin I. The weak interaction does not couple to right-handed leptons in the SM [63, 64].[6] This was incorporated in 1958 by the V-A (vector minus axial vector) Langrangian for weak interactions [65]. In the V-A theory the weak force only couples to left-handed particles and right-handed antiparticles and parity is not conserved[7]. The weak interactions can be categorised into charged-current interactions mediated by charged bosons $W^\pm$ and neutral-current in-

[5] μ is the factorisation scale separating short and long distance physics phenomena and is usually chosen to be the same as the renormalisation scale.

[6] There are no right-handed neutrinos in the SM. However, they might exist and could be massive candidates for dark matter.

[7] Actually the weak interaction is the only interaction which also violates CP-Symmetry (Charge Conjugation-Parity symmetry), which has been observed in the neutral kaon sector and various B meson decays.

teractions mediated by a neutral Z boson. The weak force is the only interaction, which is able to change quark flavors.

In the early 1960s the theory of QED and QFD were unified into the electroweak (EW) theory [66, 67] by combining the $U(1)_q$ and $SU(2)_I$ symmetry groups into one new gauge theory based on the $SU(2)_L \otimes U(1)_Y$ symmetry group[8]. The weak interaction and the electromagnetism can be described as different aspects of the same force at or above the EW scale.

Leptons are arranged in left-handed weak isospin doublets and the charged right-handed leptons in weak isospin singlets due to the maximal parity violation in the weak interaction:

$$\begin{pmatrix} I_3 = 1/2 \\ I_3 = -1/2 \end{pmatrix} = \begin{pmatrix} \nu_{e_L} \\ e_L^- \end{pmatrix}, \begin{pmatrix} \nu_{\mu_L} \\ \mu_L^- \end{pmatrix}, \begin{pmatrix} \nu_{\tau_L} \\ \tau_L^- \end{pmatrix}, \qquad (I_3 = 0) = e_R^-, \mu_R^-, \tau_R^- \tag{2.6}$$

A similar notation can be defined for the quarks (with their colour α = 1,2,3), where the weak eigenstates (d',s',b') can be transformed linearly into mass eigenstates (d,s,b) via the Cabbibo-Kobayashi-Maskawa (CKM)-Matrix [68]:

$$\begin{pmatrix} I_3 = 1/2 \\ I_3 = -1/2 \end{pmatrix} = \begin{pmatrix} u_L^\alpha \\ d_L^{\prime\alpha} \end{pmatrix}, \begin{pmatrix} c_L^\alpha \\ s_L^{\prime\alpha} \end{pmatrix}, \begin{pmatrix} t_L^\alpha \\ b_L^{\prime\alpha} \end{pmatrix}, \qquad (I_3 = 0) = u_R^\alpha, d_R^\alpha, c_R^\alpha, s_R^\alpha, t_R^\alpha, b_R^\alpha, \tag{2.7}$$

The Lagrangian of the EW Theory can be written as:

$$\mathscr{L}_{\mathrm{EWT}} = \underbrace{\sum_{j=1}^{3} i\overline{\Psi_j}(x)\gamma^\mu D_\mu \Psi_j(x)}_{\text{Fermions}} \underbrace{- \frac{1}{4} B_{\mu\nu}B^{\mu\nu} - \frac{1}{4} W^j_{\mu\nu} W_j^{\mu\nu}}_{\text{Gauge fields}} \tag{2.8}$$

The first part of the Lagrangian describes the kinetic energy of the fermions $\Psi(x)$ and their interaction with the gauge fields. The second part of the Lagrangian describes the kinetic energy of the gauge bosons and their self-interaction. $W^j_{\mu\nu}$ and $B_{\mu\nu}$ are the field strength tensors for the weak isospin and weak hypercharge fields, respectively. The three gauge fields of the weak isospin for the $SU(2)$ symmetry group are W^j_μ (j = 1,2,3). The components of the weak isospin can be expressed through the Pauli matrices σ_j, which are the generators of the $SU(2)$ symmetry group. The massless gauge field of the weak hypercharge Y from the $U(1)$ symmetry group is B_μ. The weak hypercharge Y is associated with the generator of the $U(1)$ symmetry group. The covariant derivative is defined, where g is the coupling constant of $SU(2)_L$ and g' of $U(1)_Y$, respectively:

$$D_\mu = \partial_\mu - ig\frac{\sigma_j}{2} W^j_\mu(x) - ig'\frac{Y}{2} B_\mu(x) \tag{2.9}$$

The gauge bosons W^j_μ and B_μ of the EWT can be transformed to mass eigenstates, the $W^\pm$, Z and γ bosons. The $W^\pm$ bosons are linear combinations of the W^1_μ and W^2_μ gauge bosons.

[8] The weak hypercharge is defined as $Y_W = 2(Q - I_3)$.

The neutral-current-interactions via the Z and γ bosons are orthogonal combinations of the gauge fields B_μ and W^3_μ with A_μ being the photon field and Z_μ the Z boson field:

$$W^\pm_\mu = \frac{1}{\sqrt{2}}(W^1_\mu \mp iW^2_\mu) \qquad \begin{pmatrix} A_\mu \\ Z_\mu \end{pmatrix} = \begin{pmatrix} \cos\theta_W & \sin\theta_W \\ -\sin\theta_W & \cos\theta_W \end{pmatrix} \begin{pmatrix} B_\mu \\ W^3_\mu \end{pmatrix} \tag{2.10}$$

The weak mixing angle θ_W (Weinberg angle[9]) describes the mixing between $SU(2)$ and $U(1)$ and has the following correlation: $\tan(\theta_W) = \frac{g}{g'}$.

In this form the EWT is not renormalisable (e.g. WW scattering violates unitarity). Furthermore, in contrast with observation, there is no explicit mass term for the fermions and the gauge bosons $W^\pm$ and Z are massless. The SM solution to these problems is described in the next subsection.

2.1.3 Electroweak Symmetry Breaking : Brout-Englert-Higgs Mechanism

The minimal solution for an additional mechanism preserving gauge invariance, leading to a renormalisable theory and giving mass to the fermions and the appropriate gauge bosons $(W^\pm, Z)$ was proposed in the 1960s by Brout, Englert, Higgs (BEH) and others simultaneously[4–6]. The proposed BEH-mechanism leaves the Langrangian invariant under the $SU(2)_L \otimes U(1)_Y$ symmetry group. Mass terms are generated by breaking local gauge invariance in the $SU(2)_L \otimes U(1)_Y$ symmetry group in the quantum vacuum state only. In this process a new massive scalar particle, the Higgs boson H^0 is generated[10].

The BEH-mechanism introduces a complex scalar $SU(2)$ doublet field Φ(x) with hypercharge Y = 1 adding four degrees of freedom:

$$\Phi(x) = \begin{pmatrix} \Phi^+(x) \\ \Phi^0(x) \end{pmatrix} = \frac{1}{\sqrt{2}} \begin{pmatrix} \Phi_1(x) + i\Phi_2(x) \\ \Phi_3(x) + i\Phi_4(x) \end{pmatrix} \tag{2.11}$$

In addition a specific potential $V(\Phi(x))$, which is invariant under $SU(2)_L \otimes U(1)_Y$ gauge transformations, is added to the Lagrangian to couple $\Phi(x)$ to the gauge bosons:

$$\mathscr{L}_{\text{Higgs}} = \underbrace{(D_\mu\Phi(x))^\dagger(D^\mu\Phi(x))}_{\text{EW gauge bosons}} - V(\phi) \quad \text{with} \quad V(\Phi(x)) = \underbrace{\mu^2(\Phi(x)^\dagger\Phi(x)) + \lambda(\Phi(x)^\dagger\Phi(x))^2}_{\text{Higgs boson}}, \tag{2.12}$$

where μ and λ are free parameters and D_μ is the covariant derivative from EWT, see eq. 2.9. The first term describes the masses of the gauge bosons W^j_μ and B_μ and their interac-

[9] θ_W is determined experimentally: $\sin^2(\theta_W) = 0.23126 \pm 0.00005$ at the Z scale. [35]

[10] An explicit expression for the mass of the introduced scalar particle - also a consequence of the Englert and Brout mechanism - was only derived by Higgs, which resulted in the name "Higgs" boson for the new particle.

tion with the Higgs field. The $V(\Phi(x))$-term describes the Higgs boson mass and its self-interaction. The potential is chosen to have $\mu^2 < 0$, which generates a rotationally symmetric degenerate ground state $v = \frac{\mu^2}{\lambda}$, where v is the vacuum expectation value[11]. The choice of the ground state is arbitrary, here: $\Phi_1 = \Phi_2 = \Phi_4 = 0$, $\Phi_3 = v$ and can be expanded with the Higgs field $H(x)$:

$$\Phi^0(x) = \frac{1}{\sqrt{2}} \begin{pmatrix} 0 \\ v + H(x) \end{pmatrix} \tag{2.13}$$

Once the vacuum state $\Phi^0(x)$ is chosen, the underlying $SU(2)_L \otimes U(1)_Y$ symmetry group is spontaneously broken, giving rise to three massive Nambu-Goldstone boson mass eigenstates and an additional neutral massive scalar particle H^0, the Higgs boson. The remaining three mass degrees of freedom are absorbed by giving mass to the three gauge bosons $W^\pm$, Z. The ground state is invariant under $U(1)_q$ symmetry subgroup transformations, leaving the photon γ massless.

Mass terms for the fermions in the Lagrangian are generated by coupling the Higgs doublet to the fermion fields:

$$\mathscr{L}_{\text{Yukawa}} = \underbrace{g_f^1(\overline{\Psi}_L(x)\Phi(x)\Psi_R(x))}_{\substack{\text{“down-type” -} \\ \text{fermion}}} + \underbrace{g_f^2(\overline{\Psi}_L(x)\widetilde{\Phi^c}(x)\Psi_R(x))}_{\substack{\text{“up-type”-} \\ \text{fermion}}} + h.c., \quad \widetilde{\Phi^c}(x) = -\frac{1}{\sqrt{2}} \begin{pmatrix} v + H(x) \\ 0 \end{pmatrix}, \tag{2.14}$$

where g_f^1 and g_f^2 contain the Yukawa couplings g_f of the fermions to the Higgs field. The mass terms of the gauge fields and the fermions can be extracted from the Lagrangian:

$$M_W = \frac{1}{2}vg \qquad M_Z = \frac{1}{2}\sqrt{g^2 + g'^2}\,v = \frac{M_W}{\cos\theta_W} \qquad M_H = v\sqrt{2\lambda} \qquad M_f = \frac{1}{\sqrt{2}}g_f v \tag{2.15}$$

In the SM the strength of the Yukawa couplings of fermions to the Higgs boson is proportional to the fermion masses, therefore the heaviest known fundamental particle, the top quark, with a mass close to the EW scale, might give further information about the mechanism of symmetry breaking in the EWT.

The described BEH-mechanism was combined with the EWT in the late 1960s by Weinberg and Salam [69, 70]. A couple of years later t' Hooft published the important proof that spontaneously broken non-Abelian gauge theories are renormalisable[71]. The belief in the SM was further strengthened by the discovery of the $W^\pm$ and Z bosons in 1983 at CERN [72, 73]. After decades of unsuccessful searches, a new particle consistent with the SM Higgs boson was finally discovered with a mass of 125 GeV at the LHC in 2012 [1–3].

[11] The vacuum expectation value v can be determined from muon decays via the Fermi constant G_F: $v = \sqrt{(\sqrt{2}G_F)^{-1}} \approx 246\,\text{GeV}$. This energy scale is known as the EW scale.

2.2 Limitations of the Standard Model

Despite the tremendous success of the SM and its excellent agreement with the results of particle physics experiments, a number of fundamental phenomena in nature cannot be explained, indicating that the SM is an incomplete theory. Some of the main limitations are listed in this section:

Gravity and a Grand Unification Theory Gravity is one of the four fundamental forces in nature and cannot yet be described by a renormalisable QFT in the SM framework. Furthermore the ambition to unify all forces of the SM in one interaction close to the Planck scale ($E_p \approx 10^{19}$ GeV) by a Grand Unification Theory (GUT) cannot be pursued in the SM framework without new physics.

Dark Matter and Dark Energy Cosmological observations[74, 75] have shown that SM particles represent only 5% of the content of the universe. The mechanism which expands and accelerates the universe is unknown and called the dark energy, contributing $(68.5^{+1.7}_{-1.6})\%$ [35] to its total energy density. Galactic rotation velocities and other gravitational interactions in the universe are explained by dark matter, accounting for $(26.5 \pm 0.11)\%$ [35] of its composition. An appealing scenario is, that dark matter candidates are assumed to be massive, weakly interacting, neutral, stable particles, but many alternative options have been proposed. The SM does not contain viable candidates for dark matter particles and cannot explain the accelerated expansion of the universe (dark energy).

Neutrinos Neutrinos are massless Dirac particles in the SM framework, but the observation of neutrino oscillations[76, 77] requires neutrinos to have non-zero mass. In addition, whether neutrinos are Dirac or Majorana particles is still unknown.

Matter-Antimatter Asymmetry At the big bang the same amounts of matter and antimatter should have been created, which would have resulted in their very rapid annihilation. However the absence of antimatter in the observable universe indicates that matter and antimatter are either separated in space or another unknown mechanism has led to an excess of matter. Such a mechanism could for example be CP symmetry violation, but the observed CP violation in the weak interaction is insufficient to explain this phenomenon by several orders of magnitude. No explanation has been found yet.

Strong CP Problem The strong interaction could contain a term in the Lagrangian, which violates CP symmetry: $\mathscr{L}_{\not{C}\not{P}} \propto \theta\, G_{\mu\nu}\tilde{G}^{\mu\nu}$. However these CP violating effects have not been observed in experiments, e.g. the measurement of the electric dipole moment of the neutron gives $|\theta| \lesssim 10^{-10}$ [78], suggesting that the value of θ may be zero due to some additional symmetry. Some of the most compelling scenarios require θ to be a dynamical field, corresponding to additional particles.

Number of Parameters The SM depends on a large number of numerical parameters. Their values are measured experimentally and are not predicted by theory. This leads to the idea, that the SM is an effective low-energy approximation of a more fundamental theory.

Hierarchy Problem The masses of the SM particles are introduced through the spontaneous symmetry breaking mechanism caused by the vacuum expectation value of the Higgs field (compare section 2.1.3). The bare Higgs boson mass receives large radiative corrections from loop diagrams due to the presence of virtual particles, which diverge quadratically with the cutoff scale Λ:

$$\delta m_H^2 \propto \frac{|g^*|^2}{16\pi^2} \cdot \Lambda^2, \tag{2.16}$$

where g^* is a gauge (or Yukawa) coupling constant e.g. g_f, g' or λ. The largest radiative contributions to the Higgs mass originate from one-loop diagrams with top quarks (g_f), followed by $SU(2)$ gauge bosons (g') and the Higgs boson itself (λ). The sum of these corrections is included in the total Higgs mass. The cutoff scale Λ can be interpreted as the energy scale where new physics become important and the SM computations become insufficient. This scale Λ is reached latest at the Planck scale ($E_p \approx 10^{19}$ GeV), but the observed particle at LHC consistent with the Higgs boson at $\approx$125 GeV indicates that the Higgs mass is below the Planck scale by many orders of magnitude. This is known as the Hierarchy problem. Extraordinary cancellations would be required to obtain the observed Higgs boson mass within the SM. Therefore to stabilise the Higgs boson mass a new mechanism is needed, which typically requires new heavy particles to cancel the contributions from loop corrections.

2.3 Going beyond the Standard Model

To address all these limitations theoretical particle physicists have proposed a large variety of possible extensions to the SM over the last decades. Especially the questions of the origin of the Higgs mass stability and whether the BEH mechanism is realised in the minimal realisation of the SM give rise to numerous theoretical attempts to guide the experimental searches in high energy experiments. A very brief and not complete overview of the most appealing extensions will be given in this section. In the analyses presented in this thesis searches for new heavy gauge bosons (W′ , Z′) and new heavy fermions (T′) are performed, therefore only models predicting these new heavy particles will be discussed.

One of the most general extensions of the Lorentz symmetry, inducing transformations of bosons into fermions and vice versa, are so-called **supersymmetric** models [7, 8] introducing new heavy superpartners to the SM bosons and fermions. A prominent alternative to supersymmetric models are **composite Higgs models** [79–81] where the Higgs boson is a bound state of more fundamental constituents coupled by a new strong interaction, which additionally predicts new particles. Λ is the scale, where the composite nature of the Higgs boson would become relevant. Composite Higgs models can be categorised into models where the Higgs boson is a generic bound state of a new strong force and models, where the Higgs boson appears as a Nambu-Goldstone boson[12] of a spontaneous symmetry breaking. Generic composite Higgs models face difficulties due to electroweak precision measurements, which typically reject new strong interactions below 10 TeV.

Another class of models, **Little Higgs models**, remain perturbative up to a new strong interaction scale Λ by a new mechanism called “collective symmetry breaking”. In Little Higgs models [9, 21, 24–27] the Higgs boson appears as a pseudo-Nambu-Goldstone boson. An approximate global symmetry G is spontaneously broken at a higher scale Λ with the vacuum expectation value f and generates massless Nambu-Goldstone bosons in the process. A subgroup of G is a direct product of one or more symmetry gauge groups $[G_1 \otimes G_2 \otimes ..]$ each containing a $SU(2) \otimes U(1)$ subgroup. In addition the global symmetry $[G_1 \otimes G_2 \otimes ..]$ is broken explicitly to give rise to (new) gauge and (new) Yukawa interactions to the Nambu-Goldstone bosons, now becoming massive pseudo-Nambu-Goldstone bosons. The explicit symmetry breaking is performed in a collective way e.g. simultaneous breaking of the subgroups in the little Higgs Lagrangian allows for mass and potential terms for the pseudo-Nambu-Goldstone bosons. Typically the extended gauge group $[G_1 \otimes G_2 \otimes ..]$ is broken to the SM $SU(2)_L \otimes U(1)_Y$ symmetry group at the same vacuum expectation value f and contains new heavy gauge bosons mediating new gauge interactions. The Higgs potential triggers

[12] Goldstone's theorem: For each spontaneously broken global symmetry generator the theory contains one massless scalar field: the Nambu-Goldstone Boson [82].

the usual electroweak symmetry breaking at the scale v. The collective symmetry breaking ensures the absence of quadratic divergences to the Higgs potential on one-loop level: The gauge couplings to the Higgs boson are arranged to cancel the quadratic divergences induced by the SM gauge bosons by quadratic divergences by new heavy gauge bosons at loop level. Little Higgs models also predict new fermions, which cancel the quadratic divergences from Yukawa couplings to the Higgs boson.
Little Higgs theories are valid up to a cut off scale $\Lambda \approx 4\pi f$, where the physics becomes strongly coupled and an even more fundamental theory is required.
The mechanism of Little Higgs models can be specified in one of its prominent minimal implementations: **Littlest Higgs models** [25, 83]. Littlest Higgs models start with a $SU(5)$ global symmetry group incorporating a locally gauged subgroup $G_1 \otimes G_2 = [SU(2)_1 \otimes U(1)_1] \otimes [SU(2)_2 \otimes U(1)_2]$, which is broken spontaneously down to its subgroup $SO(5)$ via its vacuum expectation value of order f giving rise to 14 massless Nambu-Goldstone-bosons. At the same time the gauge symmetry $G_1 \otimes G_2$ is also broken explicitly into its subgroup $SU(2)_L \otimes U(1)_Y$ at scale f inducing a potential for the remaining pseudo Nambu-Goldstone bosons, decomposing into a weak doublet H, the SM Higgs, and a weak triplet ϕ. At the EW scale the usual electroweak symmetry breaking of the SM gauge group down to $U(1)_q$ occurs induced by the Higgs potential.

Models avoiding elementary scalars have also been proposed e.g. **Technicolor** [84] theories, where the electroweak symmetry breaking is achieved through strong dynamics instead of a Higgs boson. Obviously the discovery of a particle consistent with the Higgs boson constrains these models immensely. Related **Topcolor** [22, 85, 86] theories describe the new strong interactions through top quark and other massive fermions, which act effectively like the Higgs boson. Massive neutral gauge bosons ('colorons') appear as a resonant structure in SM top pair continuum production due to their favoured decay into top quark pairs. Many models predict similar additional resonant components (Z$'$ s) to the SM top quark pair distribution and are studied in the Z$'$ search in this thesis. Extended gauge theories predict **heavy colourless Z-like bosons** [87–89] or coloured heavy neutral gauge bosons, **axigluons**, in chiral colour models [90, 91]. Additional **massive scalar or pseudoscalar Higgs Bosons** would preferably also decay into SM top quark pairs [92]. Other compelling theories add **extra dimensions** to the observed three spatial and one temporal dimension(s) to account for the weakness of gravity. The nature of the extra dimensions range from additional large spatial dimensions in **ADD models** [93, 94] to microscopic (but larger than the Planck length) curled up extra dimensions in **Kaluza-Klein theories** [95–97]. Extensions of **Randall-Sundrum models** [98] predict Kaluza-Klein excitations [99, 100] or gravitons [101] as an enhancement of the top pair invariant mass spectrum.

This variety of theoretical models as well as their predicted phenomena provides a strong motivation for model-independent searches. The discovery of the Higgs boson and electroweak precision tests restrict many of the predicted new particles to multi-TeV scales in indirect limits [102, 103]. Nevertheless these calculations often rely on model parameters and limits from direct experimental searches add valuable supplementary results.

2.4 Production of dilepton and missing transverse energy final states at hadron colliders

The generic decay chain presented in the diagram in figure 1.1 contains the final states considered in this thesis. A new pair produced $\mathrm{T}'\overline{\mathrm{T}'}$ quark is decaying into new W' bosons and jets, whereby each W' boson decays leptonically into one charged lepton (either electron or muon) and one neutrino. The two charged leptons, the two jets and the neutrinos, the latter measured as missing transverse energy $E_{\mathrm{T}}^{\mathrm{miss}}$ in the experiment, are the final states in this analysis. For the first one-dimensional application, the W' bosons are replaced by SM W bosons. The second one-dimensional application studies a new heavy resonance Z' decaying into top quark pairs, as in figure 2.2. SM top quarks decay dominantly into SM W bosons and b quarks, due to the CKM Matrix element $V_{tb} \approx 1$.

In the diagram of the generic signal decay chain the new T' quark can be replaced by a SM top quark and the W' boson by a SM W boson to result in the dominant SM background of this analysis. Top quark pairs are dominantly produced via gluon fusion in pp collisions at high energies. Additional SM backgrounds are expected from single top quarks as produced in electroweak interactions via the t-channel, s-channel and in associated production with a W boson as well as Drell-Yan (DY) processes: $Z/\gamma^* (\rightarrow ll)$ + jets. The production of two electroweak gauge bosons (WW, ZZ and WZ), here labelled “dibosons”, is also considered as a background source as well as single W boson production in association with jets and multijet QCD events due to their large production cross section.

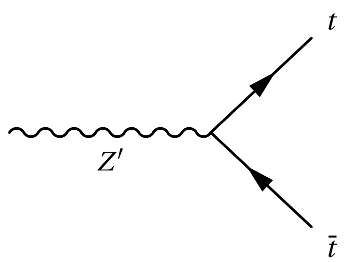

Figure 2.2: Feynman diagram of a new heavy resonance Z' , decaying into SM top quark pairs.

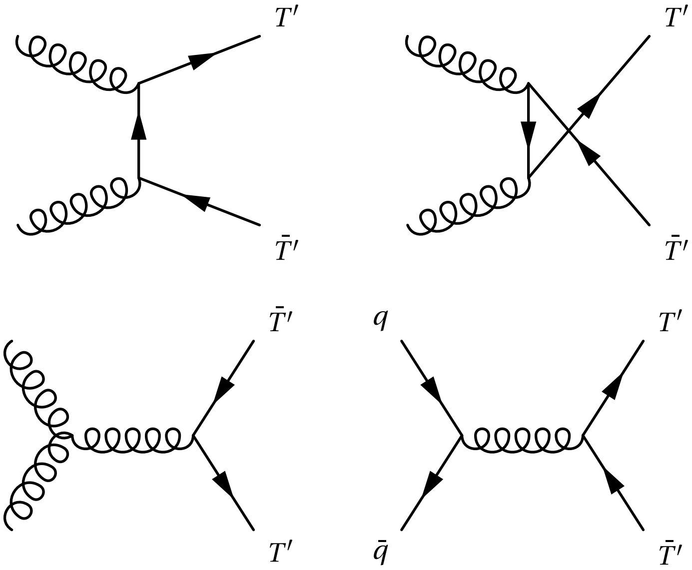

Figure 2.3: Feynman diagrams of leading order $T'\overline{T'}$ quark pair production at hadron colliders.

The leading order $T'\overline{T'}$ quark pair production Feynman diagrams at hadron colliders are shown in figure 2.3.

CHAPTER 3

Experimental Setup

The data which is analysed in this thesis was collected by the CMS experiment at the Large Hadron Collider in Geneva, Switzerland. In this chapter the collider, the CMS experiment and the reconstruction algorithms used to build the physics objects, which are required for the analysis, are described.

3.1 The Large Hadron Collider

The Large Hadron Collider (LHC) [104, 105] is a particle collider located at the European Organisation for Nuclear Research laboratory (CERN) near Geneva, Switzerland. The LHC is designed to accelerate two beams of either protons or heavy ions in opposite directions. With a circumference of 26.7 km and a design centre of mass energy $\sqrt{s} = 14\,\mathrm{TeV}$ for pp collisions, the LHC is the world's largest collider, reaching the highest energies. During the first running period (Run I) from 2010 to 2012 the LHC was operating at a centre of mass energy of 7 TeV and 8 TeV for pp collisions. The work presented here analyses the data taken at $\sqrt{s} = 8\,\mathrm{TeV}$ during pp collisions in 2012.

Protons, extracted from hydrogen gas by stripping them from the electrons, are accelerated to 50 MeV in the linear accelerator (LINAC 2). They are further formed in bunches and injected in a sequence of accelerators: Starting with the Proton Synchrotron Booster (PSB) and the Proton Synchrotron (PS), the protons are accelerated to an energy of 26 GeV . The energy of the protons is furthermore increased in the Super Proton Synchrotron (SPS) to an energy

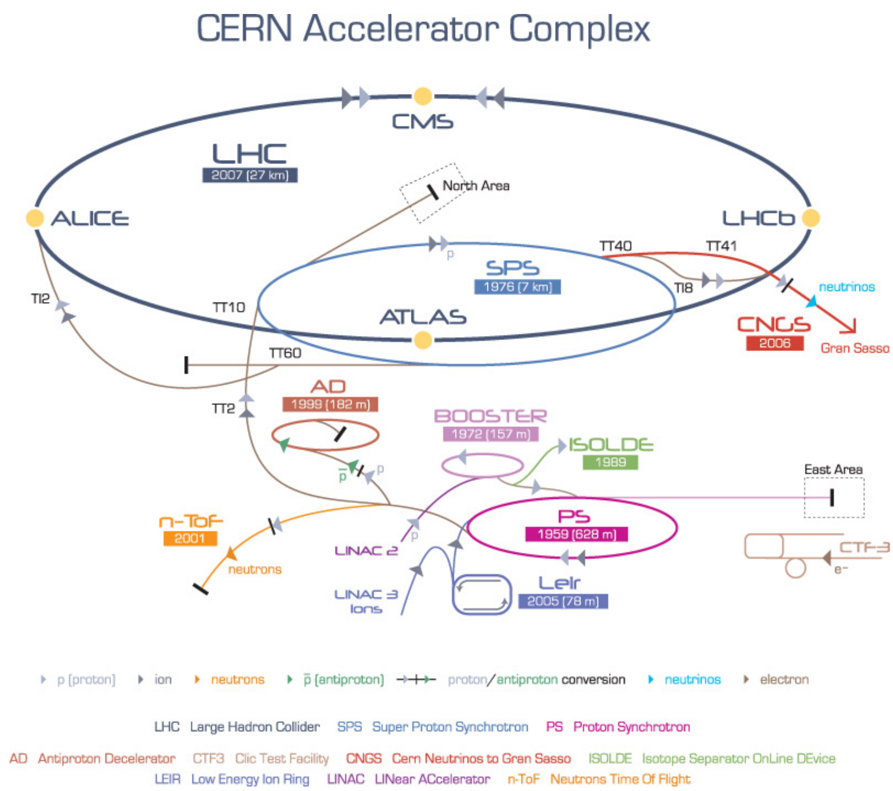

Figure 3.1: *Overview of the accelerator complex and the various experiments at CERN [107].*

of 450 GeV before being transferred to the LHC, where the protons can be accelerated up to the design energy of 7 TeV (4 TeV in 2012).
The particles are kept on a circular orbit via 1232 14.3 m long superconducting dipole magnets, which are cooled with 96 t of fluid helium to a temperature of 1.9 K to generate the required magnetic field of 8.33 T. Additionally 392 superconducting quadrupole magnets are used to focus the particles. Radio-frequency cavities increase the proton energy by 0.5 MeV per turn. At the design $\sqrt{s}$ of 14 TeV the particles will be bundled in 2808 bunches, separated by 25 ns, each containing $1.15 \cdot 10^{11}$ particles [104, 105]. In 2012 during Run I, 1374 particle bunches per fill were generated, separated by 50 ns, containing $1.6\text{-}1.7 \cdot 10^{11}$ protons per bunch [106].

In figure 3.1 the CERN accelerator complex is shown with its different pre-accelerators and experiments. In the LHC the proton (and heavy ion) beams are focused and brought to collision at four interaction points where four detectors are situated. The ATLAS (A Toroidal LHC ApparatuS) [108] and the CMS (Compact Muon Solenoid) [109] detectors, located at opposite points at the LHC (Point 1 and 5 respectively), explore a wide range of physics phenomena (general purpose detectors). The ALICE (A Large Ion Collider Experiment) [110] and the LHCb (LHC-Beauty) [111] detectors on the contrary are dedicated to more specific studies. ALICE, located at point 2, investigates the quark-gluon plasma created by heavy ion

Table 3.1: Overview of the performance parameters of the LHC in 2012 in comparison to the design values [106].

Parameter	Value in 2012	Design value
Beam energy [TeV]	4	7
β^* in interaction point 1,2,5,8 [m]	0.6, 3.0, 0.6, 3.0	0.55
Bunch spacing [ns]	50	25
Number of bunches N_b	1374	2808
Average protons per bunch $N_{i/j}$	1.6-1.7 $\cdot 10^{11}$	1.15 $\cdot 10^{11}$
Normalised emittance ϵ_n at start of fill [μm rad]	2.5	3.75
Peak luminosity L [$\mathrm{cm}^{-2}\,\mathrm{s}^{-1}$]	$7.7 \cdot 10^{33}$	$1 \cdot 10^{34}$
Maximal mean number of events per bunch crossing	≈40	19
Stored beam energy [MJ]	≈140	362

collisions and LHCb, located at point 8, focuses on B meson physics and the CP-symmetry violation.

The probability for a scattering event to occur is usually quoted in the form of a "cross section"[1] σ [28], which can be seen as an effective area. The performance of a particle collider is characterised by its luminosity. The cross section σ_s of a certain process s and the expected event rate dN_s/dt are connected through the instantaneous luminosity[2] $L(t)$ of the machine:

$$\frac{dN_s}{dt} = L(t) \cdot \sigma_s \tag{3.1}$$

In general the instantaneous luminosity for Gaussian distributed beams can be parametrised in terms of the revolution frequency f of the beams, the number of bunches N_b per beam and the number of particles per bunch $N_{i,j}$ in beam i and j, respectively:

$$L(t) = \frac{N_b N_i N_j f}{A} \overset{N_i \approx N_j}{=} \frac{N_b N_{i,j}^2 f}{4\pi\sigma_x^*\sigma_y^*} F = \frac{N_b N_{i,j}^2 f \gamma}{4\pi\epsilon_n \beta^*} F \tag{3.2}$$

The luminosity $L(t)$ is proportional to N_b, $N_{i,j}$, f and inversely proportional to A, the beam profile area perpendicular to the beam direction at the collision point, which can be expressed with the horizontal σ_x^* and vertical σ_y^* beam sizes at the interaction point. F describes the reduction factor due to the non-zero crossing angle of the beams. The second parametrisation in eq. 3.2 uses the normalised transverse emittance ϵ_n, the value of the beta function at the collision point β^* and the relativistic Lorentz factor γ.
For the LHC design instantaneous luminosity of $L = 10^{34}\ \mathrm{cm}^{-2}\,\mathrm{s}^{-1}$ up to 20 collisions per bunch crossing are expected, produced with a frequency of 40 MHz (25 ns bunch spacing). In 2012 a 50 ns bunch spacing was used resulting in a maximal mean of 40 events per bunch

[1]The cross section is measured in barn $b = 10^{-28} m^2$.
[2]The unit used for the instantaneous luminosity is $\mathrm{cm}^{-2}\,\mathrm{s}^{-1}$.

crossing, produced for a peak instantaneous luminosity of $L = 7.7 \cdot 10^{33}\ \mathrm{cm}^{-2}\mathrm{s}^{-1}$. An overview of the performance parameters of the LHC in 2012 in comparison to the design values can be found in table 3.1 [106].

The integrated luminosity[3] $\mathscr{L}$ is the delivered luminosity over the lifetime τ of a machine and is proportional to the amount of events recorded:

$$\mathscr{L} = \int^{\tau} L(t)\,dt \tag{3.3}$$

The luminosity is determined by each experiment separately and its measurement for the CMS detector is described in section 3.2.6.

3.2 Overview of the Compact Muon Solenoid Experiment

The CMS experiment is a large general purpose detector, addressing a variety of physics questions, which is located about 100 m underground at point 5 of the LHC accelerator complex [109]. It is 28.7 m long, has a diameter of 15 m and weighs 14k t. A schematic overview of the CMS detector can be found in figure 3.2. CMS is a hermetic detector consisting of a barrel part with cylindrical layers of subdetectors surrounding the beam pipe, each cylinder terminated by a plug (endcap) on each side of the interaction point. A superconducting solenoid with a length of 12.9 m and an inner diameter of 5.9 m produces a homogeneous field of up to 3.8 T, corresponding to a stored energy of 2.9 GJ. The strong field allows an accurate measurement of the momenta of charged particles crossing the magnetic volume. In addition it serves to confine low momentum particles from background processes to the region close to the interaction point, thus reducing the amount of particles reaching the outer subdetectors and assuring a lower occupancy.
Inside the magnet coil, in increasing radial distance from the interaction point, there is a silicon tracker system (pixel and strip sensors) as well as an electromagnetic (ECAL) and a hadronic (HCAL) calorimeter. As mentioned above these subdetectors are terminated by the corresponding endcaps, also placed inside the magnet volume. The muon system, serving to identify muons and provide a measurement of their momentum, is placed in the 10k t iron yoke, which returns the magnetic flux outside the magnet coil. The magnetic field in the yoke is ≈ 2 T, its polarity being opposite to that of the field inside the solenoid. The energies and momenta of all particles produced in the collisions are obtained by combining the information of all subdetectors, which are described in some detail below. A more detailed description can be found elsewhere [109].

[3] The integrated luminosity $\mathscr{L}$ is measured in inverse barn b^{-1}.

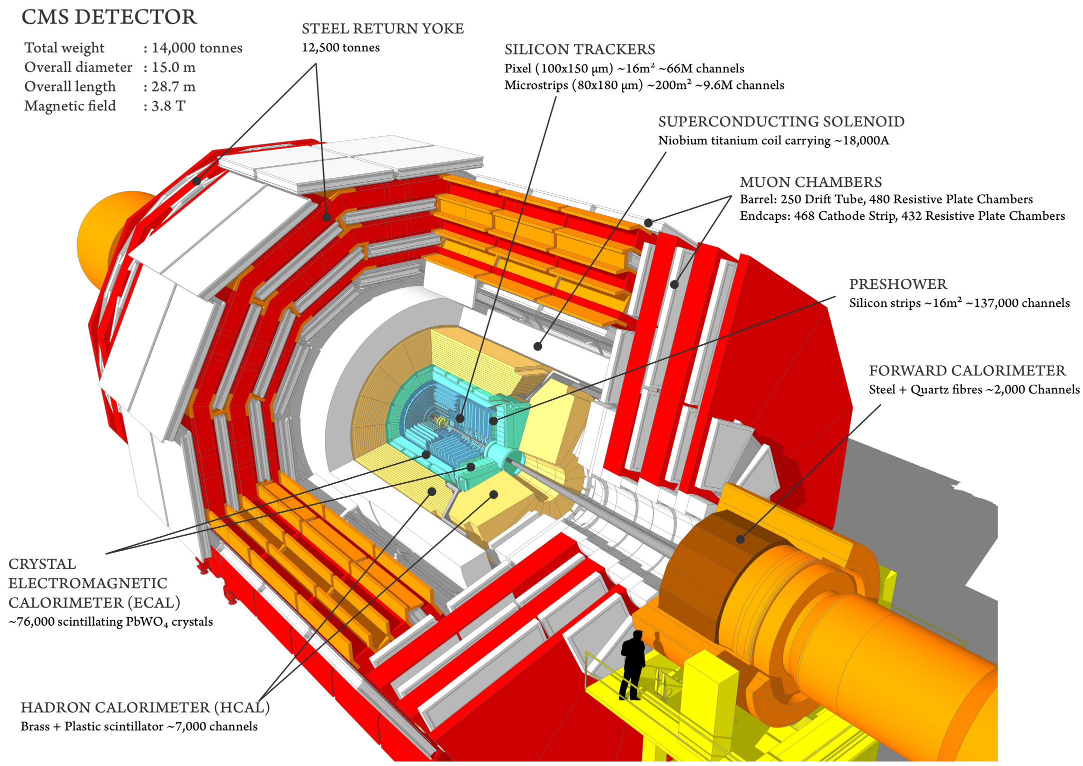

Figure 3.2: Schematic overview of the CMS detector [112].

Coordinate system conventions

The CMS experiment uses a right handed cartesian coordinate system with its origin at the nominal interaction point [113]. The x-axis points radially toward the centre of the LHC accelerator ring, the y-axis vertically upward and the z-axis along the beam direction. The azimuthal angle ϕ is measured with respect to the $+x$-axis in the $x-y$-plane and the polar angle θ with respect to the z axis, where θ is zero at the positive and π at the negative z-axis. The pseudorapidity η is defined as $\eta = -\ln(\tan(\theta/2))$. Differences in η are lorentz-invariant. The transverse momentum p_{T} is the momentum perpendicular to the LHC beam axis and the energy imbalance in the transverse plane is defined by the missing transverse energy $E_{\mathrm{T}}^{\mathrm{miss}}$. Angular distances in η and ϕ between physics objects originating at the interaction point are calculated by $\Delta R = \sqrt{(\Delta\eta)^2 + (\Delta\phi)^2}$.

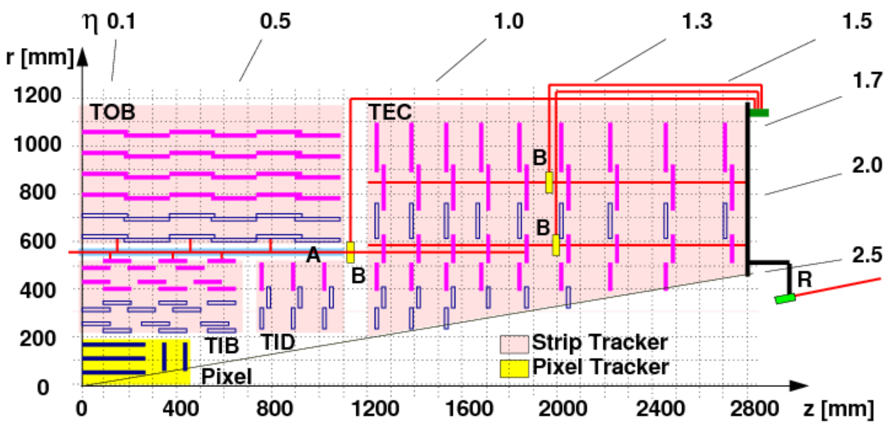

Figure 3.3: One quarter of the tracker layout of the CMS detector in the $r-z$ view: the pixel modules (dark blue on yellow) and the double sided modules (open blue rectangles) and single sided modules (solid magenta rectangles) of the strip detector [114].

3.2.1 Tracking System

The silicon tracker system is placed around the interaction point at the innermost layer of the CMS detector, where the rate of particles is around $10^7\ \frac{1}{s}$ at a distance of ≈ 10 cm from the interaction point. Handling the high track multiplicity and high bunch crossing rate requires high granularity and fast readout detectors. The system is divided into the inner pixel tracker and the outer strip tracker, where the particle flux is lower. The detectors are placed inside a volume with a length of 5.8 m and a diameter of 2.4 m, covering a pseudorapidity range $|\eta| < 2.5$, and are able to measure the trajectories of the particles and reconstruct the decay vertices. In figure 3.3 the tracker layout in a quarter of the CMS detector is shown.

Silicon Pixel Tracker Detector

The pixel tracker consists of three cylindrical barrel layers located at $r = 4.4$ cm , 7.3 cm and 10.2 cm with a length of 53 cm and two endcap disks on each side at $|z|$ of 34.5 cm and 46.5 cm covering the radial distance 6 - 15 cm in the $x-y$ plane. In total around 66 million silicon pixels are distributed over a surface of approximately 1 m^2. Each silicon pixel has a surface area of 100 x 150 μm^2, leading to an occupancy of 10^{-4} per pixel per bunch crossing and requiring the use of 16k readout chips. The spatial resolution[4] is 10 μm in the r-ϕ plane and 20 μm in the $r-z$ plane [109].

Silicon Strip Tracker Detector

The strip tracker detector consists of silicon strip layers located in the radial region from 20 to 110 cm with an overall length of 5.6 m. The 9.6 million silicon strips are structured in

[4] The r-ϕ resolution benefits from the Lorentz angle of 23^o in the barrel, spreading the ionisation charge over several pixels. In the endcap the pixel detector is rotated by 20^o to benefit from the same effect.

≈ 15.4k modules providing a total active area of approximately 200 m^2. The layout of one quarter of the tracker can be seen in figure 3.3. The detector is divided into four subsystems: the four cylindrical layers of the tracker inner barrel (TIB) covering the radial range 20 - 55 cm over a distance $|z| < 65$ cm . The six layers of the tracker outer barrel (TOB) surround the TIB up to a radius $r = 110$ cm . The nine disks of the tracker endcap (TEC) on each side are placed between 120 cm $< |z| <$ 280 cm . In the radial direction the TEC coverage extends up to $r = 100$ cm , while the innermost radius (starting at $r = 20$ cm) varies so that the range up to $|\eta| = 2.5$ is covered. The three layers of the tracker inner disks (TID) fill the gap between TIB, TOB and TEC. Both TEC and TID modules are arranged in rings with their strips pointing towards the beam line. The solid magenta rectangles in figure 3.3 represent single sided modules, where as the open blue rectangles are double-sided stereo modules, constructed from a pair of single sided modules rotated by 100 mrad with respect to each other to measure the other component (z in TIB/TOB and r in TID/TEC).
At a distance of $r < 60$ cm the particle flux is low enough to allow the use of silicon strip detectors with a minimum cell size of 10 cm x 80 μm and a thickness of 320 μm, leading to an occupancy of 2-3% per bunch crossing. The single point resolution in this detector varies from 23-35 μm in the r-ϕ plane and is 230 μm in the z direction in the TIB.
At a distance of $r > 60$ cm the approximate occupancy is around 1% with the silicon strips having a maximum cell size of 25 cm x 180 μm and a thickness of about 500 μm. Here the single point resolution in the r-ϕ plane varies from 35 to 53 μm and is 530 μm in the z direction of the TOB [109].

The transverse momentum resolution is ≈1.5% for tracks of low momentum charged particles (< 10 GeV) and ≈2.8% for high momentum muons (= 100 GeV) in the central region of the CMS experiment [115].

3.2.2 Electromagnetic Calorimeter

The ECAL consists of a total of 76k scintillating lead tungstate ($PbWO_4$) crystals located in a cylindrical barrel section and in the two endcap disks. The geometrical layout of the ECAL can be found in figure 3.4. The $PbWO_4$ crystals act as scintillator and absorber simultaneously and have been chosen due to their short radiation length [5] X_0 of 0.89 cm and their short Moliere radius [6] R_M of 2.2 cm , which ensure a high granularity with good energy resolution and a fast time response (80% of the emitted light in 25 ns). The light emitted by the

[5] The radiation length X_0 describes the length scale of the energy loss of an electromagnetic shower induced by a charged particle in a certain material and is defined as the mean distance over which a high-energy electron loses all but 1/e of its energy.
[6] The Moliere radius R_M describes the transverse expansion of an electromagnetic shower and is defined as the radius of a cylinder containing approximately 90% of the energy deposition of the electromagnetic shower.

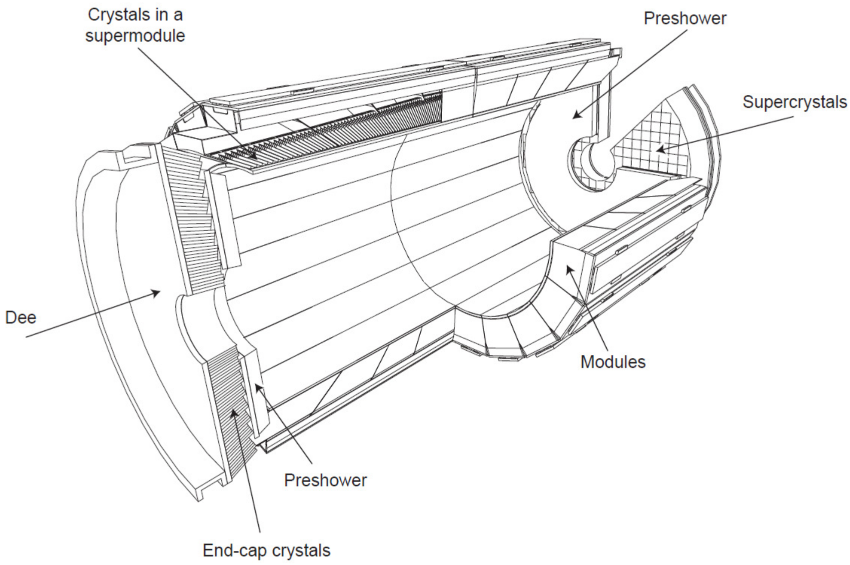

Figure 3.4: Geometric view of the ECAL [109, 116].

$PbWO_4$ crystals is read out by avalanche photodiodes in the electromagnetic barrel (EB) and vacuum phototriodes in the electromagnetic endcaps (EE).

The cylindrical EB calorimeter is located in a region of (1.29 - 1.75) m in r with a length of 6.09 m, thus covering $|\eta| < 1.479$ and has a volume of 8.14 m^3. It consists of 61200 23 cm long tapered crystals with a (2.2 x 2.2) cm^2 front face and a (2.6 x 2.6) cm^2 back face (25.8 radiation lengths). The crystals are inclined by 3^o with respect to a line through the nominal interaction point. The EB crystals are arranged into modules, whereby four modules (85 x 20 = 1700 crystals) are packed into one supermodule (compare figure 3.4).

The EE disks are located at a longitudinal distance $|z|$ = 3.14-3.9 m from the interaction point and cover the pseudorapidity range $1.479 < |\eta| < 3.0$. Each endcap disk is made of two so-called “Dee”s, each consisting of 3662 $PbWO_4$ crystals. A 22 cm long tapered $PbWO_4$ crystal has a (2.86 x 2.86) cm^2 front face and a (3 x 3) cm^2 back face pointing to a focus 1.3 m beyond the nominal interaction point. The 7324 crystals of an EE disk correspond to a thickness of 24.7 radiation lengths. An area of 5 x 5 crystals is defined as one supercrystal (compare figure 3.4). The transition region ($1.4442 < |\eta| < 1.566$) between the EB and the EE results in smaller reconstruction efficiencies and is not considered in analyses requiring good electron and/or photon reconstruction.

A preshower system is placed in front of the EE disks to improve the position resolution for electrons and photons and discriminate between highly energetic photons and two closely spaced lower energy photons coming from $\pi^0 \rightarrow \gamma\gamma$ decays. The 20 cm thick preshower detector has an inner radius of 45.7 cm , an outer radius of 123 cm and covers a region of $1.65 < |\eta| < 2.6$. This sampling calorimeter consists of two lead absorber layers with a thickness of 2 X_0 and 1 X_0, respectively, interleaved with two planes of silicon strip sensors.

The energy resolution of the ECAL is parametrised as a function of the energy E:

$$\frac{\sigma_E^{\mathrm{ECAL}}}{E} = \frac{S}{\sqrt{E/\,\mathrm{GeV}}} \oplus \frac{N}{E/\,\mathrm{GeV}} \oplus C, \tag{3.4}$$

where S is the stochastic term including contributions from shower containment and the number of photo-electrons. The term N is related to the electronics noise and C is a constant related to the calibration. Measurements taken with test beam electrons for the barrel geometry in 2004 have shown that the energy resolution and noise performance for the ECAL meet the design goals for the detector. The measured values were S = 2.8%, N = 12% and C = 0.3%[116, 117].

3.2.3 Hadronic Calorimeter

The central part of the hadron calorimeter is also located within the superconducting solenoid, surrounds the ECAL and is divided into the cylinder symmetrical hadronic barrel (HB) and the two hadronic endcaps (HE). It is a sampling calorimeter with brass absorber plates interleaved with plastic scintillator tiles acting as the active medium. The tiles are read out by multi-channel hybrid photo diodes via wavelength shifting fibres. In figure 3.5 the HCAL layout in one quarter of the CMS detector is presented.

The HB calorimeter consists of 70k scintillator tiles distributed in 2304 “towers” arranged in a projective geometry with a segmentation $\Delta\eta\, x\, \Delta\phi$ =0.087 x 0.087, each tower composed of 15 layers of 5 cm thick brass absorbers and 3.7 mm thick plastic scintillators. The innermost and outermost absorber plates are made of stainless steel to strengthen the mechanical structure. The innermost towers start with a 9 cm thick plastic scintillator layer, which col-

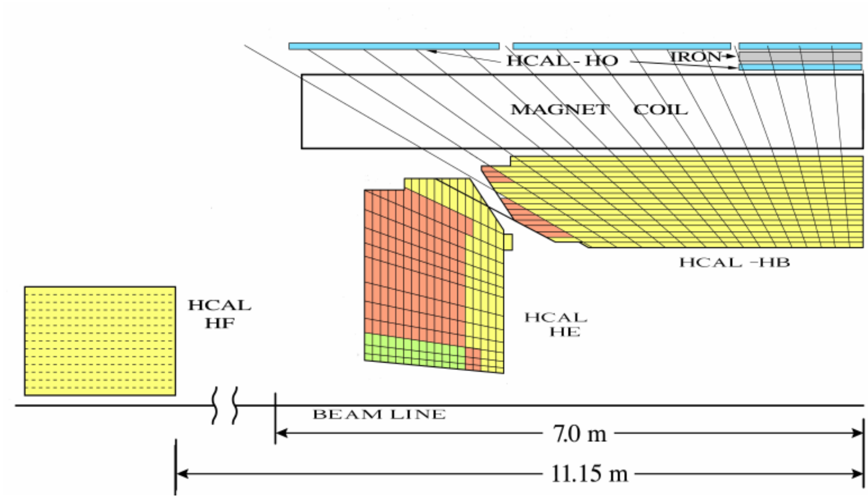

Figure 3.5: One quarter of the HCAL layout of the CMS detector in the $r-z$ view [118].

lects 1.5 times the energy in comparison to the other layers. The HB calorimeter covers a pseudorapidity of $|\eta| < 1.3$ and has an interaction length [7] 5.8 λ_I at $|\eta| = 0$ increasing to 10.6 λ_I at $|\eta| = 1.3$. The ECAL inside the HB calorimeter adds $\approx 1.1\ \lambda_I$.

In order to increase the number of interaction lengths in the barrel region and due to space limitations inside the magnet, an additional outer hadronic (HO) calorimeter is placed on the outer surface of the solenoid. It follows the segmentation geometry of the HB calorimeter, consisting of a 10 mm thick layer of scintillators, except in a region $|z| < 2.868$ m, where the HO consists of two 10 mm thick layers of scintillators on either side of a 19.5 cm thick iron absorber. The HO calorimeter covers $|\eta| < 1.3$, increases the minimal interaction lengths in the barrel region to 11.8 λ_I using the iron return yoke as an additional absorber material.

The HE calorimeter consists of 20k scintillator tiles distributed in 2304 towers per endcap disk with a granularity $\Delta\eta\, x\, \Delta\phi = 0.087\, x\, 0.087$ for $|\eta| < 1.6$ and $\Delta\eta\, x\, \Delta\phi \approx 0.17\, x\, 0.17$ for $|\eta| > 1.6$. The structure and design is similar to the HB calorimeter with larger brass absorbers of 8 cm . The HE calorimeter covers the pseudorapidity range $1.3 < |\eta| < 3.0$ and increases the interaction length to 10 λ_I using the ECAL crystals as an additional absorber material.

To close the detector hermetically and ensure a good reconstruction of $E_{\mathrm{T}}^{\mathrm{miss}}$ an additional hadronic forward (HF) calorimeter surrounds the beam pipe covering the radial range from 12.5 cm to 130 cm at a distance $|z| = 11.2$ m from the interaction point, thus enlarging the pseudorapidity coverage to $2.9 < |\eta| < 5.0$. The HF is a sampling calorimeter with 5 mm thick steel absorber plates interleaved with 0.6 mm thick layers of radiation hard quartz fibres, resulting in a thickness of 10 λ_I. They are readout by photo-multipliers in towers of $\Delta\eta\, x\, \Delta\phi = 0.175\, x\, 0.175$ except for the first ($\Delta\eta$=0.111) and the last ($\Delta\eta$=0.3) ring.

The energy resolution of the HCAL is parametrised as a function of the energy E:

$$\frac{\sigma_E^{\mathrm{HCAL}}}{E} = \frac{S}{\sqrt{E/\,\mathrm{GeV}}} \oplus C, \tag{3.5}$$

Test beam measurements in 2008 for a combined ECAL and HCAL structure for the barrel geometry resulted in the values S = (84.7±1.6)% and C = (7.4±0.8)% [118].

[7] The hadronic interaction length λ_I describes the length scale of the energy loss of an hadronic shower and is defined as the mean distance over which a high-energy hadron loses all but 1/e of its energy. It also describes the transverse expansion of a hadronic shower and is defined as the radius of a cylinder containing approximately 95% of the energy deposition by the hadronic shower. For heavy materials $\lambda_I >> X_0$, so that hadronic showers start later and are more widely spread than electromagnetic ones.

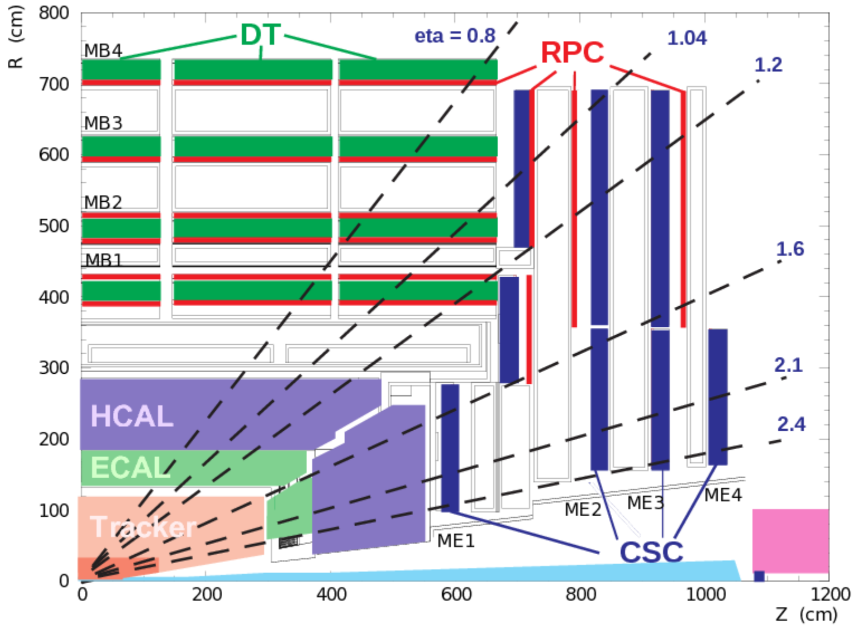

Figure 3.6: One quadrant of the muon system layout of the CMS detector in the $r-z$ view with the four DT stations in the barrel (MB1-MB4, green), the four CSC stations in the endcap (ME1-ME4, blue), and the RPC stations (red) [113].

3.2.4 Muon System

Outside the solenoid and embedded in the iron return yoke, the muon detector is equipped with three different types of gaseous subdetectors for muon identification and momentum measurement. In figure 3.6 the layout of the muon system in one quadrant of the CMS detector is pictured. In the barrel region with relatively low muon and neutron induced background rates, layers of drift tubes (DT), green-coded in the figure, are used up to $|\eta| = 1.2$. In the forward region both these rates are higher and therefore cathode strip chambers (CSC), pictured in blue in figure 3.6, are used in this region up to a pseudorapidity of 2.4. Additionally to the DTs and CSCs resistive plate chambers (RPCs) are installed (colored in red in figure 3.6). The 1400 muon chambers (250 DTs, 540 CSCs and 610 RPCs) have a total surface of 25000 m^2 with about 1 million electronic channels [119, 120].

Drift Tube Chambers

The muon barrel detector consists of 250 aluminium drift tube chambers, located in four layers inside the return yoke, labelled as muon stations MB1-4, and arranged in concentric cylinders at a distance of 4.0, 4.9, 5.9 and 7.0 m from the beam axis. Each layer is divided into 5 wheels and subdivided into 12 sectors each covering an azimuthal angle of 30^o. A DT cell consists of a high voltage carrying wire in the middle of a 4 cm diameter gas tube filled with a $Ar(85\%)/CO_2(15\%)$ mixture. A DT chamber consists of 12 layers of such cells, arranged in three groups of four, and has a size of about 2 m x 2.5 m. The middle group, rotated by 90^o, provides a measurement of the z coordinate parallel to the beam line and the two outside groups measure the perpendicular coordinate in $r-\phi$ direction. The outermost muon stations MB1 and MB4 have only eight layers of DT cells per chamber and measure only the $r-\phi$ direction. The two layers MB1 and MB2 carry RPCs on both sides, while layers MB3 and MB4 are combined with one RPC each (see figure 3.6). In the DT chambers the single point resolution is around 200 μm with a maximum drift length of 2 cm. For each reconstructed muon the position resolution is better than 1 mrad in ϕ and around 100 μm in $r-\phi$ [120]. For a highly energetic muon traversing all four DT and all six RPC stations, up to 44 measurements in the DT stations and 50 measurements in total are available for its reconstruction.

Cathode Strip Chambers

The two muon endcap detectors contain 270 CSC chambers each, distributed in four disks per endcap perpendicular to the beam line (labelled as the ME1 to ME4 stations) and covering $0.9 < |\eta| < 2.4$. A station is divided into 36 sectors each covering an azimuthal angle of 10^o. A CSC chamber is a trapezoidal proportional chamber consisting of six anode wire planes interleaved with seven radially arranged copper strip cathode panels in a gas volume filled with a $Ar(30\%)/CO_2(50\%)/CF_4(20\%)$ mixture and has a size of about 2-3 m x 1-1.5 m. A charged particle passing through the chamber produces a charge on the anode wire and an image charge on a group of cathode strips. In each CSC chamber up to six space coordinates (r, ϕ, z) are computed. The spatial resolution is about 100 μm and the angular resolution in ϕ is about 10 mrad [120].
Up to $|\eta| < 1.6$, 36 RPC modules are additionally installed in each endcap.

Resistive Plate Chambers

The 480 RPC chambers in the barrel region and the 36 RPC chambers in the endcaps consist of two 2 mm thick highly resistive plastic plates separated by a 2 mm gas volume filled with a $C_2H_2F_4(95\%)/iC_4H_{10}(5\%)$ mixture. The RPCs operate in avalanche mode, which provides a fast response of about 3 ns and is appropriate for high trigger rates. Therefore they are primarily used for triggering since their position resolution of about 1 cm is coarser than that of DTs and CSCs [120].

The transverse momentum resolution for muons in CMS with $p_{\mathrm{T}} < 100\,\mathrm{GeV}$ ranges from 1.3-2.0% in the barrel region to smaller than 6% in the endcap region [121].

3.2.5 Trigger system

At the design luminosity and centre of mass energy $\sqrt{s} = 14\,\text{TeV}$ around 10^9 interactions per second are produced at the LHC, but only 100 events/s can be archived by the online computer farms. This rate must then be reduced via online selection processes (trigger). The CMS trigger system has two levels: the hardware based first level (L1) trigger and the software based second level trigger (high level trigger - HLT).

The L1 trigger system relies on information from the calorimeters and from the muon system. The decision process starts in the local detector subsystems. Muon identification is performed separately for the different muon chambers (DT, CSC, RPC) using e.g. hit patterns to supply independent information. This information is combined in the Global Muon Trigger (GMT) system. The four best muon candidates in the endcap and barrel regions are further sent from the GMT to the Global Trigger (GT) system.
Energy deposits in the ECAL and HCAL towers are processed in the Regional Calorimeter Trigger (RCT) system. Regional energy sums, i.e. electron/photon and jet candidates are identified in the RCT and further sent to the Global Calorimeter Trigger (GCT) system. From the GCT system, the four best isolated and non-isolated electron and photon candidates as well as the four best jets per barrel, endcap and tau category and the total (and consequently also missing) E_T sums are sent to the GT system. The GT system contains 128 trigger algorithms with different requirements on the candidates from the GCT and GMT systems such as E_T , p_T and combinations of objects. After $3.2\,\mu s$ the L1 trigger system reaches a result and the detector data, which was stored in buffers, is either discarded or transferred to the front end read out devices. The L1 trigger system has zero dead time (128 events are processed in parallel and there is a pipeline delay of $\approx 3\ \mu$s) and reduces the event rate to around 100 kHz [122].

The HLT system uses a slim version of the CMS offline reconstruction software distributed on a cluster of commercial rack-mounted computers comprising over 13k CPU cores [123]. The HLT system exploits the information of the whole detector. The fast reconstruction algorithms start with the L1 trigger candidates and add information from other subdetectors such as the tracker system to reconstruct the HLT trigger objects (electrons, photons, muons, jets). A sequence of requirements on the trigger objects correspond to a specific trigger path (or data stream), addressing specific physics object selections. If the event reconstructed by the HLT system meets the requirements of any such trigger path, it is recorded. The HLT system reduces the event rate to a few hundred Hz. Events passing the HLT system are stored on disk, with an average event size of about 1.5 MB for pp interactions.

3.2.6 Luminosity Measurement in CMS

The luminosity delivered by the LHC to the different experiments is measured by each experiment separately, compare section 3.1. The luminosity delivered to the CMS experiment in pp collisions in 2012 was measured using the pixel cluster counting method [124–127] together with a calibration using Van der Meer (VdM) scanning techniques [128]. The HF calorimeter is additionally used for online cross-check measurements and systematic studies.

Pixel cluster counting is an offline luminosity measurement method, which is based on the silicon pixel detector. The very low occupancy of less than 0.1% on average and the linear detector response over time make the silicon pixel detector a good choice for precise offline luminosity measurement. The per-bunch instantaneous luminosity $L(t)$ is measured from the number of pixel clusters appearing on average in a bunch crossing in zero-bias events [127]:

$$L(t) = \frac{f < n >}{\sigma_{vis}} \quad \text{defining} \quad < n >= \mu n_1 \quad \text{and} \quad \sigma_{vis} = \sigma_T n_1 \tag{3.6}$$

where $< n >$ is the average number of pixel clusters per event defined by the average number of clusters per inelastic collision n_1 and the number of collisions per bunch crossing μ. The total inelastic cross section is σ_T and the beam revolution frequency f is 11246 Hz. The visible cross section σ_{vis} is calibrated via the VdM scan technique. The absolute luminosity calibration, as described by σ_{vis}, is obtained by fitting the beam overlap from the shape of the measured rates (here $< n >$) as a function of the beam separations individually for each bunch crossing. The scans are performed simultaneously in the horizontal and vertical planes. The weighted average was measured to be $\sigma_{vis} = (7.230 \pm 0.038\,(\text{stat}))$ barn in November 2012 [127]. In figure 3.7 the cumulative integrated luminosity as a function of time during stable beams and the mean number of interactions per bunch crossing for pp collisions at $\sqrt{s} = 8$ TeV in 2012 is shown [129].

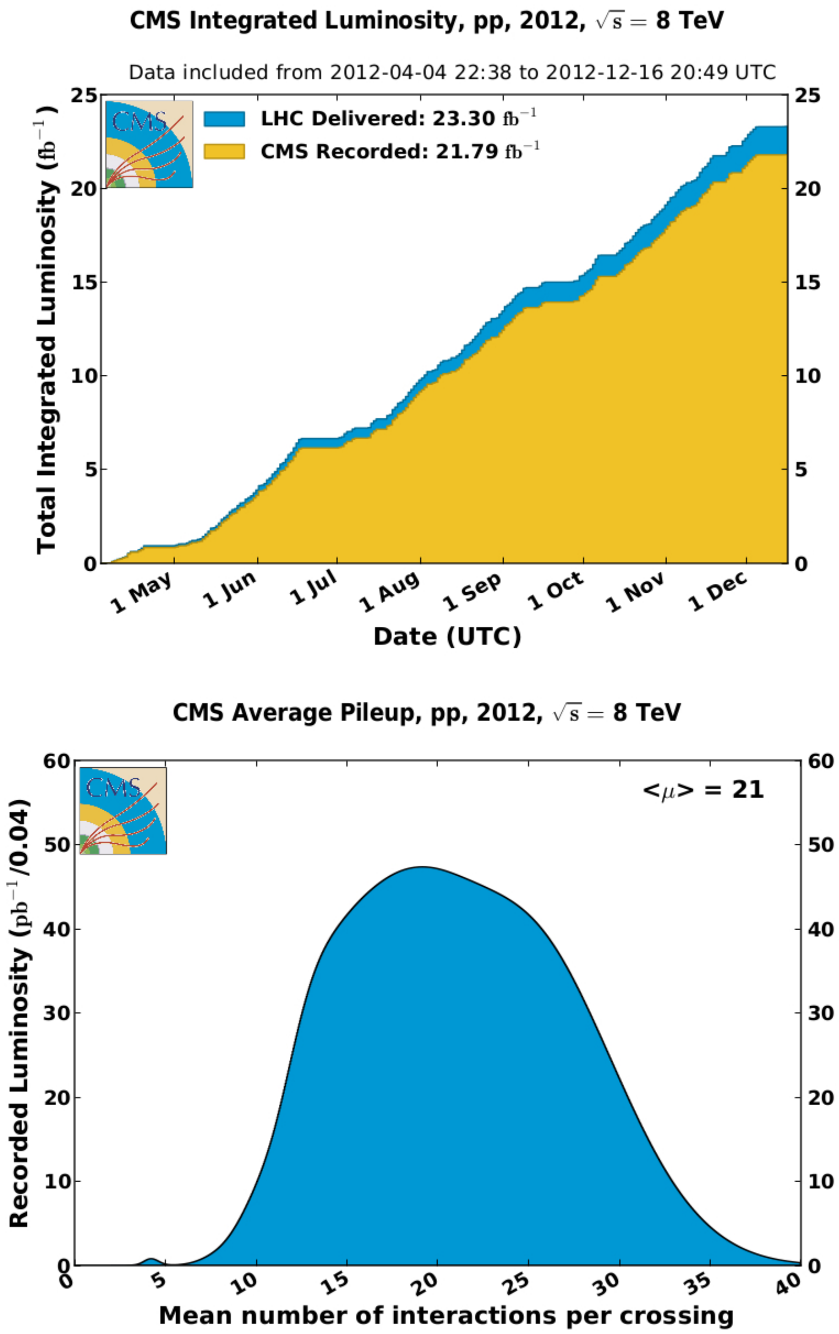

Figure 3.7: Cumulative luminosity time delivered (blue), and recorded by CMS (yellow) during stable beams (top) and mean number of interactions per bunch crossing (bottom) for pp collisions at $\sqrt{s} = 8$ TeV in 2012 [129].

3.3 Event Reconstruction in CMS

The raw data accumulated from the CMS experiment has to be further processed for physics analysis. The reconstruction of the physics objects in CMS exploits the information from all subdetectors using the Particle Flow (PF) algorithm [130, 131], which identifies all long-living individual particles in the event and determines their type, direction and energy. In figure 3.8 the different physics objects and their characteristic appearance in the CMS subdetectors are shown in a schematic overview of one section of the CMS detector. The trajectories of charged particles are bent by the magnetic field depending on their charge and momentum, leaving hits in the Si tracker. Electrons and photons deposit their energy only in the ECAL and hadrons mainly in the HCAL. Muons pass all subdetectors [113]. The detector response of the different subdetectors consisting of tracks, calorimeter clusters and muon tracks is used by the PF algorithm to identify topologically connected reconstructed elements from different subdetectors, link them via extrapolation to each other and identify particle candidates accordingly. This algorithm is performed iteratively and the elements associated with particle candidates like muons, electrons, charged/neutral hadrons and photons (in roughly this order) are removed from further processing. Afterwards the missing transverse energy $E_{\mathrm{T}}^{\mathrm{miss}}$ is calculated. The different steps are discussed in further detail in this section.

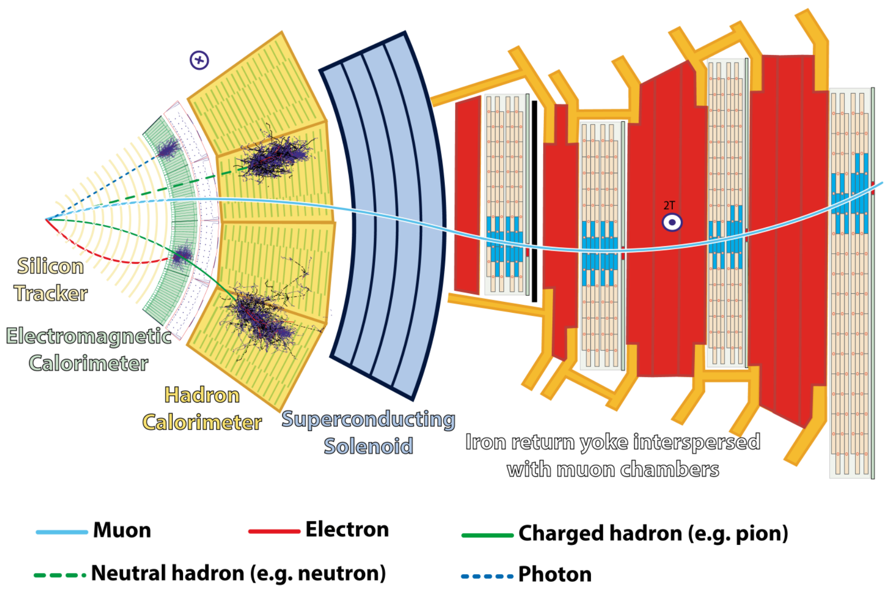

Figure 3.8: Schematic overview of the different physics objects and their interaction with the different subdetectors in one section of the CMS detector [132].

3.3.1 Track and Vertex Reconstruction

Track and vertex reconstruction are performed using information from the silicon tracker detectors [133]. Starting with the hits having the highest signal to noise ratio in the inner tracker, adjacent tracker hits are clustered and used as tracker seeds, which define the initial trajectory parameters and their uncertainties. The best track seeds are provided by the pixel detector due to its good three-dimensional position resolution. The trajectory building uses a combinatoric Kalman filter approach [134, 135]. The filter extrapolates the trajectory to the most compatible cluster in the next tracker layer taking into account energy loss in the material and multiple scattering. The trajectory with the newly assigned hits is re-fitted and the process is repeated, until no more compatible tracker clusters are found. The track candidate with the best goodness of fit (normalised χ^2) is chosen and the associated tracker clusters are removed from the next iteration of track finding. The track finding progressively relaxes the seed requirements to find less energetic tracks and tracks not crossing part or all of the pixel tracker (e.g. coming from secondary vertices).

Selected high quality tracks are grouped together according to their z coordinate at their point of closest approach to the beam line using a deterministic annealing algorithm[136] forming vertex candidates as described in [115]. An adaptive vertex fit [137] calculates the parameters of the vertex candidates and the fit quality from the chosen associated tracks. Studying the properties of the reconstructed vertex candidates allows to select the primary vertex in the event (described in section 5.2).

3.3.2 Electron and Photon Reconstruction

Electrons and photons induce electromagnetic showers depositing energy in multiple crystals of the ECAL detector. The deposited shower energy is shared by several ECAL clusters, which are merged to form so-called superclusters. Starting with these ECAL superclusters, electron candidates are reconstructed by matching the superclusters to tracks in the inner Si tracker originating from the interaction vertex [116, 138, 139]. A Gaussian Sum Filter (GSF)[140] is used, which is a non-linear generalisation of the Kalman Filter assuring improved pattern recognition of the electron tracks and taking Bremsstrahlung energy losses into account. If a supercluster from the ECAL detector cannot be matched to a track in the Si tracker detector, a photon candidate is identified. The shower shape, the comparison of ECAL energy and track momenta and other variables are used to further characterise particle candidates and are described for the electron selection in section 5.4.

3.3.3 Muon Reconstruction

Muon reconstruction starts with the local reconstruction of hits and segments in the muon chambers. In the DT chambers, muon hits with coordinates obtained from the the drift velocity are used to built three-dimensional track segments from the different DT layers. The CSCs provide the position and time of arrival of the muons, obtained from the distribution of charge induced on the cathode strips, leading to the reconstruction of three-dimensional track segments by combining the information from multiple CSC layers. The local reconstruction of the RPCs provides only the position of the muon hits[120, 121]. *Standalone* muon tracks are obtained by combining the information of all muon chambers using a Kalman filter tracking algorithm, which takes into account the information of the magnetic field and the energy loss in the material budget of the muon chambers and the iron return yoke.

If a *standalone* muon track can be matched to a tracker track reconstructed in the Si tracker system (compare 3.3.1), it is identified as a *global* muon. The matching of Si tracker tracks to standalone muon tracks is performed by first of all comparing their parameters propagated onto a reference surface on the outside of the magnet solenoid. The best combination of a Si tracker track and a standalone muon is chosen by iterating over all track combinations in this common surface with more stringent momentum and spatial matching criteria. The *global muon* candidate with the best normalised χ^2 is chosen. The trajectory is re-fitted starting from the outer muon chambers going towards the interaction point using a combinatorical Kalman Filter technique [113, 120, 121]. Energy deposits in the calorimeter and track segments close to the extrapolated trajectory are associated with the muon candidate and removed from subsequent iterations.

3.3.4 Jet and $E_{\mathrm{T}}^{\mathrm{miss}}$ Reconstruction

Because of colour confinement, partons produced in the hard process of a particle collision induce the production of large numbers of colourless secondary hadrons. This results in collimated particle showers, so-called jets, in the direction of the original parton preserving most of its initial properties. In figure 3.9 a schematic overview of a pp collision, resulting in a particle jet is shown. Hadron candidates are reconstructed using the information from large energy deposits in the ECAL and HCAL detectors combined with tracker information.

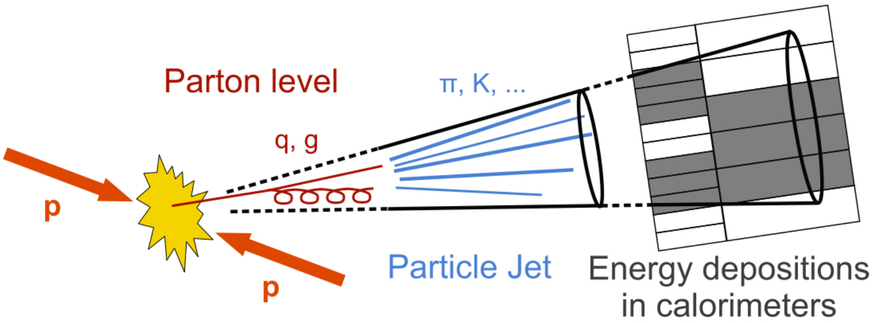

Figure 3.9: Schematic overview of a pp collision, resulting in a particle jet [141].

Subsequently, jets are reconstructed using a sequential recombination algorithm [142], which combines the pair of hadron particle candidates (i, j) with the smallest distance d_{ij} :

$$d_{ij} = \min(k_{Ti}^{2p}, k_{Tj}^{2p})\frac{\Delta R_{ij}^2}{R^2} \quad \text{with} \quad \Delta R_{ij}^2 = (y_i - y_j)^2 + (\phi_i - \phi_j)^2 \quad , \quad d_{iB} = k_{Ti}^{2p}, \tag{3.7}$$

where k_{Ti} is the transverse momentum, y_i the rapidity and ϕ_i the azimuthal angle of particle i. The algorithm is performed iteratively, including the newly merged hadron candidates (pseudo-jets). The distance d_{iB} between the object i and the beam B describes the stop criterion: If there is any object i with $d_{iB} < \min(d_{ij})$, it is called a PF jet and removed from the list. This assures that all pairs of final jet objects i and j are at least separated by $\Delta R_{ij}^2 = R^2$. The procedure continues until the list is empty. The anti-k_T-clustering-algorithm is used in this analysis, setting the parameter[8] p to -1. The algorithm is infrared safe, because it is not affected by soft radiation occurring in a parton shower, as well as safe against collinear emissions.

The measured jet energy is not equal to the true parton energy due to the non-linear response of the CMS detector. Therefore jet energy corrections are applied to the measured jet energy depositions in a factorised multi-level method developed by the CMS Collaboration. Each correction in sequence is related to different detector and physics effects and performed in a fixed order, where the output of each step is the input for the next [143].
L1 Pile-up correction : The detector responses to pile-up contribute an offset to the measured jet energy. This is subtracted by corrections determined from QCD dijet simulations with and without pile-up parametrised as a function of the energy density ρ, the jet area A, the η and p_T of the jet [144–146].
L2L3 Simulation correction : The true particle energy as a function of η and p_T is derived from QCD dijet simulations by comparing the p_T -distributions. The reconstructed jet energy is corrected accordingly to achieve a uniform response distribution in η and p_T .

[8] The Cambridge/Aachen clustering algorithm e.g. uses $p = 1$ and the k_T clustering algorithm $p = 0$.

L2L3 Residual data-driven correction : Relative residual corrections as a function of η are derived from dijet data samples by comparing the p_{T} of a jet relative to a jet with similar p_{T} in the barrel region to account for a varying response along the detector. The jet energy scale receives a p_{T} -dependence relative to the jet energy scale of the reference jet in the barrel region. Therefore the jet absolute scale is additionally corrected by determining the absolute residual corrections for barrel jets as a function of p_{T} using well measured jets from Z/γ+jets events and comparing them to multijet events in data.

After the reconstruction and identification of all physics objects in the event using the *PF* algorithm, the remaining momentum imbalance $\vec{p}_{\mathrm{T}}^{\mathrm{miss}}$ for all reconstructed *PF* particles in the transverse plane to the beam direction gives rise to the missing transverse energy $E_{\mathrm{T}}^{\mathrm{miss}}$.

$$\vec{p}_{\mathrm{T}}^{\mathrm{miss}} = -\sum_{i}^{\text{PF particles}} \vec{p}_{\mathrm{T}}^{\,i} \qquad E_{\mathrm{T}}^{\mathrm{miss}} = |\vec{p}_{\mathrm{T}}^{\mathrm{miss}}| \tag{3.8}$$

The missing transverse energy $E_{\mathrm{T}}^{\mathrm{miss}}$ identifies the presence of *invisible* particles in the detector, which are mostly neutrinos, but could also originate from new hypothetical stable, weakly interacting particles escaping the detector.

CHAPTER 4

Data and Simulation Samples

Data Samples

The data analysed in this thesis was collected in pp collisions at a centre of mass energy of $\sqrt{s} = 8\,\text{TeV}$ in 2012 with the CMS detector during Run 1 of the LHC. The data set corresponds to an integrated luminosity $\mathscr{L}$ of $19.7\,\text{fb}^{-1}$. Events are used only if all sub-detectors were fully functional and collecting data.

In this analysis events are categorised according to the final state leptons: 2 muons ($\mu\mu$), 2 electrons (ee) and 1 electron and 1 muon ($e\mu$). Within CMS the data processing is performed using data streams, which contain events collected by specific triggers. For the $\mu\mu$ and $e\mu$ channels the single muon data stream is used, which requires one muon with a p_T of at least $24\,\text{GeV}$ within $|\eta| < 2.1$. For the ee channel the double electron data stream is used, in which two electrons with a p_T above $17\,\text{GeV}$ and $8\,\text{GeV}$, respectively, are required.

Simulation Samples

Nowadays well-modelled, accurate simulations of background and signal processes are often essential for analyses in high energy physics - in direct model calculations, developments of new data-driven techniques or predictions for future experiments. Monte Carlo (MC) simulations are based on a probabilistic approach, where a sufficiently large number of pseudo-random experiments are generated to obtain numerical results.

Event generation in simulations can be divided into steps [147, 148]: Calculation of the probability distribution of the hard process, approximation of the evolution of parton showering, confinement of partons into hadrons during hadronization, simulation of the underlying event (defined later), decay of unstable particles and interaction of the final state particles with the detector.
Starting at the core of the collision the probability distribution for the process of interest (usually the one with the highest momentum transfer - **hard process**) is calculated in fixed order perturbation theory. PDFs are used to describe the momentum distributions of the incoming partons. Partons from the hard process radiate gluons due to their colour charge, which create new coloured particles, evolving in extended particle cascades. This sequential **parton shower** evolution is an approximation to higher order perturbation theory. Starting from the hard process the parton cascades evolve downwards in momentum scale until perturbation theory breaks down. This approximation derived from QCD can describe gluon emission and the internal structure of jets and is especially valid in the soft ($E \rightarrow 0$) and collinear limit (opening angle $\theta \rightarrow 0$). The confinement of a system of partons into hadrons is parametrised in **hadronization** models. Apart from the hard process, beam remnants and particles from multiple parton parton interactions occur in one single pp collision. Everything but the hard process is described and modelled by the **underlying event**. This contains mostly soft hadrons, which increase the total amount of scattered energy and particles. Models implementing the underlying event are tuned to data [149, 150].
The **decay of unstable secondary particles** is described by a combination of experimental data and theoretical assumptions. Nowadays these decays are complex and include a variety of modes and spin correlations. Multi-purpose event generators like Pythia [151] perform the simulation generation chain, whereby the Pythia Z2* tune [152] models the underlying event.

In the search for new physics, understanding and simulation of hard and well-separated jets is crucial. Matrix element calculations are better suited for this task than parton showering. **Matrix element matching** methods combine those tree-level or fixed matrix element calculations for several or lowest jet multiplicities simultaneously with parton showers without double counting of partons. Event generation using matrix element matching methods is performed by generators like MadGraph [153], PowHeg [154–156] or Whizard [157, 158]. They are usually combined with Pythia for parton showering and fragmentation. Double counting of partons during the parton matching using Pythia is avoided by the MLM algorithm [159].

Interactions between the generated particles and the CMS detector are simulated using the Geant4 toolkit [160, 161]. Furthermore, in simulations the same physics object reconstruction and identification methods are applied as in data (compare section 3.3), thus allowing direct comparisons.

Simulations as described above can be used for a variety of applications in the final state of two jets, two leptons and $E_{\mathrm{T}}^{\mathrm{miss}}$. Signals for the one-dimensional searches for new heavy top quark partners ($\mathrm{T}' \to Wb$) and for new heavy gauge bosons decaying to SM top quark pairs ($\mathrm{Z}' \to t\bar{t}$) are produced with the MadGraph 5.1.1 generator [153] and combined with the Pythia 6.424 generator [151] for parton showering and fragmentation. Simulations for vector-like T' quarks with charge $\frac{2}{3}$ are generated for T' masses ranging from 450 GeV to 1500 GeV . To avoid tensions with electroweak precision tests the T' quark has vector-like couplings, i.e. couples to right and left-handed particles. Generic high-mass resonances Z' decaying to SM top quark pairs are produced with a width of 1% of the Z' mass for Z' masses ranging from 500 GeV to 3000 GeV . The same left- and right-handed couplings to fermions are assumed as for SM Z bosons. Simulations produced with the MadGraph generator use the CTEQ6L [162, 163] PDF parametrisation.

Littlest Higgs models predict both a new heavy top partner T' and a new heave gauge boson W' , providing a suitable signal model for the two-dimensional application. Signal events for a simplified Littlest Higgs model are produced with the Whizard 2.2.0 generator using the CTEQ6L PDF parametrisation combined with Pythia 6.424. Starting at $\mathrm{M}_{T'} = 400$ GeV and $\mathrm{M}_{W'} = 200$ GeV in the two-dimensional mass plane of T' and W' , signal samples are generated up to 2 TeV in steps of 200 GeV . The generated mass space is restricted to the physically allowed region in the decay chain, where the mass of the heavy top quark partner T' is larger than the mass of the new heavy gauge boson W' . This results in 45 generated signal samples for the two-dimensional application. In generating the hard scattering process using Whizard, the free parameters are highly regulated by the masses $\mathrm{M}_{T'}$ and $\mathrm{M}_{W'}$. This and the parameter choices for the signal samples are explained in detail in appendix E. A simplified model is used to address models with similar particle content and masses. This is obtained by using a flat matrix element while performing the further decay of the T' quarks and W' bosons in Pythia. The branching ratios for the decays of T' to W' b and W' to leptons and neutrinos are set to 100%.

Top pairs decaying leptonically are the main background component because of the same decay topology. Top pairs are simulated with NLO accuracy using the PowHeg 1.0 generator, applying the CT10 [44, 164] PDF parametrisation, in combination with Pythia 6.424 for parton showering and hadronization. The number of simulated events in the most interesting high energy region of the $\mathrm{t\bar{t}}$ system is increased by combining three disjoint $\mathrm{t\bar{t}}$ samples, divided into $\mathrm{M}_{t\bar{t}} < 700$ GeV , 700 GeV $< \mathrm{M}_{t\bar{t}} < 1$ TeV and $\mathrm{M}_{t\bar{t}} > 1$ TeV . The mass filters for the last two are implemented at the production step. The low mass $\mathrm{t\bar{t}}$ sample is obtained from the inclusive top quark pair production by requesting the mass cut offline.

After top quark pair decays, Drell-Yan and single top quark processes contribute the most to the background. Multi-jet (QCD) and W + jets events will appear in some of the control distributions, but not in the final selection. The electroweak production of single top quarks is simulated with PowHeg 1.0 [165, 166] using the CTEQ6M PDF parametrisation combined with Pythia 6.424. Single boson samples (DY and W + jets) as well as $t\bar{t}$ production in association with a W/Z boson (Top pairs + W/Z jets) are produced using the MadGraph 5.1.1 generator combined with Pythia 6.424 for parton showering and fragmentation. The DY simulation sets consist of two non-overlapping samples with the invariant dilepton masses below or above 50 GeV (M_{ll} <50 GeV and M_{ll} >50 GeV). Diboson (WW, WZ, ZZ) and multi-jet (QCD) samples as well as top pairs + Higgs production are generated using Pythia 6.424. In all tables and figures the label “top quark pairs” combines top quark pairs plus jets and the associated top quark pair production with bosons (W/Z/Higgs).

Additional inelastic pp interactions occur within the same bunch crossing with the process of interest (“in-time pile-up”) as well as in the bunch-crossings before and after the collision of interest affecting the detector response (“out-of-time pile-up”). Simulated minimum bias interactions are superimposed into the generated signal and background events to simulate these effects. Furthermore, the number of pile-up interactions in the simulations are tuned to agree with the observed multiplicity in data (see section 5.7).

All simulation samples are normalised to the integrated luminosity in data using the cross sections and number of events summarised in table 4.1. The top quark pair and single top quark cross sections are calculated at Next-to-Next-to-Leading Order (NNLO) by Czakon et al [167] and Kidonakis [168], respectively. Top pair production cross sections in association with a W boson [169], a Z boson [170] or a Higgs boson [171] are calculated at NLO. The FEWZ (Fully Exclusive W and Z production) code is used for the calculation of W boson production and Drell-Yan cross sections at NNLO [172, 173]. Diboson production cross sections are calculated at NLO using the MCFM (Monte Carlo for FeMtobarn processes) tool [174, 175]. Multi-jet cross sections are obtained at LO using Pythia.

Table 4.1: Monte Carlo background samples with their corresponding event generator, cross section, event number and luminosity.

Process	Generator	$\sigma\,[pb]$	# Events	$\mathscr{L}$ [pb^{-1}]
DY $Z/\gamma^*(\to ll)$ + jets, M <50 GeV	MadGraph	899.7	7132223	7927.3
DY $Z/\gamma^*(\to ll)$ + jets, M >50 GeV	MadGraph	3503.7	30334503	8657.8
QCD p_T >20 GeV (μ enriched)	Pythia	134680.0	21484602	159.5
QCD 20 GeV < p_T <30 GeV	Pythia	2914860.0	35040695	12.0
QCD 30 GeV < p_T <80 GeV	Pythia	4615893.0	33088888	7.2
QCD 80 GeV < p_T <170 GeV	Pythia	183294.9	34517763	188.3
QCD 170 GeV < p_T <250 GeV	Pythia	4586.5	31647066	6900.0
QCD 250 GeV < p_T <350 GeV	Pythia	556.8	34561322	62071.3
QCD p_T > 350 GeV	Pythia	89.1	34055562	382217.3
Single t (s-channel)	PowHeg	3.8	259961	68410.8
Single t (t-channel)	PowHeg	56.4	3758227	66635.2
Single t (tW)	PowHeg	11.1	497658	44834.1
Single $\bar{t}$ (s-channel)	PowHeg	1.8	139974	77763.3
Single $\bar{t}$ (t-channel)	PowHeg	30.7	1935072	63031.7
Single $\bar{t}$ (tW)	PowHeg	11.1	493460	44455.9
Top pairs	PowHeg	245.8	21675970	88185.4
Top pairs 700 GeV < $\mathrm{M}_{t\bar{t}}$ <1 TeV	PowHeg	0.0741·245.8	3082812	169485.8
Top pairs $\mathrm{M}_{t\bar{t}}$ >1 TeV	PowHeg	0.0144·245.8	1234111	358628.1
Top pairs + W jets	MadGraph	0.232	196046	845025.9
Top pairs + Z jets	MadGraph	0.2057	210160	1021682.1
Top pairs + Higgs of 125 GeV	Pythia	0.1293	995697	7700672.9
W + jets → $l\nu$	MadGraph	36257.2	18393090	507.3
WW production	Pythia	54.8	10000431	182489.6
WZ production	Pythia	33.2	9975283	300460.3
ZZ production	Pythia	17.7	9799908	553667.1

CHAPTER 5

Event Selection

The objective of this analysis is to apply the developed search method (section 6) to various applications in the same final state: two leptons, two jets and missing energy $E_{\mathrm{T}}^{\mathrm{miss}}$. $E_{\mathrm{T}}^{\mathrm{miss}}$ and the momenta of jets and leptons are required as an input to the mass reconstruction algorithm, described in the next chapter. The analysed data samples are described in chapter 4. After the PF algorithm has been applied to reconstruct the event and the physics objects as described in section 3.3, the event selection, described in this chapter, ensures a reliable identification of the required physics objects. Additionally the selection reduces the number of SM background events.

To maintain as much model independence as possible no optimisation on the signal samples is performed and the same selection is used for all applications and searches.

5.1 Trigger

Considering the limitations in the bandwidth of the data acquisition system, some trigger streams need to be “prescaled” to limit the total trigger rate. A trigger stream is prescaled, if only a fixed fraction of events actually meeting the trigger conditions is stored. In this analysis events are collected using only non-prescaled trigger streams, where all events satisfying the trigger requirements are recorded.

A single muon trigger stream collects events for the $\mu\mu$ and $e\mu$ channel. This stream records all events containing an isolated muon with $p_T > 24\,\text{GeV}$ and $|\eta| < 2.1$. Events for the ee channel are collected using a double electron trigger stream requiring at least two electrons with a transverse momentum p_T greater than 17 GeV and 8 GeV , respectively. If at least one of the trigger stream requirements is met, the event is selected.

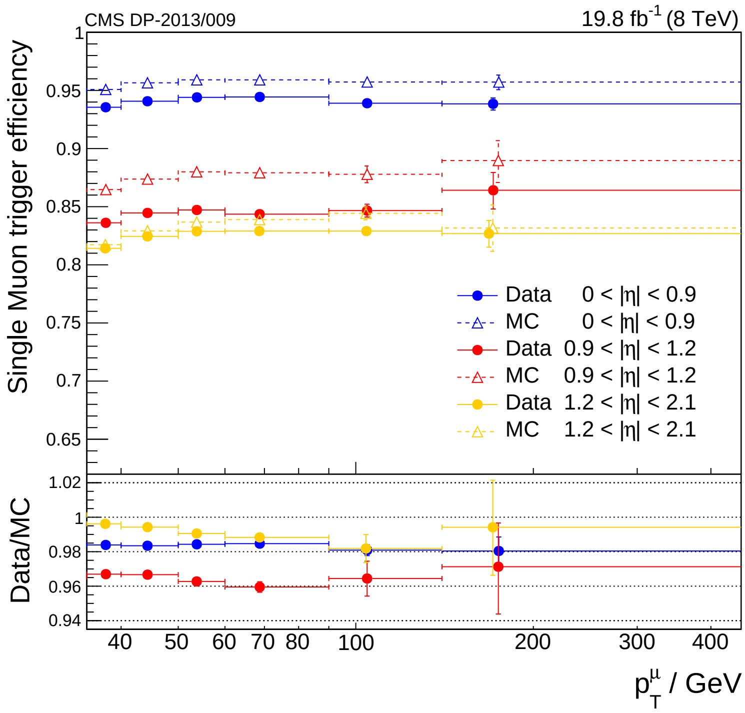

Figure 5.1: Single Muon trigger efficiency with statistical uncertainties only. The applied correction is plotted below [121, 176].

Discrepancies in the trigger efficiency between data and simulation are corrected for. The ratio of the efficiency between data and simulation is defined as the scale factor (SF) applied to the simulation samples.

The single muon trigger efficiency has been measured from data using the tag and probe method [121, 176]. Tag and probe techniques use di-object resonances like the Z boson as standard candles to estimate efficiencies from data. The single muon trigger efficiencies in data and simulation as well as the single muon trigger scale factor are shown as a function of p_T for various η bins in figure 5.1 [121, 176].

The trigger efficiency and trigger scale factor are calculated for each event combining the efficiency for each muon with $p_T > 24\,\text{GeV}$ and $|\eta| < 2.1$, which could have passed the single muon trigger:

$$\epsilon^{\text{trigger}}_{\text{Data}} = 1 - \prod_{\mu}(1 - \epsilon^{\text{trigger}}_{\mu,\text{Data}}) \qquad \epsilon^{\text{trigger}}_{MC} = 1 - \prod_{\mu}(1 - \epsilon^{\text{trigger}}_{\mu.MC}) \tag{5.1}$$

$$SF^{\text{trigger}} = \epsilon^{\text{trigger}}_{\text{Data}} / \epsilon^{\text{trigger}}_{MC}, \tag{5.2}$$

with $\epsilon^{\text{trigger}}_{\mu,\text{Data}}$ ranging from (79.4 - 94.4)% and $\epsilon^{\text{trigger}}_{\mu.MC}$ ranging from (79.0 - 95.9)% .
The statistical uncertainty of the final scale factor is added in quadrature with an additional systematic uncertainty of 0.3% due to the efficiency estimation technique [121, 176].

The double electron trigger scale factor has been measured to be 0.992 ± 0.004 over the whole phase-space using a multi-jet data stream [177]. The observed efficiencies in data ((97.3 ± 0.4)%) and the estimated efficiencies in simulation ((98.13 ± 0.01)%) agree within 1% [177]. This difference is taken into account as an additional systematic uncertainty on the global scale factor.

The overall uncertainty of the trigger scale factors is treated as a systematic uncertainty in the final results.

5.2 Vertex Selection

Vertices are reconstructed with the PF algorithm as described in section 3.3.1. At least one vertex needs to satisfy additional criteria, defining a *good primary vertex*. The number of degrees of freedom of the vertex fit must be at least 5. In addition, the absolute distance to the centre of the CMS detector has to be smaller than 24 cm along the z axis and 2 cm in the xy plane. The *good primary vertex* with the maximum sum of p_T^2 of its associated tracks is chosen as the primary vertex in the event.

5.3 Muon Selection

Global PF muons (compare section 3.3.3) need to satisfy additional quality requirements as recommended by the CMS collaboration [121, 178]. All muon identification requirements are summarised in table 5.1. The track fit of the *global* muon needs to have a χ^2 per degree of freedoms smaller than 10, when matching a track from the tracker to segments from the muon detector. Hadronic punch-through is suppressed by requiring at least one hit in the muon chamber. Muons from decays in flight are rejected by requiring at least one hit in the pixel tracker. Accidental track-to-segment matches are avoided by demanding muon segments in at least two muon stations. Cosmic muons and muons coming from pile-up are reduced by requirements on the impact parameter D^{vertex} in the transverse distance xy and longitudinal distance z of closest approach of the track trajectory to the selected primary vertex:

$$D^{\text{vertex}}_{xy} = \frac{v_x p_y - v_y p_x}{p_T} \qquad D^{\text{vertex}}_{z} = v_z - \frac{(v_x p_x + v_y p_y)\cdot p_z}{{p_T}^2}, \tag{5.3}$$

where $\vec{v}$ is defined as the vector between the selected primary vertex and the point of closest approach on the track trajectory. A good transverse momentum measurement is guaranteed by requiring hits in at least five tracker layers in the silicon tracker.

Furthermore, muons are requested to have a loose particle flow isolation (I_μ) to reject muons from hadron decays and assure a separation from other objects in the event [121, 178]. The energy deposition from other particle flow objects in a cone of $\Delta R = \sqrt{\Delta\eta^2 + \Delta\phi^2} < 0.4$ around the selected muon needs to be less than 20% of the muon transverse momentum p_T:

$$I_\mu = \frac{\sum\limits_{\substack{\text{Charged}\\\text{Hadron}}} p_T + \max(0., \sum\limits_{\substack{\text{Neutral}\\\text{Hadron}}} p_T + \sum\limits_{\text{PF Photons}} p_T - 0.5\cdot \sum\limits_{\substack{\text{Charged}\\\text{Particles}}} {p_T}^{\text{pile-up}})}{p_T}, \tag{5.4}$$

where the first term corresponds to pile-up free charged hadrons and the last term is a pile-up correction due to particles not originating from the primary vertex [179]. The factor 0.5 is an approximate average of neutral to charged particles as measured in jets [131, 179].

The pseudorapidity $|\eta|$ is required to be less than 2.1 due to the single muon trigger acceptance. This analysis is interested in new particles with high masses. Therefore the selected objects need to have a p_T of at least 50 GeV . This p_T requirement drastically reduces the contribution of background processes, while allowing the reconstruction of masses down to the top quark mass, which is used to validate the method (compare figure 5.6 later in this chapter). Muons with p_T above 50 GeV fulfilling all the identification criteria in table 5.1 are selected.

For triggered events the efficiency for a muon to be reconstructed is given by :

$$\epsilon_\mu \approx \epsilon_{\text{Track}} \cdot \epsilon_{\text{Reco \& Id}} \cdot \epsilon_{\text{Iso}}, \tag{5.5}$$

where ϵ_{Track} is the efficiency for a track in the Si tracker to be reconstructed, $\epsilon_{\text{Reco \& Id}}$ is the efficiency for this track to be matched to tracks in the muon chamber and additionally to meet the identification requirements as defined in the middle segment in table 5.1, and ϵ_{Iso} is the efficiency for a muon to meet the isolation requirement (compare eq. 5.4).

Table 5.1: All applied muon identification criteria based on the CMS collaboration recommendations [121, 178].

Muon Cut	Description
$p_{\mathrm{T}} > 50\,\mathrm{GeV}$	muon transverse momentum
$\lvert\eta\rvert < 2.1$	muon pseudorapidity
global PF Muon	match between track in the tracker and muon segments
$\chi^2/\mathrm{ndof} < 10$	goodness of the global muon track fit
$N_{\text{muon chamber}} > 0$	number of muon chamber hits in the global muon track fit
$N_{\text{muon segments}} > 1$	number of muon segments in matched muon stations
$N_{\text{pixel}} > 0$	number of pixel detector hits in the global muon track fit
$N_{\text{tracker layer}} > 5$	number of tracker layer hits in the global muon track fit
$\lvert D_{\mathrm{xy}}^{\text{track-vertex}}\rvert < 2$ mm	track transverse distance in xy plane with respect to the selected primary vertex
$\lvert D_{\mathrm{z}}^{\text{track-vertex}}\rvert < 5$ mm	track longitudinal distance in z direction with respect to the selected primary vertex
$I_{\mu} < 0.2$	relative particle flow isolation calculated using PF objects in a cone of $\Delta R < 0.4$ around the selected muon

The simulations are corrected for possible differences between simulated and measured efficiencies using [115, 121, 176]:

$$\mathrm{SF}_{\mu} = \frac{\epsilon_{\mu}^{Data}}{\epsilon_{\mu}^{MC}} \approx \mathrm{SF}_{\mathrm{Track}} \cdot \mathrm{SF}_{\mathrm{Reco\ \&\ Id}} \cdot \mathrm{SF}_{\mathrm{Iso}} \tag{5.6}$$

The tracking scale factor $\mathrm{SF}_{\mathrm{Track}}$ is measured as a function of η and ranges from 0.995 to 0.998 in the phase-space regions considered with a statistical uncertainty on the per mille level [115]. The corresponding measured efficiencies in data range from 98.4% to 99.8% and in simulation from 98.8% to 100.0% [115].

The applied identification and muon reconstruction scale factors $\mathrm{SF}_{\mathrm{Reco\ \&\ Id}}$ as well as the isolation scale factors $\mathrm{SF}_{\mathrm{Iso}}$ with their corresponding efficiencies in data and simulation are illustrated in figure 5.2 [121, 176]. For selected muons with a transverse momentum p_{T} greater than 50 GeV, the scale factors $\mathrm{SF}_{\mathrm{Reco\ \&\ Id}}$ range from 0.975 to 1.023 as a function of η with statistical uncertainties between 0.1% and 3.3%. The scale factors $\mathrm{SF}_{\mathrm{Iso}}$ range from 0.997 to 1.004 as a function of η having statistical uncertainties between 0.03% and 0.40%. The statistical uncertainties are added in quadrature with the systematic uncertainties of 0.5% (0.2%) for $\mathrm{SF}_{\mathrm{Reco\ \&\ Id}}$ ($\mathrm{SF}_{\mathrm{Iso}}$) coming from the *tag and probe* method [121, 176].

The overall uncertainty of the muon scale factors is treated as a systematic uncertainty in the final results.

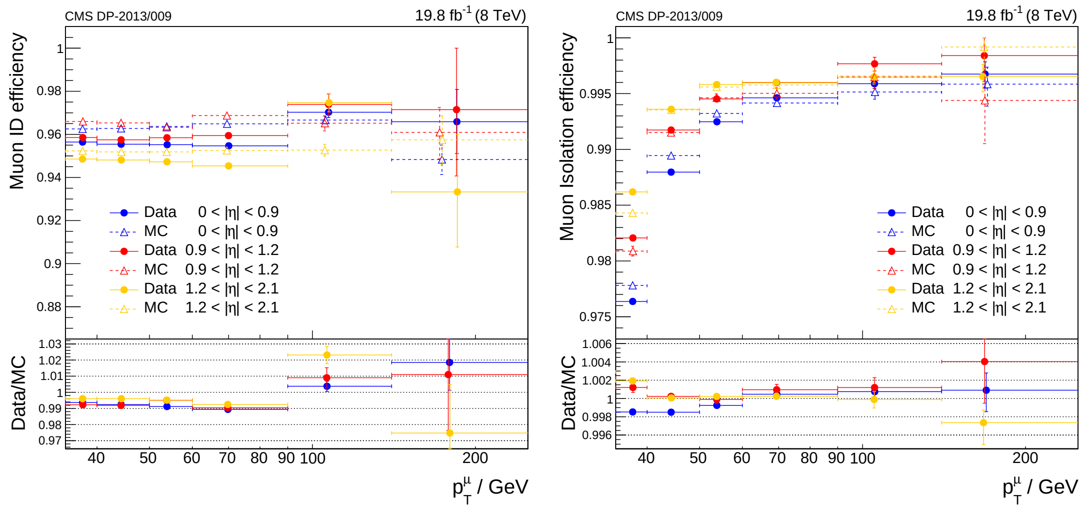

Figure 5.2: Muon reconstruction & identification (left) and isolation (right) efficiencies dependent on p_T and η. Uncertainties are statistical only. The applied correction is plotted in the ratio distribution below [121, 176].

5.4 Electron Selection

PF electrons, as described in section 3.3.2, are requested to fulfill additional quality criteria as recommended by the CMS collaboration [139]. The requirements of all electron identification variables are summarised in table 5.2. Electrons need to be within the acceptance of the tracker and the electromagnetic calorimeter, $|\eta_{SC}|$ <1.4442 and 1.566< $|\eta_{SC}|$ <2.5, where $|\eta_{SC}|$ is the pseudorapidity of the electron supercluster with respect to the origin of the coordinate system.

Requiring a small distance in η and ϕ between the supercluster position and the track position extrapolated to the ECAL surface ensures a good geometrical association between the track and the ECAL cluster and reduces misidentification [139]:

$$|\Delta\eta_{(\mathrm{SC,\,track})}| = |\eta_{SC} - \eta^{\mathrm{extrapolated}}_{\mathrm{inner\ track}}| \quad \text{and} \quad |\Delta\phi_{(\mathrm{SC,\,track})}| = |\phi_{SC} - \phi^{\mathrm{extrapolated}}_{\mathrm{inner\ track}}|\,. \tag{5.7}$$

A good agreement of the matching efficiency between the energy and momentum measurement is additionally obtained by demanding $\frac{1}{E_{\mathrm{SC}}} - \frac{1}{p_{\mathrm{track}}}$ to be smaller than 0.05 GeV $^{-1}$, where E_{SC} is the energy of the supercluster and p_{track} is the momentum of the track at the position of closest approach to the primary vertex.

Signal electrons or electrons from photon conversion are separated further from misidentified jets through cuts on calorimetric variables such as the shower shape variable $\sigma_{i\eta i\eta}$, which describes the lateral extension of the shower along η. In the following equation the summations are performed over a 5x5 crystal cluster centered around the seed crystal of the supercluster [139]:

$$\sigma_{i\eta i\eta} = \sqrt{\frac{\sum_i^{5x5} (\eta_i - \overline{\eta})^2 \omega_i}{\sum_i^{5x5} \omega_i}}, \tag{5.8}$$

where ω_i is a weight depending logarithmically on the collected energy, $\overline{\eta}$ is the average position between two adjacent crystals and η_i is the number of crystals between the seed crystal and the crystal i in η direction. In contrast to hadronic showers, elecromagnetic showers are narrower, thus making shower shape variables an effective discriminant. The ratio of energy deposited in the hadronic and the electromagnetic calorimeter $E_{\mathrm{HCAL}}/E_{\mathrm{SC}}$ is a measure for the energy leakage into the hadronic calorimeter and is typically small for electromagnetic showers. It is required to be smaller than 0.12 (0.10) in the barrel (endcaps).

Furthermore, electrons originating from converted photons are rejected by a number of cuts: The impact parameter $\mathrm{D}^{\mathrm{vertex}}$ in the transverse distance xy and longitudinal distance z of closest approach of the track trajectory to the selected primary vertex is defined as for the muons (see equation 5.3). Additionally, for prompt electrons the number of missing hits in the innermost layers of the tracker $N_{\text{tracker layer}}^{\text{missing hits}}$ should not exceed one. A χ^2 fit to the electron track candidate and the selected primary vertex is performed. The vertex fit probability for conversions is required to be smaller than 10^{-6} securing prompt electrons from the primary vertex [139].

A separation from other objects in the event is assured by requesting electrons to have a loose particle flow isolation (I_e) [139]. The energy deposition from other particle flow objects in a cone of $\Delta\mathrm{R} = \sqrt{\Delta\eta^2 + \Delta\phi^2} < 0.3$ around the selected electron should be less than 15% of the electrons transverse momentum p_{T} :

$$I_e = \frac{\sum\limits_{\substack{\text{Charged}\\\text{Hadron}}} p_{\mathrm{T}} + \max(0., \sum\limits_{\substack{\text{Neutral}\\\text{Hadron}}} p_{\mathrm{T}} + \sum\limits_{\text{PF Photons}} p_{\mathrm{T}} - p_{\mathrm{T}}{}^{\text{pileup}})}{p_{\mathrm{T}}}, \tag{5.9}$$

where $p_{\mathrm{T}}{}^{\text{pileup}} = \rho \cdot A_{eff}(\eta)$ is a computed pile-up correction using the kT-jet-clustering in a cone of $\Delta\mathrm{R} = 0.6$ with the FASTJET technique [144–146]. The effective area $A_{eff}(\eta)$ is given as a function of the pseudorapidity η. The average energy deposition ρ per event due to pile-up is estimated using the median of the energy distribution for all jets: $median\left\{\frac{\mathrm{p_T^j}}{\mathrm{A^j}}\right\}$ divided by the area A^j of any jet j in the event [144–146].

Electrons within the acceptance of the detector and with p_{T} above 50 GeV fulfilling all these identification criteria are selected.

Table 5.2: All applied electron identification criteria based on the CMS collaboration recommendations [139, 180].

Electron Cut			Description
Variable	Barrel	Endcap	
p_{T}	$> 50\,\mathrm{GeV}$	$> 50\,\mathrm{GeV}$	electron transverse momentum
$\lvert\eta_{SC}\rvert$	< 1.4442	> 1.566 < 2.5	electron supercluster (SC) pseudorapidity
$\lvert\Delta\eta_{(\mathrm{SC,\ track})}\rvert$	< 0.007	< 0.009	matching between track & position of
$\lvert\Delta\phi_{(\mathrm{SC,\ track})}\rvert$	< 0.15 rad	< 0.10 rad	closest approach to the SC in η and ϕ
$\sigma_{i\eta i\eta}$	< 0.01	< 0.03	lateral extension of the shower along η
$E_{\mathrm{HCAL}}\,/\,E_{\mathrm{SC}}$	< 0.12	< 0.10	hadronic energy veto
$\lvert\mathrm{D}_{\mathrm{xy}}^{\text{track-vertex}}\rvert$	< 0.2 mm	< 0.2 mm	track transverse distance in xy plane with respect to the sel. primary vertex
$\lvert\mathrm{D}_{\mathrm{z}}^{\text{track-vertex}}\rvert$	< 2 mm	< 2 mm	track long. distance in z direction with respect to the sel. primary vertex
$\frac{1}{E_{\mathrm{SC}}} - \frac{1}{p_{\mathrm{track}}}$	$< 0.05\,\mathrm{GeV}^{-1}$	$< 0.05\,\mathrm{GeV}^{-1}$	supercluster energy and track momentum matching
χ^2_{Conv} Prob	$< 10^{-6}$	$< 10^{-6}$	conversion-χ^2 fit probability to the selected primary vertex
$N_{\text{tracker layer}}^{\text{missing hits}}$	≤ 1	≤ 1	no missing hits in the innermost layer of the tracker
I_e	< 0.15	< 0.15	relative pf isolation calculated using pf objects in a cone of $\Delta\mathrm{R} < 0.3$ around the selected electron

For triggered events the efficiency for an electron to be reconstructed is given by :

$$\epsilon_e \approx \epsilon_{\mathrm{Reco}} \cdot \epsilon_{\mathrm{Id\ \&\ Iso}} \tag{5.10}$$

where ϵ_{Reco} is the efficiency for an electron to be reconstructed, $\epsilon_{\mathrm{Id\ \&\ Iso}}$ is the combined efficiency for this electron to meet the identification and isolation requirements.

Possible differences in data and simulation originating from these efficiencies are corrected in all simulation samples using scale factors (SF) as measured in [139, 180]:

$$\mathrm{SF}_e = \frac{\epsilon_e^{Data}}{\epsilon_e^{MC}} \approx \mathrm{SF}_{\mathrm{Reco}} \cdot \mathrm{SF}_{\mathrm{Id\ \&\ Iso}} \tag{5.11}$$

The applied scale factors with their corresponding efficiencies in data and simulation are shown in figure 5.3 [139, 180]. For selected electrons with a transverse momentum p_{T} greater than 50 GeV, the scale factors SF_{Reco} range from 0.974 to 0.998 as a function of η with statistical uncertainties between 0.1% and 0.9%. The scale factors $SF_{Id\,\&\,Iso}$ range from 0.980 to 1.023 as a function of η having statistical uncertainties between 0.1% and 0.8% . The statistical uncertainties are added in quadrature with systematic uncertainties originating from the *tag and probe* method ranging from 0.4% to 0.6% for SF_{Reco} and 0.4% to 0.5% for $SF_{Id\,\&\,Iso}$ [139, 180].

The overall uncertainty of the electron scale factors is treated as a systematic uncertainty in the final results.

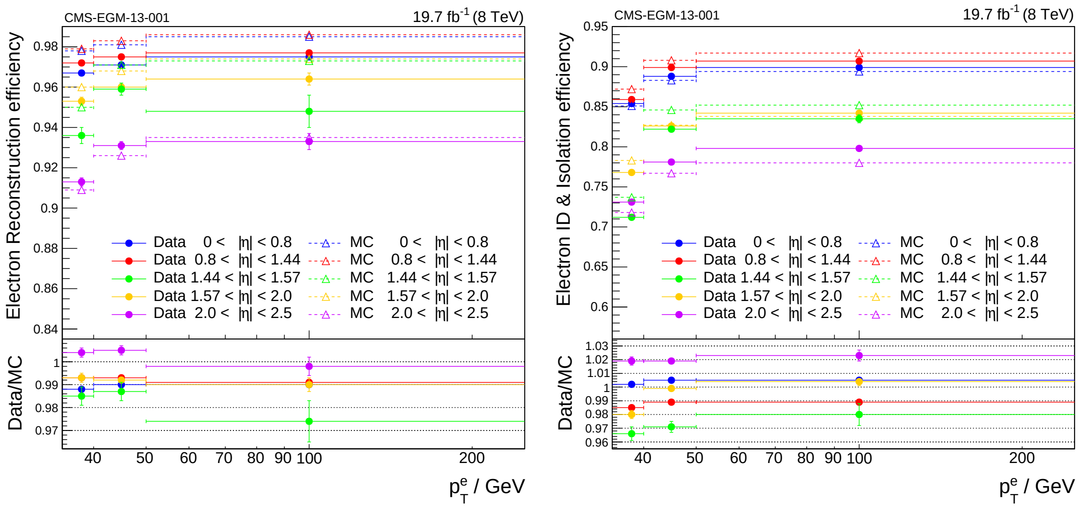

Figure 5.3: Electron reconstruction (left) and identification+isolation (right) efficiencies with statistical uncertainties only. The applied correction is plotted in the ratio distribution below [139, 180].

5.5 Jet and Missing Transverse Energy Selection

PF jets reconstructed with the anti-k_T-clustering-algorithm [142] with a size parameter ΔR of 0.5 are used in this analysis and have been described in section 3.3.4, where the factorised approach to the applied jet energy corrections is also described.

Jets within a cone of $\Delta R = \sqrt{\Delta\eta_{lj}^2 + \Delta\phi_{lj}^2} < 0.05$ with respect to any of the chosen leptons are rejected, where l corresponds to a lepton and j to the jet.

The jet energy resolution (JER) of measured jets in data is worse than in simulations [143, 181–183]. The reconstructed simulated jets need to be smeared by a jet energy resolution correction term based on the difference in transverse momentum between the reconstructed jet p_T and that on generator level $p_{T,\mathrm{GEN}}$:

$$p_T \rightarrow \max(0., p_{T,\mathrm{GEN}} + c^{\mathrm{JER}} \cdot (p_T - p_{T,\mathrm{GEN}})) \tag{5.12}$$

The core resolution scale factor c^{JER} is defined as the measured data resolution divided by the resolution in simulations: $c^{\mathrm{JER}} = \frac{\mathrm{JER}_{\mathrm{data}}}{\mathrm{JER}_{\mathrm{MC}}}$. In table 5.3 the used resolution scale factors c^{JER} are given together with their total uncertainties as a function of the jet pseudorapidity $|\eta|$. A reconstructed jet is successfully matched to a jet on generator level, if it has the smallest ΔR cone in comparison to all other generator level jets, while not exceeding 0.25 (half of the jet cone size). If no matching jet on generator level is found, no jet energy resolution correction is applied to the p_T of the reconstructed jet. The differences in the jet transverse momenta before and after the applied JER corrections are propagated to the calculation of the missing transverse energy.

Table 5.3: Core resolution scale factor c^{JER} for the applied JER correction as measured by the CMS collaboration [143, 181–183].

$\|\eta\|$	c^{JER}
0.0 - 0.5	1.079 ± 0.026
0.5 - 1.1	1.099 ± 0.028
1.1 - 1.7	1.121 ± 0.029
1.7 - 2.3	1.208 ± 0.046
2.3 - 2.8	1.254 ± 0.062
2.8 - 3.2	1.395 ± 0.063
3.2 - 5.0	1.056 ± 0.191

Overlapping low p_T jets from pile-up interactions can lead to higher p_T jets, so called “pile-up jets”. Although jets in this analysis are highly energetic due to the cut on the transverse momentum p_T of 50 GeV, an additional rejection of jets originating from pile-up collisions is performed by using a dedicated pile-up-jet-identifier [184]. “Pile-up jets” have two main features: they are wider and do not point to the primary vertex. Therefore both vertex and shape information are combined through a multivariate (MV) boosted-decision-tree (BDT) analysis technique resulting in the *pile-up-jet-ID* classifier (compare appendix A). After requiring the classifier output to be greater than -0.80 the signal efficiency for “real” jets with a $p_T > 25\,\mathrm{GeV}$ is still over 99% while “pile-up jets” are rejected with an efficiency of over 85% [184].

The remaining jets need to survive a list of minimum jet identification criteria, presented in table 5.4 [143, 181–183]. Fake jets originating from detector noise are rejected by cutting on the fraction of energy deposited by neutral and charged particles in the electromagnetic and hadronic calorimeter, as well as on the number of (charged) constituents in the jet.

Table 5.4: Applied jet identification criteria based on the CMS collaboration recommendations [143, 183].

Jet cut	Description
$p_T > 50\,\text{GeV}$	jet transverse momentum
$\lvert\eta\rvert < 2.4$	jet pseudorapidity
PuId > -0.80	pile-up-jet-ID classifier
$E^{HCAL}_{neutral}$ / $E_{jet} < 0.99$	neutral hadron fraction of the jet energy (HCAL)
$E^{ECAL}_{neutral}$ / $E_{jet} < 0.99$	neutral electromagnetic fraction of the jet energy (ECAL)
E^{HCAL}_{charge} / $E_{jet} > 0$	charged hadron fraction of the jet energy (HCAL)
E^{ECAL}_{charge} / $E_{jet} < 0.99$	charged electromagnetic fraction of the jet energy (ECAL)
$N_{charge} > 0$	number of charged constituents in the jet
$N_{Const} = N_{charge} + N_{neutral} > 1$	number of total constituents in the jet

For the mass reconstruction method in chapter 6 the input physics objects in each event need to originate from the hard process. These objects are usually the most energetic ones.

In conventional top pair selections it is customary to require that the selected jets can be identified as b-jets using a b-tagging algorithm and a corresponding discriminator variable [185]. The selected jets in this analysis are not required to be tagged as b-jets. Assuming an efficiency of around (60-70)% for one jet to be b-tagged and (36-49)% for two jets, the correct combination of jets would be frequently missed, leading to wrong input objects for the equations in the mass reconstruction method. Furthermore, the b-tag performance worsens in the interesting higher mass regions [186]. Additionally the dominant background component for the final state considered here consists mostly of top pairs. Having a similar b-jet content as possible new physics, no additional background reduction can be achieved by requiring the selected jets to be b-tagged.

The pseudorapidity $\lvert\eta\rvert$ is required to be less than 2.4. Jets with p_T above 50 GeV fulfilling all identification criteria above are selected.

Finally the events are required to have E_T^{miss} greater than 50 GeV. Missing transverse energy is reconstructed using the particle flow algorithm, as described in section 3.3.4 [187, 188]. Online applied jet energy corrections propagate to the E_T^{miss} calculation (compare section 3.3.4) as well as the offline applied corrections due to discrepancies in the jet energy resolution between data and simulation (compare equation 5.12).

5.6 Final Event Selection

Events without *good primary vertices* are rejected. Only events with at least two leptons (muons or electrons), at least two jets and $E_{\mathrm{T}}^{\mathrm{miss}}$ passing all identification requirements as described above are selected.

Leptons are sorted by their transverse momentum p_{T} and the two most energetic leptons are chosen. The two leptons need to be of opposite charge. They categorise the event into the $\mu\mu$, ee or $e\mu$ channels. Drell-Yan background and low mass resonances like Υ mesons [189] are rejected by requiring the invariant mass of the two leptons to be greater than $M_{ll}> 12\,\mathrm{GeV}$ and not within the mass window of the Z boson peak ($76\,\mathrm{GeV} > M_{ll} > 106\,\mathrm{GeV}$).

The selected jets are also sorted by their transverse momentum p_{T} and the two most energetic jets are chosen. The advantages of using an ordering in p_{T} rather than one based on a b-tag discriminator are discussed in appendix B.

The chosen leptons, jets and $E_{\mathrm{T}}^{\mathrm{miss}}$ are the input observables, which are used in the mass reconstruction method in chapter 6.

5.7 Pile-Up Reweighting

As mentioned in chapter 4 additional inelastic pp interactions appear within the same bunch crossing of interest ("in-time pile-up") and the bunch-crossing before and after affecting the detector response ("out-of-time pile-up"). These effects are reproduced by superimposing simulated minimum bias events using a cross section of 69.4 mb [190] to the generated hard interaction in all simulations. The average number of pile-up interactions per LHC bunch crossing depends on LHC running conditions, e.g. the instantaneous luminosity. The simulation samples were generated before the start of the LHC without an exact knowledge of the running conditions. Therefore the number of pile-up interactions in the simulations need to be matched to the observed multiplicity in data ("pile-up reweighting").

The impact of pile-up reweighting is illustrated in figure 5.4 by comparing the distributions of *good primary vertices* (compare definition in section 5.2). Throughout this thesis the observed counts in each bin are assumed to follow a Poisson-distribution. The systematic uncertainties are discussed in detail in chapter 8. Statistical and systematic uncertainties in simulations have been combined. Data and simulation samples agree within uncertainties after the correction is applied.

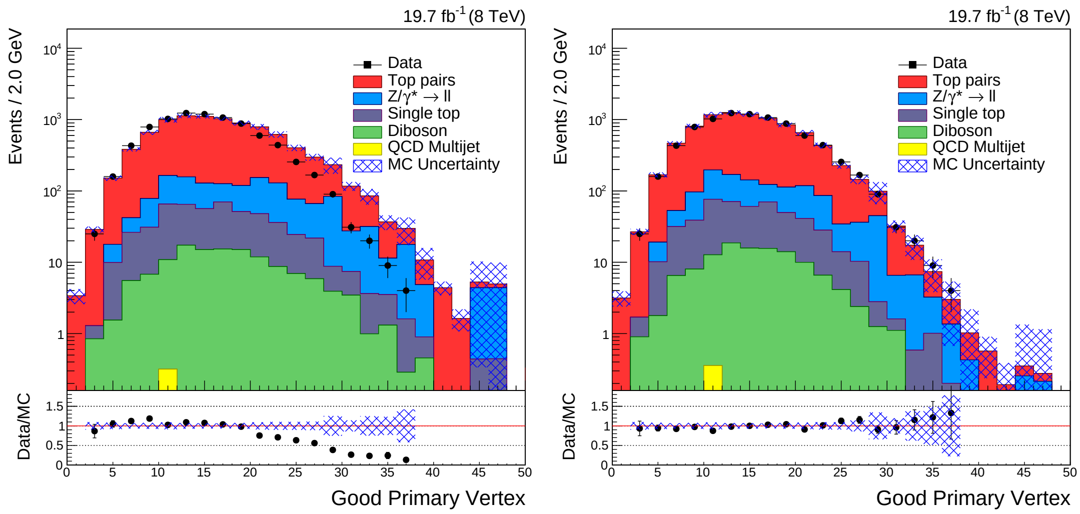

Figure 5.4: After applying all selection criteria the number of *good primary vertices* per event before (left) and after (right) pile-up reweighting to the simulated samples has been performed. Statistical and systematic uncertainties have been combined.

5.8 Drell-Yan Reweighting

In analyses requiring high missing transverse energy, the simulated Drell-Yan events deviate strongly from the observed data. Therefore DY background in events with two leptons and missing transverse energy is estimated using a data-driven technique, the $R_{\mathrm{out/in}}$ method [191–194]. The method uses events around the Z mass peak, 76 GeV > M_{ll} > 106 GeV, a region with a high purity of Drell-Yan events. Since these events are vetoed in the event selection, they form an independent control sample.

The $R_{\mathrm{out/in}}$ method estimates events outside the Z mass peak by using the ratio of events inside the Z mass peak window from data and Drell-Yan MC simulations multiplied by the events from Drell-Yan simulation outside the control region:

$$N_{DY\,MC\,corr}^{l^+l^-,out} = \frac{N_{Data}^{l^+l^-,in}}{N_{DY\,MC}^{l^+l^-,in}} \cdot N_{DY\,MC}^{l^+l^-,out} = SF_{DY}^{l^+l^-,out} \cdot N_{DY\,MC}^{l^+l^-,out} \tag{5.13}$$

The scale factor $SF_{DY}^{l^+l^-,out}$ is used to correct the Drell-Yan simulations in the off Z mass peak region (“Drell-Yan reweighting”).

The background processes in the Z mass peak region in events with high missing transverse energy can also be dominated by other physics processes. The background originating from ZZ decays is similar in shape and can be estimated together with the Drell-Yan background [191–194]. Other background processes, which are not peaking in the Z mass window, can occur from WW, W + jets, top pair and single top + W production. These backgrounds are estimated from data by analysing events in the Z mass peak region with one electron and one muon in the final state ($e\mu$). The scale factor $SF_{DY}^{l^+l^-,out}$ is modified accordingly:

$$SF_{DY}^{l^+l^-,out} = \frac{R_{\mathrm{out/in}} \cdot (N_{Data}^{l^+l^-,in} - 0.5 \cdot k_{ll} \cdot N_{Data}^{e\mu,in})}{N_{DY\,MC}^{l^+l^-,out}} \tag{5.14}$$

$$= \frac{N_{Data}^{l^+l^-,in} - 0.5 \cdot k_{ll} \cdot N_{Data}^{e\mu,in}}{N_{DY\,MC}^{l^+l^-,in}} \quad \text{with} \quad R_{\mathrm{out/in}} = \frac{N_{DY\,MC}^{l^+l^-,out}}{N_{DY\,MC}^{l^+l^-,in}} \tag{5.15}$$

The factor 0.5 takes the combinatorics between $e\mu$ and l^+l^- final states into account. The correction term k_{ll} considers the differences in reconstruction and identification efficiencies between electrons and muons. It is obtained from ee and $\mu\mu$ events in the Z mass peak region. To avoid mismeasurements due to missing transverse energy the calculation is performed by requiring a looser selection, with no $E_{\mathrm{T}}^{\mathrm{miss}}$ requirement applied:

$$k_{\mu\mu} = \sqrt{\frac{N_{Data}^{\mu^+\mu^-,in,loose}}{N_{Data}^{e^+e^-,in,loose}}} \qquad k_{ee} = \sqrt{\frac{N_{Data}^{e^+e^-,in,loose}}{N_{Data}^{\mu^+\mu^-,in,loose}}} = \frac{1}{k_{\mu\mu}} \tag{5.16}$$

The resulting correction terms are $k_{\mu\mu} = 1.050 \pm 0.003\,(\text{stat})$ for the $\mu\mu$ channel and $k_{ee} = 0.953 \pm 0.003\,(\text{stat})$ for the ee channel. Afterwards the scale factors $SF_{DY}^{l^+l^-,out}$ can be obtained from equation 5.14 for all three channels, whereby the Drell-Yan scale factor for $e\mu$ events[1] (originating from τ decays) is calculated to be $SF_{DY}^{e\mu,out} = \sqrt{SF_{DY}^{ee} \cdot SF_{DY}^{\mu\mu}}$.

Table 5.5: Applied correction scale factor $SF_{DY}^{l^+l^-,out}$ due to discrepancies in events from Drell-Yan simulations with respect to events in data. The uncertainties are statistical only.

Performed Cuts	ee channel	$\mu\mu$ channel	e μ channel
2 leptons	1.053 ± 0.007	1.023 ± 0.007	1.038 ± 0.005
2 leptons + 2 jets	1.024 ± 0.008	0.995 ± 0.008	1.009 ± 0.006
2 leptons + 2 jets + $E_{\mathrm{T}}^{\mathrm{miss}}$	1.750 ± 0.097	1.721 ± 0.092	1.736 ± 0.067

The scale factors $SF_{DY}^{l^+l^-,out}$ are obtained for different stages in the event selection and are presented in table 5.5. The scale factors in the last row are calculated after all selection requirements and used as final scale factors in the analysis. The difference between data and simulation is taken as the systematic uncertainty on the cross section measurement of the Drell-Yan production, whereby the average difference of 73.6% is used in the combined channel (ee+$\mu\mu$+$e\mu$).

The invariant mass of the two most energetic opposite charged leptons, after all lepton requirements are fulfilled, is shown in figure 5.5 for different channels. The Drell-Yan reweighting scale factor has been applied.

[1] Because these decays contain $E_{\mathrm{T}}^{\mathrm{miss}}$ in the final state ($Z \to \tau\tau \to e\mu + E_{\mathrm{T}}^{\mathrm{miss}}$) the $R_{\mathrm{out/in}}$ method cannot be applied directly.

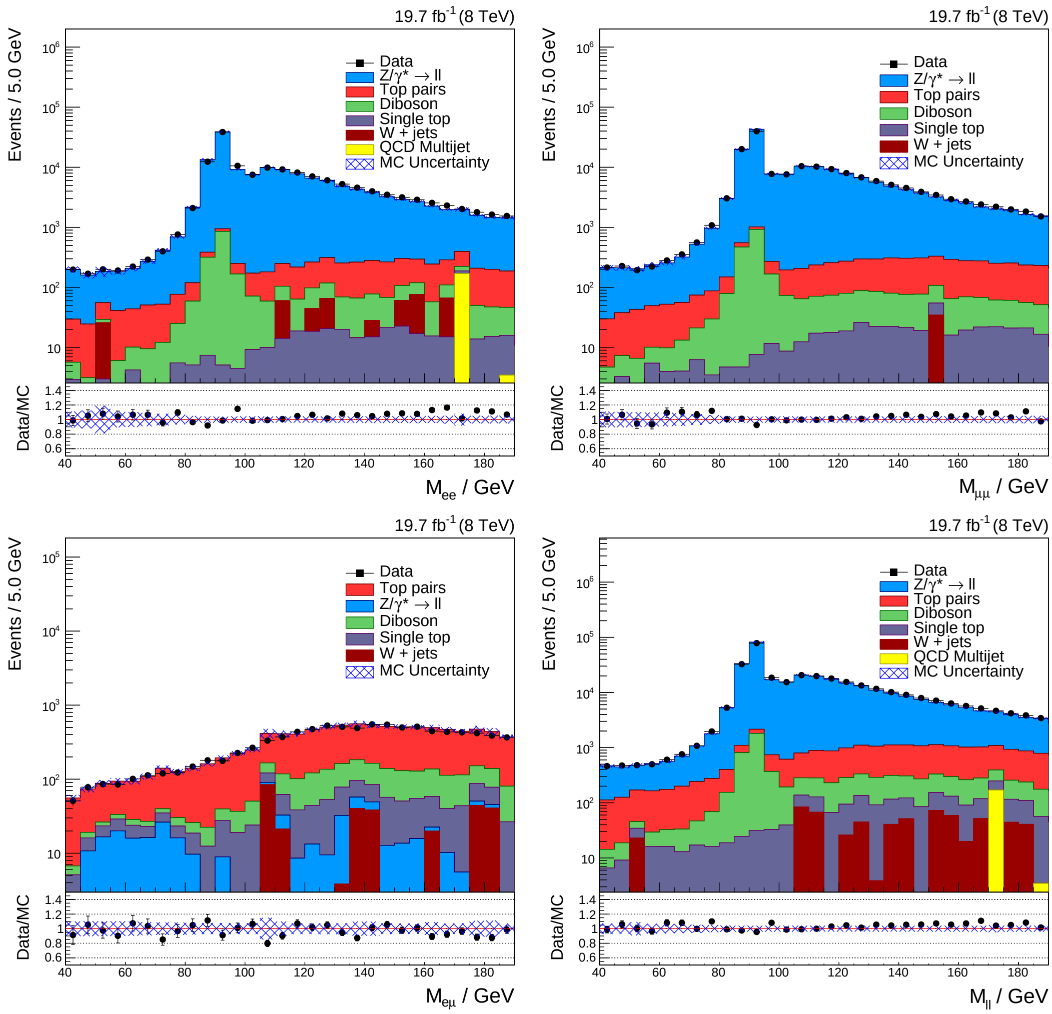

Figure 5.5: After lepton selection with applied Drell-Yan reweighting: the invariant mass of the two highest energetic electrons (top-left), the invariant mass of the two highest energetic muons (top-right), the invariant mass of the highest energetic electron and muon (bottom-left) and the invariant mass of the highest energetic leptons (bottom-right). Statistical and systematic uncertainties have been combined. The systematic uncertainties are discussed in detail in chapter 8.

5.9 Summary

In figure 5.6 the event selection is summarised in the cut flow distribution for all channels combined. Each bin corresponds to different requirements during the event selection. The corrections due to trigger and lepton efficiencies as well as pile-up and Drell-Yan reweighting are obtained at distinct stages through the selection. They are not applied in the cut flow distribution to ensure consistency in all bins. The same distribution for the three lepton channels (ee,$\mu\mu$,$e\mu$) separately can be found in appendix C.

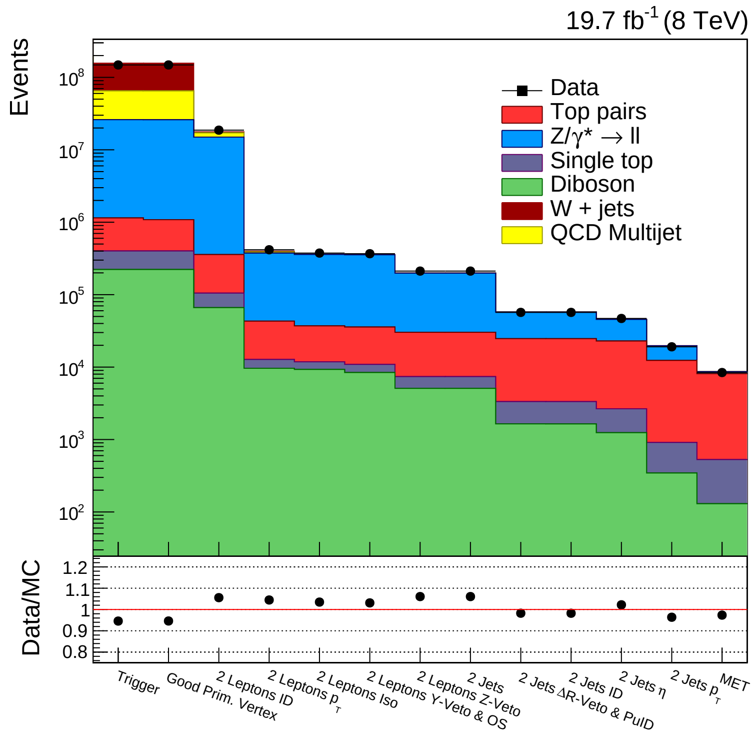

Figure 5.6: Cut flow distribution for all channels combined, where each bin corresponds to the requirements applied through the selection. No trigger SF, lepton SF, pile-up and DY reweighting are applied to maintain consistency in all bins.

The benefit of the different selection requirements can be visualised by examining the background rejection with respect to signal samples, e.g. here for the 45 generated Little Higgs samples, where only rejections of over 60% in comparison to the previous cut will be mentioned:

Requiring two well identified leptons rejects already around 99% of the background events down to almost 20 million events, while only rejecting (13-17)% of Little Higgs events[2].

[2]depending on $M_{T'}$ and $M_{W'}$.

About 98% of the remaining background is further rejected by the lepton p_T cut of 50 GeV ($4 \cdot 10^5$ events left), while only 3% to 20% of the remaining Little Higgs signal events are rejected. The *pile-up-jet-ID* discriminant and the rejection of jets too close to one of the selected leptons has almost no effect on the Little Higgs events (rejection of (0-2)%), but rejects over 70% of the remaining background events ($55 \cdot 10^3$ events left). The next significant cut requires the jet transverse momentum to be greater than 50 GeV . This removes almost 60% of the remaining background ($20 \cdot 10^3$ events left), while 1% to 10% Little Higgs events are rejected. Demanding at least 50 GeV of missing transverse energy rejects almost 60% of the remaining background ($8 \cdot 10^3$ events left). Only (0 - 10)% of the remaining Little Higgs signal events are rejected with this last cut.

Table 5.6: Background reduction for the event selection steps involving all corrections. The uncertainties are statistical only.

Sample	Performed Cuts		
	2 leptons after Z Veto	2 leptons + 2 jets	**2 leptons + 2 jets + E_T^{miss}**
Top pairs	22356.7 ± 67.4	11142.5 ± 46.9	**7345.2 ± 37.7**
Z + jets	170869.0 ± 635.7	6947.9 ± 127.8	**744.7 ± 54.6**
Single Top	2275.7 ± 31.7	559.2 ± 15.7	**389.9 ± 13.1**
Diboson	4973.5 ± 21.6	322.5 ± 4.7	**119.5 ± 3.3**
QCD	201.5 ± 133.7	5.6 ± 3.2	**0.4 ± 0.3**
W + jets	980.2 ± 195.1	76.6 ± 54.5	**0**
Total Background	201657.0 ± 682.7	19054.2 ± 147.6	**8599.7 ± 67.7**
Observed events	211602 ± 460	19063 ± 138	**8413 ± 92**

For the event selection steps involving all scale factor corrections (incl. DY and pile-up reweighting) a summary of background reduction is presented in table 5.6. W + jets events do not survive the final selection and the remaining multi-jet (QCD) background is negligible. This leaves top pair events as the main background component (85%), followed by Drell-Yan events (9%). The remaining background consists of single top and diboson events. The same cut flow table is presented in table 5.7 for signal samples for all three applications.

All final state observables needed as an input to the mass reconstruction in chapter 6, are shown in figure 5.7 for the leptons and in figure 5.8 for the jets, missing transverse energy and the invariant mass of all final state particles. The data and MC simulation show good agreement within uncertainties. More control distributions for the final state objects are presented in appendix D.

Table 5.7: Yield reduction for the event selection steps involving all corrections for generic signal samples for all applications. The production cross section is set to 1 pb for all signal samples. The uncertainties are statistical only.

Sample	Performed Cuts		
	2 lep. after Z Veto	2 lep. + 2 jets	**2 lep. + 2 jets +** $E_{\mathrm{T}}^{\mathbf{miss}}$
$\mathrm{T}'\overline{\mathrm{T}'} \to \mathrm{W}b\mathrm{W}b$,			
$\mathrm{M}_{T'}$ (500 GeV)	318.4 ± 7.9	303.5 ± 7.7	274.8 ± 7.4
$\mathrm{M}_{T'}$ (800 GeV)	384.2 ± 8.8	376.6 ± 8.7	358.0 ± 8.5
$\mathrm{Z}' \to t\bar{t} \to \mathrm{W}b\mathrm{W}b$			
$\mathrm{M}_{Z'}$ (1000 GeV)	196.4 ± 6.1	161.8 ± 5.5	125.8 ± 4.9
$\mathrm{M}_{Z'}$ (1500 GeV)	204.8 ± 3.2	182.3 ± 3.0	153.8 ± 2.8
$\mathrm{T}'\overline{\mathrm{T}'} \to \mathrm{W}'\,b\mathrm{W}'\,b$, $\mathrm{W}' \to l\nu$			
$\mathrm{M}_{T'}$ (1000 GeV) $\mathrm{M}_{W'}$ (600 GeV)	8059.9 ± 46.1	7804.9 ± 45.4	7521.0 ± 44.5
$\mathrm{M}_{T'}$ (1800 GeV) $\mathrm{M}_{W'}$ (1000 GeV)	8117.2 ± 46.3	7975.2 ± 45.9	7808.0 ± 45.4

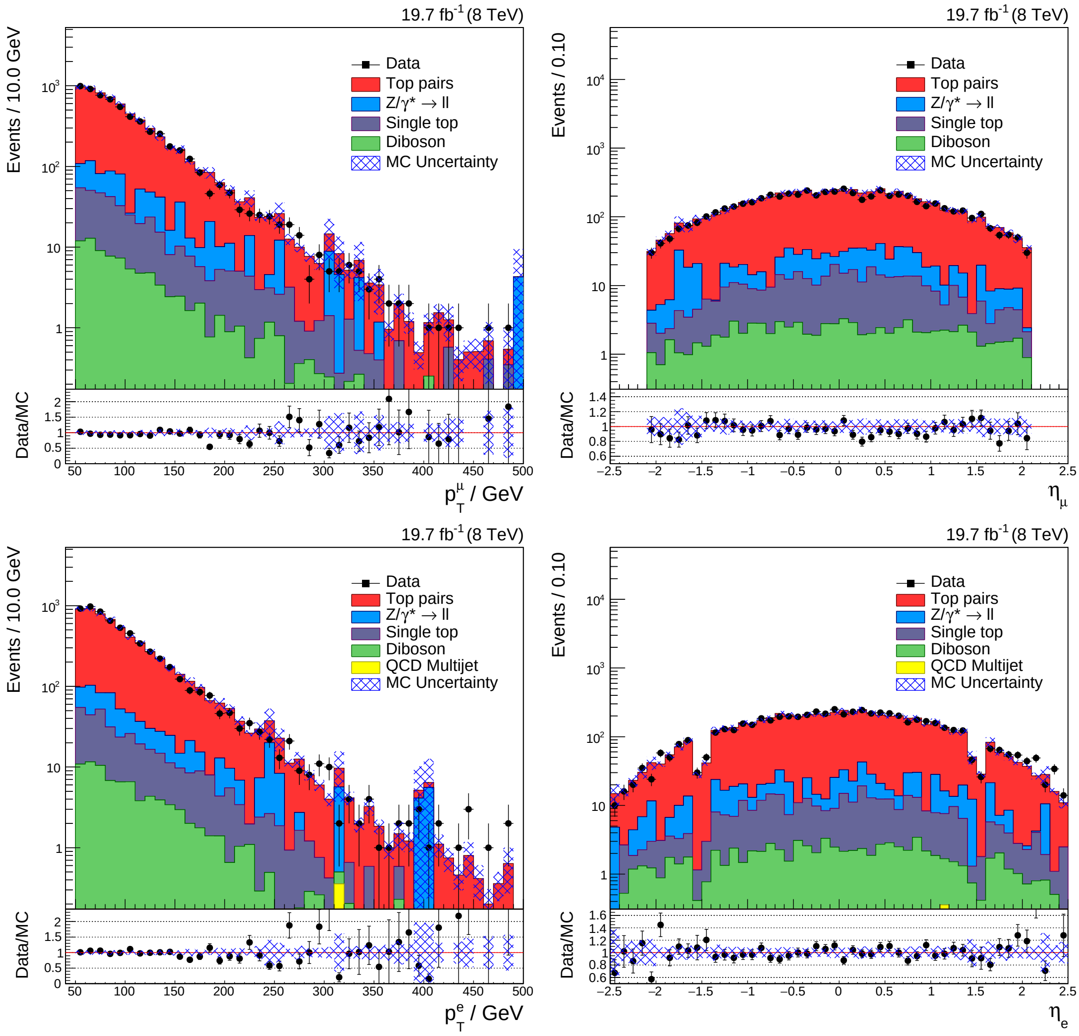

Figure 5.7: Distribution of the transverse momentum p_{T} (left) and pseudorapidity η (right) of the highest energetic muon (top) for the $\mu\mu$ and $e\mu$ channels and the highest energetic electron (bottom) for the ee and $e\mu$ channels after all selection cuts. Statistical and systematic uncertainties have been combined. The systematic uncertainties are discussed in detail in chapter 8.

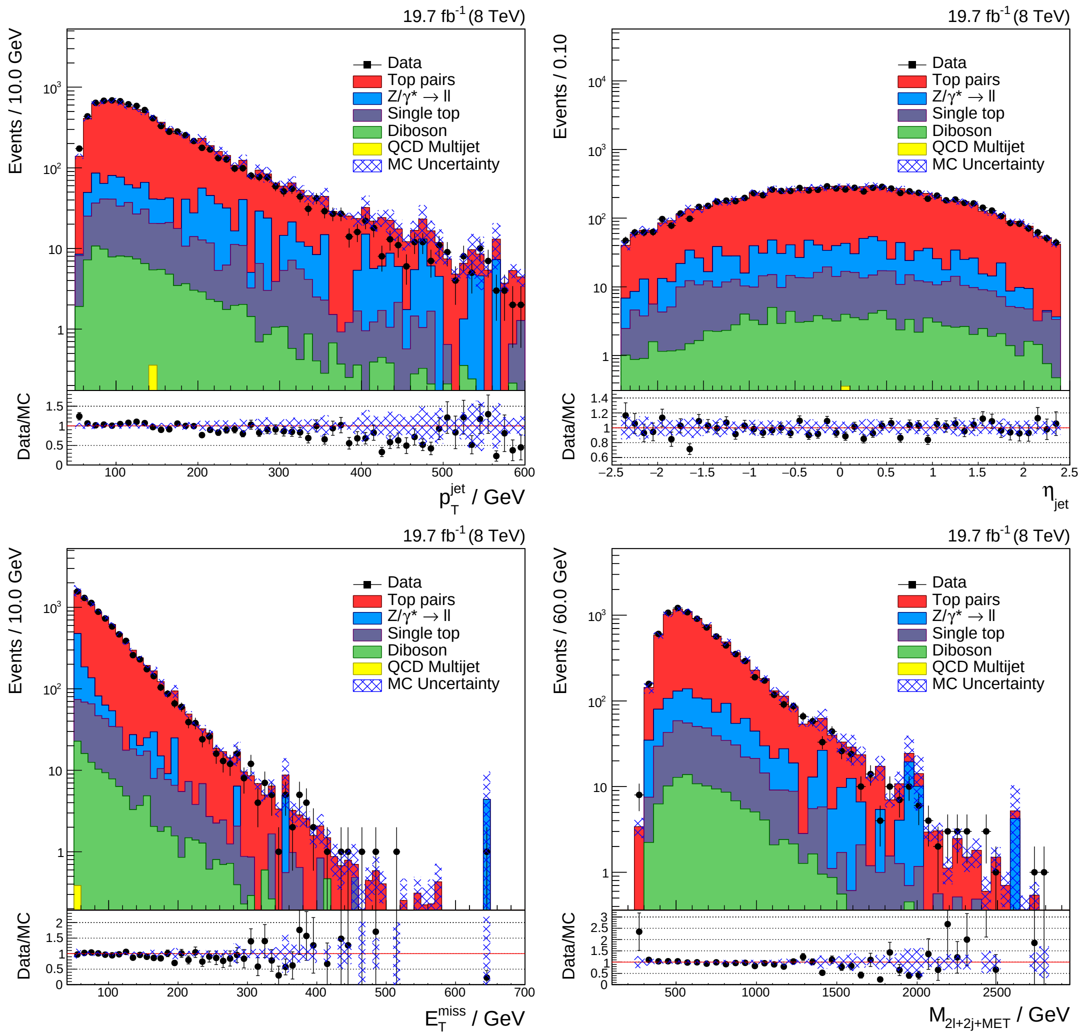

Figure 5.8: Distribution of the transverse momentum p_T (top-left) and pseudorapidity η (top-right) of the highest energetic jet after all selection cuts for all channels. The missing transverse energy (bottom-left) and the invariant mass of the system (consisting of 2 leptons, 2 jets and missing transverse energy) (bottom-right) after all selection cuts for all channels are shown in the second row. Statistical and systematic uncertainties have been combined. The systematic uncertainties are discussed in detail in chapter 8.

CHAPTER 6

Two-Dimensional Mass Reconstruction

The two-dimensional mass reconstruction of the $T'\overline{T'}$ system is performed for an assumed topology ($T'\overline{T'} \rightarrow W'^{+}\ q\ W'^{-}\ \overline{q}$) without any further assumptions on the underlying theory. The mass reconstruction method can be divided into three steps: the calculation of the analytic solution of the $T'\overline{T'}$ decay (1) and the smearing of the event kinematics with the detector resolution (2). The calculation of a weight based on parton distribution functions for each solution results in a selected solution per event (3). Each step will be explained in more detail in this chapter. Steps two and three are interchangeable in the analysis chain.

The basic method was developed using fast simulations by former RWTH colleague Anagnostou [195]. The mass reconstruction method was further studied and developed in the framework of this thesis in close cooperation with Anagnostou, whereby it was implemented independently to ensure the robustness of the method. For the first time the method is applied to different applications and analysed with LHC data within a complex experiment.

6.1 Analytic Solution of the Decay

In the first step the analytical solution of the $T'\overline{T'}$ decay is derived by solving a system of two linear and six non-linear equations for the unknown neutrino momenta components [196, 197]:

$$M^2_{W'^+} = (E_{l^+} + E_\nu)^2 - (\vec{p}_{l^+} + \vec{p}_\nu)^2 \tag{6.1}$$

$$M^2_{W'^-} = (E_{l^-} + E_{\overline{\nu}})^2 - (\vec{p}_{l^-} + \vec{p}_{\overline{\nu}})^2 \tag{6.2}$$

$$M^2_{T'} = (E_q + E_{l^+} + E_\nu)^2 - (\vec{p}_q + \vec{p}_{l^+} + \vec{p}_\nu)^2 \tag{6.3}$$

$$M^2_{\overline{T'}} = (E_{\overline{q}} + E_{l^-} + E_{\overline{\nu}})^2 - (\vec{p}_{\overline{q}} + \vec{p}_{l^-} + \vec{p}_{\overline{\nu}})^2 \tag{6.4}$$

$$E^2_\nu = m^2_\nu + p^2_{\nu_x} + p^2_{\nu_y} + p^2_{\nu_z} \tag{6.5}$$

$$E^2_{\overline{\nu}} = m^2_{\overline{\nu}} + p^2_{\overline{\nu}_x} + p^2_{\overline{\nu}_y} + p^2_{\overline{\nu}_z} \tag{6.6}$$

$$\not{E}_x = p_{\nu_x} + p_{\overline{\nu}_x} \tag{6.7}$$

$$\not{E}_y = p_{\nu_y} + p_{\overline{\nu}_y} \tag{6.8}$$

The two sides of the decay chain are coupled through eqs. (6.7)-(6.8). The mass constraints on $W'^{\pm}$ and T' / $\overline{T'}$, resulting from the invariant masses of their decay products for both branches of the symmetrical topology in eqs. (6.1) - (6.4), are rearranged to form two equations linear in the three neutrino and antineutrino momentum components : $p_{\nu_x}, p_{\nu_y}, p_{\nu_z}$ and $p_{\overline{\nu}_x}, p_{\overline{\nu}_y}, p_{\overline{\nu}_z}$. The energy of the neutrino E_ν and antineutrino $E_{\overline{\nu}}$ in eqs. (6.5)-(6.6) is used to substitute the longitudinal neutrino and anti-neutrino momenta $p_{\nu_z}, p_{\overline{\nu}_z}$ leading to two multivariate polynomials of the second degree depending only on the transverse neutrino and antineutrino momenta: p_{ν_x}, p_{ν_y} and $p_{\overline{\nu}_x}$, $p_{\overline{\nu}_y}$. A further transformation is performed using the transverse projection of the missing energy in eqs. (6.7)-(6.8) leading to two polynomial equations with two unknowns p_{ν_x} p_{ν_y}. Using the determinant of the Sylvester matrix, this is rearranged to a quartic uni-variate polynomial, which can be solved analytically following Sonnenschein's calculations [196, 197]. The lepton masses are set depending on its flavor to either the muon or the electron mass. The quark masses are set to the b quark mass.

In searching for new particles T' and W', the masses of T' and W' are unknown and the equation system is under-constrained. Testing every point ($M_{T'}$, $M_{W'}$) in the two-dimensional mass plane results in four, two or no real solutions for the neutrino momenta at each point. No constraints on the masses $M_{T'}$ and $M_{W'}$ are required.

It is difficult to associate correctly the jets from the q and $\overline{q}$ quarks with the appropriate lepton in the decay chain. Therefore the jets are interchanged in solving the equation system of the $T'\overline{T'}$ decay, thus resulting in zero, two, four, six or eight real solutions per mass point. Each solution yields the momenta of the neutrino $p_{\nu_x}, p_{\nu_y}, p_{\nu_z}$ and antineutrino $p_{\overline{\nu}_x}, p_{\overline{\nu}_y}, p_{\overline{\nu}_z}$.

In this step the solvability $S(\mathrm{M}_{T'}, \mathrm{M}_{W'}) \in \{0,1\}$ is defined as the existence (or not) of a real solution for a specific mass point. The solvability for a single event from top pair simulations is shown in figure 6.1. The equation system has a real solution for all mass points shown in yellow and no solution for all mass points in blue. The solvability is bound from below for both $\mathrm{M}_{T'}$ and $\mathrm{M}_{W'}$.

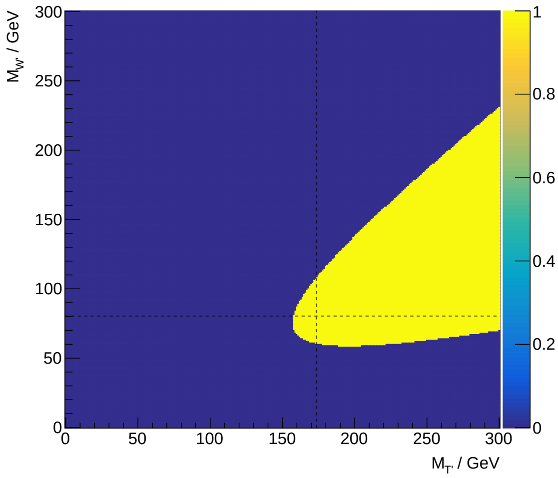

Figure 6.1: Solvability in the two-dimensional mass space $\mathrm{M}_{T'}$ vs $\mathrm{M}_{W'}$ for one single top pair event in simulations. The yellow area relates to mass points in the plane where the equation system is solvable and the blue area, where no real solution exists. The dashed lines indicate the PDG top quark and W boson mass [35].

6.2 Detector Resolution

The *true* momenta of the jets and leptons are measured with finite accuracy due to the detector resolution of the CMS experiment (compare chapter 3.2). This can change a solvable event to a non-solvable one. An expression for the solvability can be recovered by smearing the measured particle kinematics a number of times N_{Iter} according to the detector resolution. The equation system for all so created N_{Iter} test events is solved per mass point $(\mathrm{M}_{T'}, \mathrm{M}_{W'})$. The solvability $S_{Iter}(\mathrm{M}_{T'}, \mathrm{M}_{W'})$ is now defined as the fraction for which a real solution exists:

$$S_{Iter}(\mathrm{M}_{T'}, \mathrm{M}_{W'}) = \frac{1}{N_{Iter}} \sum_{i=1}^{N_{Iter}} S^i(\mathrm{M}_{T'}, \mathrm{M}_{W'}). \tag{6.9}$$

The momenta $|\vec{p}|$ of the leptons are smeared by 1 %. Both jets are smeared according to the jet energy resolution in data, which is estimated from the jet energy resolution calculated for simulations multiplied with the scale factor $\mathrm{c}^{\mathrm{JER}} = \frac{\mathrm{JER}_{\mathrm{data}}}{\mathrm{JER}_{\mathrm{MC}}}$ (see table 5.3, [143, 181–183]). More details about the used jet energy resolution can be found in appendix F. The difference in the jet momenta before and after resolution smearing is propagated to the calculation of the missing transverse energy.

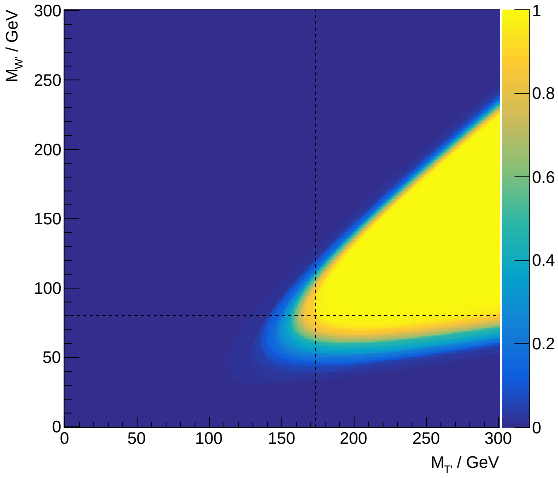

Figure 6.2: Solvability in the two-dimensional mass space $M_{T'}$ vs $M_{W'}$ for one single top pair event in simulations with 100 smearing iterations applied. The yellow area relates to mass points in the plane where the equation system is solvable and the blue area, where no real solution exists. The transition region is smeared out due to the applied detector resolution. The dashed lines indicate the PDG top quark and W boson mass [35].

The solvability $S_{Iter}(M_{T'}, M_{W'})$ for a single event from top pair simulations is shown in figure 6.2. The equation system has only real solutions for all N_{Iter} test events for mass points shown in yellow and no real solution for all mass points in blue. The transition region consists of test events which sometimes have and sometimes do not have a real solution according to the particular smearing applied.

6.3 Parton Density Functions

The beam energy E of the LHC limits the mass space allowed for new particles. As described in section 2.1.1 a hard scattering process is due to the interaction of the proton constituents, the partons (quarks and gluons). The parton density functions (PDF) $f_a(x,Q)$ describe the probability density for a certain parton a to participate in the hard scattering with a fraction x of the hadron's momentum at a hard scattering scale Q [29, 30]. The finite beam energy of the LHC is taken into account by the PDFs, which provide a measure of the probability for a certain process to originate from a proton proton collision. To obtain a PDF $f(x,Q)$ for each parton participating in the hard process, their momentum fractions x_1 and x_2 must be calculated first.

In this analysis the hard scattering process of interest results in a heavy quark pair $\mathrm{T}'\overline{\mathrm{T}'}$. In each mass point the four vector of the $\mathrm{T}'\overline{\mathrm{T}'}$ system is fully reconstructed for each solution and smearing iteration. The two incoming protons in the pp centre of mass frame can be described by four-vectors:

$$\vec{P}_1 = (E,\, 0,\, 0,\, E) \qquad \vec{P}_2 = (E,\, 0,\, 0,\, -E)\,, \tag{6.10}$$

where E is the beam energy $E = \sqrt{s}/2$. Now the four vector of the reconstructed $\mathrm{T}'\overline{\mathrm{T}'}$ system, ignoring its small transverse momentum, can be written as:

$$\vec{P}^{\mathrm{T}'\overline{\mathrm{T}'}} = x_1\vec{P}_1 + x_2\vec{P}_2 = ((x_1+x_2)\,E,\, 0,\, 0,\, (x_1-x_2)\,E) = \left(E^{\mathrm{T}'\overline{\mathrm{T}'}},\, 0,\, 0,\, p_z^{\mathrm{T}'\overline{\mathrm{T}'}}\right) \tag{6.11}$$

where x_1 is the momentum fraction of proton P_1 and x_2 the momentum fraction of proton P_2 carried by the partons involved in the hard process. Solving for x_1 and x_2:

$$x_1 = \frac{E^{\mathrm{T}'\overline{\mathrm{T}'}} + p_z^{\mathrm{T}'\overline{\mathrm{T}'}}}{\sqrt{s}} \qquad x_2 = \frac{E^{\mathrm{T}'\overline{\mathrm{T}'}} - p_z^{\mathrm{T}'\overline{\mathrm{T}'}}}{\sqrt{s}} \tag{6.12}$$

Therefore x_1 and x_2 can be reconstructed from the measured particle kinematics by solving the system of equations. The factor x_1x_2 describes the fraction of the total centre of mass energy squared ($s = (8\ \mathrm{TeV})^2$) available to the parton-parton collision.

Each parton a can be assigned a probability $f_a(x,Q)$ to originate from a pp collision. Multiplying the PDF for both partons a and b results in a PDF weight per solution, iteration and mass point:

$$\text{PDF weight} = \sum_{(a,b)} f_a(x_1,Q) f_b(x_2,Q), \tag{6.13}$$

where the hard scattering scale Q is set to $2m_{T'}$. The summation is performed over all possible leading order parton combinations (a,b) for the production of a quark pair (a,b) $\in \left\{gg, u\overline{u}, d\overline{d}, \overline{u}u, \overline{d}d\right\}$ (compare figure 2.1 and figure 2.3 in chapter 2):

$$\begin{aligned} \text{PDF weight} = {} & f_g(x_1,Q) f_g(x_2,Q) \\ & + f_u(x_1,Q) f_{\overline{u}}(x_2,Q) + f_{\overline{u}}(x_1,Q) f_u(x_2,Q) \\ & + f_d(x_1,Q) f_{\overline{d}}(x_2,Q) + f_{\overline{d}}(x_1,Q) f_d(x_2,Q) \end{aligned} \tag{6.14}$$

The $f_a(x,Q)$'s are taken from the NLO CT10 PDF set [44] obtained with the LHAPDF 5.8.8 and 6.1.6 libraries [45–48]. The PDF weight (equation 6.13-6.14) is the parton-parton luminosity [30] for a certain x_1 and x_2 using only the leading order parton combinations. In figure 6.3, left, the PDF weight for a hard scattering scale $Q = 350$ GeV ($\approx 2M_{top}$) is shown as a function of x_1 and x_2.

Among all possible solutions the one with the highest PDF weight is chosen for each mass point and smearing iteration. The momentum fraction of the protons x_1 and x_2, calculated for the highest PDF weight and averaged over all smearing iterations, is shown in figure 6.3 (right).

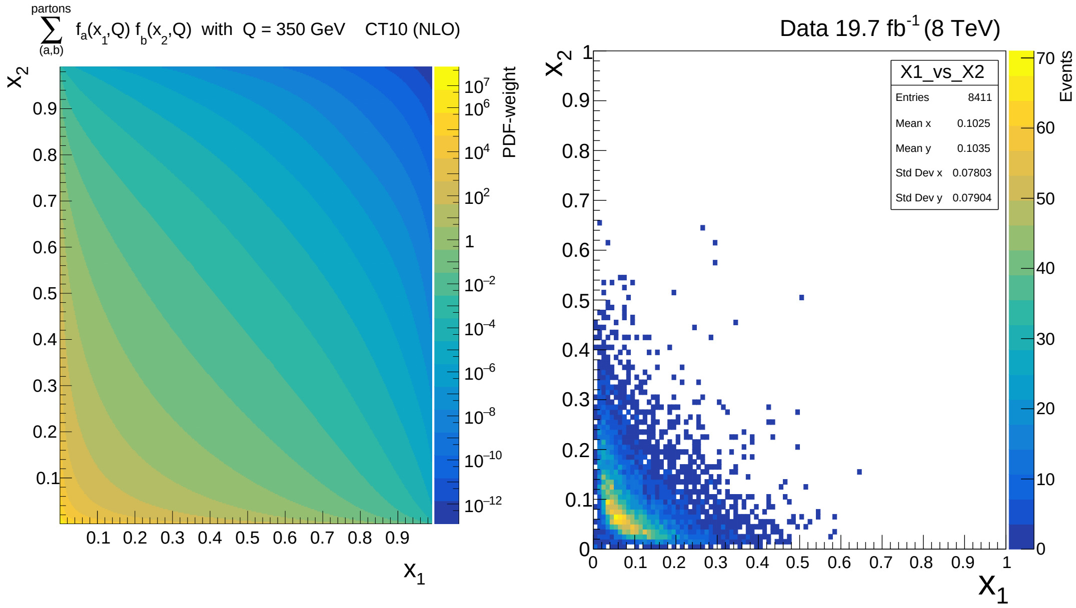

Figure 6.3: PDF weight at a hard scale Q = 350 GeV as a function of x_1 and x_2 as calculated with the CT10 PDF set [44] using LHAPDF libraries [45–48] (left). Distribution of the momentum fraction of the protons x_1 vs x_2 as calculated during this mass reconstruction method for all 2012 data events (right).

Most of the data events concentrate in regions with low momentum fractions x (compare figure 6.3 (right)). They peak around 0.05 for both x_1 and x_2 due to the main SM background process, top pair events ($x_{1/2} \cdot 4\,\mathrm{TeV} \approx M_{top}$).

The probability for an event to originate from a decay involving particles with masses $\mathrm{M}_{T'}$ and $\mathrm{M}_{W'}$ can thus be estimated:

$$P(\mathrm{M}_{T'},\mathrm{M}_{W'}) = \frac{1}{\mathrm{V}} \cdot \frac{1}{N_{Iter}} \sum_{i=1}^{N_{Iter}} \left(S^i(\mathrm{M}_{T'},\mathrm{M}_{W'}) \cdot \max_{1 \le j \le n^i_{\mathrm{Sol}}} \left(\sum_{(a,b)}^{\text{partons}} f_a(x_1^{ij},Q) \cdot f_b(x_2^{ij},Q) \right) \right) \tag{6.15}$$

$$= \frac{1}{\mathrm{V}} \cdot \frac{1}{N_{Iter}} \sum_{i=1}^{N_{Iter}} \left(S^i(\mathrm{M}_{T'},\mathrm{M}_{W'}) \cdot \max_{1 \le j \le n^i_{\mathrm{Sol}}} \left(\text{PDF weight}_{ij} \right) \right) \tag{6.16}$$

with the solvability $S \in \{0,1\}$, the parton combinations (a,b) $\in \left\{gg, u\overline{u}, d\overline{d}, \overline{u}u, \overline{d}d\right\}$ and the number of solutions for iteration i: n^i_{Sol}. The distribution is normalised to unity: $V = \int P\,\mathrm{dM}_{T'}\,\mathrm{dM}_{W'}$. The solvability in the two-dimensional mass space for the same simulated $t\bar{t}$ event with the PDF weight applied is shown in figure 6.4. The finite collision energy gives an upper bound to the allowed phase-space.

For each $P(\mathrm{M}_{T'},\mathrm{M}_{W'})$ the invariant mass of the $\mathrm{T}'\overline{\mathrm{T}'}$ quark pair system is calculated by taking the median $\mathrm{M}_{T'\overline{T'}}$ of all smearing iterations to ensure robustness against outliers.

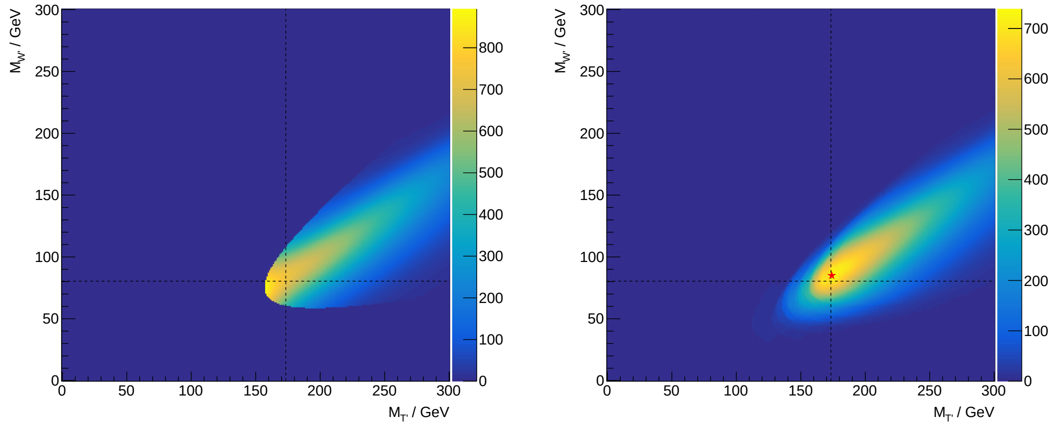

Figure 6.4: Solvability in the two-dimensional mass space $M_{T'}$ vs $M_{W'}$ for one simulated $t\bar{t}$ event including PDF weights without (left) and with (right) 100 smearing iterations. The distributions are normalised to unity. The yellow area relates to mass points in the plane where a solution with large PDF weight exists and the dark blue area where no real solution exists. The dashed lines indicate the PDG top quark and W boson mass [35]. The final estimation for $M_{T'}$ and $M_{W'}$ is given by the position of the red marker.

6.4 Final Observables

The final $M_{T'}$ and $M_{W'}$ estimation per event is the point where $P(M_{T'}, M_{W'})$ is maximal resulting in a single mass point per event. The masses of $M_{T'}$, $M_{W'}$ and $M_{T'\overline{T'}}$ are measured simultaneously per event and are the final observables used for the different BSM searches presented in this thesis.

For a better perspective into the two-dimensional mass reconstruction result, a projection on both the $M_{T'}$ and $M_{W'}$ axes can be performed, resulting in a $M_{T'}$ and $M_{W'}$ distribution, respectively. In the projection on the $M_{T'}$ axis a search for a heavy top partner T′ decaying to SM W bosons is performed. A search for a new heavy gauge boson Z′ decaying into SM top quark pairs is carried out by studying the invariant mass distribution $M_{T'\overline{T'}}$. For the simultaneous search for a new heavy top partner T′ and a new heavy gauge boson W′ the two-dimensional distribution $M_{T'}$ vs $M_{W'}$ is used.

To enhance the sensitivity in the one-dimensional applications, it is beneficial to take advantage of the known information on the SM decay products. Instead of choosing the global maximum of $P(M_{T'}, M_{W'})$ per event for the search for a T′ to SM W bosons, the maximum in a mass window $M_{W'}$ between 60 GeV and 100 GeV around the SM W boson mass is taken per event. For the Z′ search, in addition to the mass window around the SM W boson, the maximum in a mass window between 150 GeV and 200 GeV around the SM top quark mass is chosen per event. This leads to different final event yields per application, if there are no solutions within the imposed mass windows. The expected results, as discussed in chapter 9, are enhanced by 11% for the T′ search and 24% for the Z′ search, when the mentioned mass windows are chosen. For the two-dimensional application there are no conditions on the masses of T′ and W′ .

Comparisons of the resulting mass distributions on the generator level and on the reconstruction level, as well as the influence of the choice of parameters like the number of smearing iterations and the step size in which the mass space is scanned, will be shown in chapter 7 together with applications of the method to data.

CHAPTER 7

Results after Mass Reconstruction

The mass reconstruction method described in chapter 6 is applied to the 2012 CMS data set of $19.7\,\mathrm{fb}^{-1}$ produced at $\sqrt{s} = 8\,\mathrm{TeV}$. The same event selection and parameter settings are used for all applications. All mass reconstruction results are calculated using 100 smearing iterations and a step size of 5 GeV between each mass point in the two-dimensional plane in the range 0 to 2 TeV . The results are not sensitiv to the choice of the parameter settings, as shown in section 7.1. The $M_{T'}$ vs $M_{W'}$ distribution together with the event yield is shown in figure 7.1 .

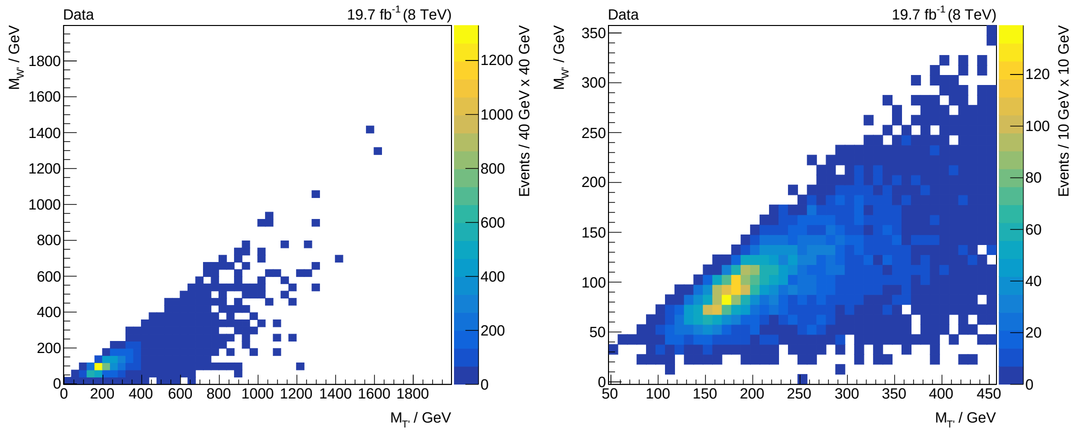

Figure 7.1: Two-dimensional mass reconstruction for the 2012 data corresponding to an integrated luminosity of $19.7\ \mathrm{fb}^{-1}$, for the full phase-space studied, ranging from 0 to 2 TeV in both $M_{T'}$ and $M_{W'}$ (left) and a zoom into the peak region (right).

For a better perspective into the results and a comparison between data and simulation, a projection on both $M_{T'}$ and $M_{W'}$ axes can be performed as already mentioned in chapter 6.4. In figure 7.2 the projection on the $M_{T'}$ axis (left) and the $M_{W'}$ axis (right) after performing the two-dimensional mass reconstruction around the observed W boson and top quark mass, respectively, are shown. To focus on the observed peak, for these two distributions slightly smaller mass windows ($70\,\text{GeV} < M_{W'} < 90\,\text{GeV}$, $160\,\text{GeV} < M_{T'} < 190\,\text{GeV}$)) are chosen (compare section 6.4). The dashed lines indicate the PDG [35] top quark and W boson mass values. The top quark and W boson resonance are observed simultaneously without any prior knowledge of their masses or the underlying theory. Data and simulation agree well within uncertainties (for uncertainty definitions compare section 5.7).

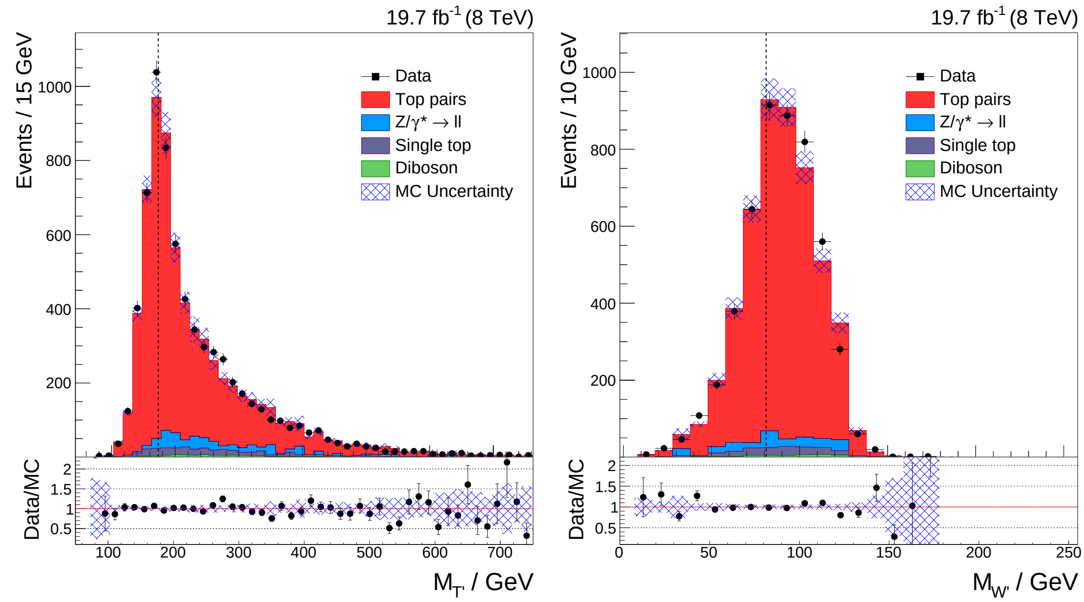

Figure 7.2: The projection on the $M_{T'}$ axis (left) and the $M_{W'}$ axis (right) after the performed two-dimensional mass reconstruction in a W boson mass window of (70 -90) GeV and a top quark mass window of (160 -190) GeV , respectively. Statistical and systematic uncertainties have been combined. The systematic uncertainties are discussed in detail in chapter 8. The dashed lines indicate the PDG top quark and W boson mass [35].

The two-dimensional mass reconstruction for all background components in simulations can be seen in figure 7.3. The distribution is normalised to the integrated luminosity in data and contains all simulated background events. The analysis is almost background free in the interesting high energy region starting from $M_{T'} > 400\,\text{GeV}$.

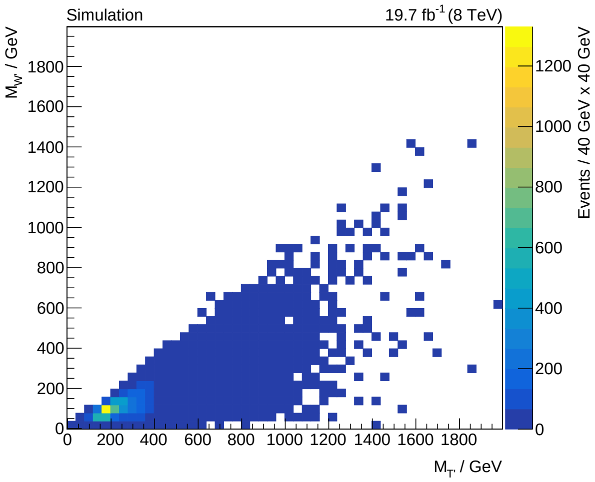

Figure 7.3: Two-dimensional mass reconstruction for all simulated background components, normalised to the integrated luminosity in data. The two-dimensional mass reconstruction for all background components separately can be found in figure G.11 in appendix G.

7.1 Parameter Settings

The choice of parameter settings for the mass reconstruction method are studied in figure 7.4 using the $M_{T'}$ observable in top pair simulations. The influence on the shape or yield of the $M_{T'}$ distribution in the full projection of different number of smearing iterations (top left) and step sizes (top right) is negligible. As described in the last chapter, the unknown association of the reconstructed jets to the two decay chain legs is accounted for by interchanging the jets in the equation system ("jet swap"). This is illustrated in the bottom distributions of figure 7.4 for the full projection (left) and in the W mass window as used by the T′ and Z′ analysis (right). When ensuring that the correct jet association in the mass reconstruction method is taken into account, the peak gets sharper and the number of events increases. Using a mass window around the SM W boson (60 GeV < $M_{W'}$ <100 GeV), corresponding to the assumption that T′ → Wb, leads to a narrower $M_{T'}$ distribution (compare red distributions in figure 7.4 bottom left and right).

The same studies using $M_{W'}$ and $M_{T'\overline{T'}}$ distributions in top pair simulations can be found in appendix G in figures G.12 and G.13.

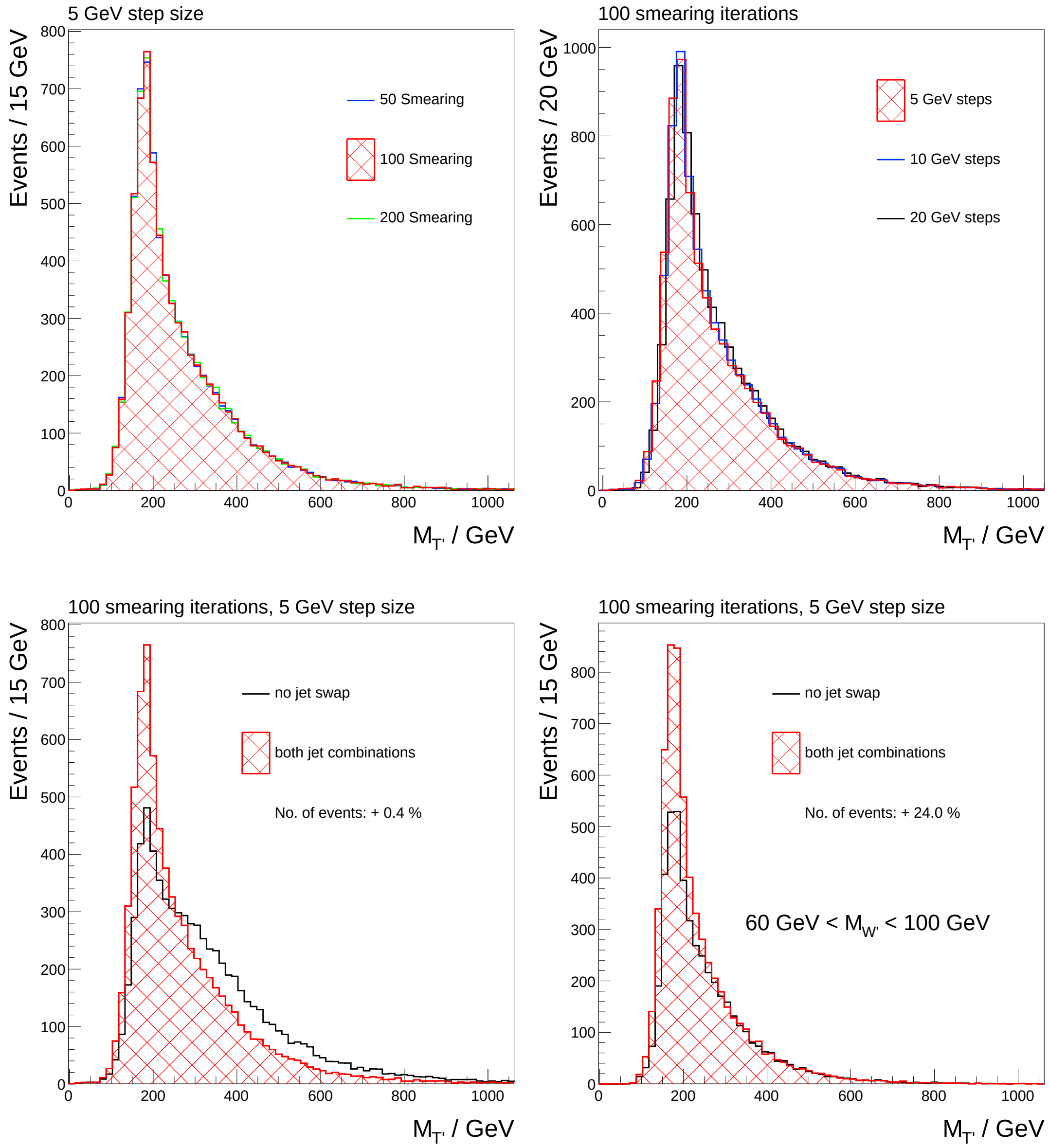

Figure 7.4: Projection on the $M_{T'}$ axis for the top pair simulation samples: for different smearing iterations (top left), different step sizes (top right) and with and without interchanging the two measured jets (bottom) during the mass reconstruction. The used settings of 100 smearing iterations, a step size of 5 GeV and the interchange of the two measured jets are shown in red. A comparison between a full projection (bottom left) and a $M_{W'}$ mass window of (60 - 100) GeV as used for both the T′ and Z′ analysis is shown (bottom right).

7.2 Invariant Mass of T′

In this section the method is applied to a search for a new heavy top partner T′ decaying to SM W bosons. In figure 7.5 the projection on the $M_{T'}$ axis for T′ signal simulations are shown after the mass reconstruction is performed in a mass window of (60 - 100) GeV around the W boson mass. The black lines indicate the input T′ mass to the generator in the production of simulation samples. The projection on the $M_{T'}$ axis for all T′ signal samples used can be found in figure G.15 in appendix G. The method is able to reconstruct successfully particles with masses larger than the top quark mass.

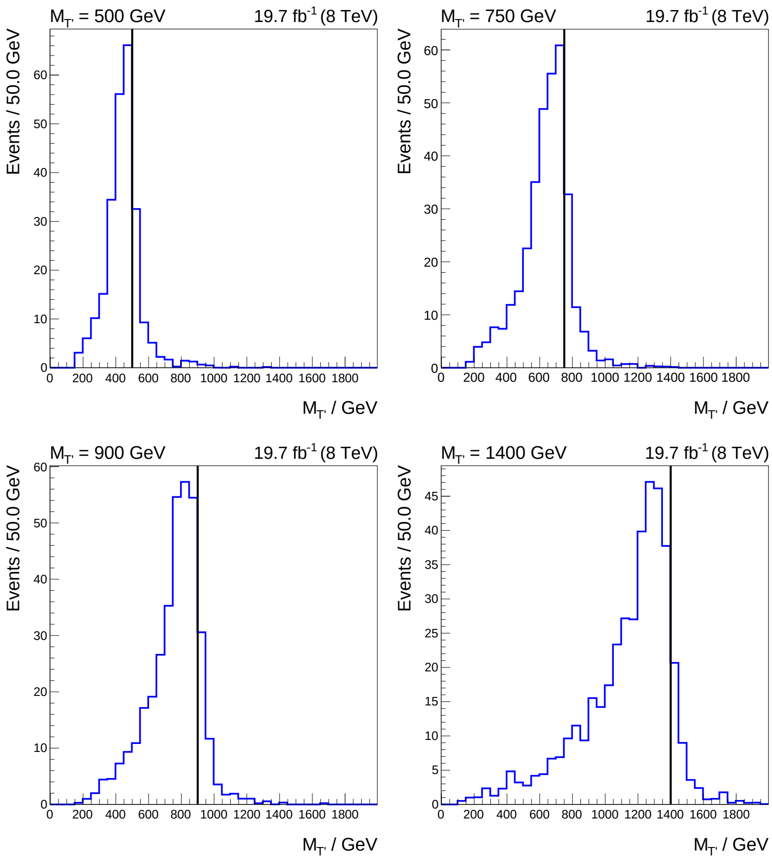

Figure 7.5: Projection on the $M_{T'}$ axis in a $M_{W'}$ window of (60 - 100) GeV for T′ signal simulation samples. The production cross section σ is set to 1 pb. The black lines indicate the mean T′ mass on the generator level. The plots for all generated T′ signal samples can be found in figure G.15 in appendix G.

The shape of the T′ mass distributions and the shift of the mass peak to slightly lower values in comparison to the mean T′ mass on the generator level (black straight line) result from various causes. This is studied in simulations by starting with the information originating from the generator level and the correct association of physics objects to the two legs of the

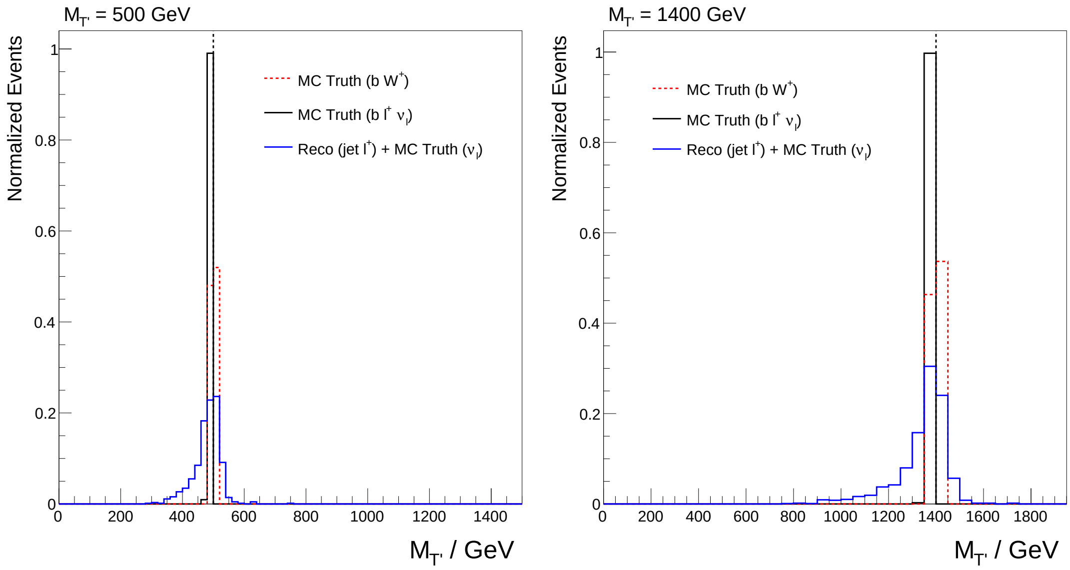

Figure 7.6: The four vector addition for a T′ of 500 GeV (left) and 1400 GeV (right) simulated signal sample after the event selection: using the generator information of the b quark and W boson (red dashed line), using the generator information of the b quark, the lepton l^+ and the neutrino ν_l (black solid line) and using the reconstructed jet and lepton together with the generator information of the neutrino ν_l (blue solid line). The black dashed lines indicate the mean T′ mass on the generator level.

decay chain. On the generator level the information of the quark, lepton and neutrino momenta originating from a dileptonic T′ $\overline{\mathrm{T}'}$ decay are available. The association to physics objects using information from the detector reconstruction is obtained by matching the reconstructed jets, as selected by the event selection from chapter 5, in a tight ΔR cone of 0.1 to the b and $\overline{\mathrm{b}}$ quarks. Only events where both selected reconstructed jets are correctly matched to the quarks on the generator level are used for this study. On reconstruction level the information of the jet and lepton momenta are available. The neutrinos can not be individually reconstructed in the detector and therefore only the measured x and y component of the $E_{\mathrm{T}}^{\mathrm{miss}}$ is available.

The correct association of the generated quarks to the two decay chain legs allows for a vector addition of the b quark and the SM W boson originating from the T′ decay, as shown in the red dashed distributions in figure 7.6 for two exemplary T′ simulation samples. The distributions for the $\overline{\mathrm{T}'}$ decay are similar. The invariant mass is symmetric around the mean T′ mass on the generator level (black dashed line). In the next step the invariant mass is calculated by taking the correct combination of b quark, lepton l^+ and neutrino ν_l on the generator level, as shown in the black distributions in figure 7.6. Photons radiated from the SM W bosons shift the invariant mass peak on the generator level to slightly lower values.

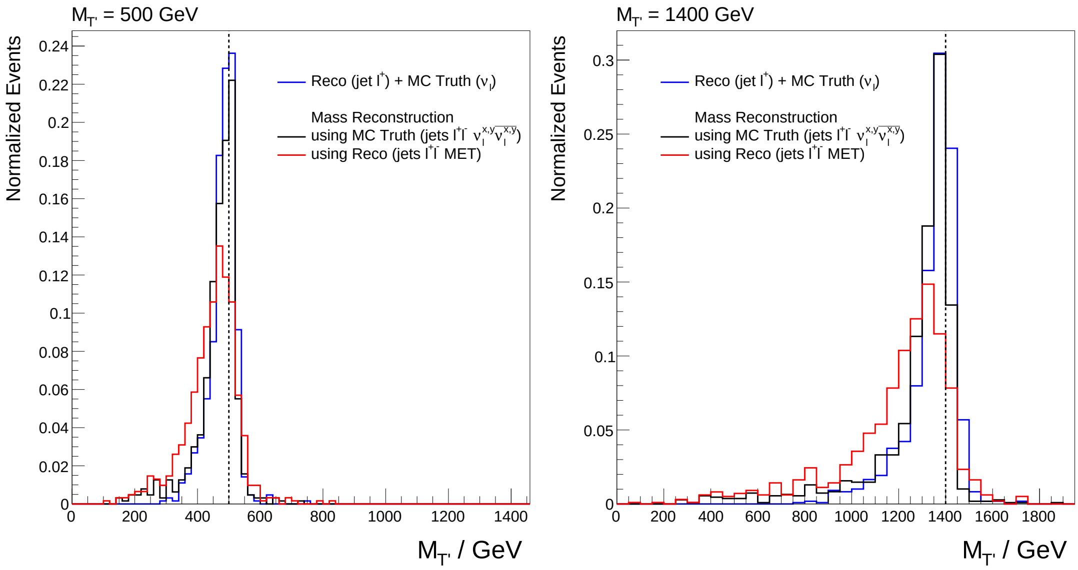

Figure 7.7: Projection on the $M_{T'}$ axis in a $M_{W'}$ window of (60 - 100) GeV for a T′ of 500 GeV (left) and 1400 GeV (right): using either the generator information of both quarks, leptons and neutrinos ($p^{x,y}_{\nu_l}$ + $p^{x,y}_{\overline{\nu_l}}$) (black solid line) or the information from the detector reconstruction for both jets, leptons and $E_{\mathrm{T}}^{\mathrm{miss}}$ (red solid line) as an input to the mass reconstruction method, whereby both jet combinations are taken into account. The four vector additions using the correctly associated jet and lepton from the detector reconstruction together with the generator information of the neutrino ν_l are shown in the blue solid distributions. The black dashed lines indicate the mean T′ mass on the generator level.

In the blue distributions in figure 7.6 the b quark and the lepton l^+ are exchanged with the matched reconstructed jet and lepton, respectively. The invariant mass is calculated by combining these objects with the true neutrino momentum. The reconstruction algorithms of CMS lead to more broadened asymmetric distributions due to initial and final state radiation and the mis-measurement of the kinematics of the physics objects even before applying the mass reconstruction method.

In addition to the evolution from generator to reconstruction level, the development from the invariant mass calculated from the four-vector addition after the event selection to the reconstruction of $M_{T'}$ in the mass reconstruction method is studied. It is important to note, that for the mass reconstruction using the method described in chapter 6 the correct association of the jets to the decay chain legs is unknown. In addition the z-components of the neutrino momenta can not be used as an input to the method. Furthermore both leptons and both jets are used, resulting in a single reconstructed mass $M_{T'}$ for the two legs of the decay chain.

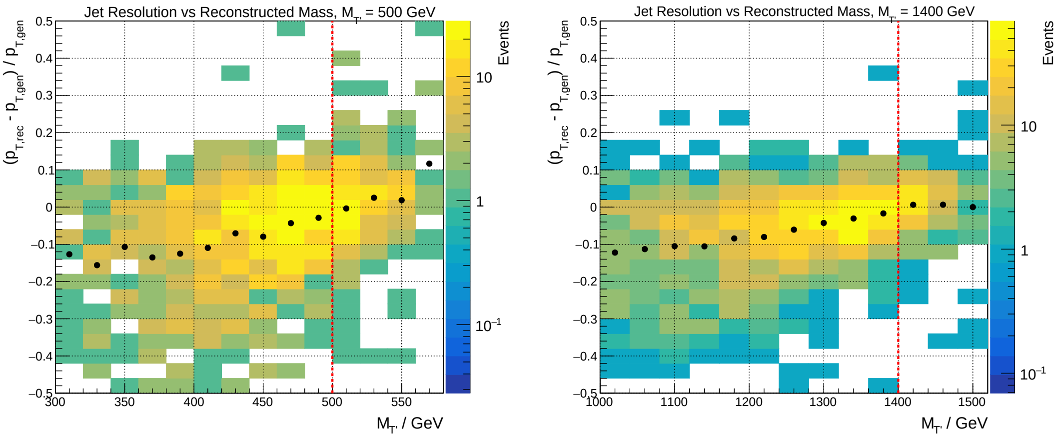

Figure 7.8: Resolution of the transverse momentum p_{T} of the reconstructed jet in comparison to the p_{T} of the matched b or $\overline{\mathrm{b}}$ quark for a T′ of 500 GeV (left) and 1400 GeV (right) simulated signal sample as a function of the reconstructed $\mathrm{M}_{T'}$ from the mass reconstruction method. The black dots correspond to the mean value per $\mathrm{M}_{T'}$ bin.

In figure 7.7 the mass reconstruction method as used in the final analysis is applied on the same events using the true momenta of the quarks and leptons as well as the true $E_{\mathrm{T}}^{\mathrm{miss}}$ (black solid line). These distributions are obtained using the full reconstruction which includes smearing with the detector resolution, the PDF weights as well as interchanging the jets in the equation system. For comparison the blue distributions from figure 7.6 are also shown. In the next step the momenta of the physics objects from the detector reconstruction are used (red solid line). Since both jets are used in the mass reconstruction, inaccurate measurement of the energy of either jet leads to a more broadened distribution and a shift to lower values in the final mass observable when comparing the red and the blue distributions. The same effect occurs due to mis-measurement of the $E_{\mathrm{T}}^{\mathrm{miss}}$ and is partly recovered in the black distributions, where the generated objects are used.
The effect of the mis-measurement of the jet momentum on the reconstructed mass $\mathrm{M}_{T'}$ is studied for the same simulated signal samples in figure 7.8. The distributions show the dependence of the reconstructed $\mathrm{M}_{T'}$ on the jet p_{T} resolution. In events where the reconstructed $\mathrm{M}_{T'}$ deviates from the expectation (red dashed line) the jet momentum is lower than the true quark momentum by up to 15%. Furthermore a bias in the jet momentum reconstruction also propagates to a bias in the $E_{\mathrm{T}}^{\mathrm{miss}}$ calculation.

In summary most of the shift and the asymmetric shape in the reconstructed mass can be explained by mis-measurement of the physics objects and is therefore not inherent in the mass reconstruction method itself. In addition a small bias remains, which can be attributed to the PDF weight, which favours lower mass points since they are more likely to originate from a pp collision. In case of a discovery a correction function can be derived.

The distributions used in the search for a new heavy top partner T′ for all different channels combined (top left) and for the ee (top right), $\mu\mu$ (bottom left) and the $e\mu$ channel (bottom right) separately, are presented in figure 7.9. A T′ signal of 750 GeV with a production cross section σ of 1 pb is injected (orange). The background event yields after mass reconstruction are given in table 7.1 for the three different channels and their combination. Statistical and systematic uncertainties are shown separately. The over-fluctuation in the ee channel and under-fluctuation in the $\mu\mu$ channel between data and total background is covered by the uncertainties. Signal event yields for all T′ simulations for the ee, $\mu\mu$, $e\mu$ and the combined dilepton channel are shown in appendix G.2.

Table 7.1: Background event yields for the T′ search in the ee, $\mu\mu$, $e\mu$ and the combined dilepton channel. The statistical and systematic uncertainties are shown separately. The systematic uncertainties are discussed in detail in chapter 8.

Sample	ee yield ± stat ± sys	$\mu\mu$ yield ± stat ± sys	$e\mu$ yield ± stat ± sys	**total** yield ± stat ± sys
Top pairs	1533.4 ± 17.2 ± 140.3	1788.1 ± 18.7 ± 129.2	2989.1 ± 24.1 ± 158.9	6310.6 ± 35.0 ± 404.2
Z + jets	175.1 ± 26.4 ± 133.6	217.1 ± 29.4 ± 159.5	54.8 ± 14.7 ± 40.6	447.1 ± 42.1 ± 333.7
Single Top	61.2 ± 5.2 ± 30.9	88.7 ± 6.3 ± 44.5	151.5 ± 8.2 ± 76.0	301.5 ± 11.5 ± 151.1
Diboson	26.0 ± 1.5 ± 7.9	27.1 ± 1.5 ± 8.2	38.9 ± 1.9 ± 11.8	92.0 ± 2.9 ± 27.9
Total Bkg	1795.7 ± 34.9 ± 196.4	2121.0 ± 38.3 ± 210.2	3234.4 ± 32.5 ± 181.2	7151.1 ± 58.8 ± 546.2
Data	**1941**	**1998**	**3239**	**7178**

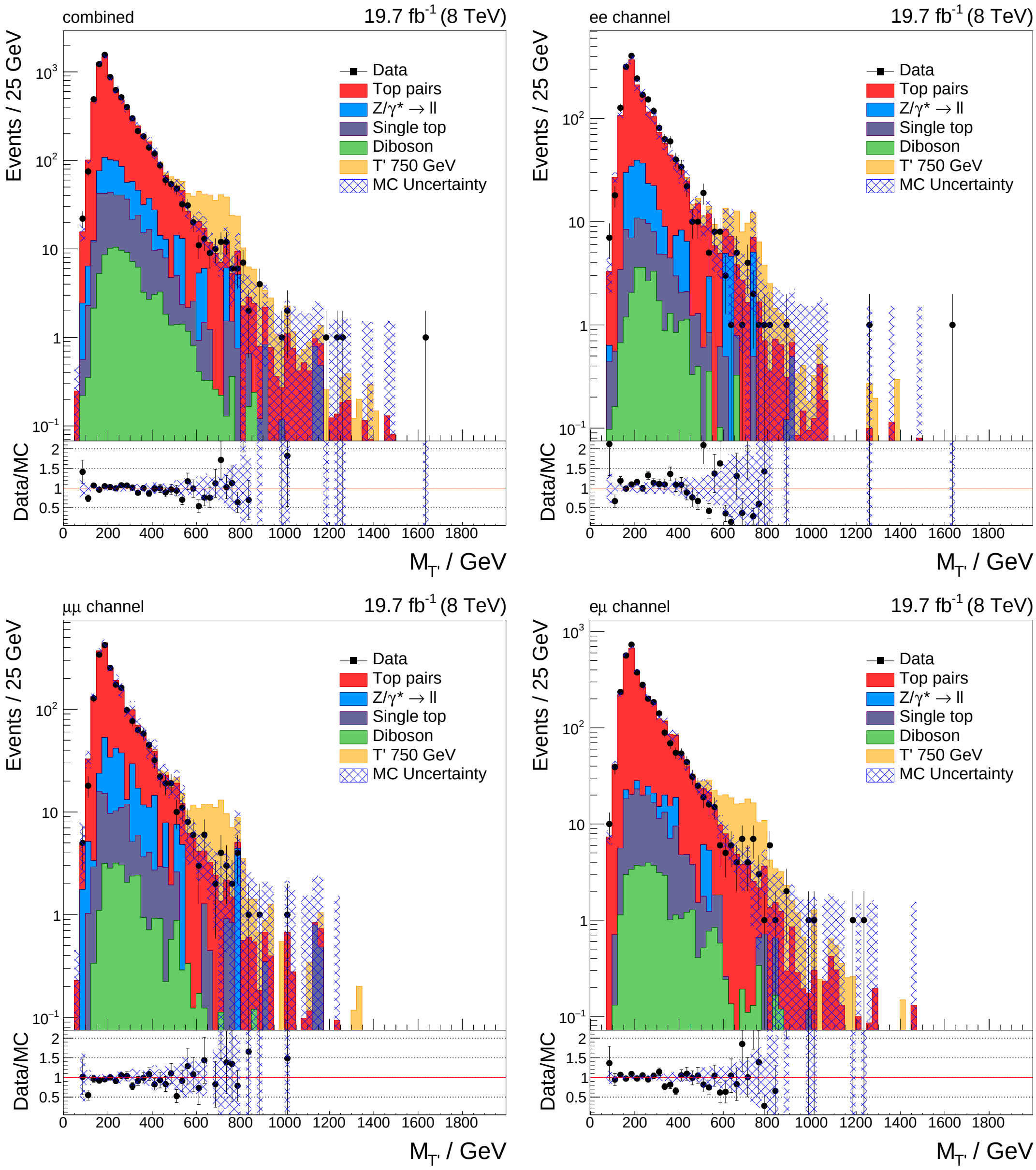

Figure 7.9: Projection on the $M_{T'}$ axis in a $M_{W'}$ mass window of (60 - 100) GeV after mass reconstruction for all channels combined (top left) and for the *ee* (top right), $\mu\mu$ (bottom left) and the $e\mu$ channel (bottom right) separately. Statistical and systematic uncertainties have been combined. The systematic uncertainties are discussed in detail in chapter 8. An injected T′ signal of 750 GeV is shown with a production cross section $\sigma = 1$ pb.

7.3 Invariant Mass of $\mathrm{T'\overline{T'}}$

The invariant mass of the $\mathrm{T'\overline{T'}}$ pair system is used as the one-dimensional final observable in the search for a new heavy $\mathrm{Z'}$ decaying to SM top pairs. In figure 7.10 this observable is successfully reconstructed for different $\mathrm{Z'}$ signal samples after the same selection and mass reconstruction is applied as in data. The $\mathrm{M}_{T'\overline{T'}}$ invariant mass distribution for all $\mathrm{Z'}$ signal samples can be found in figure G.16 in appendix G.

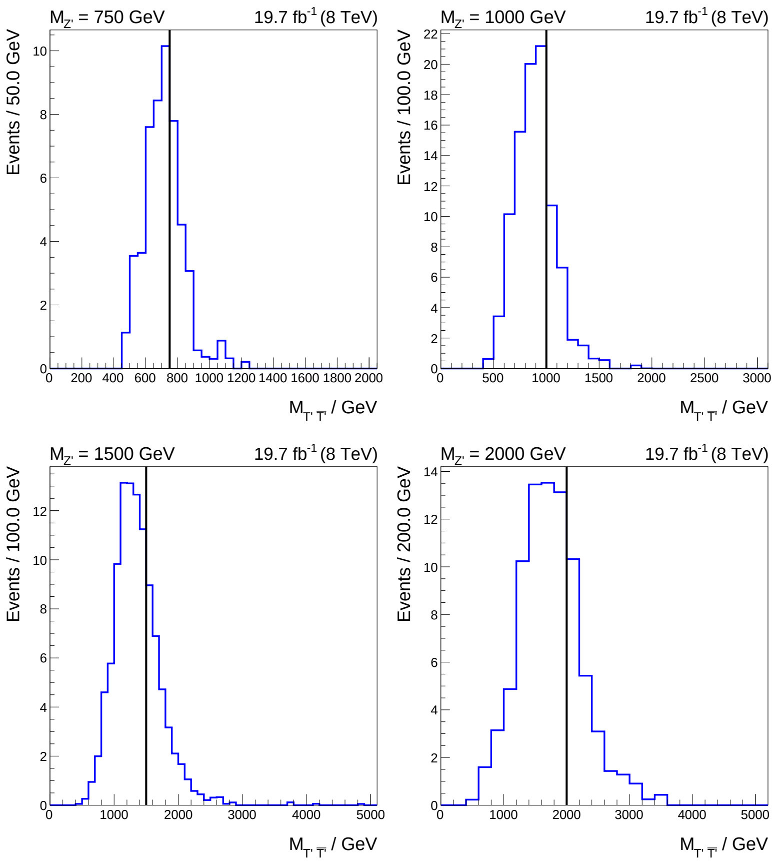

Figure 7.10: $\mathrm{M}_{T'\overline{T'}}$ invariant mass distribution in a $\mathrm{M}_{W'}$ mass window of (60 - 100) GeV and a $\mathrm{M}_{T'}$ mass window of (150 - 200) GeV for $\mathrm{Z'}$ signal simulation samples. The production cross section σ is set to 1 pb. The black lines indicate the input $\mathrm{Z'}$ mass to the generator in the production of simulation samples. The $\mathrm{M}_{T'\overline{T'}}$ invariant mass distribution for all $\mathrm{Z'}$ signal samples can be found in figure G.16 in appendix G.

Similar to the $\mathrm{T'}$ studies in the previous section, the reconstructed resonances are shifted to slightly lower mass values in comparison to the generated mean $\mathrm{Z'}$ mass (black line) in the $\mathrm{M}_{T'\overline{T'}}$ distributions in figure 7.10. This effect is again due to the CMS reconstruction algorithms, as demonstrated in section 7.2.

The distributions used in the search for a new heavy gauge partner Z′ for all different channels combined (top left) and for the ee (top right), $\mu\mu$ (bottom left) and the $e\mu$ channel (bottom right) separately, are presented in figure 7.11. The data and the simulations agree well within uncertainties giving no indication for an additional resonant top pair contribution. A Z′ signal of 1500 GeV with a production cross section σ of 2 pb is injected (orange). The corresponding overall event yields after mass reconstruction are also presented in table 7.2 for all channels combined and for the individual channels. Statistical and systematic uncertainties are shown separately. The over-fluctuation in the ee channel and under-fluctuation in the $\mu\mu$ channel between data and total background is covered by the uncertainties. Signal event yields for all Z′ simulations are shown in appendix G.3 for the ee, $\mu\mu$, $e\mu$ and the combined data set.

Table 7.2: Background event yields for the Z′ search in the ee, $\mu\mu$, $e\mu$ and the combined dilepton channel. The statistical and systematic uncertainties are shown separately. The systematic uncertainties are discussed in detail in chapter 8.

Sample	ee yield ± stat ± sys	$\mu\mu$ yield ± stat ± sys	$e\mu$ yield ± stat ± sys	**total** yield ± stat ± sys
Top pairs	1105.3 ± 14.6 ± 68.6	1312.8 ± 16.0 ± 62.4	2152.5 ± 20.5 ± 109.9	4570.7 ± 29.8 ± 208.2
Z + jets	106.8 ± 20.6 ± 80.9	93.8 ± 19.4 ± 70.4	4.3 ± 4.1 ± 3.2	204.9 ± 28.6 ± 154.0
Single Top	30.6 ± 3.7 ± 15.5	44.1 ± 4.4 ± 22.2	76.0 ± 5.8 ± 38.1	150.7 ± 8.2 ± 75.6
Diboson	10.6 ± 1.0 ± 3.3	10.5 ± 0.9 ± 3.3	15.4 ± 1.2 ± 4.7	36.6 ± 1.8 ± 11.2
Total Bkg	1253.3 ± 29.9 ± 107.2	1461.3 ± 29.8 ± 96.7	2248.2 ± 26.4 ± 116.4	4962.9 ± 45.6 ± 270.0
Data	**1346**	**1387**	**2296**	**5029**

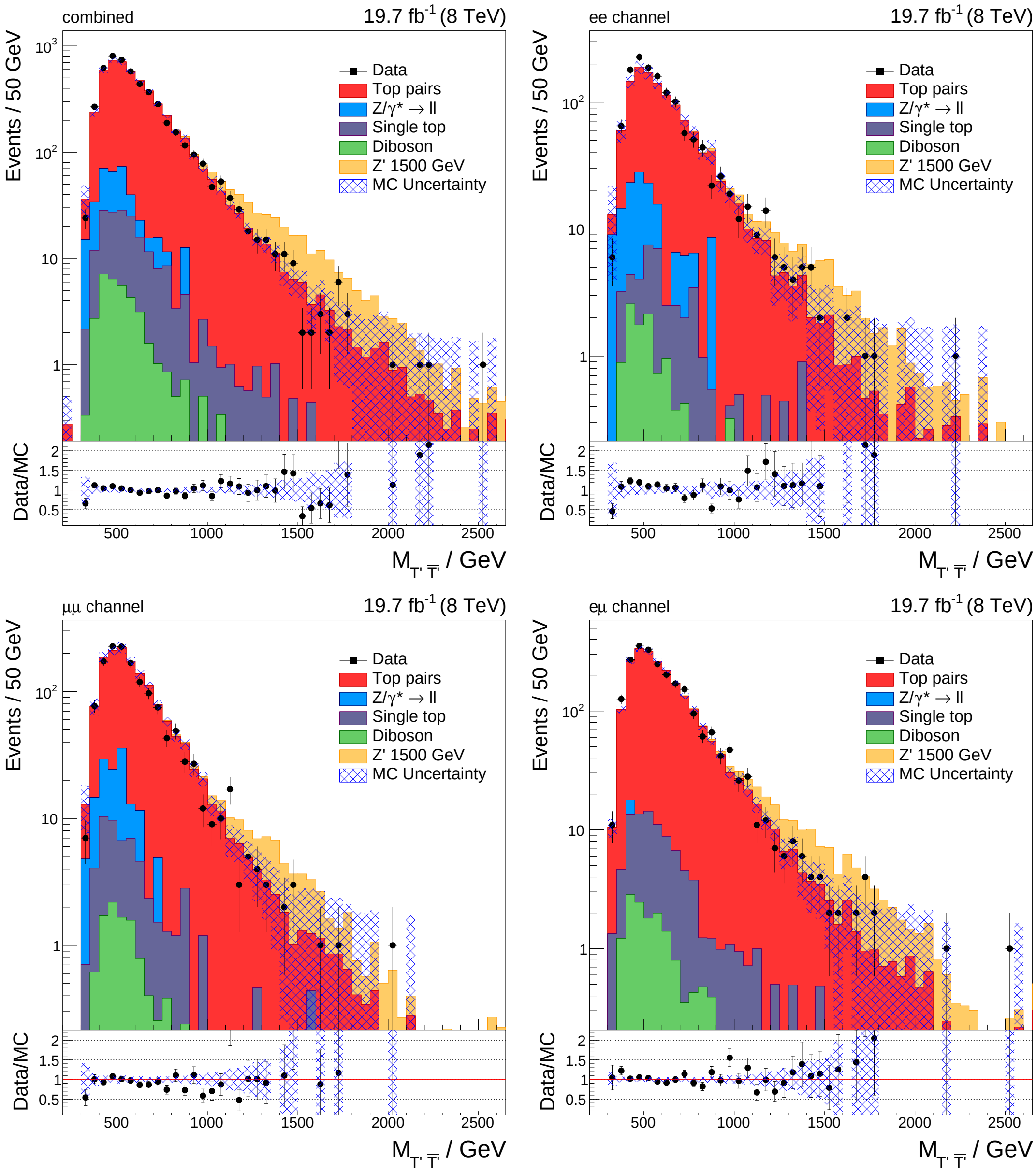

Figure 7.11: $M_{T'\overline{T'}}$ invariant mass distribution in a $M_{W'}$ mass window of (60 - 100) GeV and a $M_{T'}$ mass window of (150 - 200) GeV after mass reconstruction for all channels combined (top left) and for the *ee* (top right), $\mu\mu$ (bottom left) and the $e\mu$ channel (bottom right) separately. Statistical and systematic uncertainties have been combined. The systematic uncertainties are discussed in detail in chapter 8. An injected Z′ signal of 1500 GeV is shown with a production cross section $\sigma = 2$ pb.

7.4 Two-dimensional Mass Plane

As mentioned in 6.4 the two-dimensional search is performed without any restriction on the masses. In figure 7.12 the performance of the two-dimensional mass reconstruction for simplified Littlest Higgs signal simulated samples[1] is presented after the same selection requirements are applied as in data. The dashed lines indicate the input T′ and W′ masses to the generator in the production of simulation samples. The two-dimensional mass reconstruction for all simplified Littlest Higgs signal samples used can be found in figures G.17-G.19 in appendix G. Different $M_{T'}$ and $M_{W'}$ are successfully reconstructed in the two-dimensional plane for different input masses.

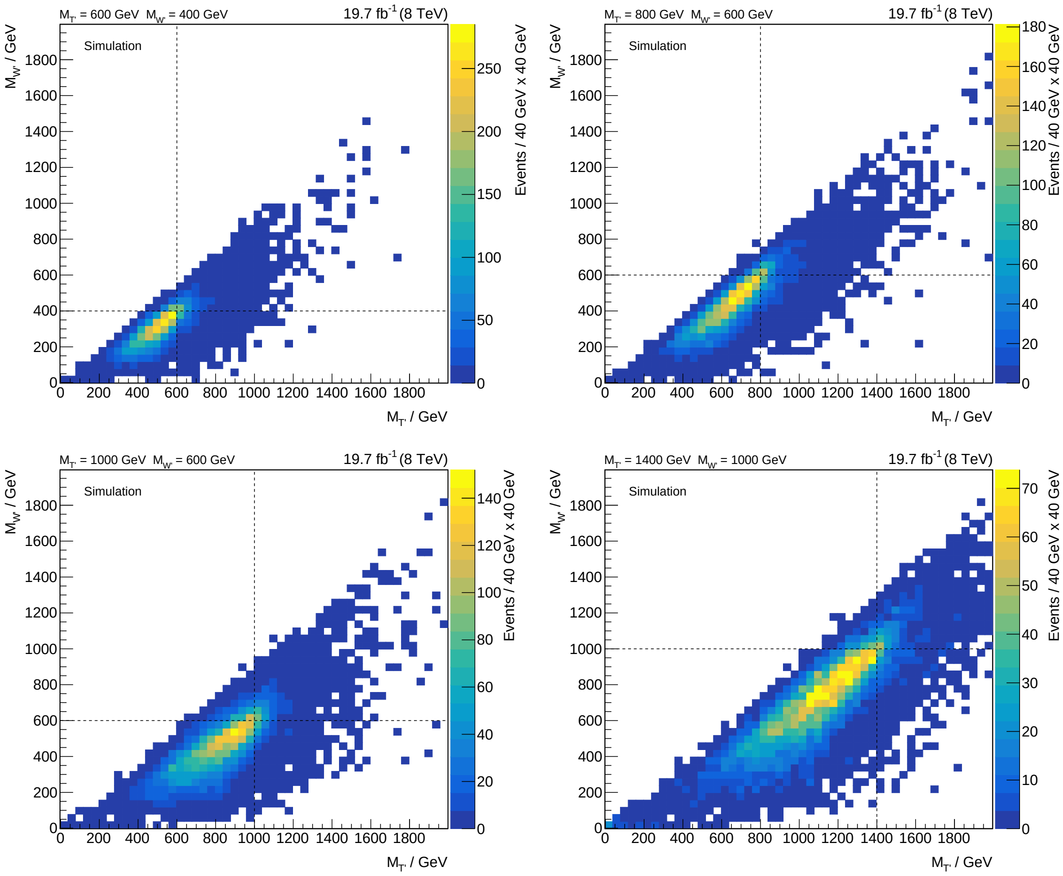

Figure 7.12: Two-dimensional mass reconstruction for simplified Littlest Higgs signal simulation samples. The production cross section σ is set to 1 pb. The dashed lines indicate the mean T′ and W′ masses on the generator level. The two-dimensional mass reconstruction for all simplified Littlest Higgs signal samples used can be found in figures G.17-G.19 in appendix G.

[1] A short description of the model is given in appendix E.

Also in the two-dimensional plane the resonances tend to peak at lower than the generated mass values. In figure 7.13 the two-dimensional mass reconstruction for the same signal simulations using pure generator level objects are shown. Comparing the mass reconstruction used in this analysis (figure 7.12) and the mass reconstruction using the quark, lepton and neutrino objects on the generator level (figure 7.13), it can be seen again that the resonances are broadened and shifted to lower mass values in $\mathrm{M}_{T'}$ and $\mathrm{M}_{W'}$. Similar to the studies demonstrated in section 7.2 this is not due to the mass reconstruction method, but due to object reconstruction within CMS. A comparison between distributions using the generator information of the momenta of the quarks, leptons and neutrinos and physics objects reconstructed in the detector matched ($\Delta R < 0.1$) to generator level objects as an input to the mass reconstruction method can be found in figure G.14 in the appendix.

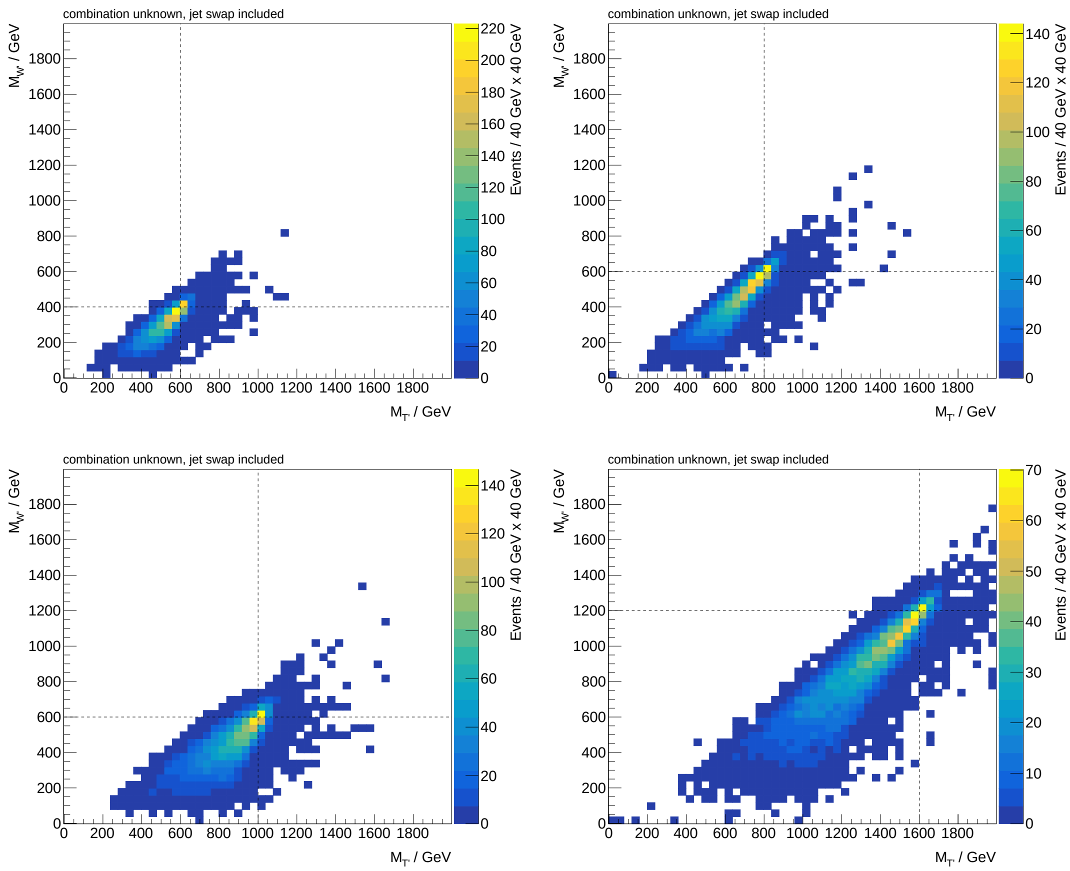

Figure 7.13: Two-dimensional mass reconstruction for simplified Littlest Higgs signal simulation samples for a T′ of 600 GeV and a W′ of 400 GeV (top, left), a T′ of 800 GeV and a W′ of 600 GeV (top, right), a T′ of 1000 GeV and a W′ of 600 GeV (bottom, left) and a T′ of 1600 GeV and a W′ of 1200 GeV (bottom, right) using generator level objects. The production cross section σ is set to 1 pb. The dashed lines indicate the input T′ and W′ masses to the generator in the production of simulation samples.

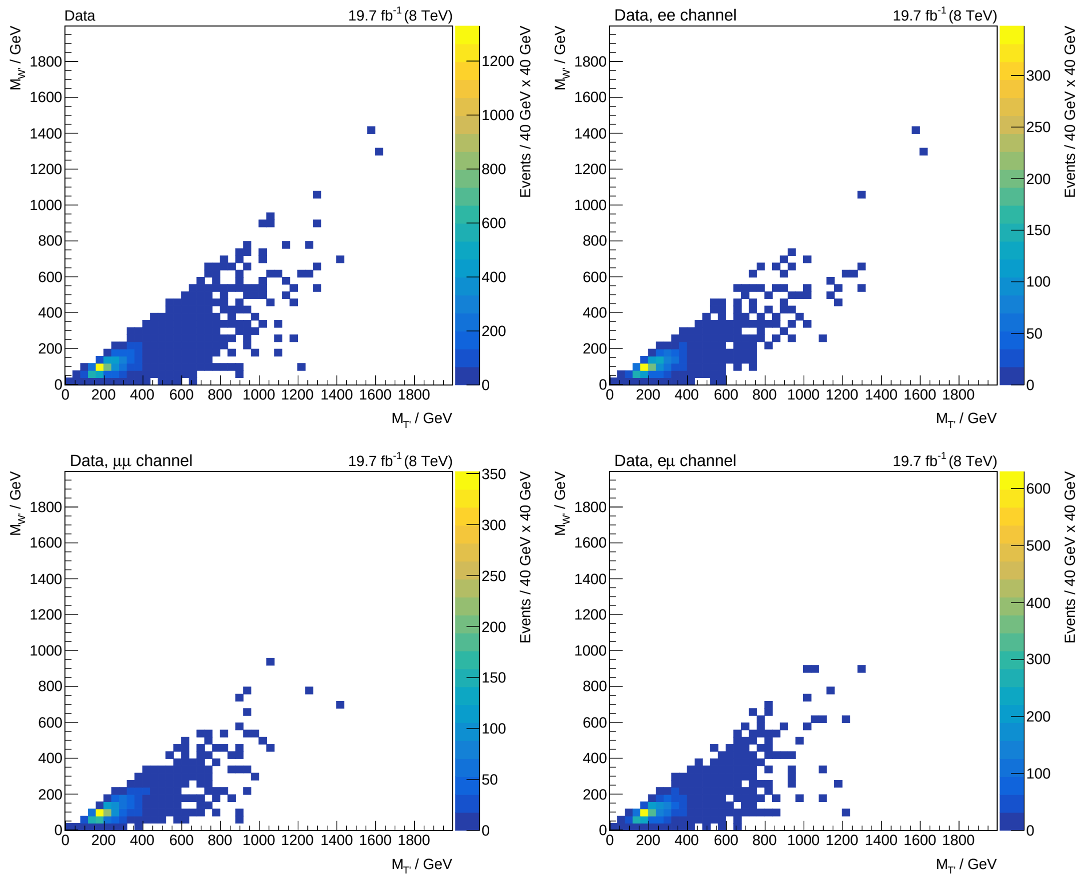

Figure 7.14: Two-dimensional mass reconstruction for the 2012 dataset corresponding to 19.7 fb^{-1} , for all channels combined (top left) and for the ee (top right), $\mu\mu$ (bottom left) and the $e\mu$ channel (bottom right) separately.

The two-dimensional mass reconstruction for all data and for the three leptonic channels separately is shown in figure 7.14 for the full 2012 data set corresponding to 19.7 fb^{-1} . This distribution can be compared to that in figure 7.3. The two-dimensional mass reconstruction for all background components separately is given in figure G.11.

The corresponding event yields for the two-dimensional search are presented in table 7.3 with their statistical and systematic uncertainties. Signal event yields for all simplified Littlest Higgs samples in the ee, $\mu\mu$, $e\mu$ and the combined dilepton channel are shown in table G.4 in the appendix.

Table 7.3: Background event yields for the two-dimensional search in the ee, $\mu\mu$, $e\mu$ and the combined dilepton channel. The statistical and systematic uncertainties are shown separately. The systematic uncertainties are discussed in detail in chapter 8.

Sample	ee yield ± stat ± sys	$\mu\mu$ yield ± stat ± sys	$e\mu$ yield ± stat ± sys	**total** yield ± stat ± sys
Top pairs	1803.4 ± 18.6 ± 170.9	2060.4 ± 20.0 ± 137.8	3478.6 ± 25.9 ± 217.5	7342.4 ± 37.7 ± 509.9
Z + jets	279.8 ± 33.5 ± 210.9	357.9 ± 38.0 ± 260.5	99.5 ± 19.8 ± 73.3	737.2 ± 54.4 ± 545.4
Single Top	87.5 ± 6.2 ± 43.9	113.1 ± 7.1 ± 56.7	187.8 ± 9.1 ± 94.1	388.4 ± 13.1 ± 194.6
Diboson	33.4 ± 1.7 ± 10.2	35.6 ± 1.7 ± 10.8	50.5 ± 2.2 ± 15.3	119.5 ± 3.3 ± 36.3
Total Bkg	2204.1 ± 38.9 ± 275.2	2567.1 ± 43.5 ± 300.3	3816.3 ± 34.0 ± 248.5	8587.5 ± 67.5 ± 772.5
Data	**2320**	**2351**	**3740**	**8411**

Finally, the influence of an injected $T'\overline{T'}$ signal with $M_{T'} = 1000\,\text{GeV}$ and $M_{W'} = 600\,\text{GeV}$ on top of the background is illustrated in figure 7.15. Comparing this with the data distributions (figure 7.14) shows that possible new signals will mostly peak in an almost background-free region. The background enhanced region is used to validate the background simulation as described in the next section.

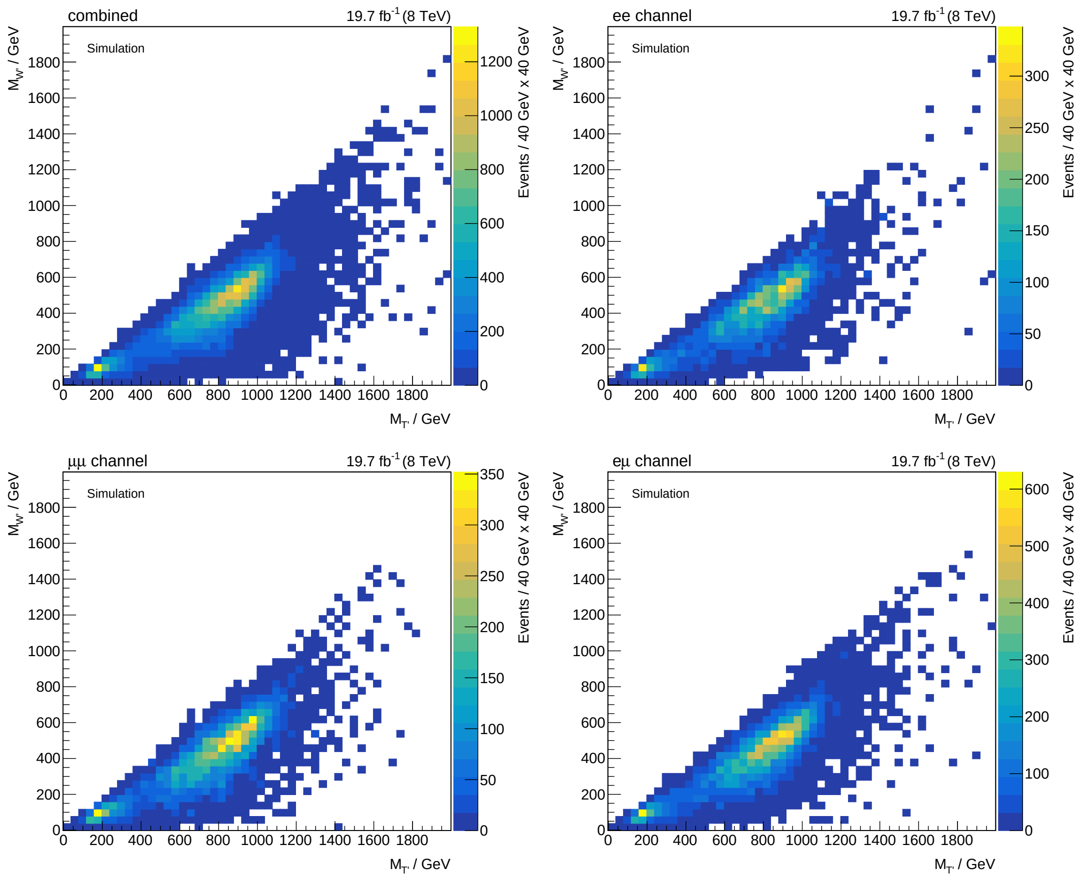

Figure 7.15: Two-dimensional mass reconstruction for simulation background samples with an injected Littlest Higgs signal of $M_{T'} = 1000\,\text{GeV}$ and $M_{W'} = 600\,\text{GeV}$ for all channels combined (top left) and the ee (top right), the $\mu\mu$ (bottom left) and the $e\mu$ channel (bottom right) separately. The production cross section σ is set to 1 pb.

7.5 Top pair Control Region

Over 85% of the background consists of top pairs. The good separation between the signal region, starting with the lowest generated Little Higgs signal at $M_{T'}$ of 400 GeV and $M_{W'}$ of 200 GeV , and the top pair background region allows the latter to be used as an effective control region to check the background simulation. The top pair control region is defined as the region with $M_{T'} < 300$ GeV and $M_{W'} < 100$ GeV . The invariant $M_{T'\overline{T'}}$ mass distribution in this region is shown in figure 7.16 (left), where good agreement between data and simulation is observed within the uncertainties. Depending on the $M_{T'}$ and $M_{W'}$ the different generated signal samples contaminate the control region by at most 1.5%. Signal contamination can be further reduced to less than 0.2% for all generated signals by applying an additional cut on the invariant mass of the $T'\overline{T'}$ system $M_{T'\overline{T'}} < 600$ GeV . The $M_{T'}$ distribution for this region is presented in figure 7.16 (right) again showing good agreement between data and simulation.

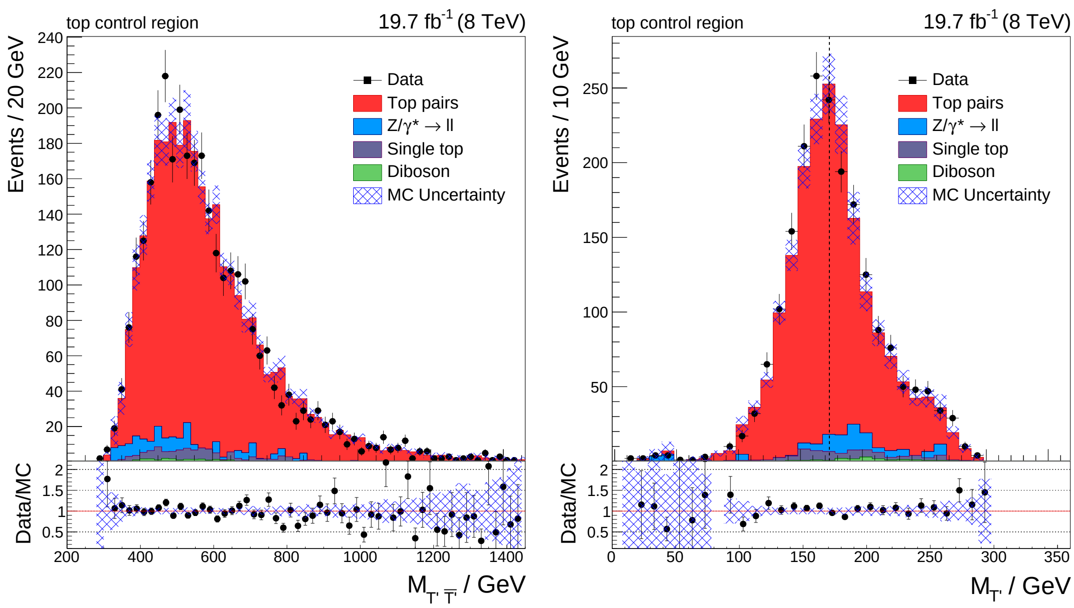

Figure 7.16: $M_{T'\overline{T'}}$ invariant mass distribution in the top pair control region (left) and the projection on the $M_{T'}$ axis with an additional cut on the $T'\overline{T'}$ mass (right). The dashed line indicates the PDG top quark mass [35]. Statistical and systematic uncertainties have been combined. The systematic uncertainties are discussed in detail in chapter 8.

An overall scale factor $SF^{t\bar{t}}$ can be derived,

$$SF^{t\bar{t}} = (\text{Data} - \text{MC}^{non-t\bar{t}})/\text{MC}^{t\bar{t}} = 1.035 \pm 0.032\,(\text{stat.})\,. \tag{7.1}$$

The top pair scale factor $SF^{t\bar{t}}$ is compatible with unity, even without considering systematic uncertainties. Therefore no additional correction is applied to the simulated top pair background.

The next most important background contribution is Drell-Yan ($\approx 9\%$) and is accounted for with the $R_{\mathrm{out/in}}$ method as described in section 5.8.

CHAPTER 8

Systematic Uncertainties

Apart from statistical uncertainties the sensitivity of a measurement is also influenced by systematic uncertainties. They reflect the imperfect knowledge of theory, the detector and its calibrations. The systematic uncertainties can affect the number and the shape of the selected events for both signal and background processes. In this chapter the different sources of systematic uncertainties are described, whereby both shape and rate systematic effects are considered. The rates are assumed to follow log-normal distributions, which are the statistical realisation of the multiplicative product of many independent positive random variables. The nominal distributions are varied according to each systematic uncertainty and the average with respect to the nominal distribution is used. The systematic uncertainties for all signal samples are calculated and the highest value is taken for each systematic effect, channel and search application. A summary of the systematic uncertainties considered for the T' , the Z' and the two-dimensional search are presented at the end of this chapter in tables 8.1 -8.3 for the combined channels. The systematic uncertainties for the separate channels can be found in the appendix in tables H.5-H.13.

Luminosity The luminosity measurement based on pixel cluster counting at CMS has been described in section 3.2.6. The uncertainty on the integrated luminosity is estimated to be 2.6% [127]. All simulated samples are scaled to match the measured luminosity in data, therefore this uncertainty affects all simulations.

Pile-Up Modelling As described in section 5.7, to account for additional multiple proton proton interactions within, before and after the same bunch crossing, the “pile-up-reweighting” is applied to simulations to match the number of pile-up interactions in data. The total inelastic cross section used for the superposition of simulated minimum bias events is varied from its nominal value of 69.4 mb by 5% to 65.9 mb and 72.9 mb [190]. The pile-up-reweighting is re-calculated with these cross sections to check the effect on the event yields.

Trigger and Lepton Identification As described in sections 5.1 to 5.4, corrections are applied to compensate for imperfect modelling of the trigger and lepton identifications for muons and electrons. These are varied within their combined statistical and systematic uncertainty, thus allowing an estimate of the systematic effect on the applied scale factors.

Jet Energy Scale Imperfect modelling of the jet energy scale is taken into account by shifting the transverse momentum p_{T} of each jet by one standard deviation of the jet energy scale systematic uncertainty. The jet energy scale uncertainty is given as a function of p_{T} and η as shown in figure 8.1 for several η regions [143, 181–183]. The change to the jet energy is propagated through the event and $E_{\mathrm{T}}^{\mathrm{miss}}$ is re-calculated. This affects the event selection and the analysis is repeated for the upward and downward variations of the jet energy scale.

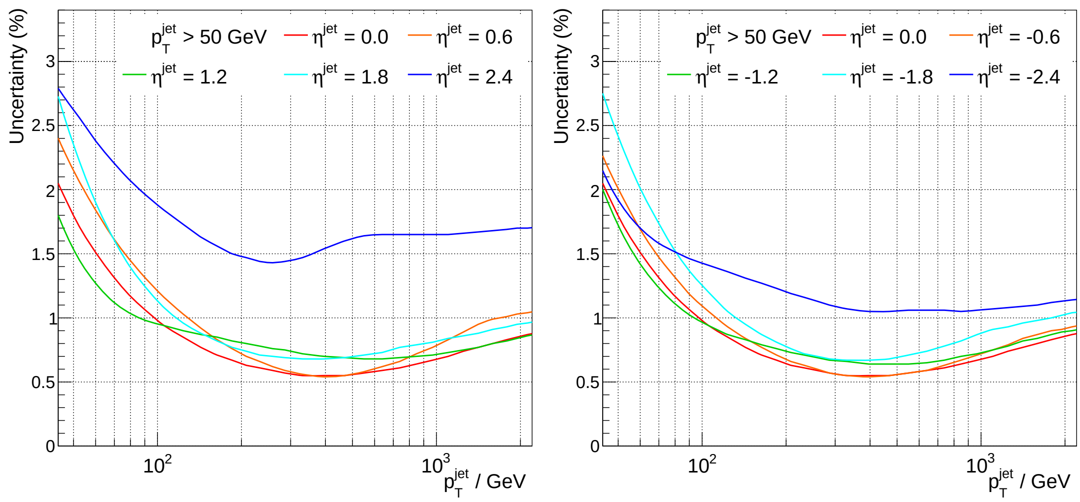

Figure 8.1: Jet energy scale uncertainty for different positive (left) and negative (right) η bins as a function of p_{T} [143, 181–183].

Jet Energy Resolution The discrepancies in the jet energy resolution between data and simulation is corrected for as described in section 5.5. The systematic effect on the jet energy resolution is calculated by shifting the core resolution scale factor c^{JER} up and down by its uncertainty, presented in table 5.3. In a similar way to the jet energy scale uncertainty, the changes due to the jet energy resolution are propagated through the event and $E_{\mathrm{T}}^{\mathrm{miss}}$ is re-calculated. The analysis is performed again for the modified jet energy resolution in order to estimate the changes in the event yields.

Renormalization and Factorization scale The systematic uncertainty related to the choice of the Q^2 scale in the generation of top pair simulations is studied by using dedicated top pair samples generated with MadGraph [153] in combination with Pythia [151], where the Q^2 scale is increased and decreased by a factor of two in the generation process [167, 198].

Matrix-Element and Partonshower Matching (ME/PS) The systematic uncertainty due to the hard parton radiation in the generation of top pair simulations is examined for two dedicated top pair samples generated with MadGraph [153] and matched to the Pythia [151] parton shower to model additional soft and co-linear radiation. The matching threshold of partons from matrix elements to parton showers is varied by a factor of 0.5 and two in the generation process to account for this uncertainty [167, 198].

Parton Density Functions The systematic effect due to the choice of the PDF in the mass reconstruction method is examined by using the *modified tolerance method* [46]. The final mass observable X is re-calculated for each event using all provided 52 eigenvector sets of the CT10 PDF [44] set. The final observable X can either be $\mathrm{M}_{T'}$, $\mathrm{M}_{W'}$ or $\mathrm{M}_{T'\overline{T'}}$ in the full range or in a certain mass window around $\mathrm{M}_{T'}$ or $\mathrm{M}_{W'}$ depending on the application. The differences with respect to the observable X_0 calculated with the nominal PDF set are combined in quadrature:

$$\Delta X^{+}_{max} = \sqrt{\sum_{i=1}^{N=52} [\max(X_i^{+} - X_0, X_i^{-} - X_0, 0)]^2} \tag{8.1}$$

$$\Delta X^{+}_{min} = \sqrt{\sum_{i=1}^{N=52} [\max(X_0 - X_i^{+}, X_0 - X_i^{-}, 0)]^2}, \tag{8.2}$$

where X_0 is the nominal value of a certain observable X. Variations in the normally symmetric eigenvectors are taken into account by considering the maximal positive and negative differences of the observables. The effect on the final mass observables is negligible.

The systematic uncertainty related to the choice of the PDF set is studied further by exchanging the nominal CT10 PDF set with the MSTW 2008 NLO PDF set[55] as well as the NNPDF 23 NLO PDF set[54]. In additional studies other CT10 PDF sets are considered using different values of α_s, 0.116 and 0.120, rather than the nominal value $\alpha_s = 0.118$. None of these studies show any significant variations on neither shape nor rate for the mass distributions.

The robustness of the mass reconstruction method under variations of the PDF set is due to the fact that the method chooses the maximum of the solvability distribution as the final mass point. The values of the re-calculated PDF weights change, but the position of the maximum of the solvability distribution is not affected significantly.

As part of the cross section uncertainty for the top pair background simulations, a systematic rate uncertainty due to the choice of the PDF of 2.6% is included [167].

Cross Section A conservative uncertainty on the normalisation of the diboson and single top cross sections of 30% and 50%, respectively, are assigned affecting the high mass phase-space in this search [199]. For the Drell-Yan production the difference between data and simulation calculated with the $R_{\mathrm{out/in}}$ method in section 5.8 is taken as an estimate for the systematic uncertainty on the cross section and amounts to 73.6% for the combined channel. The systematic uncertainty on the normalisation of the top pair cross section is composed of the systematic uncertainty due to the renormalisation/factorisation scale Q, the matrix element/parton shower matching threshold and the choice of the PDF.

In figure 8.2 the resulting shifts caused by some of the systematic uncertainties are shown for the $\mathrm{M}_{T'}$ observable and are compared to the nominal distribution. More comparisons, also for other observables, can be found in figures H.20 to H.25 in appendix H. Beyond the statistical fluctuations, no obvious trend is observed for any of the systematic uncertainties considered. Therefore no effect on the shape of the distributions is considered and the rate uncertainty is treated as an independent nuisance parameter in the final results.

The systematic uncertainties for the T′ , the Z′ and the two-dimensional search are summarised in tables 8.1 -8.3 for all data ($ee + e\mu + \mu\mu$). The systematic uncertainties for the separate channels can be found in the appendix in tables H.5-H.13. The main systematic uncertainties in the overall background yield come from the top pair and Drell-Yan processes (see the last row in the tables). These systematic uncertainties originate mainly from the normalisation uncertainty of the cross sections. The total systematic uncertainty for all background components combined is 7.6% for the T′ search, 5.4% for the Z′ search and 9% for the two-dimensional search.

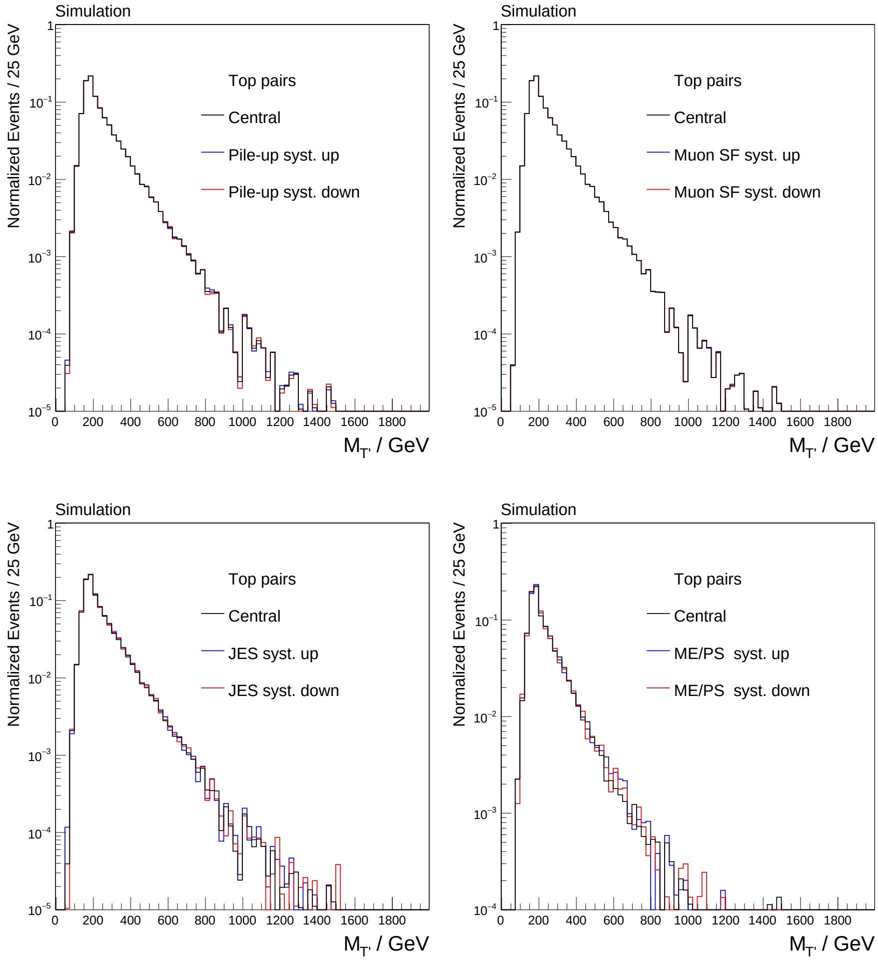

Figure 8.2: Comparison of the projection on the $M_{T'}$ axis in a $M_{W'}$ mass window of 60 - 100 GeV for the T′ application with the pile-up scale factor (top left) shifted upwards (blue) and downwards (red) with respect to the nominal shape (black) after the mass reconstruction for the top pair simulation sample for the combined channel. The same is shown also for the muon identification scale factors (top right), the JES (bottom left) and the ME/PS matching (bottom right) scales. Further plots can be found in the appendix H.

Table 8.1: Summary of all the systematic uncertainties considered for the T′ search for all data. Each row is treated as a single independent nuisance parameter.

Source	T′ Signal	Top pairs	Z + jets	Single Top	Diboson
Luminosity	2.6%	2.6%	2.6%	2.6%	2.6%
Pile-up	0.6%	0.3%	6.1%	0.1%	3.0%
Trigger	0.8%	0.4%	0.5%	0.4%	0.4%
Muon SF	1.9%	0.8%	0.8%	0.9%	0.9%
Electron SF	0.6%	0.6%	0.6%	0.6%	0.7%
Jet energy scale	0.5%	1.6%	7.9%	1.8%	2.4%
Jet energy resolution	0.8%	0.4%	6.8%	0.4%	0.5%
Q^2 scale	-	4.7%	-	-	-
ME/PS threshold	-	1.3%	-	-	-
PDF	-	2.6%	-	-	-
Cross section	-	-	73.6%	50%	30%
Total Systematic	3.6%	6.4%	74.6%	50.1%	30.4%
Total Background Systematic	-	5.7%	4.7%	2.1%	0.4%

Table 8.2: Summary of all the systematic uncertainties considered for the Z′ search for all data. Each row is treated as a single independent nuisance parameter.

Source	Z′ Signal	Top pairs	Z + jets	Single Top	Diboson
Luminosity	2.6%	2.6%	2.6%	2.6%	2.6%
Pile-up	4.2%	0.3%	10.2%	0.1%	4.6%
Trigger	0.7%	0.4%	0.6%	0.3%	0.4%
Muon SF	1.3%	0.8%	0.5%	0.8%	0.7%
Electron SF	0.7%	0.6%	0.7%	0.6%	0.7%
Jet energy scale	2.1%	1.7%	4.6%	2.3%	3.7%
Jet energy resolution	1.2%	0.5%	9.8%	0.2%	0.9%
Q^2 scale	-	1.1%	-	-	-
ME/PS threshold	-	1.2%	-	-	-
PDF	-	2.6%	-	-	-
Cross section	-	-	73.6%	50%	30%
Total Systematic	5.8%	4.6%	75.1%	50.1%	30.7%
Total Background Systematic	-	4.2%	3.1%	1.5%	0.2%

Table 8.3: Summary of all the systematic uncertainties considered for the two-dimensional search for all data. Each row is treated as a single independent nuisance parameter.

Source	2D Signal	Top pairs	Z + jets	Single Top	Diboson
Luminosity	2.6%	2.6%	2.6%	2.6%	2.6%
Pile-up	0.4%	0.4%	4.8%	0.6%	2.8%
Trigger	0.9%	0.4%	0.4%	0.4%	0.4%
Muon SF	2.3%	0.8%	1.0%	0.9%	0.9%
Electron SF	0.6%	0.6%	0.6%	0.6%	0.7%
Jet energy scale	0.6%	1.5%	2.6%	1.6%	2.4%
Jet energy resolution	0.4%	0.3%	4.3%	0.4%	0.2%
Q^2 scale	-	5.3%	-	-	-
ME/PS threshold	-	1.9%	-	-	-
PDF	-	2.6%	-	-	-
Cross section	-	-	73.6%	50%	30%
Total Systematic	3.8%	6.9%	74.0%	50.1%	30.4%
Total Background Systematic	-	5.9%	6.4%	2.3%	0.4%

CHAPTER 9

Search Results for different Applications

Since the observed distributions are compatible with the expected SM background for all observables under study, upper exclusion limits on the cross section times branching ratio $\sigma \cdot BR$ are calculated for all applications considered.

The selection efficiency times detector acceptance ϵ·A is provided for all applications in appendix J in tables J.26 to J.31 to allow further processing and analysis of the presented results in the context of other models and theoretical predictions.

9.1 Calculation of Upper Limits

The search results are analysed using a modified frequentist procedure, the CL_s method [200–202]. The observables used in the corresponding likelihood functions in the CL_s procedure are different depending on the search considered: $\mathrm{M}_{T'}$ distributions for T′ -like signals, $\mathrm{M}_{T'\overline{T'}}$ invariant mass distributions for Z′ like signals and one-dimensional distributions generated from the two-dimensional $\mathrm{M}_{T'}$ vs $\mathrm{M}_{W'}$ plane for simultaneous T′ and W′ -searches. The necessary transformation from the two-dimensional mass space into an one-dimensional distribution in order to calculate upper exclusion limits for simplified Littlest Higgs models is explained in section 9.4 of this chapter.

The general procedure to obtain an *observed* upper exclusion limit starts by constructing a likelihood function depending on the number of expected signal (s) and background (b) events:

$$\begin{aligned}\mathcal{L}(\text{data}|\mu,\theta) &= \text{Poisson}(\text{data}|\mu\cdot s(\theta)+b(\theta))\cdot p(\tilde{\theta}|\theta) && (9.1)\\ &= \prod_i \frac{(\mu s_i+b_i)^{n_i}}{n_i!}e^{-(\mu s_i+b_i)}\cdot p(\tilde{\theta}|\theta) && (9.2)\end{aligned}$$

The observed number of events per mass bin i is $\mathrm{n_i}$, while the expected signal and background events per bin i are $\mathrm{s_i}$ and $\mathrm{b_i}$, respectively, and μ is the signal strength. A full set of nuisance parameters is introduced in the vector θ. The systematic uncertainties are described using a conditional probability distribution function $p(\tilde{\theta}|\theta)$, with $\tilde{\theta}$ being the measured value under the condition of the unknown real systematic uncertainty θ. All systematic uncertainties are parametrised using log-normal distributions.

A test statistic $\tilde{q}_\mu$ based on the profile likelihood ratio is constructed to test the compatibility of data with the background only (null hypothesis H_0) and signal+background (alternate hypothesis H_1):

$$\tilde{q}_\mu = -2\ln\frac{\mathcal{L}(\text{data}|\mu,\hat{\theta}_\mu)}{\mathcal{L}(\text{data}|\hat{\mu},\hat{\theta})},\quad 0\le\hat{\mu}\le\mu \tag{9.3}$$

The value $\hat{\theta}_\mu$ maximises the likelihood in the numerator for a given μ, while $\hat{\theta}$ and $\hat{\mu}$ define the point at which the likelihood reaches its global maximum. The condition $\hat{\mu}\ge 0$ assures no unphysical signal rates, while the condition $\hat{\mu}\le\mu$ takes care, that upward fluctuations in data are not considered as evidence for a signal. For every tested signal strength μ an observed value of the test statistic $\tilde{q}_\mu^{obs}$ is obtained. The likelihood function is maximised by minimising the influence of the systematic uncertainties $\hat{\theta}_0^{obs}$ and $\hat{\theta}_\mu^{obs}$ for the hypotheses H_0 and H_1, respectively.

The probability density functions $f(\tilde{q}_\mu|0,\hat{\theta}_0^{obs})$ and $f(\tilde{q}_\mu|\mu,\hat{\theta}_\mu^{obs})$ for the hypotheses H_0 and H_1 are calculated analytically using the asymptotic method [203]. The corresponding nuisance parameters $\hat{\theta}_\mu^{obs}$ and $\hat{\theta}_0^{obs}$ are fixed to the values determined from data.

The p-values of the test statistic given the actual observation $\tilde{q}_\mu^{obs}$ are calculated for the two hypotheses, as well as their ratio, which defines the CL_s:

$$
\begin{aligned}
p_\mu &= P(\tilde{q}_\mu \geq \tilde{q}_\mu^{obs}|\text{signal} + \text{background}) = \int_{\tilde{q}_\mu^{obs}}^{\infty} f(\tilde{q}_\mu|\mu, \hat{\theta}_\mu^{obs})d\tilde{q}_\mu && (9.4)\\
1 - p_b &= P(\tilde{q}_\mu \geq \tilde{q}_\mu^{obs}|\text{background-only}) = \int_{\tilde{q}_0^{obs}}^{\infty} f(\tilde{q}_\mu|0, \hat{\theta}_0^{obs})d\tilde{q}_\mu && (9.5)\\
\Rightarrow \quad CL_s &= \frac{CL_{s+b}}{CL_b} = \frac{p_\mu}{1 - p_b} && (9.6)
\end{aligned}
$$

The level of incompatibility of data with the signal hypothesis is defined as the confidence level CL. The resulting slightly conservative limit using this procedure will give a one-sided confidence level on the signal hypothesis. For an observed 95% CL upper limit on the signal strength, μ is increased until CL_s reaches 0.05 ($CL \geq$ 1-CL_s).

The expected exclusion limits are calculated using the same procedure taking the median and the $\pm 1\sigma$ and $\pm 2\sigma$ of the background only hypotheses H_0 for the test statistic, which is the probability for the background to fluctuate and give an excess of events larger than the experimental observation.

9.2 T′ Results

The expected and observed 95% CL upper exclusion limits are calculated using the $M_{T'}$ distributions in figure 7.9 separately for ee, $\mu\mu$, $e\mu$ and for the combined dilepton channel. A branching fraction of 100% for the T′ quark to decay into bW is assumed. In the search for new heavy resonances this analysis is dominated by a lack of statistics in the interesting high mass region. Therefore a combination of the separate channels in the expected limit calculation has not been found to give major improvements compared to a calculation directly from the combined data set. This is also valid for the other applications.

The results for the search of a heavy vector-like T′ quark for the combined dilepton channel can be found in figure 9.1 and in the appendix in table I.14. The results in the three different dilepton channels are shown in figure 9.2 and tables I.15- I.17 in the appendix. The observed exclusion limits are shown in black and the expected exclusion limits are shown in blue (dashed line) along with $\pm 1\sigma$ (yellow) and $\pm 2\sigma$ (green) bands. A prediction for the T′ quark production cross sections as estimated by approximate NNLO calculations using Hathor (HAdronic Top and Heavy quarks crOss section calculatoR) [204, 205], which are confirmed by an exact NNLO calculation by Czakon et al [167], are shown in red (dashed line). The intersection of the observed or expected upper cross section limit and the theoretical production cross section sets the lower limit on the mass of the T′ quark. In this analysis, the expected lower limit for a new heavy top-partner T′ is estimated to be (614^{+55}_{-57}) GeV and the observed lower limit is 658 GeV .

A dedicated inclusive search for a new heavy top quark partner T′ with at least one isolated lepton has been published by the CMS Collaboration using the same 2012 data set and an integrated luminosity of 19.5 fb^{-1} [204]. The event selection and analysis strategy differ from the analysis presented in this more model-independent work. Their analysis is categorised into single-lepton and multi-lepton events requiring multiple high energetic jets, giving rise to additional final states. The analysis uses identification algorithms for b-jets, top quarks and W bosons in order to identify boosted objects. The single-lepton channel uses a multivariate analysis (MVA) to discriminate signal and background hypothesis. In the multi-lepton channel a requirement on the smallest invariant mass of lepton and b-jet combinations, $M_{lb} > 170$ GeV , drastically reduces the background originating from top pair production. They set an expected lower limit of 785 GeV and an observed lower Limit of 700 GeV on the T′ mass for a $BR(\mathrm{T}' \rightarrow bW)$ of 100%.

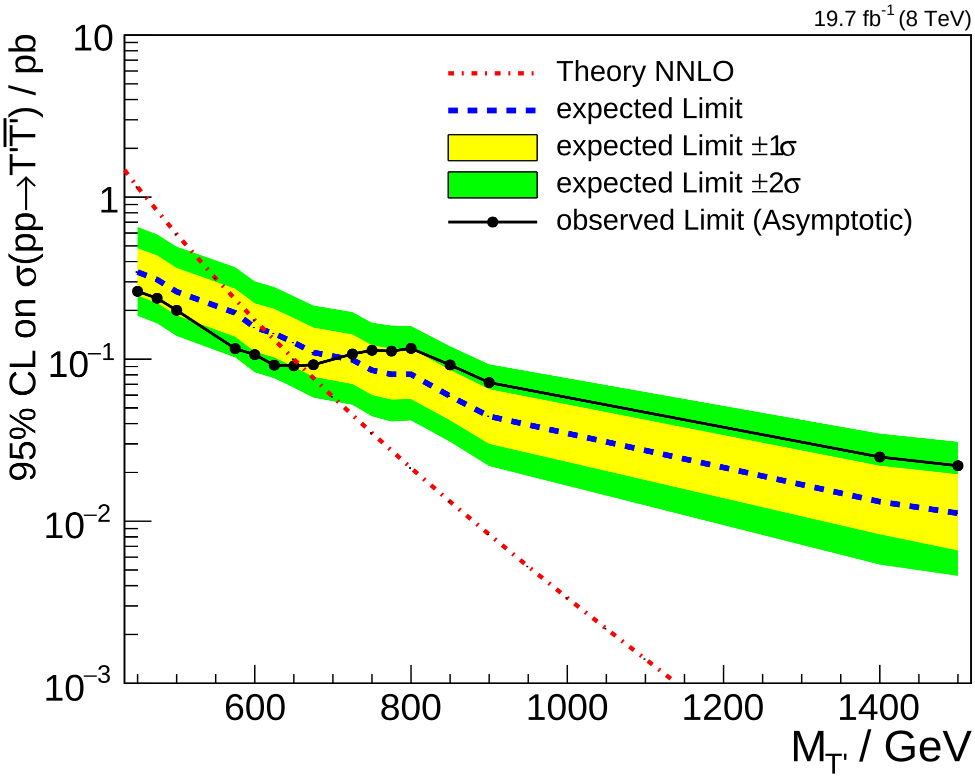

Figure 9.1: The expected (blue dashed line) and observed (black solid line) 95% CL upper exclusion limits on $\sigma \cdot BR$ for a new heavy top quark partner T′ for all channels combined compared to approximate NNLO calculations (red dashed line) [204, 205].

Similar results are obtained with this model-independent search method. In this analysis the expected lower limit on the T′ quark mass is around 20% and the observed limit is 6% lower in comparison to the dedicated MVA analysis results, which cover more final states and thus have higher statistics.

As an evaluation of the performance of the analysis a simulated signal with a T′ mass of 750 GeV is injected into the total simulated background. The cross section of the injected signal is scaled to the approximate expected limit on the cross section at this mass point: $\sigma = 0.1$ pb. A toy simulation is performed using this distribution and the expected and observed upper limit is re-calculated, as presented in figure 9.3. The observed upper limit on $\sigma \cdot BR$ for a new heavy top quark partner T′ exceeds the expectations significantly in this study, showing the sensitivity of the analysis to small signal injections.

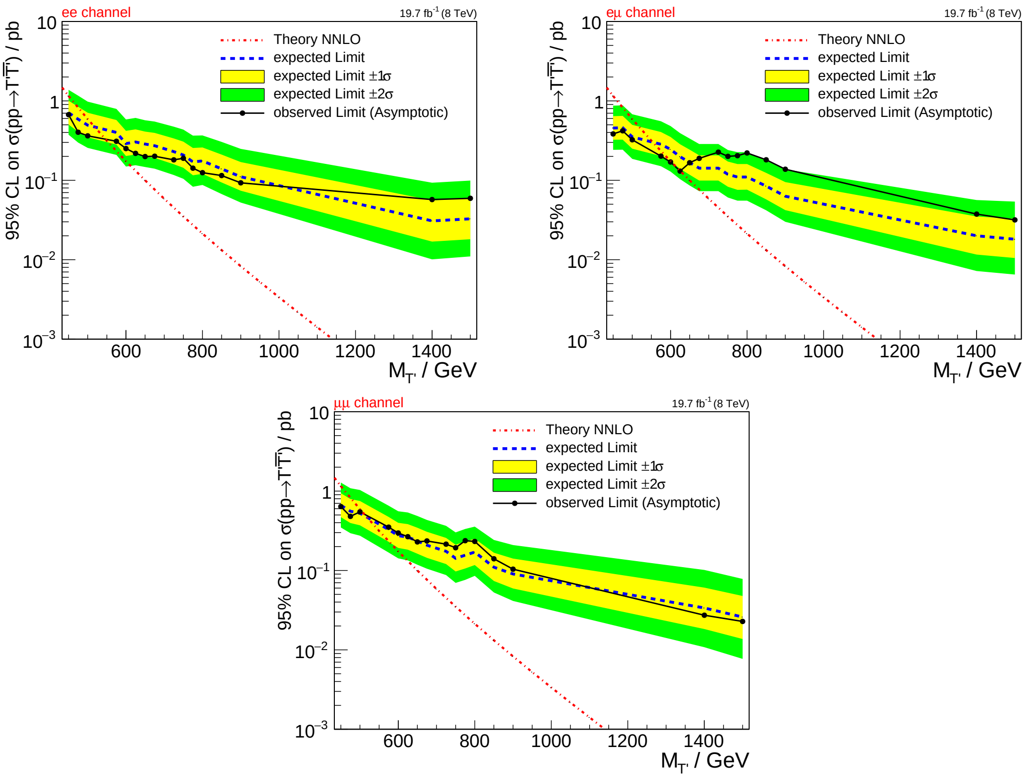

Figure 9.2: The expected (blue dashed line) and observed (black solid line) 95% CL upper exclusion limits on $\sigma \cdot BR$ for a new heavy top quark partner T′ for the $\mu\mu$ (top left), the $e\mu$ (top right) and the ee (bottom) channel separately compared to approximate NNLO calculations (red dashed line) [204, 205].

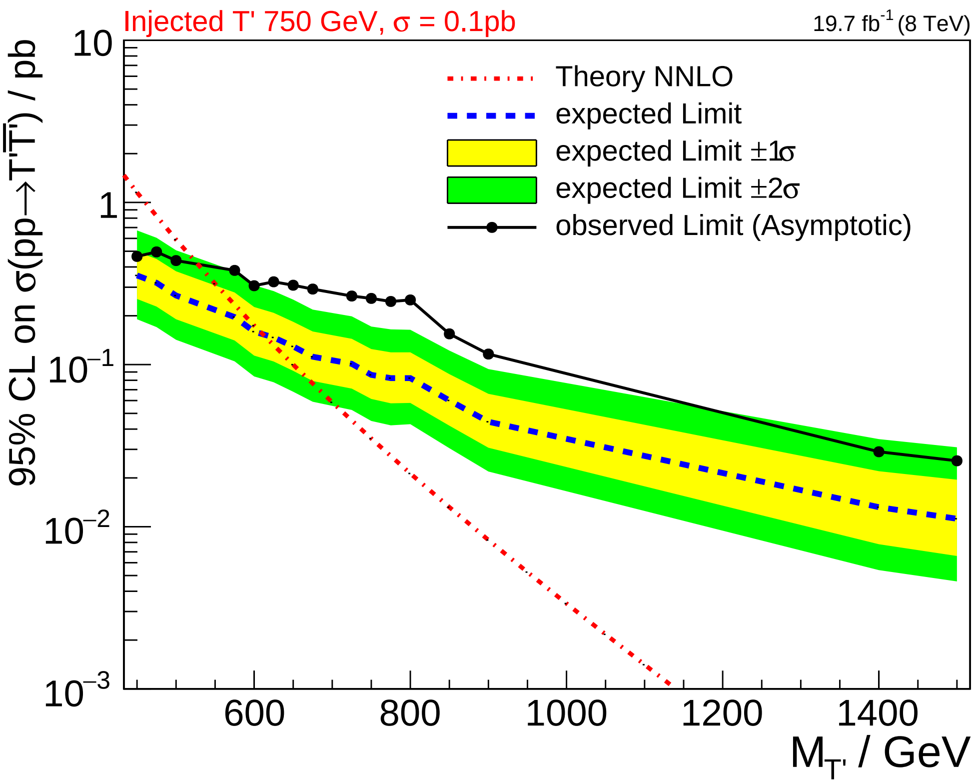

Figure 9.3: The expected (blue dashed line) and observed (black solid line) 95% CL upper exclusion limits on $\sigma \cdot BR$ for a new heavy top quark partner T′ with an injected signal of $M_{T'} = 750\,\text{GeV}$ and a cross section σ of 0.1 pb in toy simulation studies compared to approximate NNLO calculations (red dashed line) [204, 205].

9.3 Z' Results

The 95% CL upper limits on $\sigma \cdot BR$ for a narrow width Z′ decaying to SM top pairs as a function of the resonance mass $M_{Z'}$ are calculated using the $M_{T'\overline{T'}}$ distributions in figure 7.11. They are shown in figure 9.4 for the combined dilepton channel and in table I.18 in the appendix. The results for the three different dilepton channels separately can be found in figure 9.5 and in the appendix in tables I.19- I.21. LO theoretical predictions for a leptophobic narrow width Z' [22] multiplied by a K factor of 1.3 [23] to approximate NNLO effects are compared to the observed and expected upper cross section limits to set lower limits on the Z' mass. The lower 95% CL observed and expected mass limits for a new heavy gauge boson Z' are 1369 GeV and (1377^{+146}_{-157}) GeV , respectively. Cross sections for a Z' resonance with a mass of 1.5 TeV decaying into top pairs are excluded at 95% CL above 0.27 pb. The expected cross section limit for a $M_{Z'}$ of 1.5 TeV is 0.28 pb.

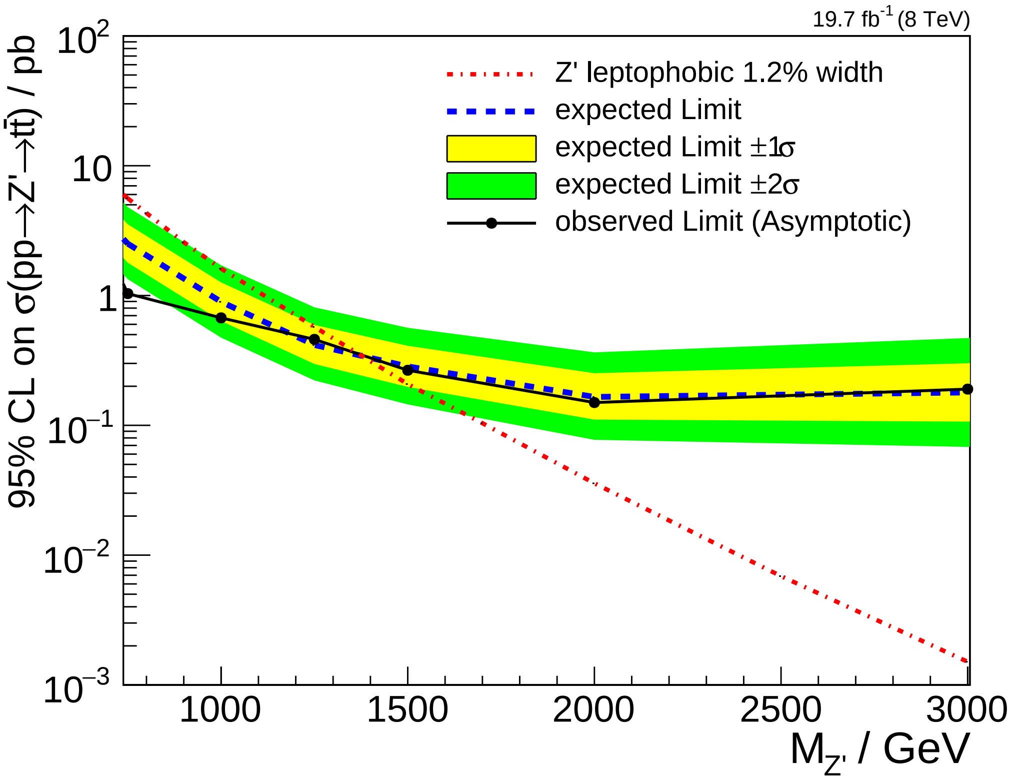

Figure 9.4: The expected (blue dashed line) and observed (black solid line) 95% CL upper exclusion limits on $\sigma \cdot BR$ for a new heavy gauge boson Z' for all channels combined compared to theoretical predictions (red dashed line) for a leptophobic Z' [22, 23].

A dedicated search for a new heavy resonance decaying into top pairs in the dilepton plus jets final states has been published by the CMS Collaboration using an integrated luminos-

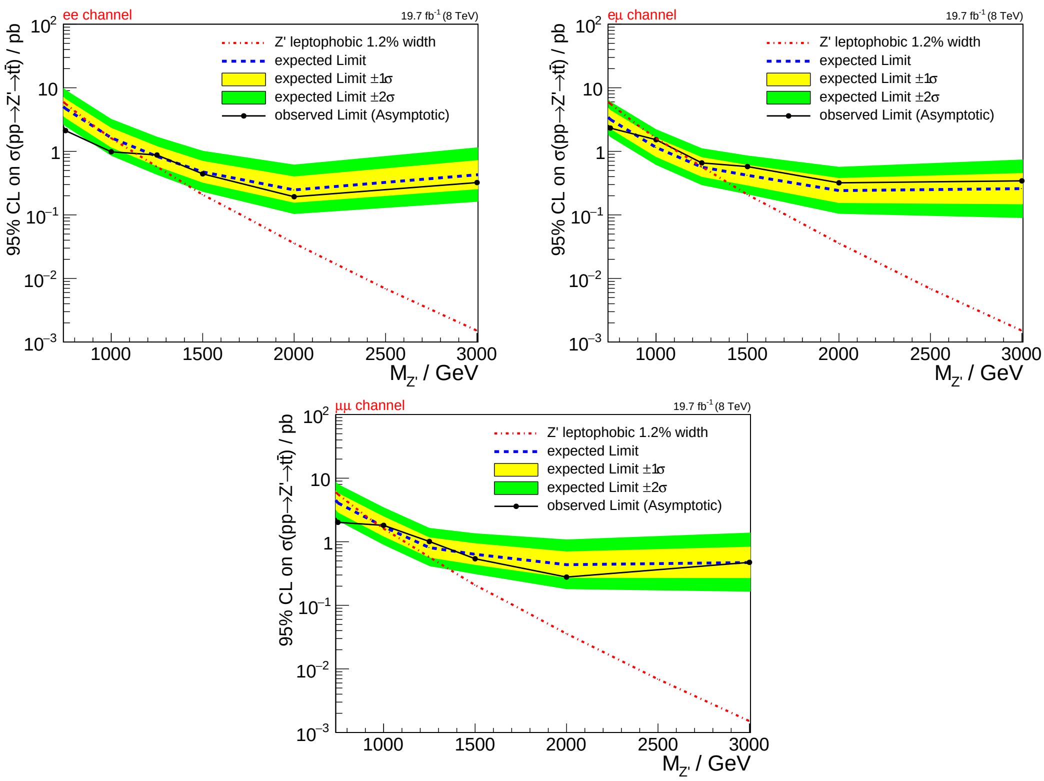

Figure 9.5: The expected (blue dashed line) and observed (black solid line) 95% CL upper exclusion limits on $\sigma \cdot BR$ for a new heavy gauge boson Z′ for the $\mu\mu$ (top left), the $e\mu$ (top right) and the ee (bottom) channel separately compared to theoretical predictions (red dashed line) for a leptophobic Z′ [22, 23].

ity of 19.7 fb^{-1} of 2012 data [199]. Their analysis and the model independent one presented here are more comparable than the T′ searches in the previous section, since they address the same final state. The analysis in [199] is optimised using the boosted nature of the top quarks originating from heavy resonances. To account for the possible overlap of the decay products no lepton isolation is required on the trigger or selection level. Additional requirements on the cone size ΔR(l, jet) and the relative transverse momentum $p_{T,rel}$(l,jet) between leptons and jets further reduce the background. Their data is divided into two categories, depending on whether at least one or two jets satisfy b-jet tagging requirements. Only the ee and $\mu\mu$ channel need to have $E_{\mathrm{T}}^{\mathrm{miss}}$ in the final state. The mass observable used in the limit calculations is built of the four momenta of the two leading leptons and jets together with the neutrinos calculated from $E_{\mathrm{T}}^{\mathrm{miss}}$ assuming their p_z component to be zero. The lower 95% CL limits on the M$_{Z'}$ mass are 1.5 TeV for the observed and 1.4 TeV for the expected case. They stress, that they exclude cross sections above 0.24 pb at 95% CL for a M$_{Z'}$ of 1.5 TeV with an expected cross section limit of 0.33 pb.

In this analysis the expected lower limit on the Z′ mass is 2% and the observed limit 9% lower in comparison to the optimised search results. The upper limits on the cross sections for a $M_{Z'}$ of 1.5 TeV are 12% below in the observed and in fact over 15% better in the expected case in comparison to the dedicated Z′ analysis results.

Very competitive results are obtained with this model-independent search method, which employs the same event selection for the T′ and the Z′ (and also for the two-dimensional) searches. The one-dimensional search results for T′ and Z′ resonances are important benchmark studies to establish the robustness of the search method.

Following the T′ application, a signal injection study with toy simulations is also performed for a $M_{Z'}$ of 1500 GeV with a cross-section scaled to the expected limit and can be found in figure I.26 in the appendix.

9.4 Two-dimensional Results: T′ and W′

The two-dimensional limits are calculated similarly to the one-dimensional limits in the T′ and Z′ search by mapping the two-dimensional distributions of the $M_{T'}$ vs $M_{W'}$ mass space into one-dimensional histograms. The problem of low occupancy and empty bins for the simulated background distributions in the two-dimensional mass space is eliminated by a merging algorithm. Empty bins are merged with the adjacent bin of the lowest occupancy to form new combined bins. The algorithm is applied iteratively until at least one event is expected in each bin, according to the simulations. The merging scheme is derived by using the distribution of the total simulated background events, normalised to the data integrated luminosity, with all the scale factors and reweightings applied. The merging scheme is used to transform all two-dimensional distributions employed in the limit calculation. The result for all channels is shown in figure 9.6. For the $ee, \mu\mu$ and $e\mu$ channels separately it is presented in figure I.27. Bins with the same colour have been merged. The numbers represent the total number of expected events in each merged bin.

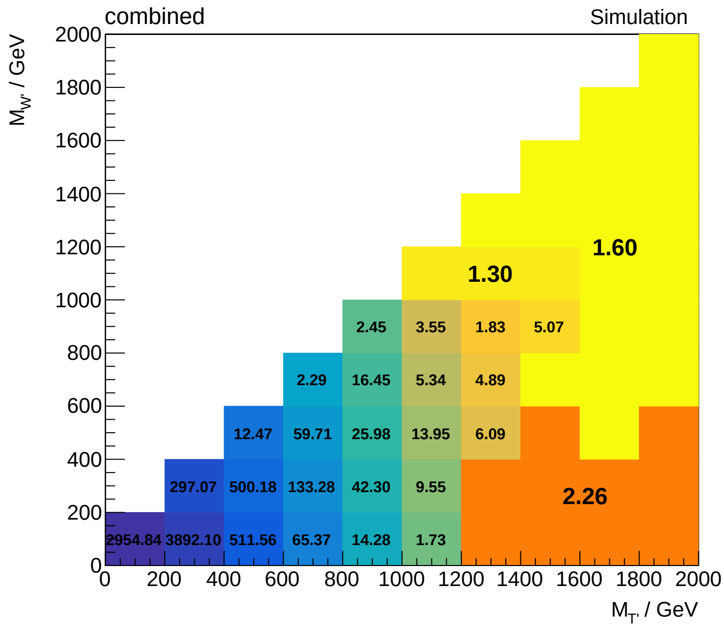

Figure 9.6: Merging scheme with at least one entry per bin for all channels combined. Bins with the same colour have been merged. The numbers represent the total number of expected events in each merged bin.

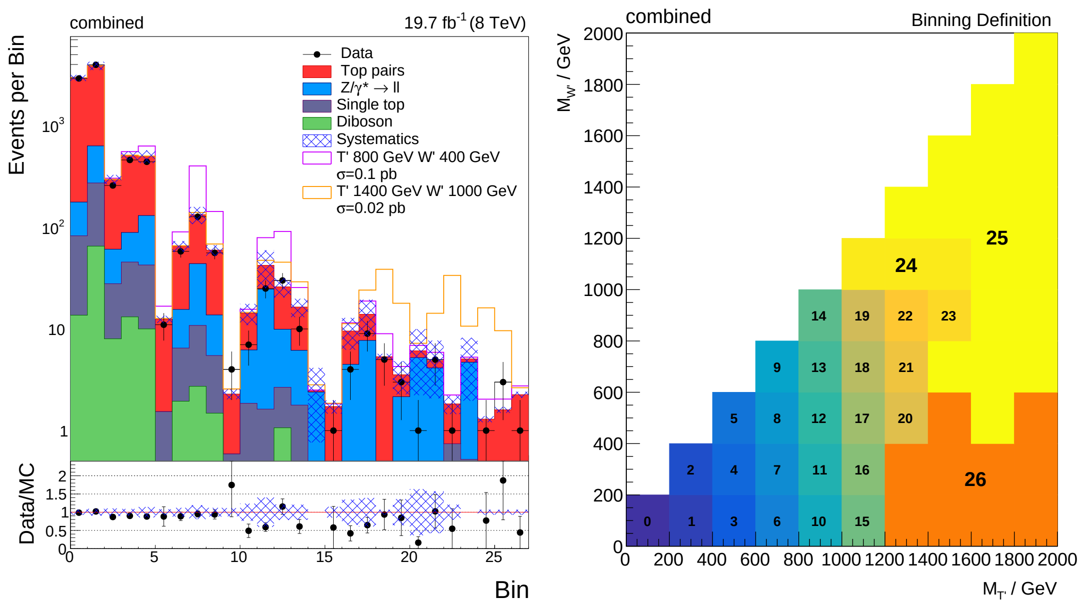

Figure 9.7: One-dimensional representation (left) of the two-dimensional mass space distribution as used for the limit calculation as a function of the bin number for the combined channel. The systematic uncertainties considered are shown by the blue hatched bands. Two different injected signal samples are shown on top of the simulated background. The transformation of the bin number in the two-dimensional plane to the one-dimensional representation is indicated in the right distribution, where the labels denote the number of the merged bin.

The expected and observed 95% CL upper exclusion limits are calculated using the resulting one-dimensional representations of the two-dimensional mass space distributions, as presented in figure 9.7 for the combined data and figure 9.8 for $ee, \mu\mu$ and $e\mu$ separately. The systematic uncertainties calculated in chapter 8 are indicated by the blue hatched bands. The violet and orange lines represent the contributions of two injected Littlest Higgs signal samples with different production cross sections on top of the simulated background. The bin number on the x axis is obtained from the two-dimensional distribution on the right, which is the same as in figure 9.6 with the mark " number of events" replaced by the mark "bin number". The limits are calculated for all 45 generated signal samples, starting with the lowest at $\mathrm{T}' = 400\,\mathrm{GeV}$ and $\mathrm{W}' = 200\,\mathrm{GeV}$. Limits for points between the generated mass values are obtained by interpolation. A branching fraction of 100% for the T' quark to decay into $b\,\mathrm{W}'$ is assumed.

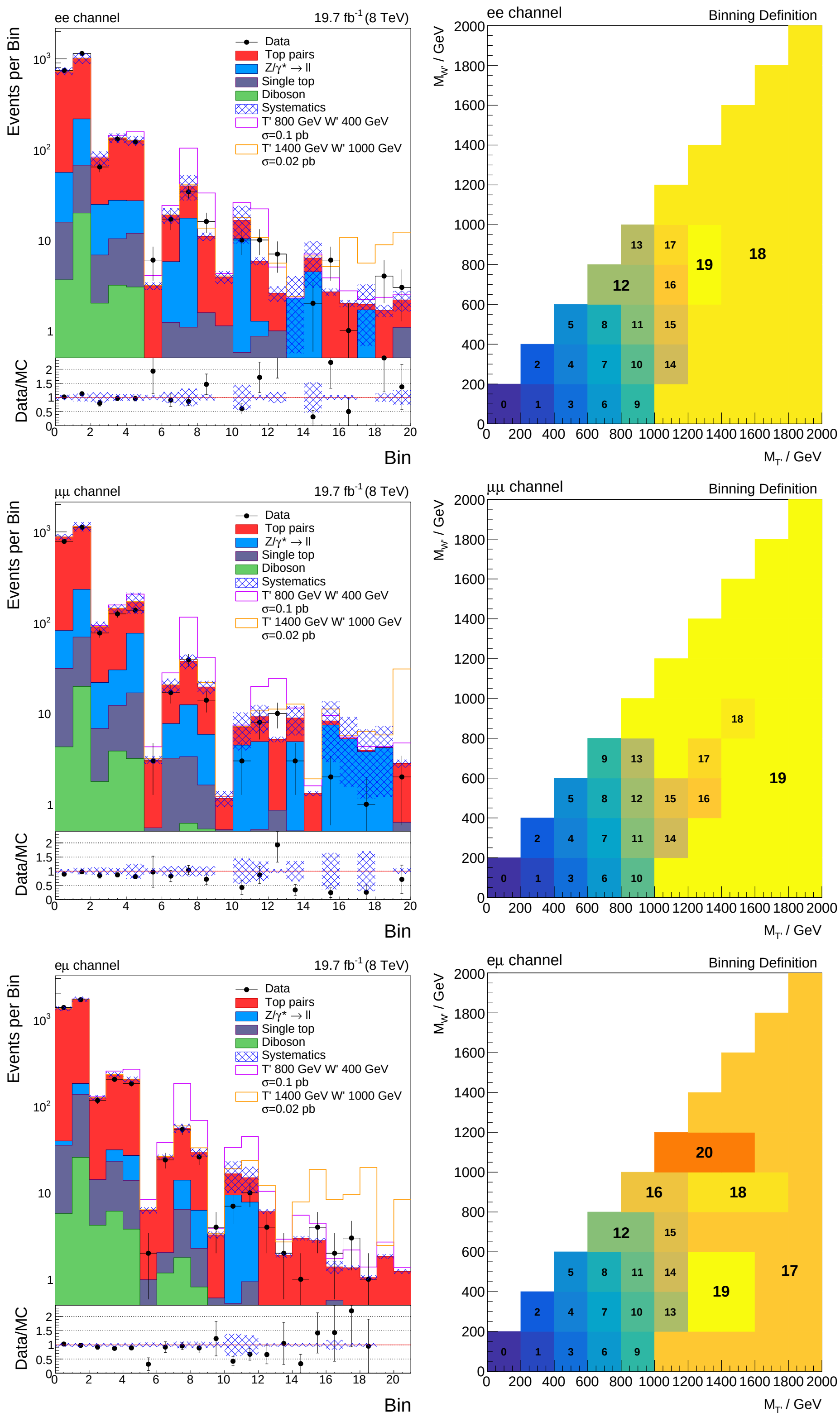

Figure 9.8: One-dimensional representation (left) of the two-dimensional mass space distribution as used for the limit calculation as a function of the bin number for the *ee* (1rst row), the $\mu\mu$ (2nd row) and the $e\mu$ (3rd row) channel. The systematic uncertainties considered are shown by the blue hatched bands. Two different injected signal samples are shown on top of the simulated background. The transformation of the bin number in the two-dimensional plane to the one-dimensional representation is indicated in the right distribution, where the labels denote the number of the merged bin.

The results for the expected and observed 95% CL upper exclusion limits in the combined dilepton data are shown in figure 9.9 (for the three different dilepton channels in figure 9.10) limited to the region $M_{T'} < 1200\,\text{GeV}$. The results for the full $M_{T'}$ range up to 2 TeV can be found in figure I.28 in the appendix as well as in tables I.22- I.24. The strength of the observed 95% CL upper limit on the cross section $\sigma \cdot BR$ per $M_{T'}$ and $M_{W'}$ is presented with the color coding. Cross sections above 0.7 fb to 32.2 fb depending on $M_{T'}$ and $M_{W'}$ are excluded at 95% CL. The corresponding expected cross section limits range from 0.9 fb to 44.6 fb.

A prediction for the production cross section $pp \to \mathrm{T}'\overline{\mathrm{T}'}$, with $\mathrm{T}' \to \mathrm{W}'\, b$, in a Littlest Higgs model is estimated by LO calculations using Whizard [157, 158]. The intersection plane of the observed or expected upper cross section limit and the theoretical production cross section sets the lower limit on the mass of the T′ quark and the W′ boson. The expected 95% CL lower limit on the mass $M_{T'}$ for a new heavy top-partner T′ is ranging from (870^{+60}_{-80}) GeV to (930^{+20}_{-60}) GeV depending on $M_{W'}$. The observed 95% CL lower mass limit on $M_{T'}$ is ranging between 870 GeV and 950 GeV depending on $M_{W'}$.

The highest local significance in the combined data is calculated with 0.86 at $M_{T'} = 1000\,\text{GeV}$ and $M_{W'} = 600\,\text{GeV}$ with a corresponding local p-value of 0.19. No significant discrepancies are observed when the ee, $\mu\mu$ and $e\mu$ channels are considered separately.

Following the T′ application, a signal injection study with toy simulations is also performed for a $M_{T'}$ of 800 GeV and a $M_{W'}$ of 400 GeV with a cross-section scaled to the expected limit and can be found in figure I.29 in the appendix.

This is the first search performed at LHC for both a new heavy top quark partner T′ and a new heavy charged gauge boson W′ as predicted by simplified Littlest Higgs models.

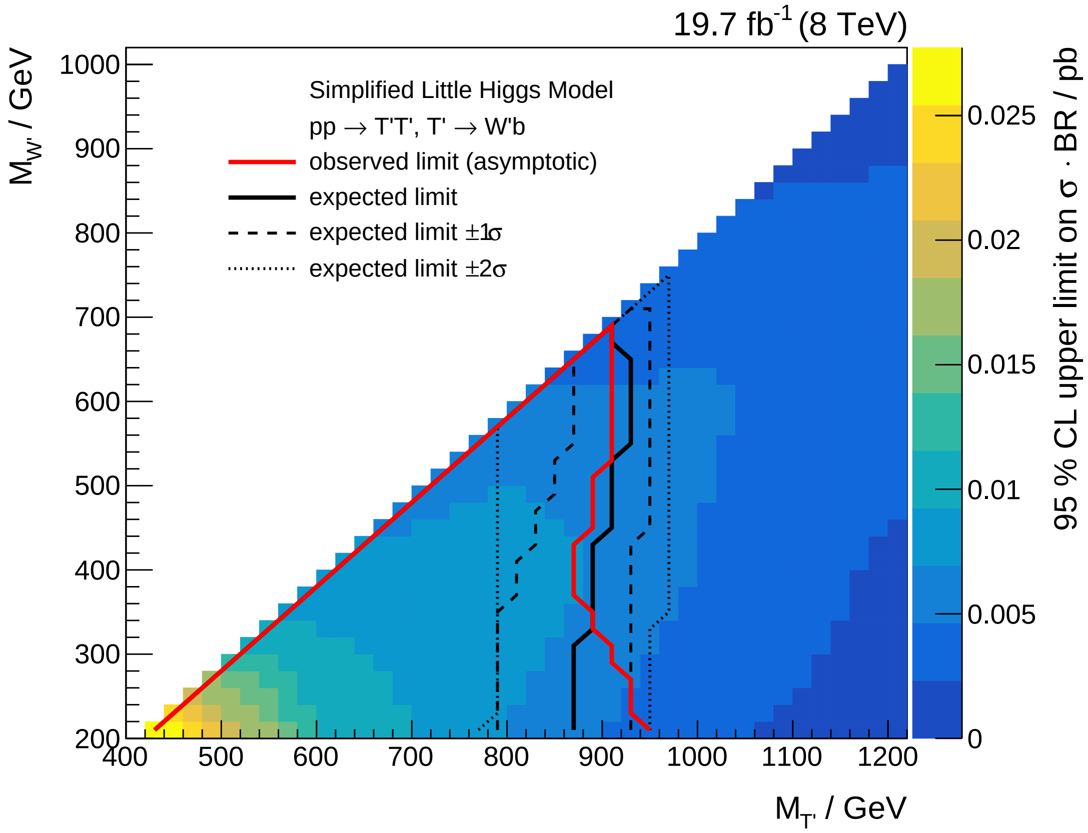

Figure 9.9: The expected and observed 95% CL upper exclusion limits on $\sigma \cdot BR$ for a new heavy top quark partner T′ and a new heavy gauge boson W′ for all channels combined compared to LO calculations [157, 158]. The strength of the observed 95% CL upper limit on the cross section $\sigma \cdot BR$ per $M_{T'}$ and $M_{W'}$ is given by the color coding.

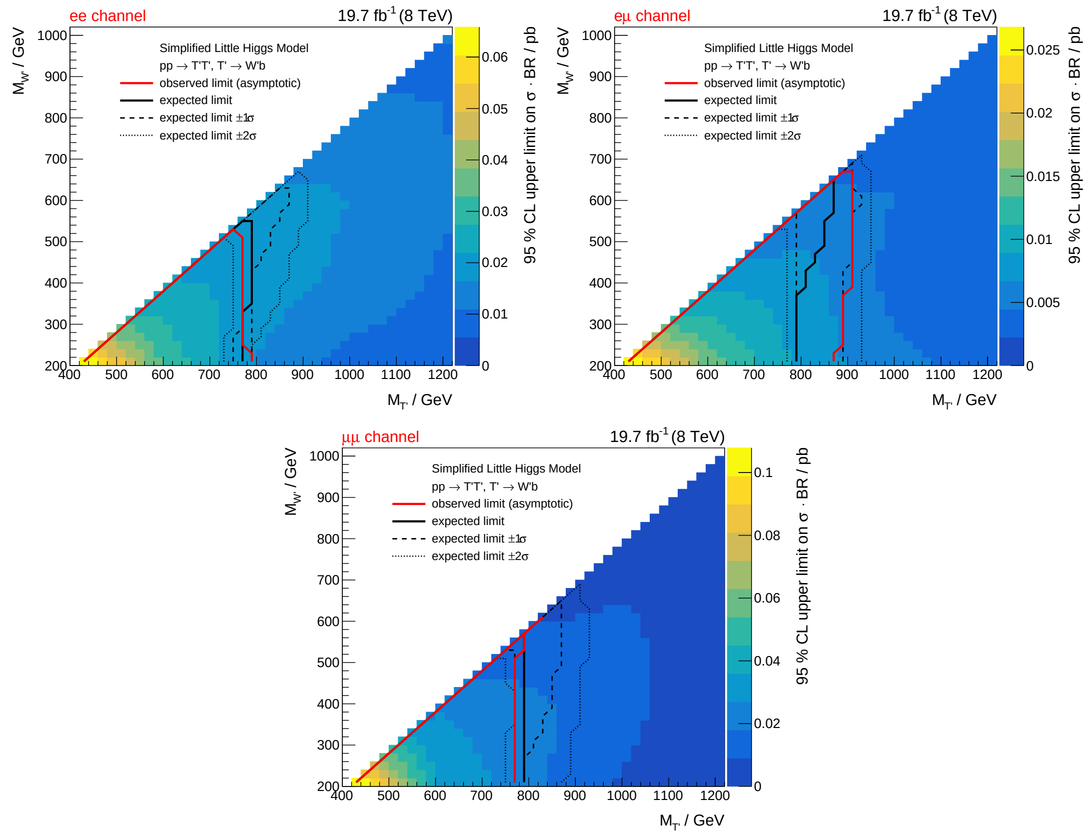

Figure 9.10: The expected and observed 95% CL upper exclusion limits on $\sigma \cdot BR$ for a new heavy top quark partner T$'$ and a new heavy gauge boson W$'$ for the $\mu\mu$ (top,left), the $e\mu$ (top,right) and the ee (bottom) channel separately compared to LO calculations [157, 158]. The strength of the observed 95% CL upper limit on the cross section $\sigma \cdot BR$ per M$_{T'}$ and M$_{W'}$ is given by the color coding.

9.4.1 T$'$ and Standard Model W

After presenting the two-dimensional limit calculation of the Littlest Higgs signal samples an additional study in two-dimensions is performed by re-calculating the limits for the signal samples for vector-like $T'\overline{T'}$ production decaying to SM W bosons and b quarks as presented in the one-dimensional projection in section 9.2. There are no constraints on the W boson mass. The bins in the two-dimensional plane are finer in $M_{W'}$ up to 200 GeV ($\Delta M_{W'} = 5$ GeV) and coarse afterwards ($\Delta M_{W'} \geq 50$ GeV). The same bin-merging algorithm as in the search for new particles predicted by Little Higgs models has been applied. The obtained expected upper exclusion limits on the $\sigma \cdot BR$ are presented in figure 9.11 in the black dashed lines with their $2\,\sigma$ uncertainty bands (black solid lines).

The upper plot shows the result from the one-dimensional search in which no constraints on the W boson mass are applied using only the reconstructed $M_{T'}$ for the limit calculation (blue dashed line). The two-dimensional expected upper limit on the $\sigma \cdot BR$ is better by a factor of up to 1.5, resulting in an improvement of the expected lower exclusion limit on $M_{T'}$ of 11%. The additional separation power in the two-dimensional mass plane is an advantage to distinguish signal and background distributions, leading to stricter exclusion limits.

The result for the one-dimensional projection on the $M_{T'}$ axis in a $M_{W'}$ window of 60 GeV to 100 GeV as used for the analysis in section 9.2 is also presented in the lower plot (blue dashed line). The sensitivity in the one-dimensional application is enhanced by taking advantage of the known mass of the SM W boson. Although no constraints on the $M_{W'}$ mass are used in the two-dimensional reconstruction, the result is comparable to the one-dimensional projection for $M_{T'}$ masses up to 800 GeV . Afterwards the limit calculation is statistically dominated and there is no benefit in taking the two-dimensional plane for the limit calculation in this data-taking period.

The expected 95% CL lower exclusion limits on the mass $M_{T'}$ for a new heavy top quark partner T$'$ as predicted by an approximate NNLO calculation [204, 205] are consistent for the one-dimensional and the two-dimensional limit calculation.

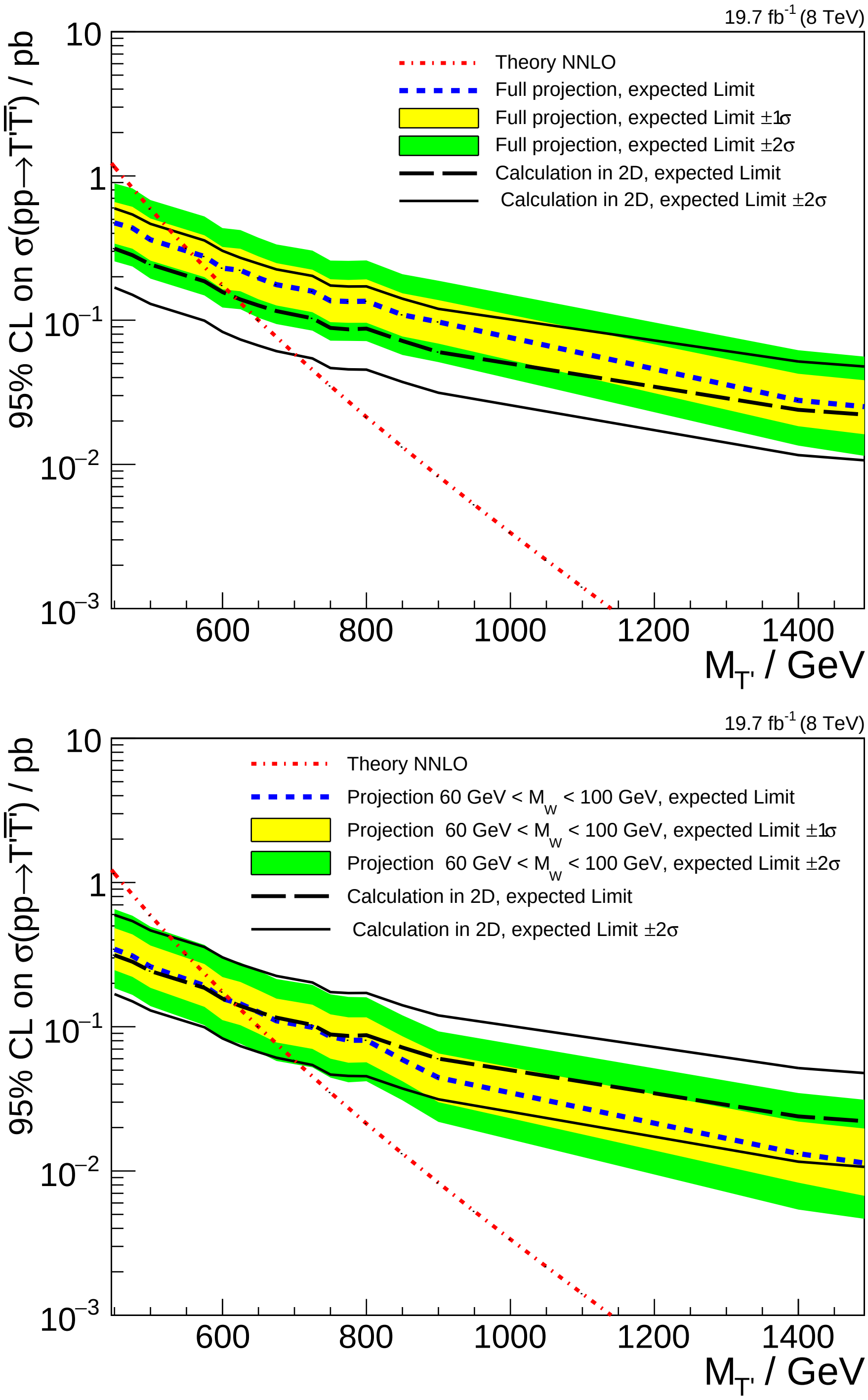

Figure 9.11: The expected 95% CL upper exclusion limits on $\sigma \cdot BR$ for a new heavy top quark partner T$'$ using the one-dimensional projection on the M$_{T'}$ axis (blue dashed line) and using the two-dimensional phase space (black dashed line) for the limit calculation. The one-dimensional projection on the M$_{T'}$ axis is compared to the full projection (top) and the projection in the M$_{W'}$ mass windows as used in section 9.2 (bottom). The red dashed line corresponds to the cross section predicted by an approximate NNLO calculations [204, 205].

CHAPTER 10

Summary

A model independent search in two-dimensional mass space in events with missing transverse energy is presented using $19.7\,\mathrm{fb}^{-1}$ of collision data recorded by the CMS detector in pp collisions at $\sqrt{s} = 8\,\mathrm{TeV}$ at the LHC.

The method searches for new heavy particles with missing transverse energy in the final state. Unknown pair produced heavy particles T' decay further into unknown heavy particles W' and SM q quarks: $pp \to \mathrm{T}'\overline{\mathrm{T}'} \to \mathrm{W}'\ q\ \overline{\mathrm{W}'}\ q$. The masses of the two unknown particles T' and W' are reconstructed simultaneously. Although the mass reconstruction method could examine other final states with missing transverse energy, in this thesis the W' is assumed to decay leptonically: $\mathrm{W}' \to l\nu$, where the charged leptons are either electrons or muons. The SM particles q form highly energetic jets, which are measured. There are no constraints on the masses of T' and W' and no further assumptions apart from the topology of the decay chain. The final state is defined by the decay chain consisting of four physics objects (two charged leptons and two jets) and missing transverse energy. The two-dimensional mass reconstruction of the $\mathrm{T}'\overline{\mathrm{T}'}$ system uses the analytic solutions of the system of the kinematic equations, together with constraints from the parton distribution functions, to select the most probable $\mathrm{M}_{T'}$ and $\mathrm{M}_{W'}$ per event. This analysis can search for the existence of any particle decaying with the same topology into the final state mentioned.

The same event sample is used for a variety of applications. As a proof of principle the top quark and the W boson are observed simultaneously in the data in the two-dimensional mass space ($\mathrm{M}_{T'}$, $\mathrm{M}_{W'}$).
Further studies are performed looking into one-dimensional applications. A new heavy top

quark partner T′ decaying to SM W bosons and b quarks is shown to be successfully reconstructed for various assumed mass values. No deviations from standard model predictions are observed. An expected 95% CL lower mass limits for a new vector-like heavy top quark partner T′ [204, 205] is set at (614^{+55}_{-57}) GeV with an observed lower limit of 658 GeV .
In addition a search for a new heavy neutral gauge boson Z′ decaying to SM top pairs is studied in the invariant mass distribution of the $t\bar{t}$ system. The search method successfully reconstructs assumed Z′ particles for different values $M_{Z'}$, but no indication for an additional resonant top pair contribution is observed. The lower 95% CL observed and expected mass limits for a new narrow width leptophobic heavy gauge boson Z′ [22, 23] are 1369 GeV and (1377^{+146}_{-157}) GeV , respectively.
Comparing the T′ and Z′ searches to dedicated published CMS results [199, 204] using similar final states and event selections is an important test for the mass reconstruction method. In these dedicated studies very similar and compatible lower mass limits are obtained, thus establishing the robustness of the method presented here, which thus provides additional information through a largely model-independent analysis.

The main advantage of this search method is the simultaneous reconstruction of two unknown particles in the two-dimensional mass space. A search for pair-produced new heavy top quark partners T′ , decaying into new heavy charged gauge bosons W′ and SM b quarks as predicted by Littlest Higgs models is studied in the two-dimensional mass-plane. A simplified model is used to enable easier access to models with similar particle content and masses. After successfully reconstructing different mass points in the $M_{T'}$ and $M_{W'}$ plane and in the absence of a significant excess over standard model predictions, 95% CL upper limits on the cross section times branching ratio $\sigma \cdot BR$ are calculated. The expected 95% CL lower limit on the mass $M_{T'}$ for a new heavy top-partner T′ [157, 158] ranges from (870^{+60}_{-80}) GeV to (930^{+20}_{-60}) GeV depending on the mass $M_{W'}$. The corresponding values for the observed limit are in the range of 870 GeV to 950 GeV .
This is the first search performed at the LHC for both a new heavy top quark partner T′ and a new heavy charged gauge boson W′ as predicted by the Littlest Higgs model.

To enable further process and analysis of the presented results in the context of other models and theoretical predictions, the selection efficiency times detector acceptance $\epsilon \cdot$A is provided for all applications in the appendix in tables J.26 to J.31.

The next LHC run is already underway with pp collisions at a centre of mass energy $\sqrt{s}$ of 13 TeV . Up to the summer of 2016 the CMS detector has already recorded roughly 15 fb^{-1} , with more to come [129]. The accumulation of large amounts of events and the increase in centre of mass energy allows the search for new physics, including the production of new heavy particles, in an expanded region of phase-space.
The model independent method presented here provides a valuable instrument for such

searches. In addition, it could easily be implemented to look for a new heavy Z' decaying into two heavy particles $T'\overline{T'}$. It could also be used to search for new particles in other final states, e.g. with four leptons and $E_{\mathrm{T}}^{\mathrm{miss}}$, as predicted by supersymmetric cascades.

Appendix

A Pile-up Jet MVA identifier

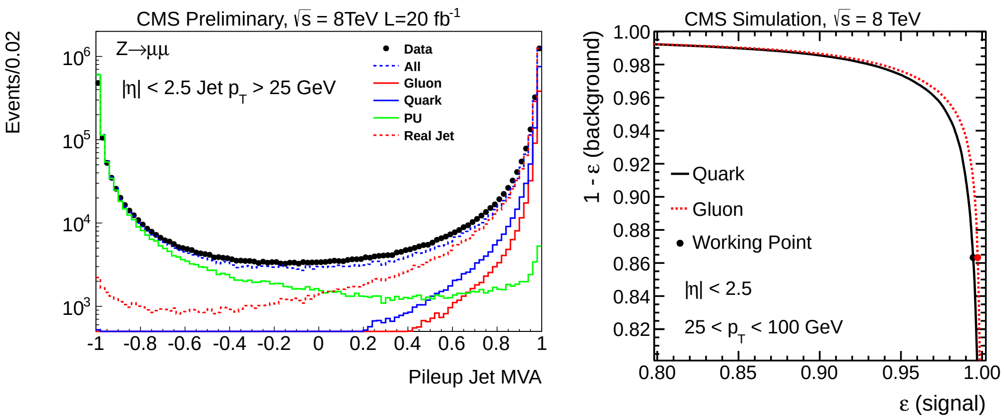

Figure A.1: Distribution of the *pile-up-jet-ID* MVA classifier for particle flow jets with $p_T{}^{\text{jet}} > 25\,\text{GeV}$ and $|\eta^{\text{jet}}| < 2.5$ as measured in [184] (left).
In this analysis a loose working point is used: *pile-up-jet-ID* MVA > -0.80 (valid for all jets with $|\eta^{\text{jet}}| < 2.4$ and $p_T{}^{\text{jet}} > 50\,\text{GeV}$). This corresponds to a signal efficiency for "real" jets of over 99% while "pile-up-jets" are rejected with an efficiency of over 85% (right) [184].

B Jet Selection: p_T -ordering vs b-tag-ordering

In this analysis the two highest energetic jets in p_T are selected. A comparison has been performed with ordering the two jets by the value of the b-tag discriminator, here the Combined Secondary Vertex (CSV) [186]. All 45 simplified Littlest Higgs signal samples are used for this study. Reconstructed jets surviving all selection criteria as described in section 5.5 have been sorted via p_T and the b-tag-discriminator and the two highest, respectively, are chosen as the selected jets in both cases. The generated b and $\bar{b}$ quarks coming from the T' and $\overline{\mathrm{T}'}$ quark are matched to the chosen reconstructed jets within a ΔR cone of 0.5. The fraction of all selected events with both jets successfully matched to the correct generated b and $\bar{b}$ quarks are shown in figure B.2 for the ordering via p_{T} and the b-tag discriminator.

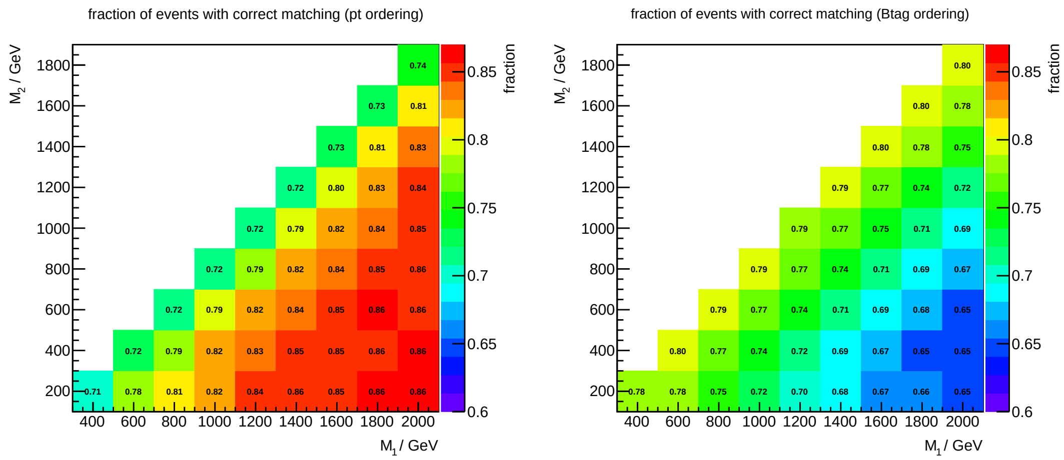

Figure B.2: Fraction of all selected events with correct matching of both jets to the b and $\bar{b}$ quark originating from the T' and $\overline{\mathrm{T}'}$ quark for p_{T} ordering (left) and b-tag-discriminator-ordering (right).

The ratio of these efficiency distributions is presented in figure B.3. Using the p_{T} ordering the correct jets are selected more often in the whole two-dimensional mass space, except along the diagonal, where the mass difference between $\mathrm{M}_{T'}$ and $\mathrm{M}_{W'}$ is small. The ordering in p_{T} is the preferred choice in searching for new physics in the high mass region.

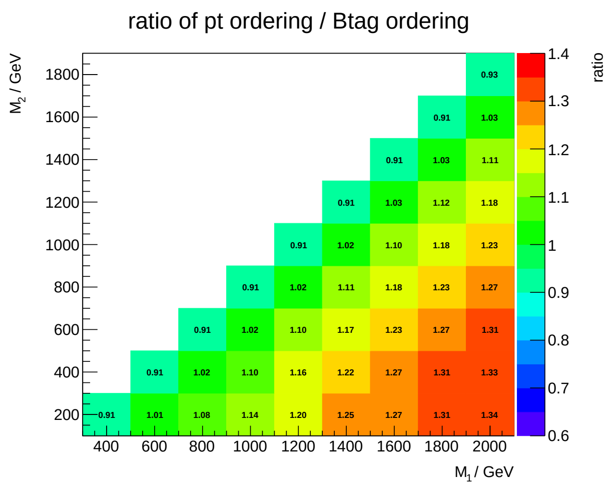

Figure B.3: Ratio for successfully matched jets: p_{T} ordering divided by b-tag-discriminator-ordering.

C Cut flow plots for all channels

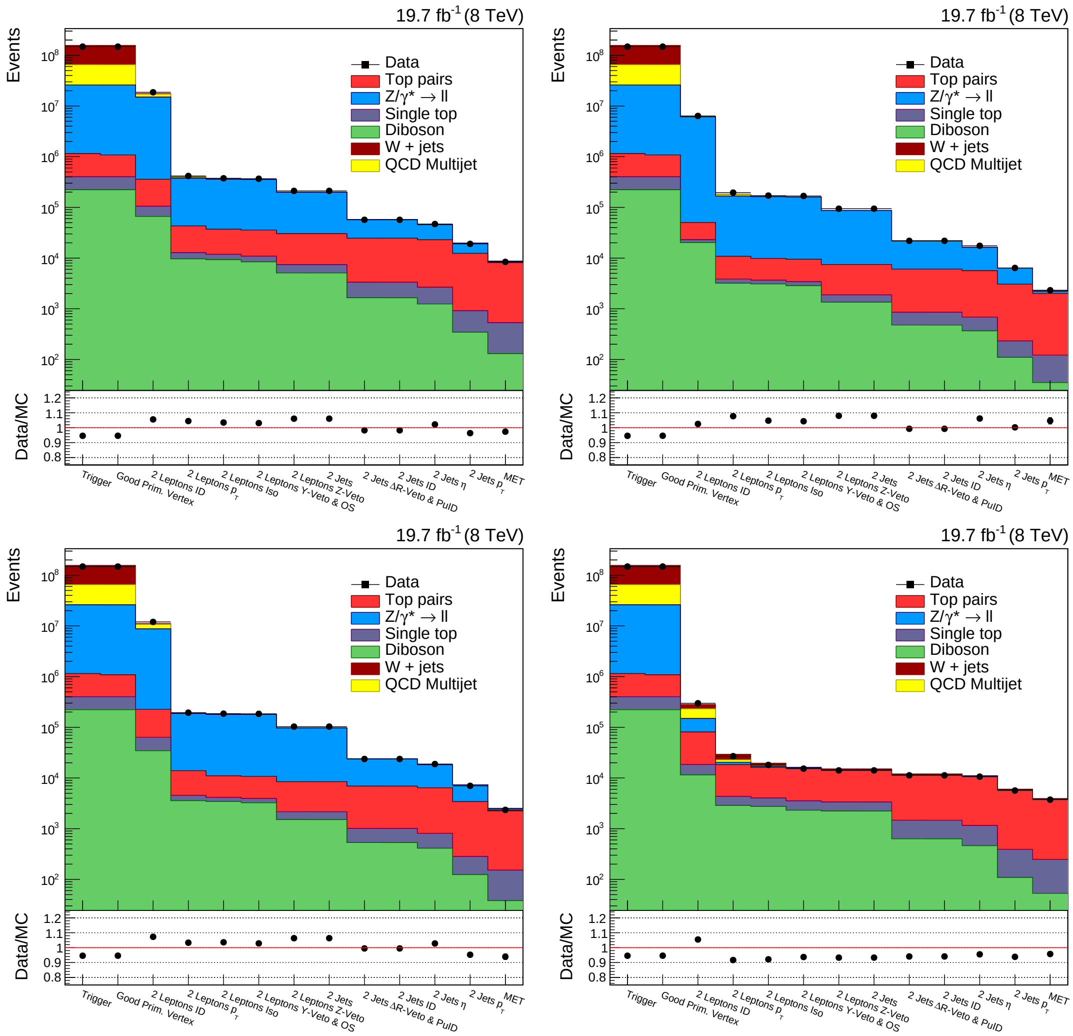

Figure C.4: Cut flow distributions for all channels combined (top-left), the ee channel (top-right), the $\mu\mu$ channel (bottom-left) and the $e\mu$ (bottom-right) channel, where each bin corresponds to requirements applied in the selection. To maintain consistency in all bins no trigger SF, lepton SF, pile-up and DY reweighting are applied.

D Control Plots after the event selection

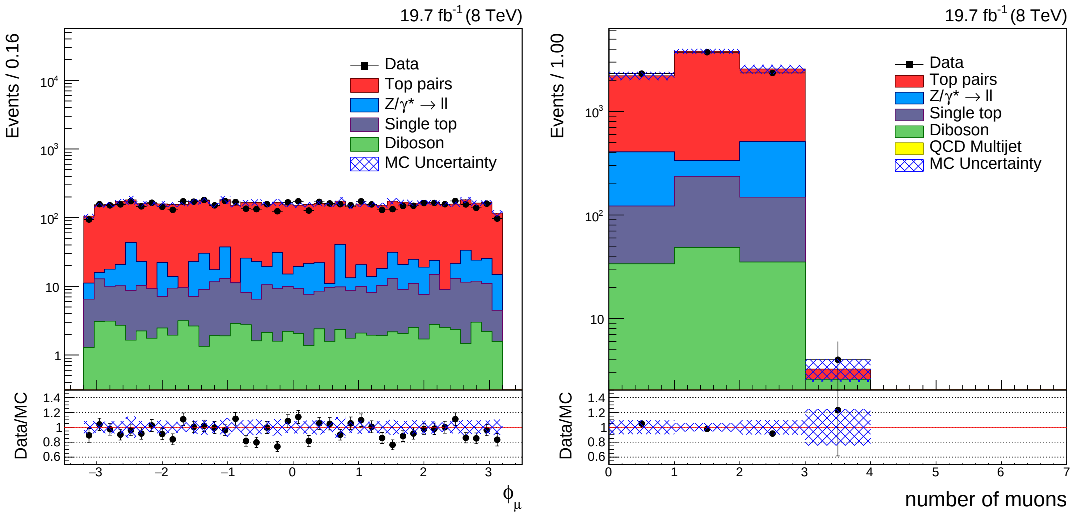

Figure D.5: Distribution of the azimuth angle ϕ of the highest energetic muon for the $\mu\mu$ and $e\mu$ channel (left) and the number of muons (right) for all channels after all selection cuts. Statistical and systematic uncertainties have been combined.

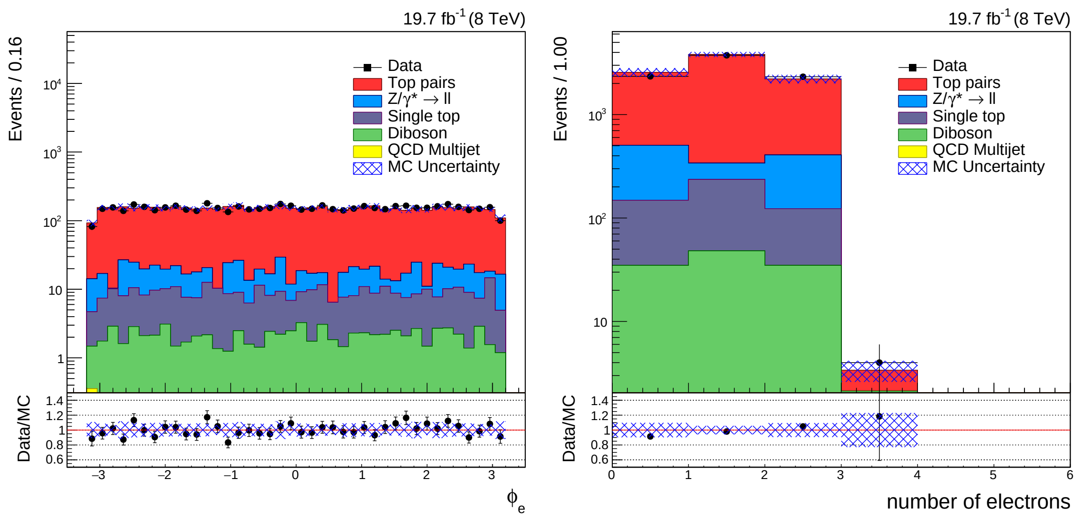

Figure D.6: Distribution of the azimuth angle ϕ of the highest energetic electron for the *ee* and $e\mu$ channel (left) and the number of electrons (right) for all channels after all selection cuts. Statistical and systematic uncertainties have been combined.

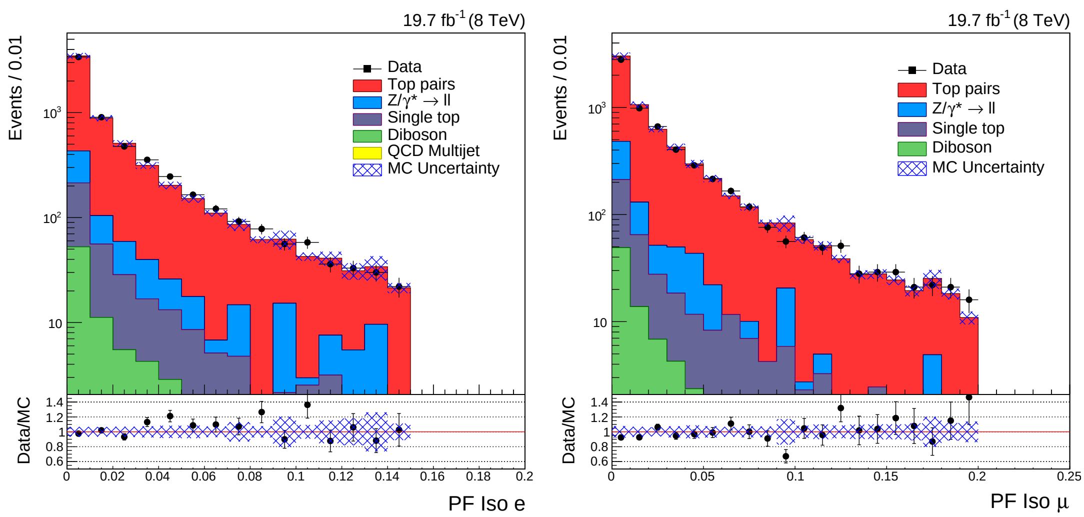

Figure D.7: Distribution of the particle-flow isolation variable for the highest energetic muon for the $\mu\mu$ and $e\mu$ channel (left) and highest energetic electron for the *ee* and $e\mu$ channel (right) after all selection cuts. Statistical and systematic uncertainties have been combined.

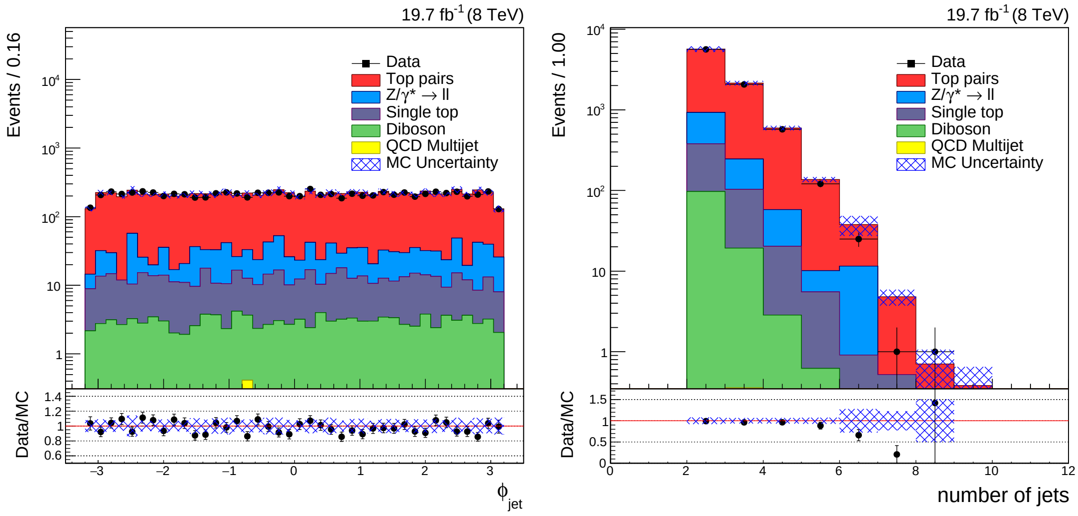

Figure D.8: Distribution of the azimuth angle ϕ of the highest energetic jet (left) and the number of jets (right) for all channels after all selection cuts. Statistical and systematic uncertainties have been combined.

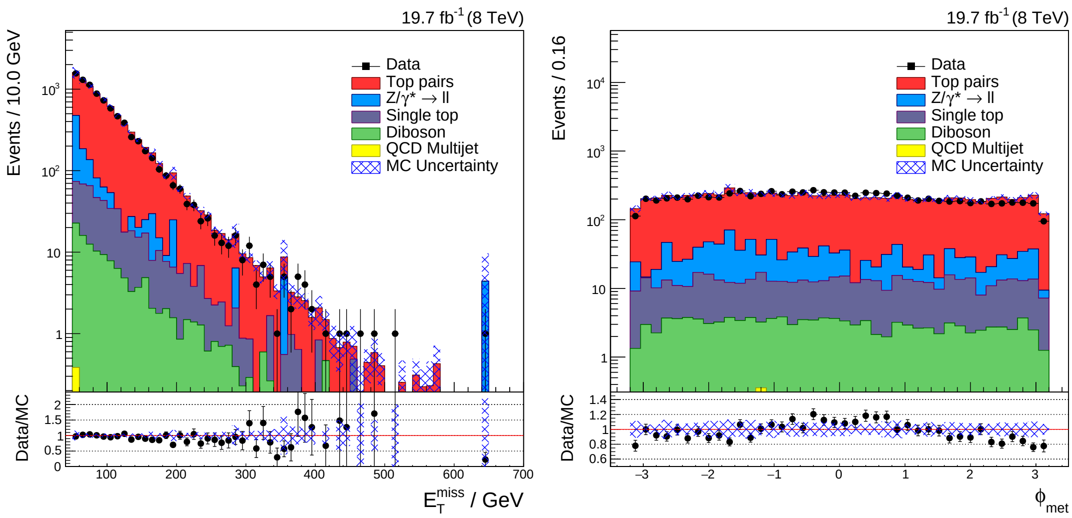

Figure D.9: Distribution of the missing transverse energy (left) and the azimuth angle ϕ of the missing transverse energy (right) for all channels after all selection cuts. Statistical and systematic uncertainties have been combined.

E Littlest Higgs Signal Samples

The signal samples generated for the two-dimensional application are using a Littlest Higgs model[1] as defined in [25], which predicts new fermions and gauge bosons. New masses for the gauge bosons are of order f, the vacuum expectation value of the $SU(5)$ symmetry breaking:

$$M'_{\mathrm{W}} = \frac{f}{2}\sqrt{g_1^2+g_2^2} \qquad M_{B'} = \frac{f}{2\sqrt{s}}\sqrt{g_1'^2+g_2'^2} \tag{E.1}$$

with the four gauge couplings $g_1, g_2, g'_1 g'_2$ and their rotation mass eigenstates:

$$W = sW_1 + cW_2 \qquad W' = -cW_1 + sW_2 \qquad B = s'B_1 + c'B_2 \qquad B' = -c'B_1 + s'B_2 \tag{E.2}$$

The mixing angles of $SU(2)$ and $U(1)$ are defined as:

$$s = \frac{g_2}{\sqrt{g_1^2+g_2^2}} \qquad s' = \frac{g_2}{\sqrt{g_1'^2+g_2'^2}} \tag{E.3}$$

W and B are the SM gauge bosons with couplings g = $g_1 s$ and g' = $g'_1 s'$. The electroweak symmetry breaking induces further mixing between light and new heavy gauge bosons, where the Higgs masses are:

$$M_\Phi^2 = \frac{2m_H^2 f^2}{v^2}\frac{1}{1-(4v'f/v^2)^2}, \tag{E.4}$$

with v is the vacuum expectation value of the higgs doublet H and v' the vacuum expectation value of the higgs triplet Φ. The corresponding mass of the heavy gauge bosons is:

$$M_{W_H^\pm}^2 = m_w^2\left(\frac{f^2}{s^2c^2v^2}-1\right) \quad \text{with} \quad m_w = \frac{gv}{2} \tag{E.5}$$

A similar equation is available for $M_{W_L^\pm}^2$ and the other gauge bosons, but is not important for the decay chain. Apart from new heavy gauge bosons, also new heavy fermions acquire mass up to order v^2/f^2:

$$M_T = -f\sqrt{\lambda_1^2+\lambda_2^2} \quad \text{with the relation} \quad \frac{1}{\lambda_1^2}+\frac{1}{\lambda_2^2} \approx \frac{v^2}{m_t^2} \tag{E.6}$$

and m_t being the mass of the SM top quark and the new Yukawa couplings λ_1^2 and λ_2^2.

The couplings used in the generated samples for a new heavy top partner T_H and a new heavy gauge boson W_H are written in table E.1.

The five free parameters are the mixing angles s of SU(2), s' of U(1), the symmetry breaking scales f, v' and the new top Yukawa coupling λ_1, whereby the lightest Higgs mass M_H is set

[1] We thank the authors of Whizard[158] and [27, 103] for guiding us in the choice of the parameters and implementing the vertices needed.

Table E.1: The couplings used in the generated signal samples for a new heavy top partner T_H and a new heavy gauge boson W_H.

process	coupling
$T_H \to W_H b$	$\frac{g}{\sqrt{2}} \frac{v}{f} x_L \frac{c}{s} \gamma^\mu V_{tb}^{SM}$ with $x_L = \lambda_1 / (\lambda_1 + \lambda_2^2)$
$W_H \to l\nu$	$\frac{ig}{\sqrt{2}} \frac{c}{s} \gamma^\mu$

to 125 GeV . For a specific point in the $\mathrm{M}_{T'}$ $\mathrm{M}_{W'}$ plane a small mixing angle s is chosen for $SU(2)$ due to the presence of the ratio c/s in both couplings. The couplings are suppressed by (v/f), therefore $c/s = f/v$ is set to keep the decay open for higher values of the scale f. The scale f and the coupling λ_1 are calculated setting the masses of the new degrees of freedom: M_{T_H}, $M_{W_H^\pm}$. The vacuum expectation value f can be calculated with equation E.5 using a fixed value for $M_{W_H^\pm}$. The scale f is increased by $M_{W_H^\pm}$ more naturally than fixing it globally for the whole two-dimensional phase-space. The value of M_{T_H} fixes the value of λ_1 using relations E.6:

$$\lambda_1^2 = \frac{-\frac{M_{T_H}^2}{f^2} \pm \sqrt{(\frac{M_{T_H}^2}{f^2})^2 - 4\frac{m_t^2}{v^2}\frac{M_{T_H}^2}{f^2}}}{2} \tag{E.7}$$

The remaining parameters are not important for the masses M_{T_H} and $M_{W_H^\pm}$ and the used decay chain, so $s' = 1/\sqrt{2}$ and $v' = 0$ is set. The masses of the other gauge and higgs bosons can be calculated accordingly: M_{A_H}, M_{Z_H}, M_ϕ.

F Jet Energy Resolution

The jet energy resolution in data is calculated from the jet energy resolution in MC simulations multiplied with the scale factor $c^{\mathrm{JER}} = \frac{\mathrm{JER_{data}}}{\mathrm{JER_{MC}}}$ (compare table 5.3, [143, 181–183]) and is shown in figure F.10 for $p_{\mathrm{T}}{}^{\mathrm{jet}} > 50\,\mathrm{GeV}$. The MC jet energy resolution is obtained using an average number of 22 true pile-up interactions (compare figure 3.7). The jet energy resolution is used to smear the reconstructed jets in the mass reconstruction method.

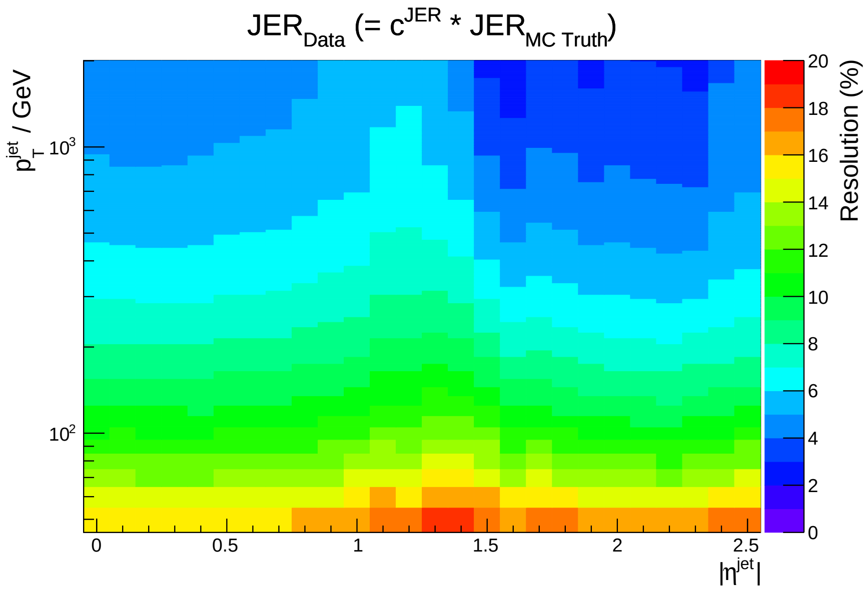

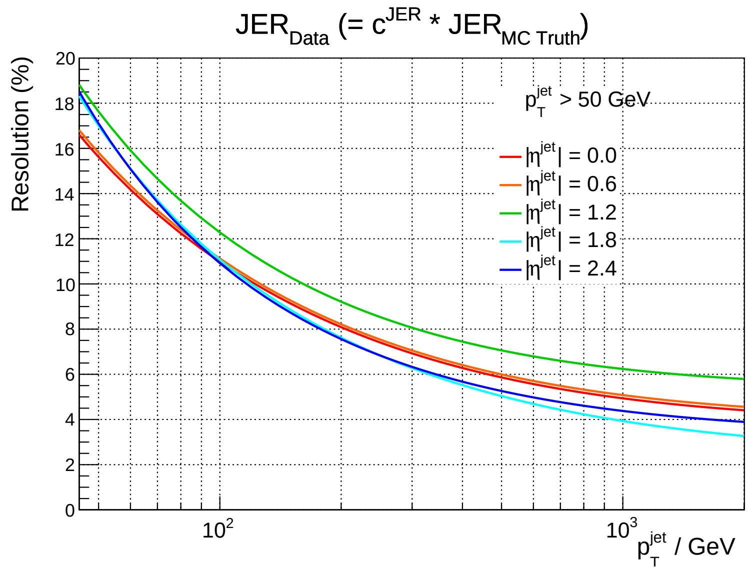

Figure F.10: The distribution of the jet energy resolution (JER) as a function of $p_{\mathrm{T}}{}^{\mathrm{jet}}$ and $|\eta^{\mathrm{jet}}|$ (top) and as a projection for selected η values (bottom).

G Results after Mass Reconstruction

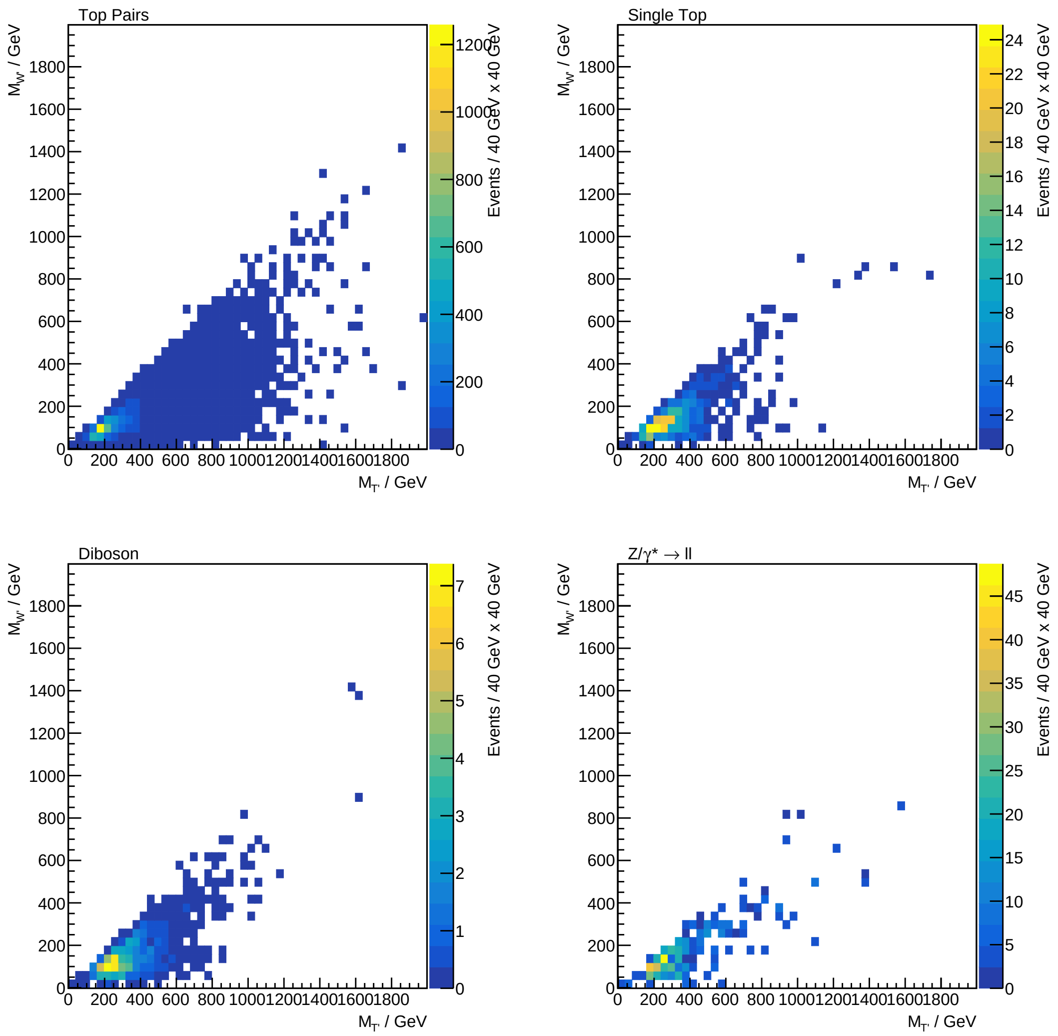

Figure G.11: Two-dimensional mass reconstruction of the different background components in simulations. Top pairs (top left), single top (top right), diboson (bottom left) and DY events (bottom right) are shown separately.

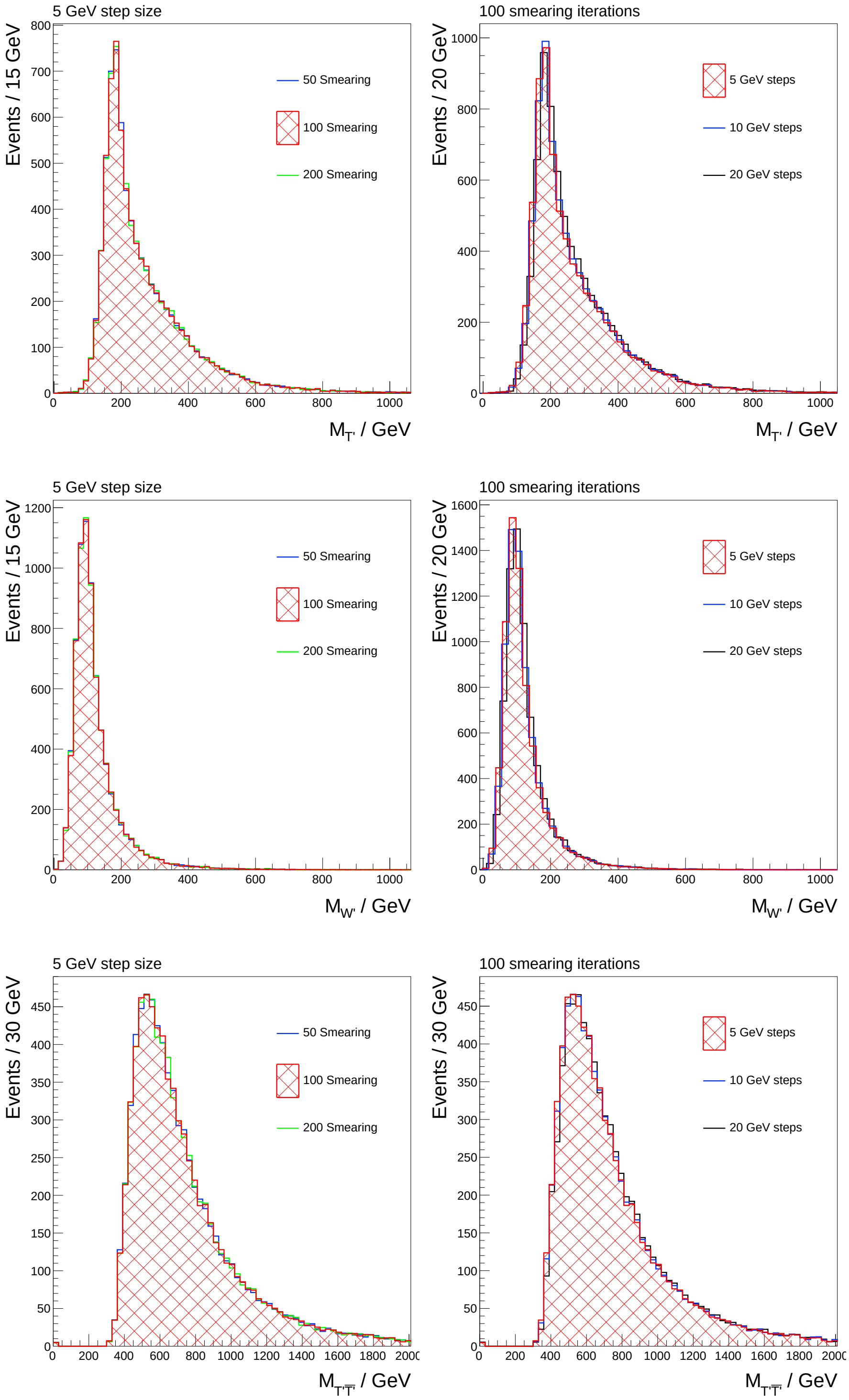

Figure G.12: Projection on the $M_{T'}$ axis (first row), on the $M_{W'}$ axis (second row) and the invariant mass of the $M_{T'\overline{T'}}$ system (third row) for the simulated top pair samples. The first column shows the results for a different number of smearing iterations and the second column for different step sizes in the mass reconstruction. The results for the used settings of 100 smearing iterations and a step size of 5 GeV are shown in red.

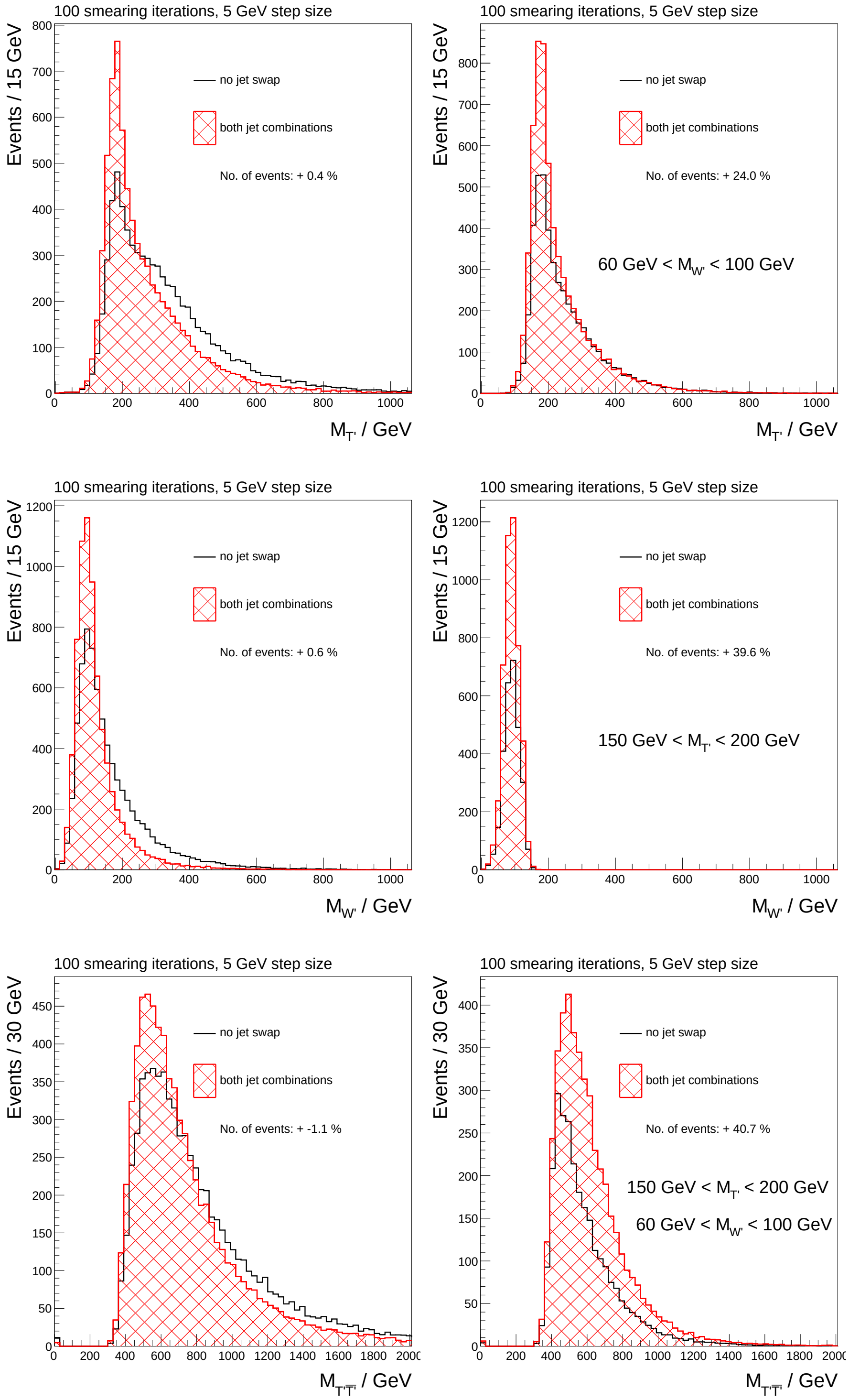

Figure G.13: Projection on the $M_{T'}$ axis (first row), on the $M_{W'}$ axis (second row) and the invariant mass of the $M_{T'\overline{T'}}$ system (third row) for the simulated top pair samples - with and without interchange of the two measured jets (black and red distributions, respectively). For the first column no requirement on the $M_{W'}$ and $M_{T'}$ masses is imposed, while for the second column the restrictions $(60 < M_{W'} < 100)$ GeV and $(150 < M_{T'} < 200)$ GeV are used. These mass windows are only employed for the T$'$ and Z$'$ applications.

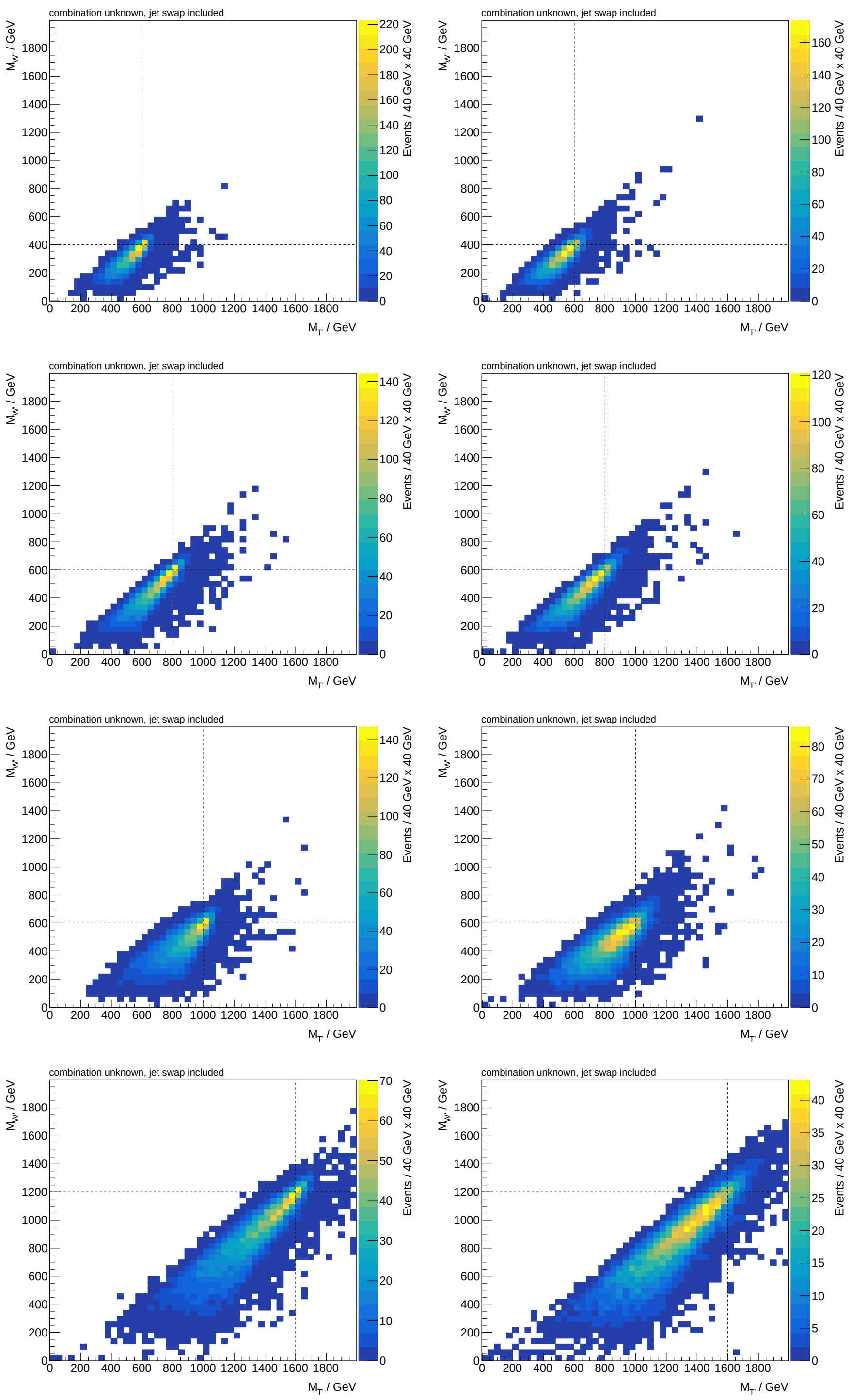

Figure G.14: Two-dimensional mass reconstruction of simulated Little Higgs signal samples for a T′ of 600 GeV and a W′ of 400 GeV (1rst row), a T′ of 800 GeV and a W′ of 600 GeV (2nd row), a T′ of 1000 GeV and a W′ of 600 GeV (3rd row) and a T′ of 1600 GeV and a W′ of 1200 GeV (last row). In the distributions on the left the generator information for the quarks, leptons and neutrino $p_{x,y}$ momenta are used as an input to the mass reconstruction method. The physics objects reconstructed in the detector and matched ($\Delta R < 0.1$) to generator level objects are used in the distributions on the right.

Table G.2: Signal event yields for all T′ samples in the *ee*, *μμ*, *eμ* and the combined dilepton channel. The production cross section σ is set to 1 pb. The statistical and systematic uncertainties are shown separately.

Signal T′ [GeV]	*ee* yield ± stat ± sys	*μ μ* yield ± stat ± sys	*eμ* yield ± stat ± sys	**total** yield ± stat ± sys
450	52.3 ± 3.2 ± 2.0	61.3 ± 3.5 ± 3.2	102.4 ± 4.5 ± 4.3	216.0 ± 6.5 ± 7.7
475	55.3 ± 3.3 ± 2.2	66.3 ± 3.6 ± 3.4	102.6 ± 4.5 ± 4.3	224.2 ± 6.6 ± 8.0
500	61.4 ± 3.5 ± 2.4	64.5 ± 3.6 ± 3.3	120.5 ± 4.9 ± 5.1	246.4 ± 7.0 ± 8.8
575	61.1 ± 3.4 ± 2.4	76.4 ± 3.8 ± 3.9	117.9 ± 4.8 ± 4.9	255.3 ± 7.0 ± 9.1
600	72.3 ± 3.8 ± 2.8	80.6 ± 4.0 ± 4.2	119.2 ± 4.9 ± 5.0	272.1 ± 7.4 ± 9.7
625	69.5 ± 3.9 ± 2.7	80.6 ± 4.2 ± 4.2	133.9 ± 5.4 ± 5.6	284.0 ± 7.9 ± 10.2
650	73.1 ± 3.9 ± 2.8	79.6 ± 4.0 ± 4.1	148.0 ± 5.5 ± 6.2	300.6 ± 7.8 ± 10.8
675	73.6 ± 3.8 ± 2.9	82.5 ± 4.0 ± 4.3	150.2 ± 5.4 ± 6.3	306.3 ± 7.7 ± 11.0
725	79.1 ± 3.9 ± 3.1	86.9 ± 4.1 ± 4.5	142.7 ± 5.2 ± 6.0	308.6 ± 7.7 ± 11.0
750	73.7 ± 3.8 ± 2.9	98.6 ± 4.4 ± 5.1	161.7 ± 5.7 ± 6.8	334.0 ± 8.1 ± 11.9
775	84.1 ± 4.1 ± 3.3	88.4 ± 4.2 ± 4.6	159.2 ± 5.6 ± 6.7	331.7 ± 8.1 ± 11.9
800	81.7 ± 4.1 ± 3.2	81.5 ± 4.1 ± 4.2	147.6 ± 5.5 ± 6.2	310.8 ± 7.9 ± 11.1
850	82.9 ± 4.0 ± 3.2	101.9 ± 4.4 ± 5.3	172.0 ± 5.7 ± 7.2	356.8 ± 8.3 ± 12.8
900	87.4 ± 4.1 ± 3.4	98.1 ± 4.4 ± 5.1	171.6 ± 5.8 ± 7.2	357.1 ± 8.4 ± 12.8
1400	100.9 ± 4.7 ± 3.9	103.3 ± 4.7 ± 5.3	203.6 ± 6.6 ± 8.5	407.8 ± 9.4 ± 14.6
1500	93.7 ± 4.3 ± 3.7	110.0 ± 4.6 ± 5.7	193.5 ± 6.1 ± 8.1	397.2 ± 8.8 ± 14.2

Table G.3: Signal event yields for all Z′ samples in the *ee*, *μμ*, *eμ* and the combined dilepton channel. The production cross section σ is set to 1 pb. The statistical and systematic uncertainties are shown separately.

Signal Z′ [GeV]	*ee* yield ± stat ± sys	*μ μ* yield ± stat ± sys	*eμ* yield ± stat ± sys	**total** yield ± stat ± sys
500	4.3 ± 0.8 ± 0.4	3.0 ± 0.7 ± 0.3	5.9 ± 1.0 ± 0.4	13.1 ± 1.5 ± 0.8
750	12.2 ± 1.5 ± 1.2	14.3 ± 1.6 ± 1.2	26.0 ± 2.2 ± 1.6	52.5 ± 3.1 ± 3.0
1000	25.0 ± 2.2 ± 2.5	22.6 ± 2.1 ± 1.9	45.4 ± 2.9 ± 2.8	93.1 ± 4.2 ± 5.4
1250	29.3 ± 2.4 ± 2.9	29.3 ± 2.4 ± 2.5	53.7 ± 3.3 ± 3.4	112.2 ± 4.7 ± 6.5
1500	31.0 ± 1.3 ± 3.1	25.1 ± 1.1 ± 2.1	48.4 ± 1.6 ± 3.0	104.4 ± 2.3 ± 6.0
2000	26.9 ± 2.4 ± 2.7	18.0 ± 1.9 ± 1.5	38.4 ± 2.8 ± 2.4	83.3 ± 4.2 ± 4.8
3000	12.3 ± 1.8 ± 1.2	8.8 ± 1.6 ± 0.7	20.0 ± 2.3 ± 1.3	41.0 ± 3.4 ± 2.4

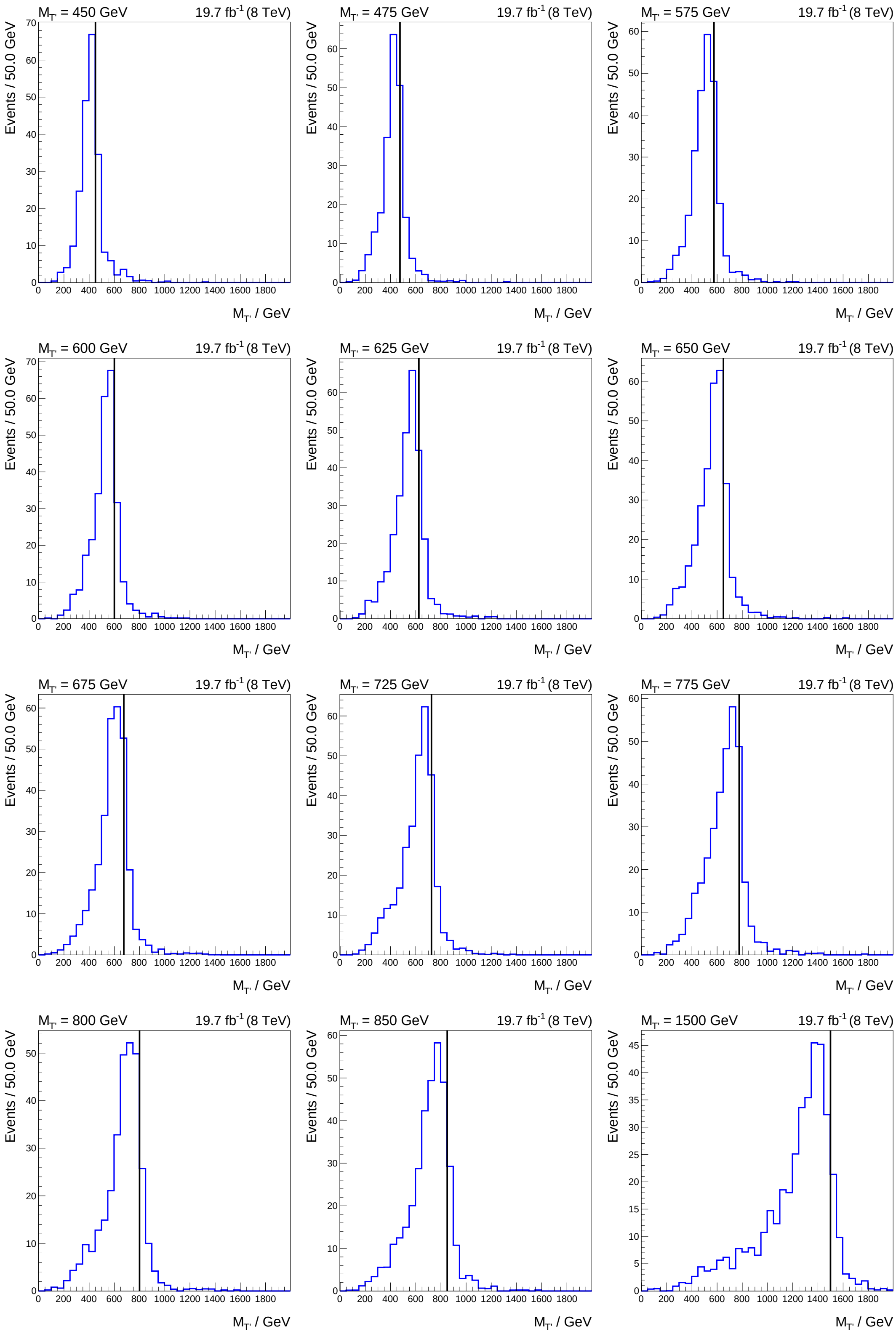

Figure G.15: Projection on the M$_{T'}$ axis for all simulated T$'$ signal samples. The production cross section σ is set to 1 pb. The black lines indicate the mean T$'$ mass on the generator level. M$_{W'}$ is restricted to 60 - 100 GeV around the W mass.

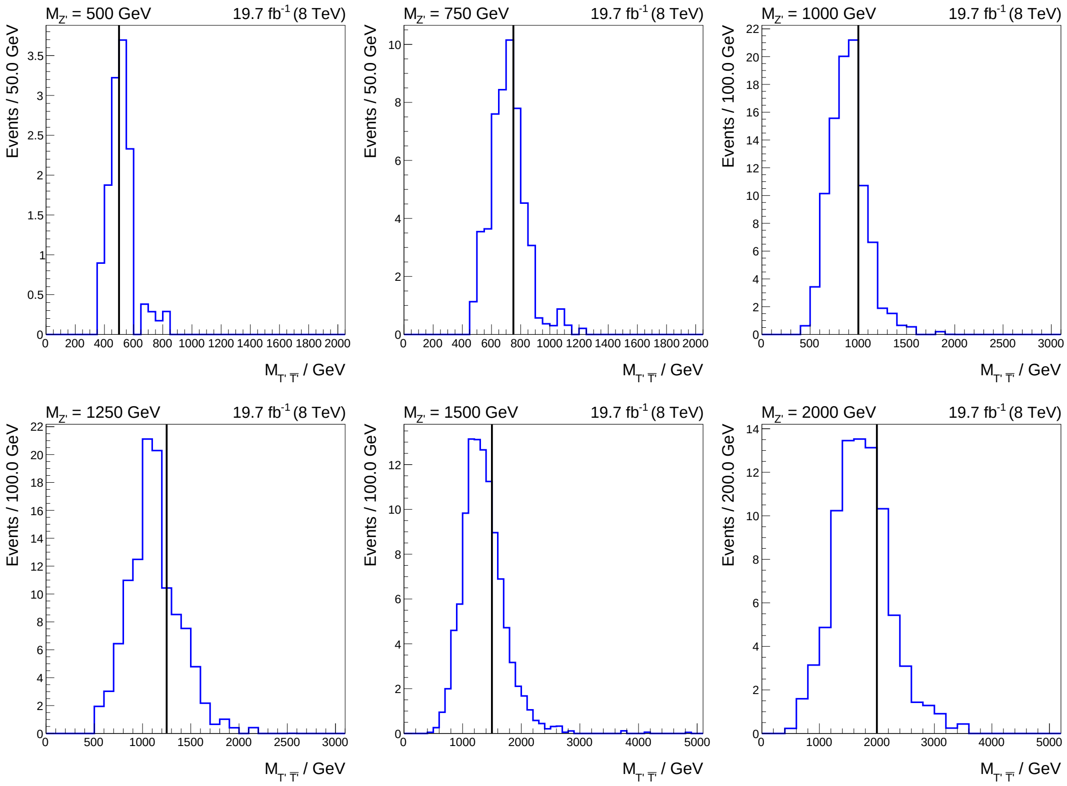

Figure G.16: $M_{T'\overline{T'}}$ invariant mass distribution for a $M_{W'}$ mass window of 60 - 100 GeV and a $M_{T'}$ mass window of 150 - 200 GeV for simulated Z' signal samples. The production cross section σ is set to 1 pb. The black lines indicate the mean Z' mass on the generator level.

Table G.4: Signal event yields for all simplified Littlest Higgs samples in the ee, $\mu\mu$, $e\mu$ and the combined dilepton channel. The production cross section σ is set to 1 pb. The statistical and systematic uncertainties are shown separately.

Signal T′	[GeV] W′	ee yield ± stat ± sys	$\mu\,\mu$ yield ± stat ± sys	$e\mu$ yield ± stat ± sys	**total** yield ± stat ± sys
400	200	964.5 ± 15.9 ± 33.0	1170.2 ± 17.5 ± 61.9	2005.9 ± 23.0 ± 87.5	4140.7 ± 33.0 ± 155.4
600	200	1153.5 ± 17.4 ± 39.4	1501.8 ± 19.9 ± 79.4	2464.5 ± 25.4 ± 107.5	5119.8 ± 36.7 ± 192.1
600	400	1488.9 ± 19.8 ± 50.9	1725.2 ± 21.3 ± 91.2	2938.6 ± 27.8 ± 128.2	6152.6 ± 40.2 ± 230.9
800	200	1320.5 ± 18.6 ± 45.1	1605.7 ± 20.5 ± 84.9	2761.7 ± 26.9 ± 120.5	5687.9 ± 38.7 ± 213.4
800	400	1706.9 ± 21.2 ± 58.4	2006.8 ± 23.0 ± 106.1	3369.2 ± 29.7 ± 147.0	7082.9 ± 43.1 ± 265.8
800	600	1669.7 ± 21.0 ± 57.1	1917.7 ± 22.5 ± 101.4	3191.4 ± 29.1 ± 139.3	6778.8 ± 42.4 ± 254.4
1000	200	1418.0 ± 19.3 ± 48.5	1726.0 ± 21.3 ± 91.3	2858.4 ± 27.4 ± 124.7	6002.3 ± 39.7 ± 225.2
1000	400	1626.1 ± 20.7 ± 55.6	2036.1 ± 23.2 ± 107.7	3581.3 ± 30.7 ± 156.3	7243.5 ± 43.7 ± 271.8
1000	600	1806.9 ± 21.8 ± 61.8	2163.7 ± 23.9 ± 114.4	3534.2 ± 30.5 ± 154.2	7504.8 ± 44.5 ± 281.6
1000	800	1654.5 ± 20.9 ± 56.6	1971.5 ± 22.8 ± 104.2	3351.6 ± 29.7 ± 146.2	6977.5 ± 42.9 ± 261.8
1200	200	1444.7 ± 19.5 ± 49.4	1937.0 ± 22.6 ± 102.4	3052.9 ± 28.4 ± 133.2	6434.5 ± 41.2 ± 241.4
1200	400	1751.4 ± 21.5 ± 59.9	2080.5 ± 23.4 ± 110.0	3460.7 ± 30.2 ± 151.0	7292.5 ± 43.8 ± 273.6
1200	600	1864.4 ± 22.2 ± 63.7	2135.5 ± 23.7 ± 112.9	3653.5 ± 31.0 ± 159.4	7653.4 ± 44.9 ± 287.2
1200	800	1859.6 ± 22.1 ± 63.6	2124.4 ± 23.6 ± 112.3	3611.4 ± 30.8 ± 157.6	7595.4 ± 44.7 ± 285.0
1200	1000	1585.9 ± 20.5 ± 54.2	2021.7 ± 23.1 ± 106.9	3264.1 ± 29.3 ± 142.4	6871.7 ± 42.6 ± 257.8
1400	200	1555.4 ± 20.2 ± 53.2	1961.1 ± 22.7 ± 103.7	3116.5 ± 28.6 ± 136.0	6633.1 ± 41.7 ± 248.9
1400	400	1789.4 ± 21.8 ± 61.2	2037.8 ± 23.2 ± 107.8	3439.2 ± 30.2 ± 150.1	7266.4 ± 43.9 ± 272.7
1400	600	1846.1 ± 22.0 ± 63.1	2190.1 ± 24.0 ± 115.8	3656.6 ± 31.0 ± 159.6	7692.8 ± 45.0 ± 288.6
1400	800	1822.6 ± 22.0 ± 62.3	2195.9 ± 24.1 ± 116.1	3725.0 ± 31.4 ± 162.5	7743.5 ± 45.3 ± 290.5
1400	1000	1884.3 ± 22.3 ± 64.4	2112.4 ± 23.6 ± 111.7	3610.7 ± 30.9 ± 157.5	7607.4 ± 44.8 ± 285.4
1400	1200	1639.8 ± 20.8 ± 56.1	2008.5 ± 23.0 ± 106.2	3381.3 ± 29.8 ± 147.5	7029.6 ± 43.0 ± 263.8
1600	200	1655.6 ± 20.9 ± 56.6	1937.1 ± 22.6 ± 102.4	3245.9 ± 29.2 ± 141.6	6838.6 ± 42.4 ± 256.6
1600	400	1696.2 ± 21.1 ± 58.0	2085.5 ± 23.4 ± 110.3	3490.6 ± 30.3 ± 152.3	7272.4 ± 43.7 ± 272.9
1600	600	1775.2 ± 21.6 ± 60.7	2249.8 ± 24.3 ± 119.0	3687.9 ± 31.1 ± 160.9	7712.9 ± 45.0 ± 289.4
1600	800	1855.5 ± 22.1 ± 63.4	2198.0 ± 24.1 ± 116.2	3702.1 ± 31.2 ± 161.5	7755.6 ± 45.2 ± 291.0
1600	1000	1871.0 ± 22.2 ± 64.0	2257.8 ± 24.4 ± 119.4	3586.7 ± 30.7 ± 156.5	7715.6 ± 45.0 ± 289.5
1600	1200	1734.4 ± 21.3 ± 59.3	2179.1 ± 23.9 ± 115.2	3657.4 ± 31.0 ± 159.6	7570.9 ± 44.6 ± 284.1
1600	1400	1634.9 ± 20.8 ± 55.9	2054.1 ± 23.3 ± 108.6	3289.8 ± 29.5 ± 143.5	6978.8 ± 42.9 ± 261.9
1800	200	1600.8 ± 20.5 ± 54.7	1939.0 ± 22.6 ± 102.5	3253.6 ± 29.3 ± 142.0	6793.4 ± 42.3 ± 254.9
1800	400	1691.4 ± 21.1 ± 57.8	2068.5 ± 23.4 ± 109.4	3457.0 ± 30.2 ± 150.8	7216.9 ± 43.6 ± 270.8
1800	600	1789.6 ± 21.7 ± 61.2	2215.9 ± 24.1 ± 117.2	3586.8 ± 30.7 ± 156.5	7592.4 ± 44.7 ± 284.9
1800	800	1805.2 ± 21.8 ± 61.7	2229.9 ± 24.2 ± 117.9	3650.1 ± 31.0 ± 159.3	7685.2 ± 44.9 ± 288.4
1800	1000	1874.7 ± 22.2 ± 64.1	2215.2 ± 24.2 ± 117.1	3598.4 ± 30.8 ± 157.0	7688.3 ± 45.0 ± 288.5
1800	1200	1790.3 ± 21.7 ± 61.2	2248.2 ± 24.3 ± 118.9	3563.6 ± 30.7 ± 155.5	7602.1 ± 44.8 ± 285.2
1800	1400	1717.9 ± 21.3 ± 58.7	2160.0 ± 23.9 ± 114.2	3549.0 ± 30.7 ± 154.9	7426.9 ± 44.3 ± 278.7
1800	1600	1560.9 ± 20.3 ± 53.4	1940.8 ± 22.6 ± 102.6	3097.9 ± 28.6 ± 135.2	6599.5 ± 41.7 ± 247.6
2000	200	1583.0 ± 20.4 ± 54.1	1933.6 ± 22.5 ± 102.2	3285.9 ± 29.4 ± 143.4	6802.4 ± 42.3 ± 255.2
2000	400	1744.0 ± 21.4 ± 59.6	2098.0 ± 23.5 ± 110.9	3476.4 ± 30.2 ± 151.7	7318.5 ± 43.8 ± 274.6
2000	600	1837.9 ± 22.0 ± 62.8	2176.1 ± 24.0 ± 115.1	3505.1 ± 30.4 ± 152.9	7519.1 ± 44.5 ± 282.1
2000	800	1848.1 ± 22.0 ± 63.2	2180.7 ± 23.9 ± 115.3	3528.6 ± 30.4 ± 154.0	7557.4 ± 44.6 ± 283.6
2000	1000	1968.4 ± 22.8 ± 67.3	2164.0 ± 23.9 ± 114.4	3629.1 ± 30.9 ± 158.3	7761.4 ± 45.2 ± 291.2
2000	1200	1795.1 ± 21.7 ± 61.4	2184.2 ± 24.0 ± 115.5	3584.0 ± 30.7 ± 156.4	7563.3 ± 44.6 ± 283.8
2000	1400	1770.2 ± 21.7 ± 60.5	2090.1 ± 23.5 ± 110.5	3464.7 ± 30.3 ± 151.2	7324.9 ± 44.0 ± 274.8
2000	1600	1636.6 ± 20.7 ± 56.0	2061.8 ± 23.3 ± 109.0	3435.2 ± 30.0 ± 149.9	7133.6 ± 43.3 ± 267.7
2000	1800	1515.4 ± 20.0 ± 51.8	1877.5 ± 22.2 ± 99.3	3127.6 ± 28.7 ± 136.5	6520.5 ± 41.4 ± 244.7

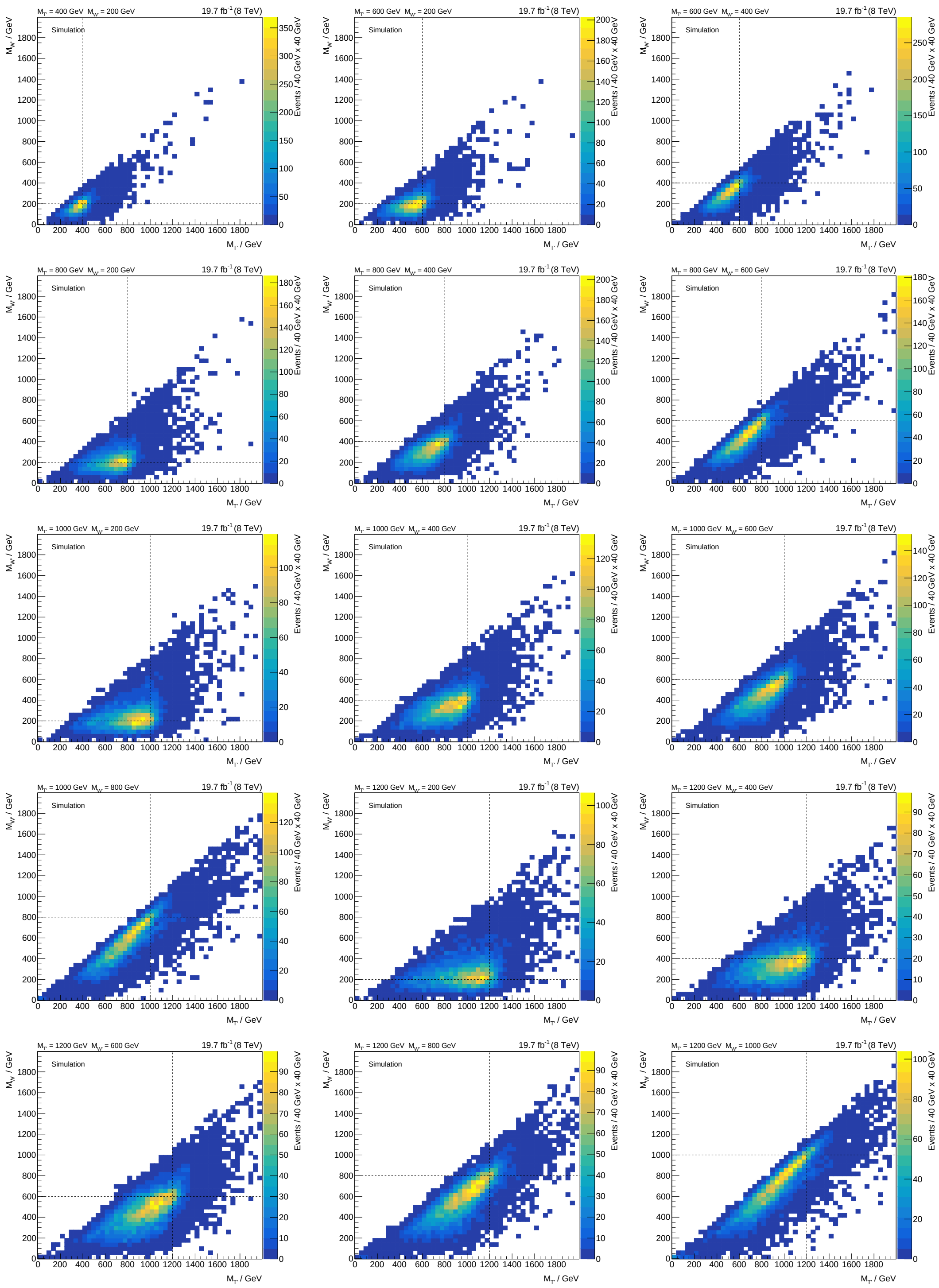

Figure G.17: Two-dimensional mass reconstruction for the simplified Littlest Higgs signal samples. The production cross section σ is set to 1 pb. The dashed lines indicate the mean T′ and W′ masses on the generator level.

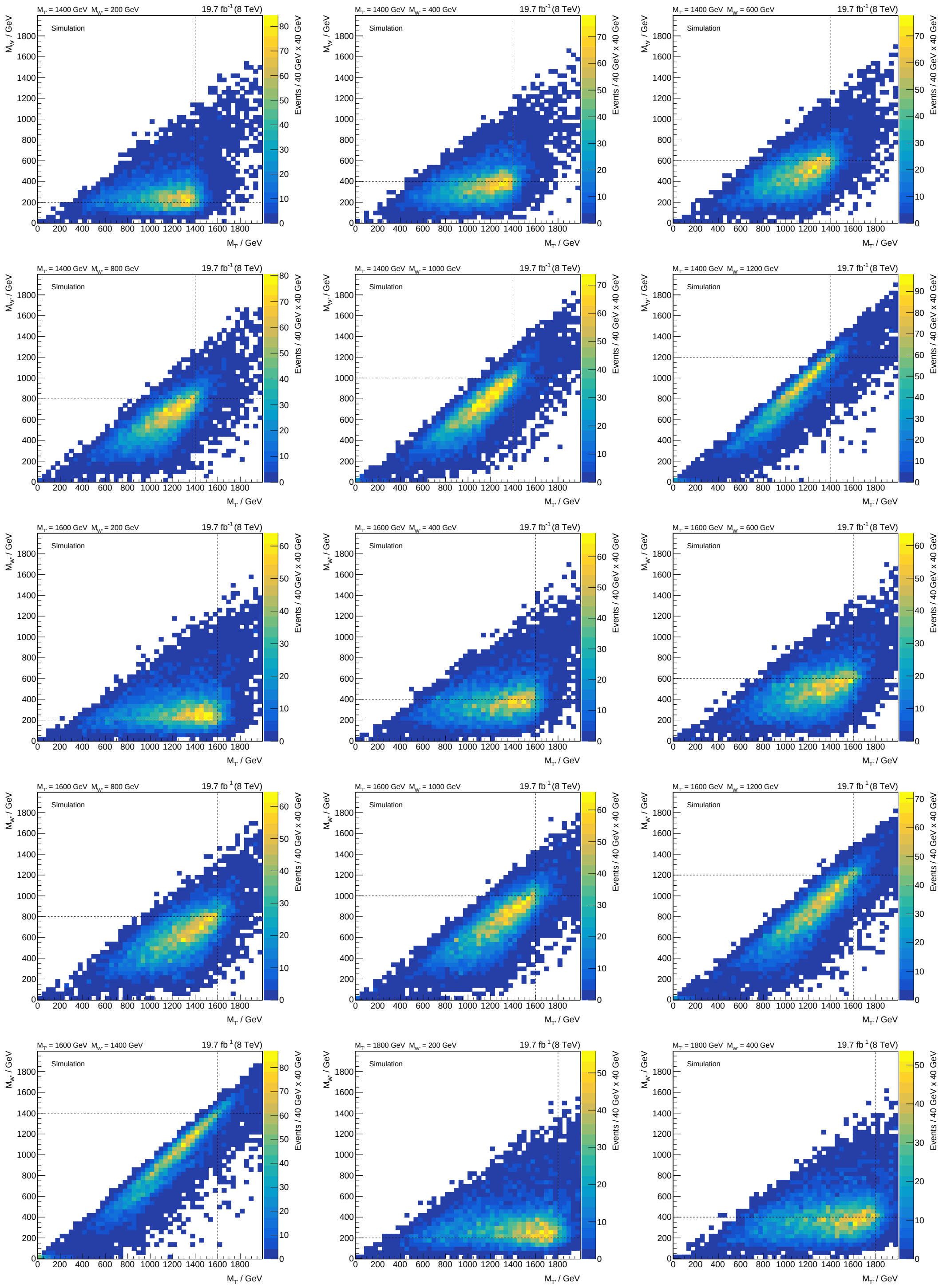

Figure G.18: Two-dimensional mass reconstruction for the simplified Littlest Higgs signal samples. The production cross section σ is set to 1 pb. The dashed lines indicate the mean T' and W' masses on the generator level.

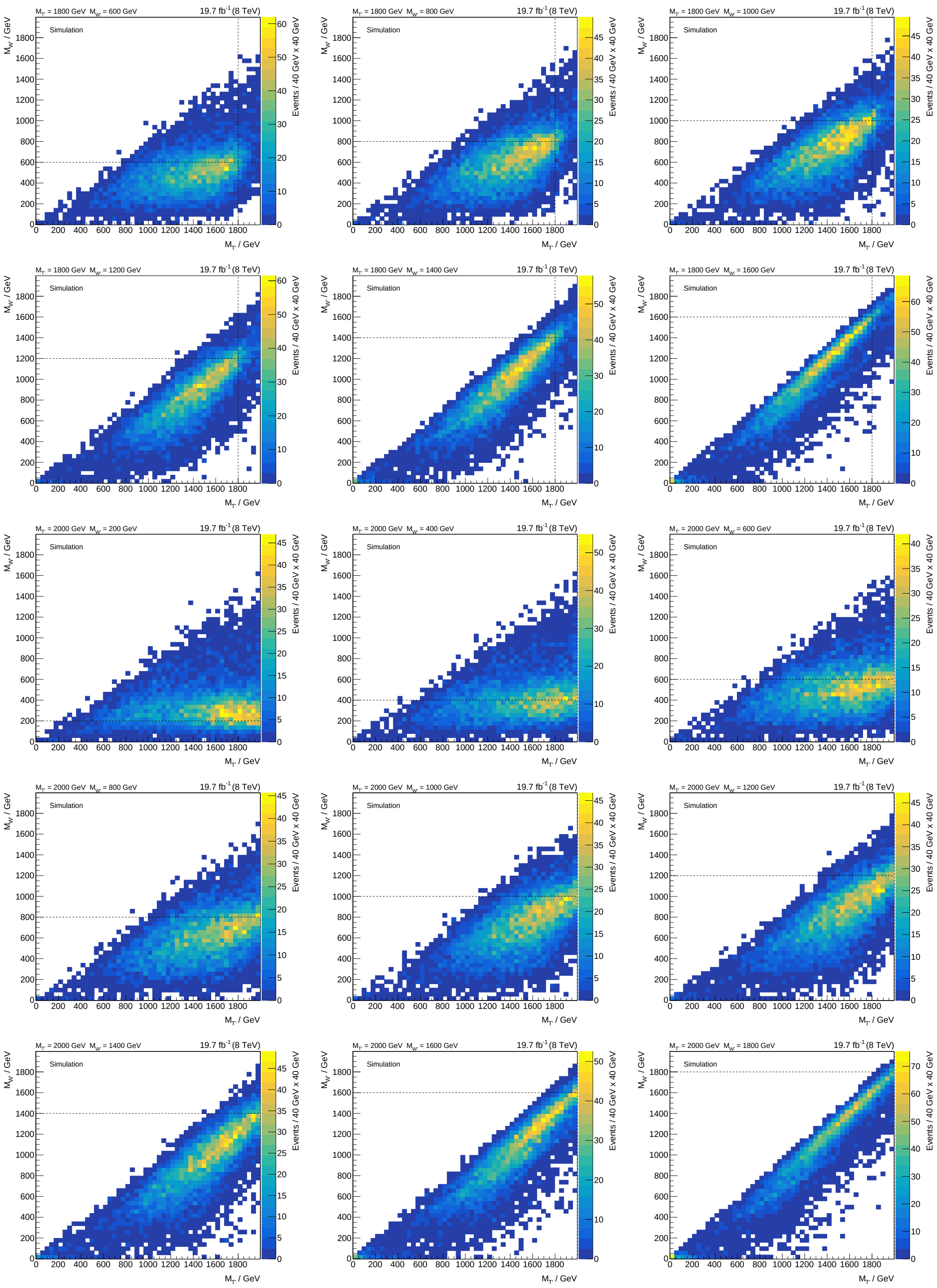

Figure G.19: Two-dimensional mass reconstruction for the simplified Littlest Higgs signal samples. The production cross section σ is set to 1 pb. The dashed lines indicate the mean T′ and W′ masses on the generator level.

H Systematic Uncertainties

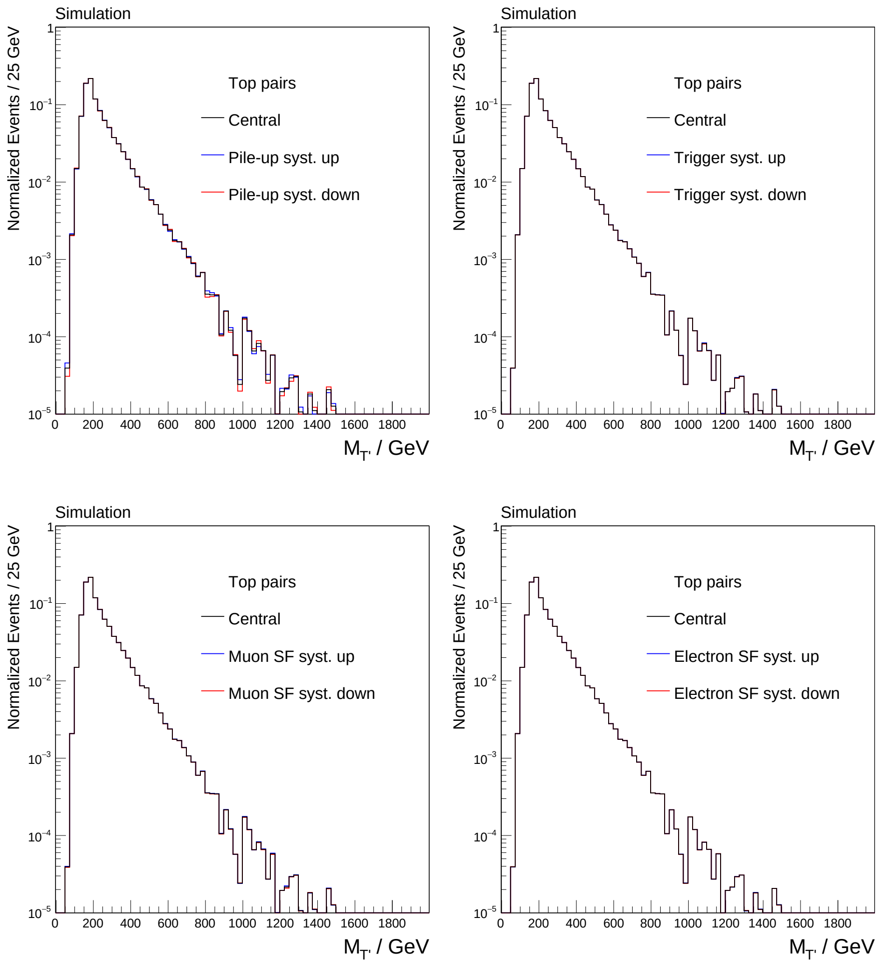

Figure H.20: Comparison of the projection on the $M_{T'}$ axis for $(60 < M_{W'} < 100)$ GeV in the T' application with the pile-up scale factor (top left) shifted upwards (blue) and downwards (red) with respect to its nominal value (black) for the top pair simulation samples. The same is shown for the trigger (top right), the muon (bottom left) and the electron (bottom right) scale factors.

Table H.5: Summary of all systematic uncertainties considered for the T′ search in the ee channel. Each row is treated as a single independent nuisance parameter.

Source	T′ Signal	Top pairs	Z + jets	Single Top	Diboson
Luminosity	2.6%	2.6%	2.6%	2.6%	2.6%
Pile-up	1.9%	0.5%	6.3%	0.7%	2.6%
Trigger	1.1%	1.1%	1.1%	1.1%	1.1%
Lepton SF	1.3%	1.3%	1.4%	1.3%	1.3%
Jet energy scale	0.9%	1.5%	9.8%	5.7%	3.6%
Jet energy resolution	1.1%	0.3%	7.3%	1.1%	1.0%
Q^2 scale	-	7.9%	-	-	-
ME/PS threshold	-	1.5%	-	-	-
PDF	-	2.6%	-	-	-
Cross section	-	-	75.0%	50%	30%
Total Systematic	3.9%	9.2%	76.3%	50.4%	30.5%
Total Background Systematic	-	7.8%	7.4%	1.7%	0.4%

Table H.6: Summary of all systematic uncertainties considered for the T′ search in the $\mu\mu$ channel. Each row is treated as a single independent nuisance parameter.

Source	T′ Signal	Top pairs	Z + jets	Single Top	Diboson
Luminosity	2.6%	2.6%	2.6%	2.6%	2.6%
Pile-up	1.3%	0.1%	7.8%	0.2%	3.5%
Trigger	0.4%	0.3%	0.3%	0.3%	0.3%
Lepton SF	3.8%	1.5%	1.5%	1.6%	1.8%
Jet energy scale	0.8%	1.9%	6.7%	1.4%	1.7%
Jet energy resolution	1.8%	0.5%	9.1%	1.4%	0.5%
Q^2 scale	-	5.7%	-	-	-
ME/PS threshold	-	0.2%	-	-	-
PDF	-	2.6%	-	-	-
Cross section	-	-	72.1%	50%	30%
Total Systematic	5.2%	7.2%	73.5%	50.1%	30.4%
Total Background Systematic	-	6.1%	7.5%	2.1%	0.4%

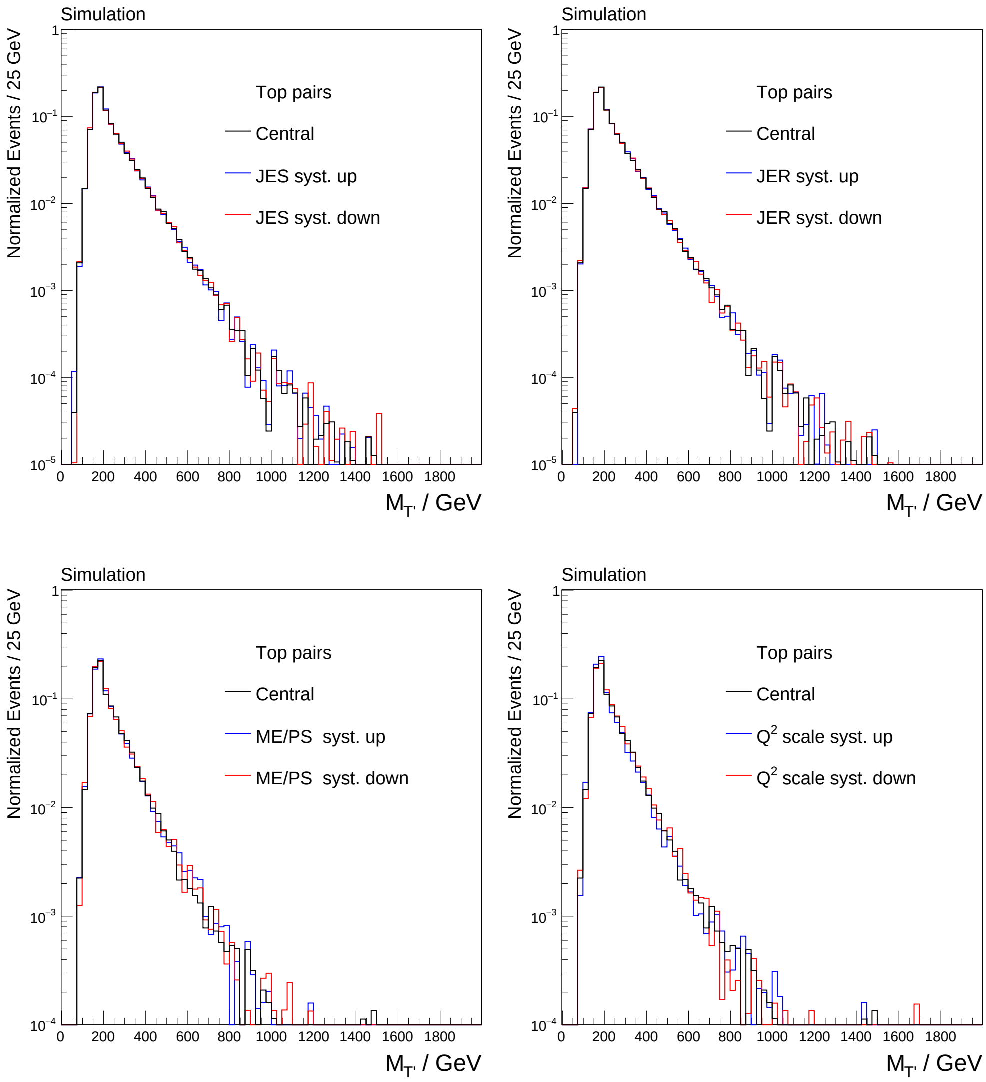

Figure H.21: Comparison of the projection on the $M_{T'}$ axis for $(60 < M_{W'} < 100)$ GeV in the T′ application with the JES scale factor (top left) shifted upwards (blue) and downwards (red) with respect to its nominal value (black) for the top pair simulation samples. The same is also shown for the JER (top right), the Q^2 (bottom left) and the ME/PS matching (bottom right) scales.

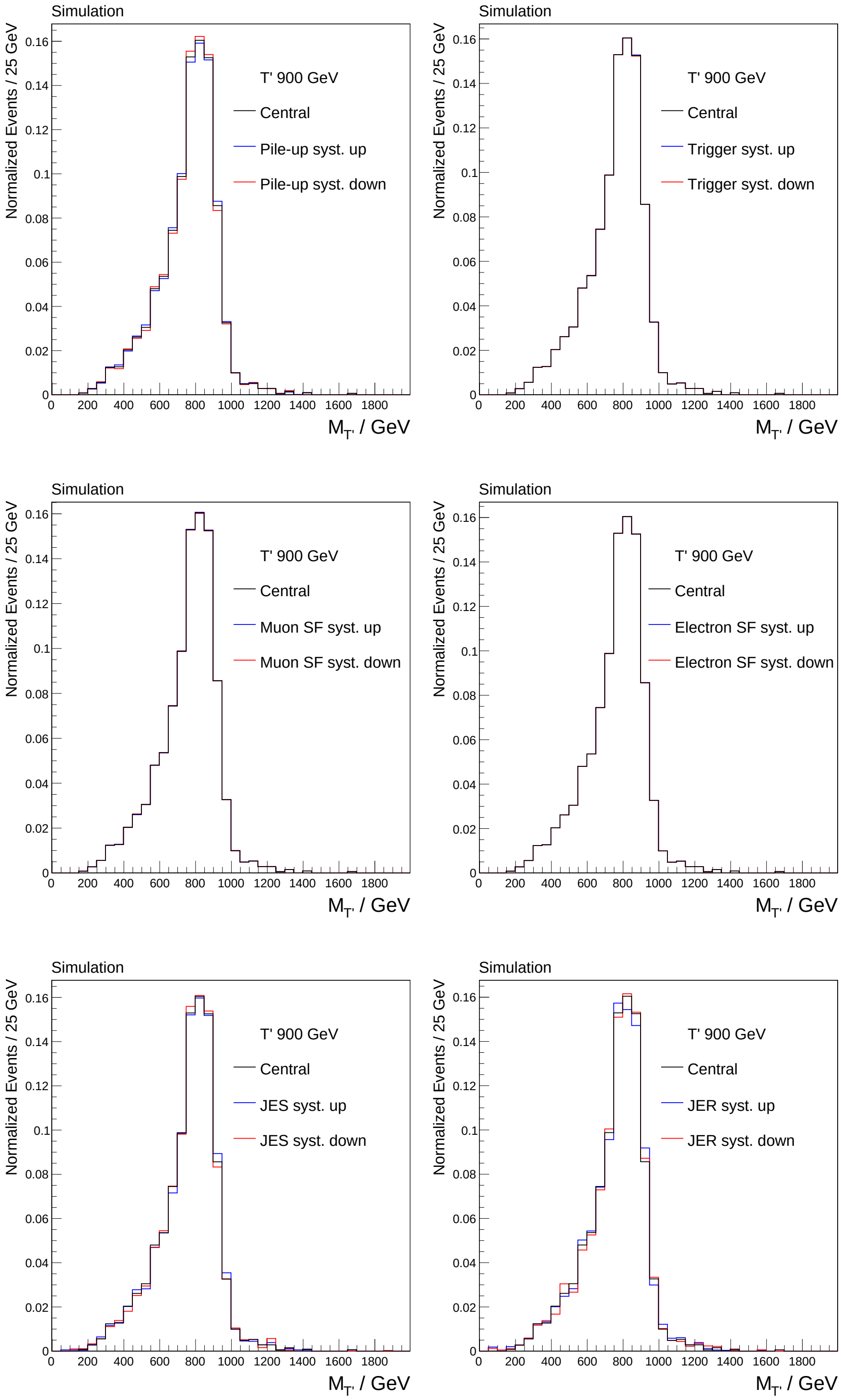

Figure H.22: Comparison of the projection on the $M_{T'}$ axis for $(60 < M_{W'} < 100)$ GeV in the T′ application with the pile-up scale factor (top left) shifted upwards (blue) and downwards (red) with respect to its nominal value (black) for the a T′ signal simulation samples. The same is also shown for the trigger (top right), the muon (middle left), the electron (middle right), the JES (bottom left) and the JER (bottom right) scale factors.

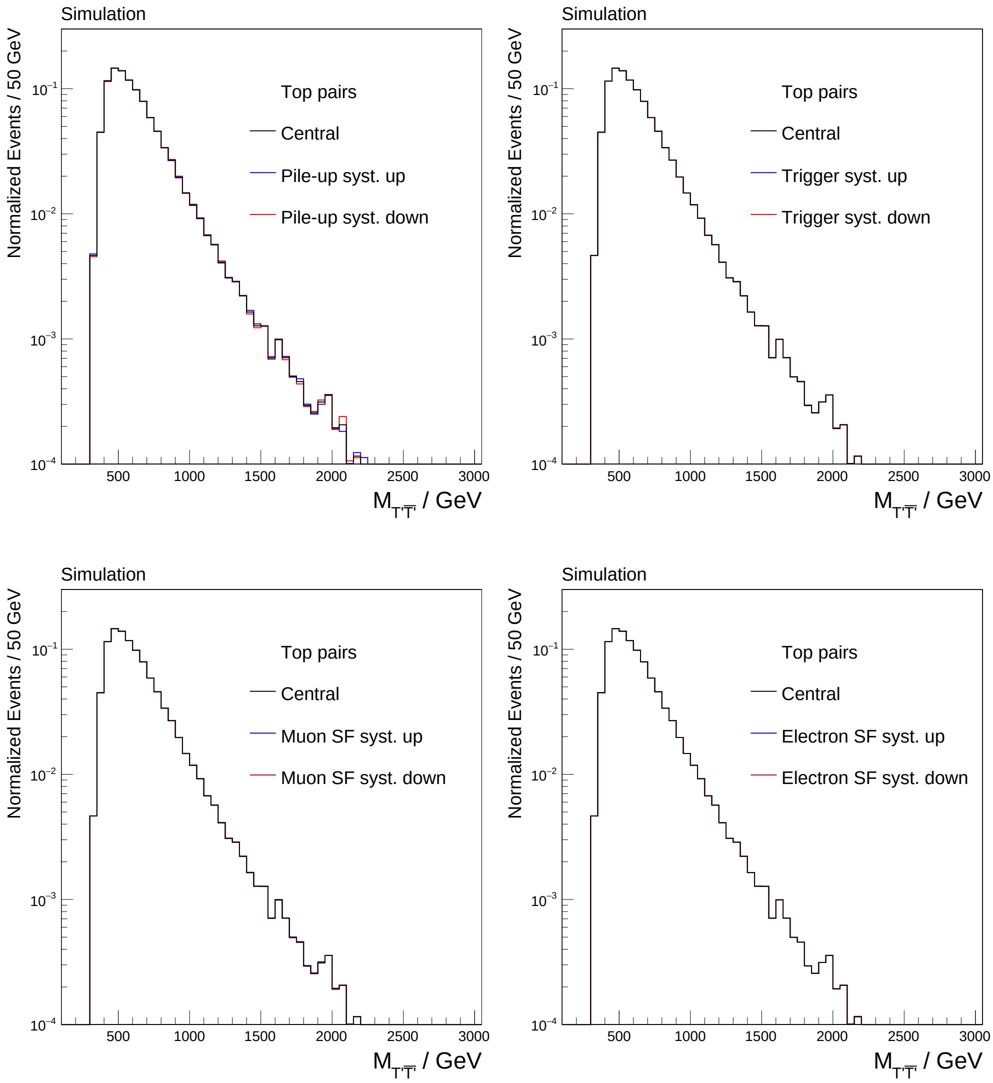

Figure H.23: Comparison of the $M_{T'\overline{T'}}$ invariant mass distribution for $(60 < M_{W'} < 100)$ GeV and $(150 < M_{T'} < 200)$ GeV in the Z' application with the pile-up scale factor (top left) shifted upwards (blue) and downwards (red) with respect to its nominal value (black) for the top pair simulation samples. The same is also shown for the trigger (top right), the muon (bottom left) and the electron (bottom right) scale factors.

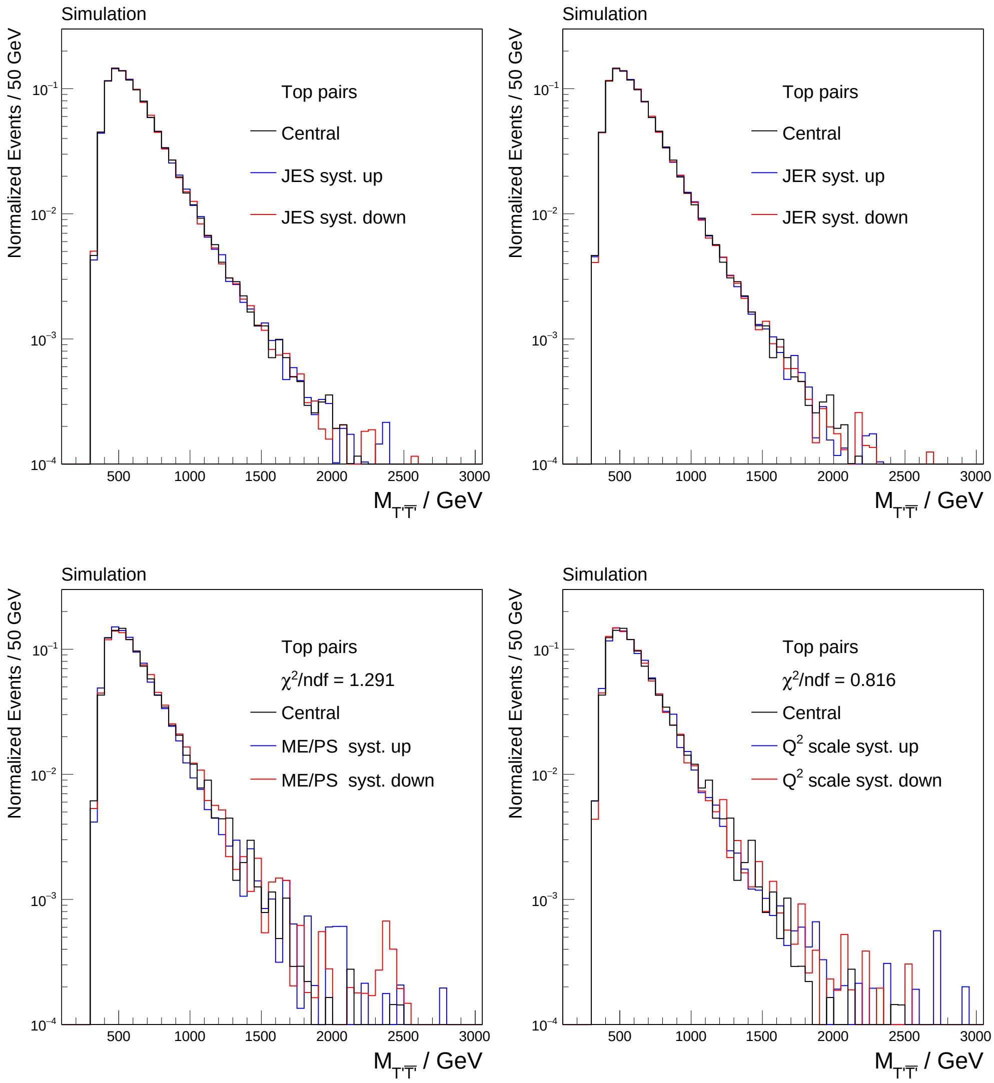

Figure H.24: Comparison of the $M_{T'\overline{T'}}$ invariant mass distribution for $(60 < M_{W'} < 100)$ GeV and $(150 < M_{T'} < 200)$ GeV in the Z' application with the JES scale factor (top left) shifted upwards (blue) and downwards (red) with respect to its nominal value (black) for the top pair simulation samples. The same is also shown for the JER (top right), the Q^2 (bottom left) and the ME/PS matching (bottom right) scales.

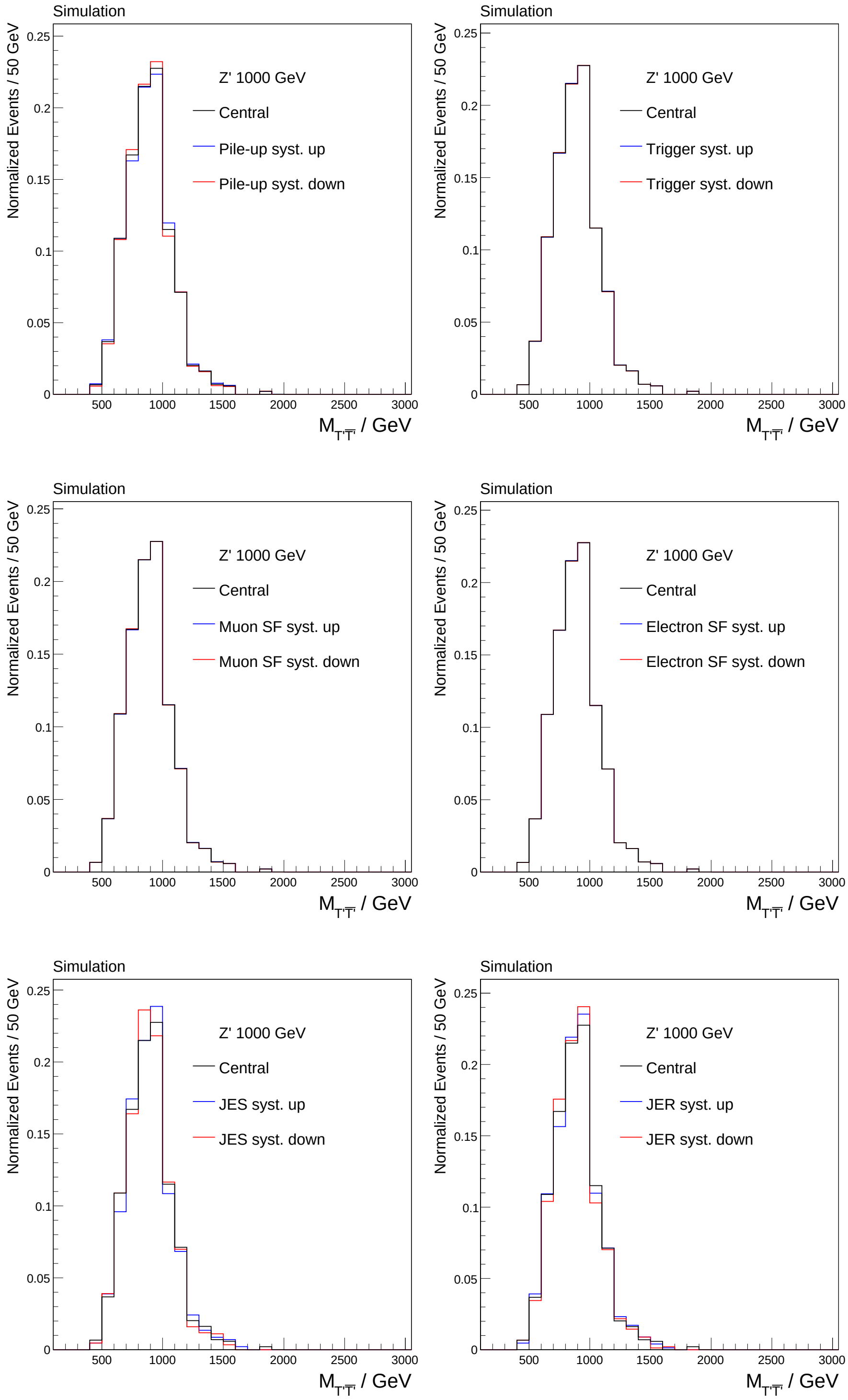

Figure H.25: Comparison of the $M_{T'\overline{T'}}$ invariant mass distribution for $(60 < M_{W'} < 100)$ GeV and $(150 < M_{T'} < 200)$ GeV in the Z' application with the pile-up scale factor (top left) shifted upwards (blue) and downwards (red) with respect to its nominal value (black) for the Z' signal simulation samples. The same is also shown for the trigger (top right), the muon (middle left), the electron (middle right), the JES (bottom left) and the JER (bottom right) scale factors.

Table H.7: Summary of all systematic uncertainties considered for the T′ search in the $e\mu$ channel. Each row is treated as a single independent nuisance parameter.

Source	T′ Signal	Top pairs	Z + jets	Single Top	Diboson
Luminosity	2.6%	2.6%	2.6%	2.6%	2.6%
Pile-up	0.9%	0.4%	1.2%	0.3%	2.8%
Trigger	1.4%	0.6%	0.4%	0.5%	0.7%
Lepton SF	2.5%	1.4%	1.2%	1.4%	1.5%
Jet energy scale	0.9%	1.4%	6.6%	1.9%	2.2%
Jet energy resolution	1.1%	0.3%	3.9%	1.3%	0.3%
Q^2 scale	-	2.4%	-	-	-
ME/PS threshold	-	2.1%	-	-	-
PDF	-	2.6%	-	-	-
Cross section	-	-	73.6%	50%	30%
Total Systematic	4.2%	5.3%	74.1%	50.1%	30.4%
Total Background Systematic	-	4.9%	1.3%	2.3%	0.4%

Table H.8: Summary of all systematic uncertainties considered for the Z′ search in the ee channel. Each row is treated as a single independent nuisance parameter.

Source	Z′ Signal	Top pairs	Z + jets	Single Top	Diboson
Luminosity	2.6%	2.6%	2.6%	2.6%	2.6%
Pile-up	5.8%	0.6%	4.3%	0.7%	4.3%
Trigger	1.1%	1.1%	1.1%	1.1%	1.1%
Lepton SF	1.3%	1.3%	1.4%	1.3%	1.3%
Jet energy scale	7.1%	1.8%	4.8%	7.0%	5.9%
Jet energy resolution	2.2%	0.4%	7.5%	0.5%	1.0%
Q^2 scale	-	4.3%	-	-	-
ME/PS threshold	-	0.5%	-	-	-
PDF	-	2.6%	-	-	-
Cross section	-	-	75.0%	50%	30%
Total Systematic	9.9%	6.2%	75.7%	50.6%	31.0%
Total Background Systematic	-	5.5%	6.5%	1.2%	0.3%

Table H.9: Summary of all systematic uncertainties considered for the Z′ search in the $\mu\mu$ channel. Each row is treated as a single independent nuisance parameter.

Source	Z′ Signal	Top pairs	Z + jets	Single Top	Diboson
Luminosity	2.6%	2.6%	2.6%	2.6%	2.6%
Pile-up	4.0%	0.1%	17.4%	1.5%	7.2%
Trigger	0.4%	0.3%	0.3%	0.3%	0.3%
Lepton SF	3.0%	1.4%	1.1%	1.4%	1.5%
Jet energy scale	3.5%	2.1%	2.1%	2.4%	3.8%
Jet energy resolution	5.2%	0.8%	11.3%	0.9%	0.6%
Q^2 scale	-	1.4%	-	-	-
ME/PS threshold	-	0.1%	-	-	-
PDF	-	2.6%	-	-	-
Cross section	-	-	72.1%	50%	30%
Total Systematic	8.4%	4.8%	75.1%	50.2%	31.2%
Total Background Systematic	-	4.3%	4.8%	1.5%	0.2%

Table H.10: Summary of all systematic uncertainties considered for the Z′ search in the $e\mu$ channel. Each row is treated as a single independent nuisance parameter.

Source	Z′ Signal	Top pairs	Z + jets	Single Top	Diboson
Luminosity	2.6%	2.6%	2.6%	2.6%	2.6%
Pile-up	4.0%	0.4%	1.7%	1.1%	3.1%
Trigger	1.3%	0.5%	0.3%	0.5%	0.5%
Lepton SF	2.1%	1.4%	1.2%	1.3%	1.3%
Jet energy scale	2.6%	1.5%	-	2.0%	2.0%
Jet energy resolution	1.9%	0.4%	-	0.8%	1.7%
Q^2 scale	-	0.6%	-	-	-
ME/PS threshold	-	2.7%	-	-	-
PDF	-	2.6%	-	-	-
Cross section	-	-	73.6%	50%	30%
Total Systematic	6.3%	5.1%	73.7%	50.1%	30.4%
Total Background Systematic	-	4.9%	0.1%	1.7%	0.2%

Table H.11: Summary of all systematic uncertainties considered for the two-dimensional search in the ee channel. Each row is treated as a single independent nuisance parameter.

Source	2D Signal	Top pairs	Z + jets	Single Top	Diboson
Luminosity	2.6%	2.6%	2.6%	2.6%	2.6%
Pile-up	1.1%	0.5%	5.2%	0.8%	2.6%
Trigger	1.1%	1.1%	1.1%	1.1%	1.1%
Lepton SF	1.3%	1.3%	1.3%	1.3%	1.3%
Jet energy scale	0.6%	1.3%	3.2%	3.1%	3.3%
Jet energy resolution	0.7%	0.2%	3.6%	1.2%	0.2%
Q^2 scale	-	8.1%	-	-	-
ME/PS threshold	-	2.2%	-	-	-
PDF	-	2.6%	-	-	-
Cross section	-	-	75.0%	50%	30%
Total Systematic	3.4%	9.5%	75.4%	50.2%	30.5%
Total Background Systematic	-	7.8%	9.6%	2.0%	0.5%

Table H.12: Summary of all systematic uncertainties considered for the two-dimensional search in the $\mu\mu$ channel. Each row is treated as a single independent nuisance parameter.

Source	2D Signal	Top pairs	Z + jets	Single Top	Diboson
Luminosity	2.6%	2.6%	2.6%	2.6%	2.6%
Pile-up	1.1%	0.2%	6.5%	0.4%	3.6%
Trigger	0.4%	0.3%	0.3%	0.3%	0.3%
Lepton SF	4.4%	1.5%	1.9%	1.8%	1.9%
Jet energy scale	0.6%	1.7%	2.9%	1.9%	1.3%
Jet energy resolution	0.4%	0.3%	6.1%	0.6%	0.3%
Q^2 scale	-	5.0%	-	-	-
ME/PS threshold	-	0.5%	-	-	-
PDF	-	2.6%	-	-	-
Cross section	-	-	72.1%	50%	30%
Total Systematic	5.3%	6.7%	72.8%	50.1%	30.4%
Total Background Systematic	-	5.4%	10.1%	2.2%	0.4%

Table H.13: Summary of all systematic uncertainties considered for the two-dimensional search in the $e\mu$ channel. Each row is treated as a single independent nuisance parameter.

Source	2D Signal	Top pairs	Z + jets	Single Top	Diboson
Luminosity	2.6%	2.6%	2.6%	2.6%	2.6%
Pile-up	0.6%	0.4%	2.2%	0.6%	2.5%
Trigger	1.8%	0.6%	0.6%	0.6%	0.7%
Lepton SF	2.8%	1.4%	1.4%	1.5%	1.5%
Jet energy scale	0.8%	1.4%	0.0%	1.4%	2.6%
Jet energy resolution	0.4%	0.3%	0.0%	0.7%	0.5%
Q^2 scale	-	3.9%	-	-	-
ME/PS threshold	-	2.5%	-	-	-
PDF	-	2.6%	-	-	-
Cross section	-	-	73.6%	50%	30%
Total Systematic	4.4%	6.3%	73.7%	50.1%	30.4%
Total Background Systematic	-	5.7%	1.9%	2.5%	0.4%

I Applications

Table I.14: Expected and observed upper limits in pb for the T′ search using all data.

		Expected		
T′ Mass [GeV]	Observed	Median	68% C.L. Range	95% C.L. Range
450	0.26	0.34	[0.25,0.48]	[0.19,0.65]
475	0.24	0.31	[0.22,0.44]	[0.17,0.59]
500	0.20	0.26	[0.19,0.37]	[0.14,0.49]
575	0.12	0.19	[0.14,0.27]	[0.10,0.37]
600	0.11	0.16	[0.11,0.22]	[0.08,0.30]
625	0.09	0.14	[0.10,0.20]	[0.08,0.28]
650	0.09	0.13	[0.09,0.18]	[0.07,0.24]
675	0.09	0.11	[0.08,0.16]	[0.06,0.21]
725	0.11	0.10	[0.07,0.14]	[0.05,0.20]
750	0.11	0.09	[0.06,0.12]	[0.04,0.17]
775	0.11	0.08	[0.06,0.12]	[0.04,0.16]
800	0.12	0.08	[0.06,0.12]	[0.04,0.16]
850	0.09	0.06	[0.04,0.09]	[0.03,0.12]
900	0.07	0.04	[0.03,0.07]	[0.02,0.09]
1400	0.02	0.01	[0.01,0.02]	[0.01,0.03]
1500	0.02	0.01	[0.01,0.02]	[0.00,0.03]

Table I.15: Expected and observed upper limits in pb for the T′ search in the *ee* channel.

		Expected		
T′ Mass [GeV]	Observed	Median	68% C.L. Range	95% C.L. Range
450	0.67	0.71	[0.50,1.01]	[0.38,1.38]
475	0.40	0.59	[0.41,0.84]	[0.30,1.16]
500	0.36	0.49	[0.35,0.71]	[0.26,0.98]
575	0.31	0.40	[0.28,0.57]	[0.21,0.79]
600	0.25	0.29	[0.20,0.42]	[0.15,0.58]
625	0.22	0.30	[0.21,0.44]	[0.15,0.61]
650	0.20	0.29	[0.20,0.41]	[0.15,0.57]
675	0.20	0.27	[0.19,0.40]	[0.14,0.55]
725	0.18	0.23	[0.16,0.34]	[0.12,0.47]
750	0.19	0.21	[0.14,0.31]	[0.10,0.44]
775	0.14	0.17	[0.12,0.26]	[0.08,0.37]
800	0.12	0.18	[0.12,0.26]	[0.09,0.37]
850	0.11	0.14	[0.09,0.21]	[0.07,0.30]
900	0.09	0.11	[0.07,0.17]	[0.05,0.25]
1400	0.06	0.03	[0.02,0.06]	[0.01,0.09]
1500	0.06	0.03	[0.02,0.06]	[0.01,0.10]

Table I.16: Expected and observed upper limits in pb for the T′ search in the $e\mu$ channel.

		Expected		
T′ Mass [GeV]	Observed	Median	68% C.L. Range	95% C.L. Range
450	0.38	0.46	[0.32,0.64]	[0.24,0.87]
475	0.42	0.46	[0.32,0.65]	[0.24,0.88]
500	0.32	0.35	[0.25,0.50]	[0.19,0.68]
575	0.20	0.28	[0.20,0.41]	[0.15,0.55]
600	0.17	0.25	[0.17,0.35]	[0.13,0.48]
625	0.13	0.20	[0.14,0.28]	[0.10,0.39]
650	0.17	0.17	[0.12,0.24]	[0.09,0.34]
675	0.19	0.14	[0.10,0.21]	[0.07,0.29]
725	0.23	0.14	[0.10,0.21]	[0.07,0.29]
750	0.20	0.12	[0.08,0.17]	[0.06,0.24]
775	0.20	0.11	[0.08,0.16]	[0.06,0.23]
800	0.22	0.11	[0.08,0.16]	[0.06,0.23]
850	0.18	0.08	[0.06,0.12]	[0.04,0.18]
900	0.14	0.06	[0.04,0.09]	[0.03,0.14]
1400	0.04	0.02	[0.01,0.04]	[0.01,0.06]
1500	0.03	0.02	[0.01,0.03]	[0.01,0.05]

Table I.17: Expected and observed upper limits in pb for the T′ search in the $\mu\mu$ channel.

T′ Mass [GeV]	Observed	Expected Median	Expected 68% C.L. Range	Expected 95% C.L. Range
450	0.64	0.66	[0.47,0.94]	[0.35,1.28]
475	0.48	0.56	[0.40,0.79]	[0.29,1.09]
500	0.55	0.53	[0.37,0.75]	[0.27,1.03]
575	0.35	0.33	[0.23,0.47]	[0.17,0.65]
600	0.30	0.27	[0.19,0.40]	[0.14,0.56]
625	0.27	0.26	[0.18,0.38]	[0.13,0.54]
650	0.23	0.24	[0.16,0.35]	[0.12,0.49]
675	0.24	0.21	[0.14,0.31]	[0.11,0.43]
725	0.21	0.17	[0.12,0.26]	[0.09,0.36]
750	0.19	0.14	[0.10,0.21]	[0.07,0.30]
775	0.24	0.16	[0.11,0.23]	[0.08,0.33]
800	0.23	0.17	[0.12,0.25]	[0.09,0.36]
850	0.14	0.11	[0.07,0.17]	[0.05,0.24]
900	0.10	0.09	[0.06,0.14]	[0.04,0.21]
1400	0.03	0.03	[0.02,0.06]	[0.01,0.10]
1500	0.02	0.03	[0.01,0.05]	[0.01,0.08]

Table I.18: Expected and observed upper limits in pb for the Z′ search using all data.

Z′ Mass [GeV]	Observed	Expected Median	Expected 68% C.L. Range	Expected 95% C.L. Range
500	38.66	14.91	[10.72,20.91]	[8.04,28.06]
750	1.03	2.51	[1.79,3.54]	[1.34,4.80]
1000	0.67	0.89	[0.64,1.26]	[0.47,1.71]
1250	0.46	0.42	[0.30,0.59]	[0.22,0.81]
1500	0.27	0.28	[0.20,0.41]	[0.14,0.56]
2000	0.15	0.17	[0.11,0.25]	[0.08,0.36]
3000	0.19	0.18	[0.11,0.30]	[0.07,0.47]

Table I.19: Expected and observed upper limits in pb for the Z′ search in the ee channel.

Z′ Mass [GeV]	Observed	Expected Median	Expected 68% C.L. Range	Expected 95% C.L. Range
500	49.49	20.69	[14.72,29.51]	[10.95,40.34]
750	2.12	4.70	[3.33,6.71]	[2.47,9.29]
1000	0.98	1.63	[1.15,2.34]	[0.85,3.23]
1250	0.88	0.83	[0.58,1.21]	[0.43,1.70]
1500	0.44	0.47	[0.32,0.71]	[0.23,1.02]
2000	0.19	0.25	[0.16,0.40]	[0.10,0.62]
3000	0.32	0.43	[0.25,0.72]	[0.16,1.15]

Table I.20: Expected and observed upper limits in pb for the Z′ search in the $e\mu$ channel.

		Expected		
Z′ Mass [GeV]	Observed	Median	68% C.L. Range	95% C.L. Range
500	21.42	17.44	[12.45,24.60]	[9.30,33.15]
750	2.32	3.17	[2.26,4.47]	[1.68,6.07]
1000	1.52	1.15	[0.82,1.63]	[0.61,2.23]
1250	0.66	0.56	[0.40,0.81]	[0.29,1.12]
1500	0.58	0.42	[0.29,0.61]	[0.21,0.86]
2000	0.32	0.24	[0.15,0.38]	[0.10,0.57]
3000	0.34	0.26	[0.15,0.45]	[0.09,0.74]

Table I.21: Expected and observed upper limits in pb for the Z′ search in the $\mu\mu$ channel.

		Expected		
Z′ Mass [GeV]	Observed	Median	68% C.L. Range	95% C.L. Range
500	56.92	32.91	[23.49,46.68]	[17.55,63.57]
750	2.02	4.08	[2.88,5.85]	[2.14,8.08]
1000	1.81	1.73	[1.21,2.50]	[0.89,3.48]
1250	1.01	0.81	[0.56,1.17]	[0.41,1.65]
1500	0.54	0.63	[0.43,0.95]	[0.31,1.36]
2000	0.28	0.44	[0.27,0.70]	[0.18,1.09]
3000	0.47	0.47	[0.27,0.83]	[0.16,1.39]

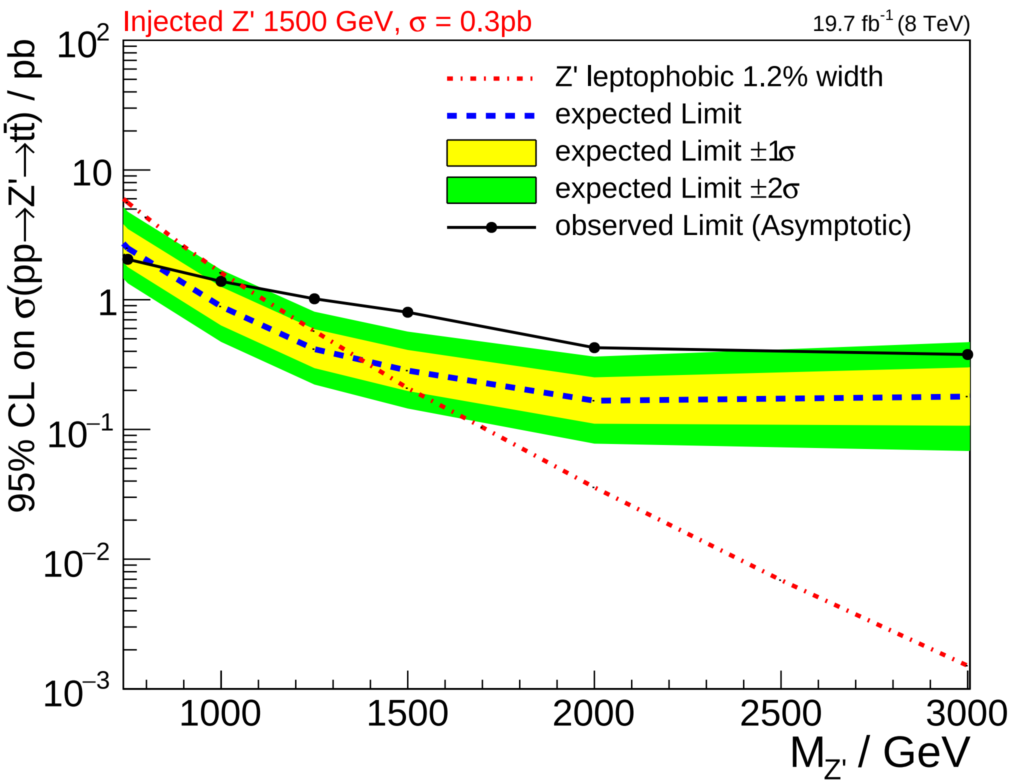

Figure I.26: The expected (blue dashed line) and observed (black solid line) 95% CL upper exclusion limits on $\sigma \cdot BR$ for a new heavy gauge boson Z′ with an injected signal of $M_{Z'}$ = 1500 GeV and a cross section σ of 0.3 pb in toy simulation studies compared to theoretical predictions (red dashed line) for a leptophobic Z′ [22, 23].

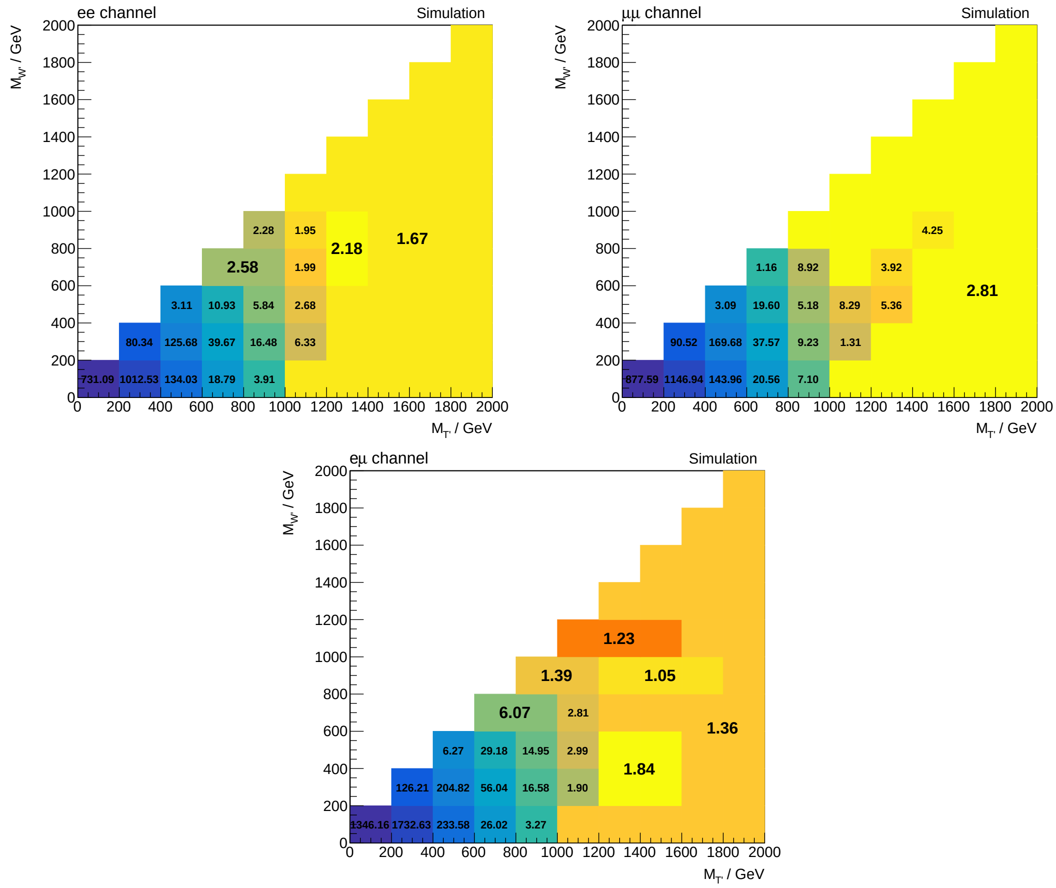

Figure I.27: Merging scheme with at least one entry per bin for the *ee* channel (top left), the $\mu\mu$ channel (top right) and the $e\mu$ channel (bottom). Bins with the same colour have been merged. The numbers represent the total number of expected events in each merged bin.

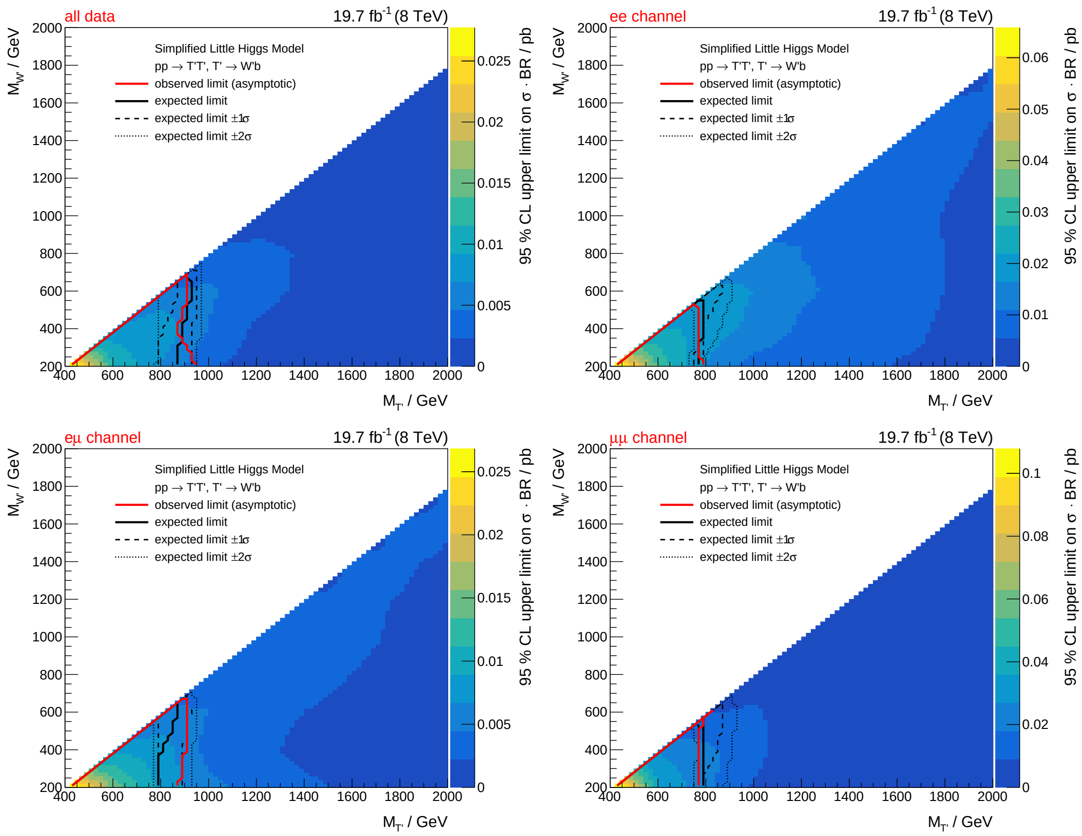

Figure I.28: Limits in the $(M_{T'}, M_{W'})$ mass plane for the full range of values considered.

Table I.22: Expected and observed upper limits in pb for the two-dimensional search using all data.

			Expected		
T' Mass [GeV]	W' Mass [GeV]	Observed	Median	68% C.L. Range	95% C.L. Range
400	200	0.0322	0.0446	[0.0324,0.0621]	[0.0243,0.0831]
600	200	0.0117	0.0192	[0.0138,0.0268]	[0.0104,0.0361]
600	400	0.0078	0.0113	[0.0081,0.0160]	[0.0061,0.0215]
800	200	0.0067	0.0088	[0.0063,0.0124]	[0.0047,0.0168]
800	400	0.0089	0.0071	[0.0051,0.0100]	[0.0038,0.0136]
800	600	0.0050	0.0053	[0.0038,0.0076]	[0.0028,0.0103]
1000	200	0.0026	0.0051	[0.0036,0.0073]	[0.0027,0.0100]
1000	400	0.0045	0.0050	[0.0036,0.0070]	[0.0027,0.0095]
1000	600	0.0050	0.0038	[0.0027,0.0055]	[0.0020,0.0075]
1000	800	0.0029	0.0034	[0.0024,0.0050]	[0.0018,0.0069]
1200	1000	0.0019	0.0022	[0.0015,0.0033]	[0.0011,0.0047]
1200	200	0.0014	0.0028	[0.0019,0.0041]	[0.0014,0.0058]
1200	400	0.0019	0.0034	[0.0024,0.0048]	[0.0018,0.0066]
1200	600	0.0032	0.0031	[0.0022,0.0045]	[0.0016,0.0062]
1200	800	0.0026	0.0025	[0.0017,0.0037]	[0.0013,0.0051]
1400	1000	0.0017	0.0018	[0.0013,0.0027]	[0.0009,0.0039]
1400	1200	0.0016	0.0016	[0.0011,0.0025]	[0.0008,0.0036]
1400	200	0.0010	0.0017	[0.0011,0.0025]	[0.0008,0.0037]
1400	400	0.0011	0.0020	[0.0013,0.0029]	[0.0010,0.0042]
1400	600	0.0018	0.0023	[0.0016,0.0034]	[0.0012,0.0047]
1400	800	0.0022	0.0021	[0.0015,0.0031]	[0.0011,0.0044]
1600	1000	0.0015	0.0017	[0.0011,0.0025]	[0.0008,0.0035]
1600	1200	0.0014	0.0014	[0.0010,0.0022]	[0.0007,0.0032]
1600	1400	0.0015	0.0014	[0.0009,0.0021]	[0.0006,0.0030]
1600	200	0.0008	0.0012	[0.0008,0.0019]	[0.0006,0.0028]
1600	400	0.0009	0.0013	[0.0009,0.0020]	[0.0006,0.0030]
1600	600	0.0012	0.0015	[0.0010,0.0023]	[0.0007,0.0033]
1600	800	0.0016	0.0016	[0.0011,0.0024]	[0.0008,0.0035]
1800	1000	0.0012	0.0012	[0.0008,0.0018]	[0.0006,0.0027]
1800	1200	0.0013	0.0012	[0.0008,0.0019]	[0.0006,0.0028]
1800	1400	0.0013	0.0012	[0.0008,0.0018]	[0.0006,0.0026]
1800	1600	0.0014	0.0012	[0.0008,0.0019]	[0.0006,0.0028]
1800	200	0.0008	0.0011	[0.0007,0.0017]	[0.0005,0.0025]
1800	400	0.0009	0.0011	[0.0008,0.0018]	[0.0005,0.0026]
1800	600	0.0011	0.0011	[0.0008,0.0018]	[0.0005,0.0026]
1800	800	0.0012	0.0011	[0.0008,0.0018]	[0.0005,0.0026]
2000	1000	0.0010	0.0009	[0.0006,0.0014]	[0.0004,0.0021]
2000	1200	0.0011	0.0009	[0.0006,0.0015]	[0.0004,0.0022]
2000	1400	0.0011	0.0010	[0.0007,0.0016]	[0.0005,0.0023]
2000	1600	0.0012	0.0010	[0.0007,0.0016]	[0.0005,0.0024]
2000	1800	0.0013	0.0011	[0.0007,0.0017]	[0.0005,0.0025]
2000	200	0.0007	0.0010	[0.0006,0.0015]	[0.0005,0.0023]
2000	400	0.0008	0.0010	[0.0006,0.0015]	[0.0005,0.0023]
2000	600	0.0010	0.0010	[0.0007,0.0016]	[0.0005,0.0023]
2000	800	0.0011	0.0010	[0.0006,0.0015]	[0.0004,0.0023]

Table I.23: Expected and observed upper limits in pb for the two-dimensional search in the *ee* channel.

			Expected		
T' Mass [GeV]	W' Mass [GeV]	Observed	Median	68% C.L. Range	95% C.L. Range
400	200	0.0757	0.0925	[0.0663,0.1290]	[0.0497,0.1737]
600	200	0.0319	0.0431	[0.0308,0.0608]	[0.0231,0.0819]
600	400	0.0238	0.0240	[0.0171,0.0342]	[0.0127,0.0465]
800	200	0.0162	0.0215	[0.0153,0.0307]	[0.0114,0.0417]
800	400	0.0196	0.0153	[0.0109,0.0220]	[0.0080,0.0301]
800	600	0.0207	0.0112	[0.0078,0.0162]	[0.0058,0.0227]
1000	200	0.0083	0.0141	[0.0099,0.0203]	[0.0073,0.0283]
1000	400	0.0150	0.0126	[0.0088,0.0181]	[0.0065,0.0250]
1000	600	0.0163	0.0088	[0.0061,0.0129]	[0.0045,0.0183]
1000	800	0.0147	0.0079	[0.0054,0.0117]	[0.0039,0.0168]
1200	1000	0.0111	0.0067	[0.0046,0.0101]	[0.0033,0.0146]
1200	200	0.0080	0.0087	[0.0059,0.0130]	[0.0043,0.0187]
1200	400	0.0099	0.0083	[0.0058,0.0122]	[0.0042,0.0173]
1200	600	0.0120	0.0070	[0.0049,0.0104]	[0.0035,0.0149]
1200	800	0.0108	0.0066	[0.0046,0.0099]	[0.0033,0.0141]
1400	1000	0.0081	0.0057	[0.0039,0.0084]	[0.0028,0.0119]
1400	1200	0.0083	0.0055	[0.0037,0.0083]	[0.0026,0.0121]
1400	200	0.0063	0.0051	[0.0034,0.0079]	[0.0024,0.0119]
1400	400	0.0072	0.0052	[0.0035,0.0080]	[0.0025,0.0119]
1400	600	0.0092	0.0057	[0.0038,0.0085]	[0.0028,0.0124]
1400	800	0.0093	0.0059	[0.0041,0.0088]	[0.0030,0.0125]
1600	1000	0.0069	0.0045	[0.0030,0.0068]	[0.0022,0.0098]
1600	1200	0.0074	0.0050	[0.0034,0.0076]	[0.0024,0.0110]
1600	1400	0.0073	0.0047	[0.0031,0.0073]	[0.0022,0.0107]
1600	200	0.0053	0.0038	[0.0025,0.0060]	[0.0018,0.0091]
1600	400	0.0059	0.0039	[0.0026,0.0062]	[0.0018,0.0093]
1600	600	0.0065	0.0040	[0.0027,0.0063]	[0.0019,0.0094]
1600	800	0.0069	0.0043	[0.0029,0.0066]	[0.0020,0.0097]
1800	1000	0.0053	0.0034	[0.0023,0.0053]	[0.0016,0.0080]
1800	1200	0.0057	0.0037	[0.0024,0.0057]	[0.0017,0.0085]
1800	1400	0.0063	0.0041	[0.0027,0.0063]	[0.0019,0.0094]
1800	1600	0.0069	0.0044	[0.0029,0.0069]	[0.0021,0.0103]
1800	200	0.0053	0.0036	[0.0024,0.0057]	[0.0017,0.0087]
1800	400	0.0052	0.0035	[0.0023,0.0055]	[0.0016,0.0083]
1800	600	0.0054	0.0034	[0.0022,0.0053]	[0.0015,0.0080]
1800	800	0.0054	0.0034	[0.0022,0.0053]	[0.0016,0.0080]
2000	1000	0.0044	0.0028	[0.0018,0.0044]	[0.0013,0.0066]
2000	1200	0.0048	0.0031	[0.0020,0.0049]	[0.0014,0.0074]
2000	1400	0.0051	0.0033	[0.0022,0.0052]	[0.0015,0.0078]
2000	1600	0.0056	0.0037	[0.0024,0.0058]	[0.0017,0.0087]
2000	1800	0.0060	0.0040	[0.0026,0.0063]	[0.0019,0.0095]
2000	200	0.0050	0.0033	[0.0022,0.0053]	[0.0015,0.0080]
2000	400	0.0048	0.0031	[0.0020,0.0049]	[0.0014,0.0075]
2000	600	0.0046	0.0029	[0.0019,0.0046]	[0.0013,0.0071]
2000	800	0.0047	0.0030	[0.0019,0.0047]	[0.0014,0.0071]

Table I.24: Expected and observed upper limits in pb for the two-dimensional search in the $\mu\mu$ channel.

			Expected		
T′ Mass [GeV]	W′ Mass [GeV]	Observed	Median	68% C.L. Range	95% C.L. Range
400	200	0.1268	0.0813	[0.0586,0.1140]	[0.0440,0.1530]
600	200	0.0371	0.0348	[0.0249,0.0491]	[0.0186,0.0661]
600	400	0.0255	0.0233	[0.0166,0.0330]	[0.0124,0.0449]
800	200	0.0208	0.0162	[0.0114,0.0232]	[0.0085,0.0320]
800	400	0.0207	0.0128	[0.0090,0.0184]	[0.0067,0.0254]
800	600	0.0087	0.0112	[0.0078,0.0162]	[0.0058,0.0226]
1000	200	0.0081	0.0091	[0.0063,0.0134]	[0.0046,0.0190]
1000	400	0.0112	0.0084	[0.0058,0.0122]	[0.0043,0.0172]
1000	600	0.0099	0.0072	[0.0050,0.0106]	[0.0036,0.0151]
1000	800	0.0051	0.0075	[0.0052,0.0111]	[0.0038,0.0156]
1200	1000	0.0035	0.0048	[0.0032,0.0074]	[0.0023,0.0108]
1200	200	0.0036	0.0056	[0.0038,0.0085]	[0.0027,0.0124]
1200	400	0.0041	0.0062	[0.0042,0.0093]	[0.0030,0.0134]
1200	600	0.0055	0.0066	[0.0045,0.0096]	[0.0033,0.0135]
1200	800	0.0049	0.0051	[0.0035,0.0078]	[0.0025,0.0113]
1400	1000	0.0032	0.0040	[0.0027,0.0062]	[0.0019,0.0091]
1400	1200	0.0029	0.0037	[0.0025,0.0058]	[0.0018,0.0087]
1400	200	0.0029	0.0043	[0.0029,0.0067]	[0.0021,0.0098]
1400	400	0.0029	0.0050	[0.0034,0.0075]	[0.0024,0.0109]
1400	600	0.0030	0.0054	[0.0038,0.0080]	[0.0027,0.0113]
1400	800	0.0033	0.0050	[0.0034,0.0074]	[0.0025,0.0107]
1600	1000	0.0024	0.0039	[0.0026,0.0058]	[0.0019,0.0085]
1600	1200	0.0025	0.0033	[0.0022,0.0052]	[0.0016,0.0077]
1600	1400	0.0026	0.0033	[0.0022,0.0051]	[0.0015,0.0077]
1600	200	0.0026	0.0038	[0.0025,0.0058]	[0.0018,0.0087]
1600	400	0.0026	0.0039	[0.0026,0.0059]	[0.0018,0.0088]
1600	600	0.0024	0.0040	[0.0027,0.0061]	[0.0020,0.0089]
1600	800	0.0025	0.0044	[0.0030,0.0066]	[0.0022,0.0096]
1800	1000	0.0022	0.0035	[0.0023,0.0053]	[0.0017,0.0078]
1800	1200	0.0022	0.0033	[0.0022,0.0051]	[0.0016,0.0075]
1800	1400	0.0022	0.0030	[0.0020,0.0046]	[0.0014,0.0069]
1800	1600	0.0025	0.0031	[0.0020,0.0048]	[0.0014,0.0073]
1800	200	0.0025	0.0033	[0.0022,0.0052]	[0.0016,0.0078]
1800	400	0.0024	0.0034	[0.0023,0.0053]	[0.0016,0.0079]
1800	600	0.0022	0.0033	[0.0022,0.0050]	[0.0015,0.0075]
1800	800	0.0022	0.0034	[0.0022,0.0052]	[0.0016,0.0077]
2000	1000	0.0021	0.0030	[0.0020,0.0046]	[0.0014,0.0070]
2000	1200	0.0021	0.0030	[0.0020,0.0046]	[0.0014,0.0069]
2000	1400	0.0022	0.0031	[0.0021,0.0048]	[0.0015,0.0072]
2000	1600	0.0022	0.0029	[0.0019,0.0046]	[0.0014,0.0069]
2000	1800	0.0025	0.0031	[0.0021,0.0049]	[0.0015,0.0074]
2000	200	0.0024	0.0032	[0.0021,0.0050]	[0.0015,0.0074]
2000	400	0.0022	0.0030	[0.0020,0.0047]	[0.0014,0.0070]
2000	600	0.0021	0.0031	[0.0020,0.0047]	[0.0014,0.0071]
2000	800	0.0021	0.0030	[0.0020,0.0047]	[0.0014,0.0070]

Table I.25: Expected and observed upper limits in pb for the two-dimensional search in the $e\mu$ channel.

			Expected		
T′ Mass [GeV]	W′ Mass [GeV]	Observed	Median	68% C.L. Range	95% C.L. Range
400	200	0.0305	0.0564	[0.0403,0.0791]	[0.0302,0.1062]
600	200	0.0149	0.0253	[0.0181,0.0356]	[0.0136,0.0480]
600	400	0.0086	0.0152	[0.0108,0.0214]	[0.0080,0.0293]
800	200	0.0082	0.0114	[0.0081,0.0163]	[0.0061,0.0223]
800	400	0.0078	0.0103	[0.0074,0.0146]	[0.0055,0.0198]
800	600	0.0053	0.0076	[0.0053,0.0110]	[0.0040,0.0152]
1000	200	0.0050	0.0061	[0.0042,0.0089]	[0.0031,0.0127]
1000	400	0.0037	0.0064	[0.0046,0.0092]	[0.0034,0.0126]
1000	600	0.0045	0.0059	[0.0042,0.0085]	[0.0031,0.0118]
1000	800	0.0039	0.0047	[0.0033,0.0070]	[0.0024,0.0099]
1200	1000	0.0031	0.0034	[0.0023,0.0051]	[0.0016,0.0075]
1200	200	0.0036	0.0037	[0.0025,0.0056]	[0.0018,0.0081]
1200	400	0.0026	0.0039	[0.0026,0.0058]	[0.0019,0.0083]
1200	600	0.0029	0.0040	[0.0028,0.0059]	[0.0020,0.0084]
1200	800	0.0038	0.0037	[0.0026,0.0056]	[0.0019,0.0079]
1400	1000	0.0029	0.0027	[0.0018,0.0041]	[0.0013,0.0061]
1400	1200	0.0027	0.0028	[0.0019,0.0043]	[0.0014,0.0062]
1400	200	0.0025	0.0028	[0.0019,0.0042]	[0.0013,0.0062]
1400	400	0.0018	0.0027	[0.0018,0.0041]	[0.0013,0.0060]
1400	600	0.0022	0.0028	[0.0019,0.0043]	[0.0014,0.0062]
1400	800	0.0029	0.0027	[0.0018,0.0041]	[0.0013,0.0060]
1600	1000	0.0024	0.0022	[0.0015,0.0034]	[0.0010,0.0050]
1600	1200	0.0023	0.0023	[0.0015,0.0034]	[0.0011,0.0050]
1600	1400	0.0028	0.0025	[0.0017,0.0038]	[0.0012,0.0056]
1600	200	0.0020	0.0023	[0.0015,0.0035]	[0.0011,0.0053]
1600	400	0.0016	0.0021	[0.0014,0.0033]	[0.0010,0.0049]
1600	600	0.0017	0.0021	[0.0014,0.0033]	[0.0010,0.0048]
1600	800	0.0022	0.0021	[0.0014,0.0033]	[0.0010,0.0049]
1800	1000	0.0021	0.0019	[0.0012,0.0029]	[0.0009,0.0044]
1800	1200	0.0022	0.0019	[0.0013,0.0030]	[0.0009,0.0044]
1800	1400	0.0023	0.0020	[0.0013,0.0031]	[0.0009,0.0046]
1800	1600	0.0028	0.0023	[0.0015,0.0036]	[0.0011,0.0054]
1800	200	0.0021	0.0020	[0.0013,0.0031]	[0.0009,0.0047]
1800	400	0.0019	0.0020	[0.0013,0.0031]	[0.0009,0.0046]
1800	600	0.0019	0.0019	[0.0012,0.0029]	[0.0009,0.0044]
1800	800	0.0020	0.0019	[0.0012,0.0029]	[0.0009,0.0043]
2000	1000	0.0020	0.0016	[0.0011,0.0025]	[0.0007,0.0038]
2000	1200	0.0020	0.0017	[0.0011,0.0026]	[0.0008,0.0039]
2000	1400	0.0021	0.0017	[0.0011,0.0027]	[0.0008,0.0041]
2000	1600	0.0023	0.0018	[0.0012,0.0029]	[0.0009,0.0043]
2000	1800	0.0027	0.0021	[0.0014,0.0033]	[0.0010,0.0049]
2000	200	0.0021	0.0018	[0.0012,0.0028]	[0.0008,0.0043]
2000	400	0.0019	0.0017	[0.0011,0.0027]	[0.0008,0.0041]
2000	600	0.0019	0.0017	[0.0011,0.0027]	[0.0008,0.0041]
2000	800	0.0020	0.0017	[0.0011,0.0026]	[0.0008,0.0040]

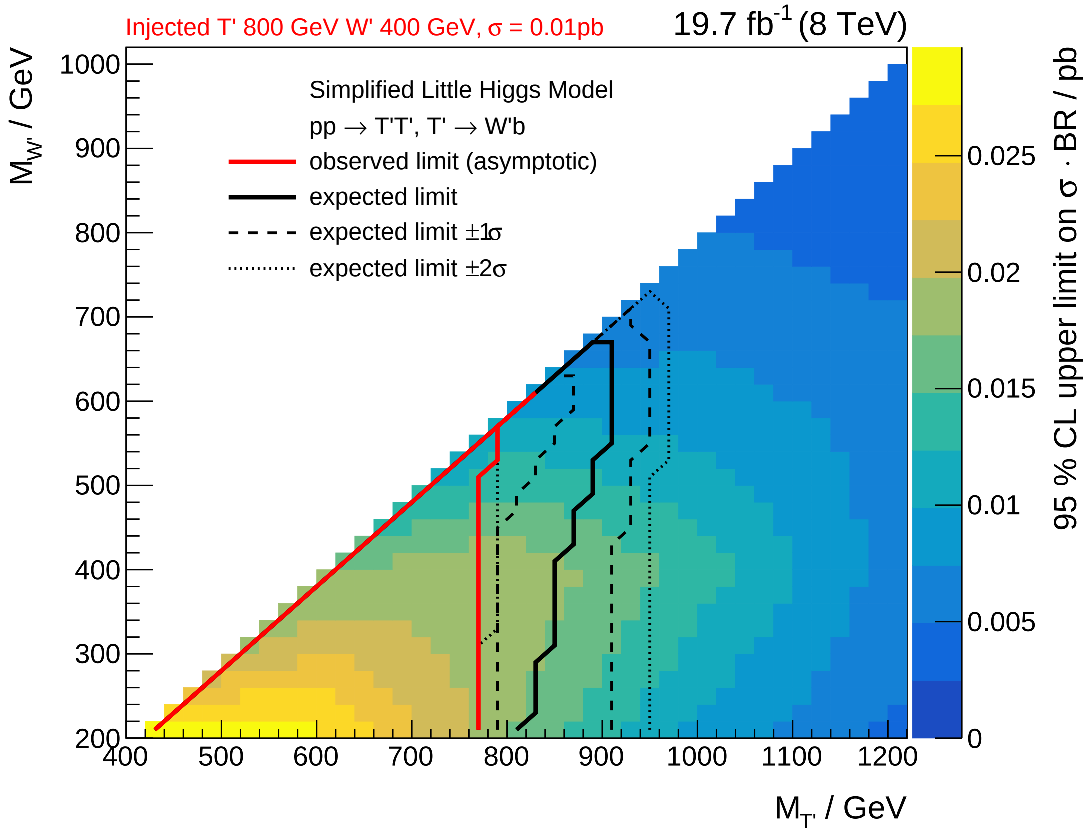

Figure I.29: The expected and observed 95% CL upper exclusion limits on $\sigma \cdot BR$ for a new heavy top quark partner T′ and a new heavy gauge boson W′ with an injected signal of $M_{T'}$ = 800 GeV and $M_{W'}$ = 400 GeV and a cross section σ of 0.01 pb in toy simulation studies compared to LO calculations [157, 158]. The strength of the observed 95% CL upper limit on the cross section $\sigma \cdot BR$ per $M_{T'}$ and $M_{W'}$ is given by the color coding.

J Selection efficiency times Acceptance

Table J.26: Selection efficiency times acceptance $\epsilon\cdot$A and its statistical uncertainty for all generated inclusive vector-like T′ quark samples. The branching fraction for the T′ quark to decay into bW is set to 100%. The SM W boson branching ratios are included in the acceptance.

	ee	$\mu\mu$	$e\mu$	combined
T′ Mass [GeV]	$\epsilon\cdot$A [%]	$\epsilon\cdot$A [%]	$\epsilon\cdot$A [%]	$\epsilon\cdot$A [%]
450	0.27 ± 0.02	0.31 ± 0.02	0.52 ± 0.02	1.10 ± 0.03
475	0.28 ± 0.02	0.34 ± 0.02	0.52 ± 0.02	1.14 ± 0.03
500	0.31 ± 0.02	0.33 ± 0.02	0.61 ± 0.02	1.25 ± 0.04
575	0.31 ± 0.02	0.39 ± 0.02	0.60 ± 0.02	1.30 ± 0.04
600	0.37 ± 0.02	0.41 ± 0.02	0.61 ± 0.02	1.38 ± 0.04
625	0.35 ± 0.02	0.41 ± 0.02	0.68 ± 0.03	1.44 ± 0.04
650	0.37 ± 0.02	0.40 ± 0.02	0.75 ± 0.03	1.53 ± 0.04
675	0.37 ± 0.02	0.42 ± 0.02	0.76 ± 0.03	1.55 ± 0.04
725	0.40 ± 0.02	0.44 ± 0.02	0.72 ± 0.03	1.57 ± 0.04
750	0.37 ± 0.02	0.50 ± 0.02	0.82 ± 0.03	1.70 ± 0.04
775	0.43 ± 0.02	0.45 ± 0.02	0.81 ± 0.03	1.68 ± 0.04
800	0.41 ± 0.02	0.41 ± 0.02	0.75 ± 0.03	1.58 ± 0.04
850	0.42 ± 0.02	0.52 ± 0.02	0.87 ± 0.03	1.81 ± 0.04
900	0.44 ± 0.02	0.50 ± 0.02	0.87 ± 0.03	1.81 ± 0.04
1400	0.51 ± 0.02	0.52 ± 0.02	1.03 ± 0.03	2.07 ± 0.05
1500	0.48 ± 0.02	0.56 ± 0.02	0.98 ± 0.03	2.02 ± 0.04

Table J.27: Selection efficiency times acceptance $\epsilon{\cdot}$A and its statistical uncertainty for all generated inclusive Z′ resonance samples. The branching fraction for the Z′ quark to decay into top pairs is set to 100%. The SM W boson branching ratios are included in the acceptance.

	ee	$\mu\mu$	$e\mu$	combined
Z′ Mass [GeV]	$\epsilon{\cdot}$A [%]	$\epsilon{\cdot}$A [%]	$\epsilon{\cdot}$A [%]	$\epsilon{\cdot}$A [%]
500	0.02 ± 0.00	0.03 ± 0.01	0.03 ± 0.01	0.07 ± 0.01
750	0.06 ± 0.01	0.13 ± 0.01	0.13 ± 0.01	0.27 ± 0.02
1000	0.13 ± 0.01	0.23 ± 0.01	0.23 ± 0.01	0.47 ± 0.02
1250	0.15 ± 0.01	0.27 ± 0.02	0.27 ± 0.02	0.57 ± 0.02
1500	0.16 ± 0.01	0.25 ± 0.01	0.25 ± 0.01	0.53 ± 0.01
2000	0.14 ± 0.01	0.19 ± 0.01	0.19 ± 0.01	0.42 ± 0.02
3000	0.06 ± 0.01	0.10 ± 0.01	0.10 ± 0.01	0.21 ± 0.02

Table J.28: Selection efficiency times acceptance ϵ·A and its statistical uncertainty for all 45 generated simplified Littlest Higgs samples in the combined channel. The branching fraction for the T′ quark to decay into bW′ is set to 100%. Here only decays of W′ to μ or e are considered.

T′ Mass [GeV]	W′ Mass [GeV]	ϵ·A [%]	T′ Mass [GeV]	W′ Mass [GeV]	ϵ·A [%]
400	200	31.5 ± 0.2	1600	600	58.7 ± 0.2
600	200	39.0 ± 0.2	1600	800	59.1 ± 0.2
600	400	46.8 ± 0.2	1600	1000	58.7 ± 0.2
800	200	43.3 ± 0.2	1600	1200	57.6 ± 0.2
800	400	53.9 ± 0.2	1600	1400	53.1 ± 0.2
800	600	51.6 ± 0.2	1800	200	51.7 ± 0.2
1000	200	45.7 ± 0.2	1800	400	55.0 ± 0.2
1000	400	55.2 ± 0.2	1800	600	57.8 ± 0.2
1000	600	57.1 ± 0.2	1800	800	58.5 ± 0.2
1000	800	53.1 ± 0.2	1800	1000	58.5 ± 0.2
1200	200	49.0 ± 0.2	1800	1200	57.9 ± 0.2
1200	400	55.5 ± 0.2	1800	1400	56.5 ± 0.2
1200	600	58.3 ± 0.2	1800	1600	50.3 ± 0.2
1200	800	57.8 ± 0.2	2000	200	51.8 ± 0.2
1200	1000	52.3 ± 0.2	2000	400	55.7 ± 0.2
1400	200	50.5 ± 0.2	2000	600	57.3 ± 0.2
1400	400	55.3 ± 0.2	2000	800	57.5 ± 0.2
1400	600	58.6 ± 0.2	2000	1000	59.1 ± 0.2
1400	800	59.0 ± 0.2	2000	1200	57.6 ± 0.2
1400	1000	57.9 ± 0.2	2000	1400	55.8 ± 0.2
1400	1200	53.5 ± 0.2	2000	1600	54.3 ± 0.2
1600	200	52.1 ± 0.2	2000	1800	49.6 ± 0.2
1600	400	55.4 ± 0.2			

Table J.29: Selection efficiency times acceptance $\epsilon\cdot$A and its statistical uncertainty for all 45 generated simplified Littlest Higgs samples in the ee channel. The branching fraction for the T′ quark to decay into bW′ is set to 100%. Here only decays of W′ to μ or e are considered.

T′ Mass [GeV]	W′ Mass [GeV]	$\epsilon\cdot$A [%]	T′ Mass [GeV]	W′ Mass [GeV]	$\epsilon\cdot$A [%]
400	200	7.3 ± 0.1	1600	600	13.5 ± 0.2
600	200	8.8 ± 0.1	1600	800	14.1 ± 0.2
600	400	11.3 ± 0.1	1600	1000	14.2 ± 0.2
800	200	10.1 ± 0.1	1600	1200	13.2 ± 0.2
800	400	13.0 ± 0.2	1600	1400	12.4 ± 0.1
800	600	12.7 ± 0.1	1800	200	12.2 ± 0.1
1000	200	10.8 ± 0.1	1800	400	12.9 ± 0.2
1000	400	12.4 ± 0.1	1800	600	13.6 ± 0.2
1000	600	13.8 ± 0.2	1800	800	13.7 ± 0.2
1000	800	12.6 ± 0.1	1800	1000	14.3 ± 0.2
1200	200	11.0 ± 0.1	1800	1200	13.6 ± 0.2
1200	400	13.3 ± 0.2	1800	1400	13.1 ± 0.2
1200	600	14.2 ± 0.2	1800	1600	11.9 ± 0.1
1200	800	14.2 ± 0.2	2000	200	12.1 ± 0.1
1200	1000	12.1 ± 0.1	2000	400	13.3 ± 0.2
1400	200	11.8 ± 0.1	2000	600	14.0 ± 0.2
1400	400	13.6 ± 0.2	2000	800	14.1 ± 0.2
1400	600	14.1 ± 0.2	2000	1000	15.0 ± 0.2
1400	800	13.9 ± 0.2	2000	1200	13.7 ± 0.2
1400	1000	14.3 ± 0.2	2000	1400	13.5 ± 0.2
1400	1200	12.5 ± 0.1	2000	1600	12.5 ± 0.1
1600	200	12.6 ± 0.1	2000	1800	11.5 ± 0.1
1600	400	12.9 ± 0.1			

Table J.30: Selection efficiency times acceptance ϵ·A and its statistical uncertainty for all 45 generated simplified Littlest Higgs samples in the $e\mu$ channel. The branching fraction for the T′ quark to decay into bW′ is set to 100%. Here only decays of W′ to μ or e are considered.

T′ Mass [GeV]	W′ Mass [GeV]	ϵ·A [%]	T′ Mass [GeV]	W′ Mass [GeV]	ϵ·A [%]
400	200	15.3 ± 0.2	1600	600	28.1 ± 0.2
600	200	18.8 ± 0.2	1600	800	28.2 ± 0.2
600	400	22.4 ± 0.2	1600	1000	27.3 ± 0.2
800	200	21.0 ± 0.2	1600	1200	27.8 ± 0.2
800	400	25.7 ± 0.2	1600	1400	25.0 ± 0.2
800	600	24.3 ± 0.2	1800	200	24.8 ± 0.2
1000	200	21.8 ± 0.2	1800	400	26.3 ± 0.2
1000	400	27.3 ± 0.2	1800	600	27.3 ± 0.2
1000	600	26.9 ± 0.2	1800	800	27.8 ± 0.2
1000	800	25.5 ± 0.2	1800	1000	27.4 ± 0.2
1200	200	23.2 ± 0.2	1800	1200	27.1 ± 0.2
1200	400	26.4 ± 0.2	1800	1400	27.0 ± 0.2
1200	600	27.8 ± 0.2	1800	1600	23.6 ± 0.2
1200	800	27.5 ± 0.2	2000	200	25.0 ± 0.2
1200	1000	24.9 ± 0.2	2000	400	26.5 ± 0.2
1400	200	23.7 ± 0.2	2000	600	26.7 ± 0.2
1400	400	26.2 ± 0.2	2000	800	26.9 ± 0.2
1400	600	27.8 ± 0.2	2000	1000	27.6 ± 0.2
1400	800	28.4 ± 0.2	2000	1200	27.3 ± 0.2
1400	1000	27.5 ± 0.2	2000	1400	26.4 ± 0.2
1400	1200	25.7 ± 0.2	2000	1600	26.2 ± 0.2
1600	200	24.7 ± 0.2	2000	1800	23.8 ± 0.2
1600	400	26.6 ± 0.2			

Table J.31: Selection efficiency times acceptance ϵ·A and its statistical uncertainty for all 45 generated simplified Littlest Higgs samples in the $\mu\mu$ channel. The branching fraction for the T′ quark to decay into bW′ is set to 100%. Here only decays of W′ to μ or e are considered.

T′ Mass [GeV]	W′ Mass [GeV]	ϵ·A [%]	T′ Mass [GeV]	W′ Mass [GeV]	ϵ·A [%]
400	200	8.9 ± 0.1	1600	600	17.1 ± 0.2
600	200	11.4 ± 0.1	1600	800	16.7 ± 0.2
600	400	13.1 ± 0.2	1600	1000	17.2 ± 0.2
800	200	12.2 ± 0.1	1600	1200	16.6 ± 0.2
800	400	15.3 ± 0.2	1600	1400	15.6 ± 0.2
800	600	14.6 ± 0.2	1800	200	14.8 ± 0.2
1000	200	13.1 ± 0.2	1800	400	15.7 ± 0.2
1000	400	15.5 ± 0.2	1800	600	16.9 ± 0.2
1000	600	16.5 ± 0.2	1800	800	17.0 ± 0.2
1000	800	15.0 ± 0.2	1800	1000	16.9 ± 0.2
1200	200	14.7 ± 0.2	1800	1200	17.1 ± 0.2
1200	400	15.8 ± 0.2	1800	1400	16.4 ± 0.2
1200	600	16.3 ± 0.2	1800	1600	14.8 ± 0.2
1200	800	16.2 ± 0.2	2000	200	14.7 ± 0.2
1200	1000	15.4 ± 0.2	2000	400	16.0 ± 0.2
1400	200	14.9 ± 0.2	2000	600	16.6 ± 0.2
1400	400	15.5 ± 0.2	2000	800	16.6 ± 0.2
1400	600	16.7 ± 0.2	2000	1000	16.5 ± 0.2
1400	800	16.7 ± 0.2	2000	1200	16.6 ± 0.2
1400	1000	16.1 ± 0.2	2000	1400	15.9 ± 0.2
1400	1200	15.3 ± 0.2	2000	1600	15.7 ± 0.2
1600	200	14.7 ± 0.2	2000	1800	14.3 ± 0.2
1600	400	15.9 ± 0.2			

Bibliography

[1] G. Aad *et al.*, "Observation of a new particle in the search for the Standard Model Higgs boson with the ATLAS detector at the LHC," *Phys. Lett.*, vol. B716, pp. 1–29, 2012.

[2] S. Chatrchyan *et al.*, "Observation of a new boson at a mass of 125 GeV with the CMS experiment at the LHC," *Phys. Lett.*, vol. B716, pp. 30–61, 2012.

[3] S. Chatrchyan *et al.*, "Observation of a new boson with mass near 125 GeV in pp collisions at $\sqrt{s} = 7$ and 8 TeV," *JHEP*, vol. 06, p. 081, 2013.

[4] F. Englert and R. Brout, "Broken Symmetry and the Mass of Gauge Vector Mesons," *Phys. Rev. Lett.*, vol. 13, pp. 321–323, 1964.

[5] G. S. Guralnik, C. R. Hagen, and T. W. B. Kibble, "Global Conservation Laws and Massless Particles," *Phys. Rev. Lett.*, vol. 13, pp. 585–587, 1964.

[6] P. W. Higgs, "Broken Symmetries and the Masses of Gauge Bosons," *Phys. Rev. Lett.*, vol. 13, pp. 508–509, 1964.

[7] S. P. Martin, "Perspectives on Supersymmetry - A Supersymmetry Primer," *Adv.Ser.Direct.High Energy Phys.*, vol. 18, pp. 1–98, 1998.

[8] S. P. Martin, "Perspectives on Supersymmetry II - A Supersymmetry Primer," *Adv.Ser.Direct.High Energy Phys.*, vol. 21, pp. 1–153, 2010.

[9] M. Schmaltz and D. Tucker-Smith, "Little Higgs review," *Ann. Rev. Nucl. Part. Sci.*, vol. 55, pp. 229–270, 2005.

[10] CMS Collaboration, "Search in two-dimensional mass space for T'T' to W'b W' b in the dilepton final state in proton-proton collisions at 8 TeV," Tech. Rep. CMS-PAS-B2G-12-025, CERN, Geneva, 2015.

[11] S. Beranek, "Search in two-dimensional mass space for $\mathrm{T'\bar{T}'} \to \mathrm{W'^{+}bW'^{-}\bar{b}}$ in the dilepton final state with the CMS detector," in *Proceedings of Science, 27th International*

Symposium on Lepton Photon Interactions at High Energies, vol. LeptonPhoton2015, (Ljubljana, Slovenia), p. 075, 2015.

[12] R. H. Dalitz and G. R. Goldstein, "The Decay and polarization properties of the top quark," *Phys. Rev.*, vol. D45, pp. 1531–1543, 1992.

[13] K. Kondo, "Dynamical Likelihood Method for Reconstruction of Events With Missing Momentum. 1: Method and Toy Models," *J. Phys. Soc. Jap.*, vol. 57, pp. 4126–4140, 1988.

[14] K. Kondo, "Dynamical likelihood method for reconstruction of events with missing momentum. 2: Mass spectra for $2 \to 2$ processes," *J. Phys. Soc. Jap.*, vol. 60, pp. 836–844, 1991.

[15] B. Abbott *et al.*, "Measurement of the top quark mass using dilepton events," *Phys. Rev. Lett.*, vol. 80, pp. 2063–2068, 1998.

[16] F. Abe *et al.*, "Measurement of the top quark mass and $t\bar{t}$ production cross section from dilepton events at the Collider Detector at Fermilab," *Phys. Rev. Lett.*, vol. 80, pp. 2779–2784, 1998.

[17] V. M. Abazov *et al.*, "A precision measurement of the mass of the top quark," *Nature*, vol. 429, pp. 638–642, 2004.

[18] V. M. Abazov *et al.*, "Measurement of the Top Quark Mass in Final States with Two Leptons," *Phys. Rev.*, vol. D80, p. 092006, 2009.

[19] S. Chatrchyan *et al.*, "Measurement of the top-quark mass in $t\bar{t}$ events with dilepton final states in pp collisions at $\sqrt{s} = 7$ TeV," *Eur. Phys. J.*, vol. C72, p. 2202, 2012.

[20] V. Khachatryan *et al.*, "Measurement of the top quark mass using proton-proton data at $\sqrt{s} = 7$ and 8 TeV," *Submitted to Phys. Rev. D*, 2015.

[21] N. Arkani-Hamed, A. G. Cohen, and H. Georgi, "Electroweak symmetry breaking from dimensional deconstruction," *Phys. Lett.*, vol. B513, pp. 232–240, 2001.

[22] R. M. Harris and S. Jain, "Cross Sections for Leptophobic Topcolor Z' Decaying to Top-Antitop," *Eur. Phys. J.*, vol. C72, p. 2072, 2012.

[23] J. Gao, C. S. Li, B. H. Li, C. P. Yuan, and H. X. Zhu, "Next-to-leading order QCD corrections to the heavy resonance production and decay into top quark pair at the LHC," *Phys. Rev.*, vol. D82, p. 014020, 2010.

[24] M. Schmaltz, "Physics beyond the standard model (theory): Introducing the little Higgs," *Nucl. Phys. Proc. Suppl.*, vol. 117, pp. 40–49, 2003. [,40(2002)].

[25] T. Han, H. E. Logan, B. McElrath, and L.-T. Wang, "Phenomenology of the little Higgs model," *Phys. Rev.*, vol. D67, p. 095004, 2003.

[26] M. Perelstein, "Little Higgs models and their phenomenology," *Prog. Part. Nucl. Phys.*, vol. 58, pp. 247–291, 2007.

[27] J. Reuter, M. Tonini, and M. de Vries, "Littlest Higgs with T-parity: Status and Prospects," *JHEP*, vol. 02, p. 053, 2014.

[28] F. Halzen and A. Martin, *Quarks and leptons: an introductory course in modern particle physics.* Wiley, 1984.

[29] M. E. Peskin and D. V. Schroeder, *An introduction to quantum field theory.* Advanced book program, Boulder (Colo.): Westview Press Reading (Mass.), 1995. Autre tirage : 1997.

[30] R. Ellis, W. Stirling, and B. Webber, *QCD and Collider Physics.* Cambridge Monographs on Particle Physics, Nuclear Physics and Cosmology, Cambridge University Press, 2003.

[31] D. Griffiths, *Introduction to Elementary Particle Physics.* 3, Wiley-VCH, 2008.

[32] P. A. M. Dirac, "The quantum theory of the electron," *Proc. Roy. Soc. Lond.*, vol. A117, pp. 610–624, 1928.

[33] E. Noether, "Invariant Variation Problems," *Gott. Nachr.*, vol. 1918, pp. 235–257, 1918. [Transp. Theory Statist. Phys.1,186(1971)].

[34] A. Einstein, *On the Relativity Principle and the Conclusions Drawn from It*, vol. 4. Jahrbuch der Radioaktivität, 1907.

[35] K. A. Olive *et al.*, "Review of Particle Physics," *Chin. Phys.*, vol. C 38, p. 090001, 2014 and 2015 update.

[36] M. Gell-Mann, "The Eightfold Way: A Theory of strong interaction symmetry," 1961.

[37] M. Gell-Mann, "A Schematic Model of Baryons and Mesons," *Phys. Lett.*, vol. 8, pp. 214–215, 1964.

[38] G. Zweig, "An SU(3) model for strong interaction symmetry and its breaking. Version 2," in *Developments in the Quark Theory of Hadrons. VOL. 1. 1964 - 1978* (D. Lichtenberg and S. P. Rosen, eds.), pp. 22–101, 1964.

[39] D. J. Gross and F. Wilczek, "Ultraviolet Behavior of Nonabelian Gauge Theories," *Phys. Rev. Lett.*, vol. 30, pp. 1343–1346, 1973.

[40] H. D. Politzer, "Reliable Perturbative Results for Strong Interactions?," *Phys. Rev. Lett.*, vol. 30, pp. 1346–1349, 1973.

[41] D. J. Gross and F. Wilczek, "Asymptotically Free Gauge Theories. 1," *Phys. Rev.*, vol. D8, pp. 3633–3652, 1973.

[42] H. D. Politzer, "Asymptotic Freedom: An Approach to Strong Interactions," *Phys. Rept.*, vol. 14, pp. 129–180, 1974.

[43] C.-N. Yang and R. L. Mills, "Conservation of Isotopic Spin and Isotopic Gauge Invariance," *Phys. Rev.*, vol. 96, pp. 191–195, 1954.

[44] H.-L. Lai *et al.*, "New parton distributions for collider physics," *Phys. Rev.*, vol. D82, p. 074024, 2010.

[45] M. R. Whalley, D. Bourilkov, and R. C. Group, "The Les Houches accord PDFs (LHAPDF) and LHAGLUE," in *A Workshop on the implications of HERA for LHC physics. Proceedings, Part B*, 2005.

[46] D. Bourilkov, R. C. Group, and M. R. Whalley, "LHAPDF: PDF use from the Tevatron to the LHC," in *TeV4LHC Workshop - 4th meeting ,October 20-22, 2005*, (Batavia, Illinois), 2006.

[47] A. Buckley, "New access to pdf data via lhapdf6," in *Les Houches 2013: Physics at TeV Colliders: Standard Model Working Group Report*, 2014.

[48] A. Buckley *et al.*, "LHAPDF6: parton density access in the LHC precision era," *Eur. Phys. J.*, vol. C75, p. 132, 2015.

[49] P. Skands, "Introduction to QCD," in *Proceedings, Theoretical Advanced Study Institute in Elementary Particle Physics: Searching for New Physics at Small and Large Scales (TASI 2012): June 4-29, 2012*, (Boulder, Colorado, USA), pp. 341–420, 2013, Update Nov 2014.

[50] R. P. Feynman, "Very high-energy collisions of hadrons," *Phys. Rev. Lett.*, vol. 23, pp. 1415–1417, 1969.

[51] G. Altarelli and G. Parisi, "Asymptotic Freedom in Parton Language," *Nucl. Phys.*, vol. B126, pp. 298–318, 1977.

[52] V. N. Gribov and L. N. Lipatov, "Deep inelastic ep scattering in perturbation theory," *Sov. J. Nucl. Phys.*, vol. 15, pp. 438–450, 1972. [Yad. Fiz.15,781(1972)].

[53] Y. L. Dokshitzer, "Calculation of the Structure Functions for Deep Inelastic Scattering and e^+e^- Annihilation by Perturbation Theory in Quantum Chromodynamics.," *Sov. Phys. JETP*, vol. 46, pp. 641–653, 1977. [Zh. Eksp. Teor. Fiz.73,1216(1977)].

[54] R. D. Ball *et al.*, "Parton distributions with LHC data," *Nucl. Phys.*, vol. B867, pp. 244–289, 2013.

[55] A. D. Martin, W. J. Stirling, R. S. Thorne, and G. Watt, "Parton distributions for the LHC," *Eur. Phys. J.*, vol. C63, pp. 189–285, 2009.

[56] S. Tomonaga, "On a relativistically invariant formulation of the quantum theory of wave fields," *Prog. Theor. Phys.*, vol. 1, pp. 27–42, 1946.

[57] R. P. Feynman, "Space - time approach to quantum electrodynamics," *Phys. Rev.*, vol. 76, pp. 769–789, 1949.

[58] J. S. Schwinger, "Quantum electrodynamics. III: The electromagnetic properties of the electron: Radiative corrections to scattering," *Phys. Rev.*, vol. 76, pp. 790–817, 1949.

[59] F. J. Dyson, "The Radiation theories of Tomonaga, Schwinger, and Feynman," *Phys. Rev.*, vol. 75, pp. 486–502, 1949.

[60] E. Fermi, "An attempt of a theory of beta radiation. 1.," *Z. Phys.*, vol. 88, pp. 161–177, 1934.

[61] J. S. Schwinger, "A Theory of the Fundamental Interactions," *Annals Phys.*, vol. 2, pp. 407–434, 1957.

[62] R. P. Feynman and M. Gell-Mann, "Theory of Fermi interaction," *Phys. Rev.*, vol. 109, pp. 193–198, 1958.

[63] T. D. Lee and C.-N. Yang, "Question of Parity Conservation in Weak Interactions," *Phys. Rev.*, vol. 104, pp. 254–258, 1956.

[64] C. S. Wu *et al.*, "Experimental Test of Parity Conservation in Beta Decay," *Phys. Rev.*, vol. 105, pp. 1413–1414, 1957.

[65] E. C. G. Sudarshan and R. E. Marshak, "Chirality invariance and the universal Fermi interaction," *Phys. Rev.*, vol. 109, pp. 1860–1860, 1958.

[66] S. L. Glashow, "Partial Symmetries of Weak Interactions," *Nucl. Phys.*, vol. 22, pp. 579–588, 1961.

[67] A. Salam and J. C. Ward, "Electromagnetic and weak interactions," *Phys. Lett.*, vol. 13, pp. 168–171, 1964.

[68] M. Kobayashi and T. Maskawa, "CP Violation in the Renormalizable Theory of Weak Interaction," *Prog. Theor. Phys.*, vol. 49, pp. 652–657, 1973.

[69] S. Weinberg, "A Model of Leptons," *Phys. Rev. Lett.*, vol. 19, pp. 1264–1266, 1967.

[70] A. Salam, “Weak and Electromagnetic Interactions,” in *8th Nobel Symposium Lerum, May 19-25, 1968*, vol. C680519, (Sweden), pp. 367–377, 1968.

[71] G. ’t Hooft, “Renormalizable Lagrangians for Massive Yang-Mills Fields,” *Nucl. Phys.*, vol. B35, pp. 167–188, 1971.

[72] G. Arnison *et al.*, “Experimental Observation of Lepton Pairs of Invariant Mass Around 95 GeV/c^2 at the CERN SPS Collider,” *Phys. Lett.*, vol. B126, pp. 398–410, 1983.

[73] G. Arnison *et al.*, “Experimental Observation of Isolated Large Transverse Energy Electrons with Associated Missing Energy at $\sqrt{s} = 540\,\mathrm{GeV}$,” *Phys. Lett.*, vol. B122, pp. 103–116, 1983.

[74] G. Hinshaw *et al.*, “Nine-Year Wilkinson Microwave Anisotropy Probe (WMAP) Observations: Cosmological Parameter Results,” *Astrophys. J. Suppl.*, vol. 208, p. 19, 2013.

[75] P. A. R. Ade *et al.*, “Planck 2015 results. XIII. Cosmological parameters,” *Astron. Astrophys.*, vol. 594, p. A13, 2015.

[76] R. Davis, Jr. *et al.*, “Search for neutrinos from the sun,” *Phys. Rev. Lett.*, vol. 20, pp. 1205–1209, 1968.

[77] Y. Ashie *et al.*, “Evidence for an oscillatory signature in atmospheric neutrino oscillation,” *Phys. Rev. Lett.*, vol. 93, p. 101801, 2004.

[78] C. A. Baker *et al.*, “An Improved experimental limit on the electric dipole moment of the neutron,” *Phys. Rev. Lett.*, vol. 97, p. 131801, 2006.

[79] D. B. Kaplan and H. Georgi, “SU(2) x U(1) Breaking by Vacuum Misalignment,” *Phys. Lett.*, vol. B136, pp. 183–186, 1984.

[80] D. B. Kaplan, H. Georgi, and S. Dimopoulos, “Composite Higgs Scalars,” *Phys. Lett.*, vol. B136, pp. 187–190, 1984.

[81] M. J. Dugan, H. Georgi, and D. B. Kaplan, “Anatomy of a Composite Higgs Model,” *Nucl. Phys.*, vol. B254, pp. 299–326, 1985.

[82] J. Goldstone, A. Salam, and S. Weinberg, “Broken Symmetries,” *Phys. Rev.*, vol. 127, pp. 965–970, 1962.

[83] N. Arkani-Hamed, A. G. Cohen, E. Katz, and A. E. Nelson, “The Littlest Higgs,” *JHEP*, vol. 07, p. 034, 2002.

[84] C. T. Hill and E. H. Simmons, “Strong dynamics and electroweak symmetry breaking,” *Phys. Rept.*, vol. 381, pp. 235–402, 2003. [Erratum: Phys. Rept.390,553(2004)].

[85] C. T. Hill, "Topcolor: Top quark condensation in a gauge extension of the standard model," *Phys. Lett.*, vol. B266, pp. 419–424, 1991.

[86] C. T. Hill, "Topcolor assisted technicolor," *Phys. Lett.*, vol. B345, pp. 483–489, 1995.

[87] J. L. Rosner, "Prominent decay modes of a leptophobic Z'," *Phys. Lett.*, vol. B387, pp. 113–117, 1996.

[88] K. R. Lynch *et al.*, "Finding Z' bosons coupled preferentially to the third family at LEP and the Tevatron," *Phys. Rev.*, vol. D63, p. 035006, 2001.

[89] M. Carena *et al.*, "Z' gauge bosons at the Tevatron," *Phys. Rev.*, vol. D70, p. 093009, 2004.

[90] P. H. Frampton and S. L. Glashow, "Chiral Color: An Alternative to the Standard Model," *Phys. Lett.*, vol. B190, pp. 157–161, 1987.

[91] D. Choudhury *et al.*, "Top production at the Tevatron/LHC and nonstandard, strongly interacting spin one particles," *Phys. Lett.*, vol. B657, pp. 69–76, 2007.

[92] D. Dicus, A. Stange, and S. Willenbrock, "Higgs decay to top quarks at hadron colliders," *Phys. Lett.*, vol. B333, pp. 126–131, 1994.

[93] N. Arkani-Hamed, S. Dimopoulos, and G. R. Dvali, "The Hierarchy problem and new dimensions at a millimeter," *Phys. Lett.*, vol. B429, pp. 263–272, 1998.

[94] I. Antoniadis *et al.*, "New dimensions at a millimeter to a Fermi and superstrings at a TeV," *Phys. Lett.*, vol. B436, pp. 257–263, 1998.

[95] T. Kaluza, "Zum unitätsproblem in der physik," *Sitzungsber. Preuss. Akad. Wiss. Berlin (Math. Phys.)*, p. 966, 1921.

[96] O. Klein, "Quantentheorie und fünfdimensionale relativitätstheorie," *Zeitschrift für Physik*, vol. 37, no. 12, pp. 895–906, 1926.

[97] O. Klein, "The Atomicity of Electricity as a Quantum Theory Law," *Nature*, vol. 118, p. 516, 1926.

[98] L. Randall and R. Sundrum, "A Large mass hierarchy from a small extra dimension," *Phys. Rev. Lett.*, vol. 83, pp. 3370–3373, 1999.

[99] T. G. Rizzo, "Probes of universal extra dimensions at colliders," *Phys. Rev.*, vol. D64, p. 095010, 2001.

[100] K. Agashe *et al.*, "LHC Signals from Warped Extra Dimensions," *Phys. Rev.*, vol. D77, p. 015003, 2008.

[101] H. Davoudiasl, J. L. Hewett, and T. G. Rizzo, "Phenomenology of the Randall-Sundrum Gauge Hierarchy Model," *Phys. Rev. Lett.*, vol. 84, p. 2080, 2000.

[102] J. Reuter, M. Tonini, and M. de Vries, "Little Higgs Model Limits from LHC - Input for Snowmass 2013," in *Snowmass 2013: Workshop on Energy Frontier, June 30-July 3, 2013*, (Seattle, USA), 2013.

[103] J. Reuter and M. Tonini, "Can the 125 GeV Higgs be the Little Higgs?," *JHEP*, vol. 02, p. 077, 2013.

[104] O. S. Brüning *et al.*, *LHC Design Report.* Geneva: CERN, 2004.

[105] L. Evans and P. Bryant, "LHC Machine," *JINST*, vol. 3, p. S08001, 2008.

[106] M. Lamont, "Status of the lhc," *Journal of Physics: Conference Series*, vol. 455, no. 1, p. 012001, 2013.

[107] C. Lefevre, "The CERN accelerator complex. Complexe des accelerateurs du CERN." https://cds.cern.ch/record/1260465, Dec 2008.

[108] G. Aad *et al.*, "The ATLAS Experiment at the CERN Large Hadron Collider," *JINST*, vol. 3, p. S08003, 2008.

[109] S. Chatrchyan *et al.*, "The CMS experiment at the CERN LHC," *JINST*, vol. 3, p. S08004, 2008.

[110] K. Aamodt *et al.*, "The ALICE experiment at the CERN LHC," *JINST*, vol. 3, p. S08002, 2008.

[111] A. A. Alves, Jr. *et al.*, "The LHCb Detector at the LHC," *JINST*, vol. 3, p. S08005, 2008.

[112] T. Sakuma and T. McCauley, "Detector and Event Visualization with SketchUp at the CMS Experiment," *J. Phys. Conf. Ser.*, vol. 513, p. 022032, 2014.

[113] G. L. Bayatian *et al.*, *CMS Physics: Technical Design Report Volume 1: Detector Performance and Software.* Technical Design Report CMS, Geneva: CERN, 2006.

[114] S. Chatrchyan *et al.*, "Alignment of the CMS tracker with LHC and cosmic ray data," *JINST*, vol. 9, p. P06009, 2014.

[115] S. Chatrchyan *et al.*, "Description and performance of track and primary-vertex reconstruction with the CMS tracker," *JINST*, vol. 9, no. 10, p. P10009, 2014.

[116] S. Chatrchyan *et al.*, "Energy Calibration and Resolution of the CMS Electromagnetic Calorimeter in pp Collisions at $\sqrt{s} = 7$ TeV," *JINST*, vol. 8, p. P09009, 2013.

[117] P. Adzic *et al.*, "Energy resolution of the barrel of the CMS electromagnetic calorimeter," *JINST*, vol. 2, p. P04004, 2007.

[118] S. Chatrchyan *et al.*, "Performance of the CMS Hadron Calorimeter with Cosmic Ray Muons and LHC Beam Data," *JINST*, vol. 5, p. T03012, 2010.

[119] CMS Collaborations, *The CMS muon project: Technical Design Report*. Technical Design Report CMS, Geneva: CERN, 1997.

[120] S. Chatrchyan *et al.*, "The performance of the CMS muon detector in proton-proton collisions at $\sqrt{s} = 7$ TeV at the LHC," *JINST*, vol. 8, p. P11002, 2013.

[121] S. Chatrchyan *et al.*, "Performance of CMS muon reconstruction in pp collision events at $\sqrt{s} = 7$ TeV," *JINST*, vol. 7, p. P10002, 2012.

[122] J. Brooke, "Performance of the CMS Level-1 Trigger," in *Proceedings, 36th International Conference on High Energy Physics: July 4-11, 2012*, vol. ICHEP2012, (Melbourne, Australia), p. 508, 2013.

[123] V. Gori, "The CMS High Level Trigger," in *Proceedings, 33rd International Symposium on Physics in Collision: September 3-7, 2013*, vol. 31, (Beijing, China), p. 1460297, 2014.

[124] CMS Collaboration, "Measurement of CMS Luminosity ," Tech. Rep. CMS-PAS-EWK-10-004, CERN, Geneva, 2010.

[125] CMS Collaboration, "CMS Luminosity Based on Pixel Cluster Counting - Summer 2012 Update," Tech. Rep. CMS-PAS-LUM-12-001, CERN, Geneva, 2012.

[126] CMS Collaboration, "Absolute Calibration of the Luminosity Measurement at CMS: Winter 2012 Update," Tech. Rep. CMS-PAS-SMP-12-008, CERN, Geneva, 2012.

[127] CMS Collaboration, "CMS Luminosity Based on Pixel Cluster Counting - Summer 2013 Update," Tech. Rep. CMS-PAS-LUM-13-001, CERN, Geneva, 2013.

[128] S. van der Meer, "Calibration of the effective beam height in the ISR," Tech. Rep. CERN-ISR-PO-68-31. ISR-PO-68-31, CERN, Geneva, 1968.

[129] CMS Collaboration, "Cms luminosity - public results," 2016. `https://twiki.cern.ch/twiki/bin/view/CMSPublic/LumiPublicResults`.

[130] CMS Collaboration, "Particle-Flow Event Reconstruction in CMS and Performance for Jets, Taus, and MET," Tech. Rep. CMS-PAS-PFT-09-001, CERN, Geneva, 2009.

[131] CMS Collaboration, "Commissioning of the Particle-Flow reconstruction in Minimum-Bias and Jet Events from pp Collisions at 7 TeV," Tech. Rep. CMS-PAS-PFT-10-002, CERN, Geneva, 2010.

[132] D. Barney, "CMS Detector Slice." CMS Collection `https://cds.cern.ch/record/2120661`, Jan 2016.

[133] S. Cucciarelli *et al.*, “Track reconstruction, primary vertex finding and seed generation with the Pixel Detector,” Tech. Rep. CMS-NOTE-2006-026, CERN, Geneva, Jan 2006.

[134] R. E. Kalman, “A new approach to linear filtering and prediction problems,” *Transactions of the ASME–Journal of Basic Engineering*, vol. 82, no. Series D, pp. 35–45, 1960.

[135] R. Fruhwirth, “Application of Kalman filtering to track and vertex fitting,” *Nucl. Instrum. Meth.*, vol. A262, pp. 444–450, 1987.

[136] K. Rose, “Deterministic annealing for clustering, compression, classification, regression, and related optimization problems,” in *Proceedings of the IEEE*, pp. 2210–2239, 1998.

[137] R. Fruhwirth, W. Waltenberger, and P. Vanlaer, “Adaptive vertex fitting,” *J. Phys.*, vol. G34, p. N343, 2007.

[138] CMS Collaboration, “Electron reconstruction and identification at $\sqrt{s} = 7$ TeV,” Tech. Rep. CMS-PAS-EGM-10-004, CERN, Geneva, 2010.

[139] V. Khachatryan *et al.*, “Performance of Electron Reconstruction and Selection with the CMS Detector in Proton-Proton Collisions at $\sqrt{s} = 8$ TeV,” *JINST*, vol. 10, no. 06, p. P06005, 2015.

[140] J. H. Kotecha, P. M. Djuric, and S. Member, “Gaussian particle filtering,” *IEEE Transactions on Signal Processing*, vol. 51, pp. 2592–2601, 2003.

[141] H. Kirschenmann, “Jets at cms and the determination of their energy scale,” 2012. http://cms.web.cern.ch/news/jets-cms-and-determination-their-energy-scale.

[142] M. Cacciari, G. P. Salam, and G. Soyez, “The Anti-k(t) jet clustering algorithm,” *JHEP*, vol. 04, p. 063, 2008.

[143] S. Chatrchyan *et al.*, “Determination of Jet Energy Calibration and Transverse Momentum Resolution in CMS,” *JINST*, vol. 6, p. P11002, 2011.

[144] M. Cacciari, G. P. Salam, and G. Soyez, “FastJet User Manual,” *Eur. Phys. J.*, vol. C72, p. 1896, 2012.

[145] M. Cacciari, G. P. Salam, and G. Soyez, “The Catchment Area of Jets,” *JHEP*, vol. 04, p. 005, 2008.

[146] M. Cacciari and G. P. Salam, “Pileup subtraction using jet areas,” *Phys. Lett.*, vol. B659, pp. 119–126, 2008.

[147] A. Buckley *et al.*, “General-purpose event generators for LHC physics,” *Phys. Rept.*, vol. 504, pp. 145–233, 2011.

[148] M. H. Seymour and M. Marx, "Monte Carlo Event Generators," in *Proceedings, 69th Scottish Universities Summer School in Physics : LHC Phenomenology*, pp. 287–319, 2013.

[149] S. Chatrchyan *et al.*, "Measurement of the Underlying Event Activity at the LHC with $\sqrt{s} = 7$ TeV and Comparison with $\sqrt{s} = 0.9$ TeV," *JHEP*, vol. 09, p. 109, 2011.

[150] G. Aad *et al.*, "Measurement of the underlying event in jet events from 7 TeV proton-proton collisions with the ATLAS detector," *Eur. Phys. J.*, vol. C74, no. 8, p. 2965, 2014.

[151] T. Sjostrand, S. Mrenna, and P. Z. Skands, "PYTHIA 6.4 Physics and Manual," *JHEP*, vol. 05, p. 026, 2006.

[152] R. Field, "Min-Bias and the Underlying Event at the LHC," *Acta Phys. Polon.*, vol. B42, pp. 2631–2656, 2011.

[153] J. Alwall *et al.*, "The automated computation of tree-level and next-to-leading order differential cross sections, and their matching to parton shower simulations," *JHEP*, vol. 07, p. 079, 2014.

[154] P. Nason, "A New method for combining NLO QCD with shower Monte Carlo algorithms," *JHEP*, vol. 11, p. 040, 2004.

[155] S. Frixione, P. Nason, and C. Oleari, "Matching NLO QCD computations with Parton Shower simulations: the POWHEG method," *JHEP*, vol. 11, p. 070, 2007.

[156] S. Alioli *et al.*, "A general framework for implementing NLO calculations in shower Monte Carlo programs: the POWHEG BOX," *JHEP*, vol. 06, p. 043, 2010.

[157] M. Moretti, T. Ohl, and J. Reuter, "O'Mega: An Optimizing matrix element generator," *2nd ECFA/DESY Study 1998-2001*, p. 29, Feb 2001.

[158] W. Kilian, T. Ohl, and J. Reuter, "WHIZARD: Simulating Multi-Particle Processes at LHC and ILC," *Eur. Phys. J.*, vol. C71, p. 1742, 2011.

[159] M. L. Mangano *et al.*, "Matching matrix elements and shower evolution for top-quark production in hadronic collisions," *JHEP*, vol. 01, p. 013, 2007.

[160] S. Agostinelli *et al.*, "GEANT4: A Simulation toolkit," *Nucl. Instrum. Meth.*, vol. A506, pp. 250–303, 2003.

[161] J. Allison *et al.*, "Geant4 developments and applications," *IEEE Trans. Nucl. Sci.*, vol. 53, p. 270, 2006.

[162] J. Pumplin *et al.*, "New generation of parton distributions with uncertainties from global QCD analysis," *JHEP*, vol. 07, p. 012, 2002.

[163] P. M. Nadolsky *et al.*, "Implications of CTEQ global analysis for collider observables," *Phys. Rev.*, vol. D78, p. 013004, 2008.

[164] J. Gao *et al.*, "CT10 next-to-next-to-leading order global analysis of QCD," *Phys. Rev.*, vol. D89, no. 3, p. 033009, 2014.

[165] S. Alioli *et al.*, "NLO single-top production matched with shower in POWHEG: s- and t-channel contributions," *JHEP*, vol. 09, p. 111, 2009. [Erratum: JHEP02,011(2010)].

[166] E. Re, "Single-top Wt-channel production matched with parton showers using the POWHEG method," *Eur. Phys. J.*, vol. C71, p. 1547, 2011.

[167] M. Czakon, P. Fiedler, and A. Mitov, "Total Top-Quark Pair-Production Cross Section at Hadron Colliders Through $O(\alpha\frac{4}{S})$," *Phys. Rev. Lett.*, vol. 110, p. 252004, 2013.

[168] N. Kidonakis, "NNLL threshold resummation for top-pair and single-top production," *Phys. Part. Nucl.*, vol. 45, no. 4, pp. 714–722, 2014.

[169] J. M. Campbell and R. K. Ellis, "$t\bar{t}W^{+-}$ production and decay at NLO," *JHEP*, vol. 07, p. 052, 2012.

[170] M. V. Garzelli *et al.*, "$t\bar{t}$ W^{+-} and $t\bar{t}$ Z Hadroproduction at NLO accuracy in QCD with Parton Shower and Hadronization effects," *JHEP*, vol. 11, p. 056, 2012.

[171] J. R. Andersen *et al.*, "Handbook of LHC Higgs Cross Sections: 3. Higgs Properties," Tech. Rep. CERN-2013-004, CERN, 2013.

[172] R. Gavin, Y. Li, F. Petriello, and S. Quackenbush, "FEWZ 2.0: A code for hadronic Z production at next-to-next-to-leading order," *Comput. Phys. Commun.*, vol. 182, pp. 2388–2403, 2011.

[173] R. Gavin, Y. Li, F. Petriello, and S. Quackenbush, "W Physics at the LHC with FEWZ 2.1," *Comput. Phys. Commun.*, vol. 184, pp. 208–214, 2013.

[174] J. M. Campbell and R. K. Ellis, "An Update on vector boson pair production at hadron colliders," *Phys. Rev.*, vol. D60, p. 113006, 1999.

[175] J. M. Campbell, R. K. Ellis, and C. Williams, "Vector boson pair production at the LHC," *JHEP*, vol. 07, p. 018, 2011.

[176] CMS Collaboration, "Single Muon efficiencies in 2012 Data," Tech. Rep. CMS-DP-2013-009, CERN, Geneva, 2013.

[177] CMS Collaboration, "Search for pair-produced vector-like quarks of charge -1/3 in dilepton+jets final state in pp collisions at $\sqrt{s}$ = 8 TeV," Tech. Rep. CMS-PAS-B2G-12-021, CERN, Geneva, 2013.

[178] CMS Collaboration, "Performance of muon identification in pp collisions at $\sqrt{s}$ = 7 TeV," Tech. Rep. CMS-PAS-MUO-10-002, CERN, Geneva, 2010.

[179] S. Chatrchyan *et al.*, "Search for neutral Higgs bosons decaying to tau pairs in pp collisions at $\sqrt{s}$ = 7 TeV," *Phys. Lett.*, vol. B713, pp. 68–90, 2012.

[180] CMS Collaboration, "Electron performance with 19.6 fb^{-1} of data collected at $\sqrt{s}$ = 8 TeV with the CMS detector.," Tech. Rep. CMS-DP-2013-003, CERN, Geneva, 2013.

[181] CMS Collaboration, "8 TeV Jet Energy Corrections and Uncertainties based on 19.8 fb^{-1} of data in CMS," Tech. Rep. CMS-DP-2013-033, CERN, Geneva, Oct 2013.

[182] CMS Collaboration, "CMS JEC Run I legacy performance plots," Tech. Rep. CMS-DP-2015-044, CERN, Geneva, Sep 2015.

[183] V. Khachatryan *et al.*, "Jet energy scale and resolution in the CMS experiment in pp collisions at 8 TeV," *submitted to JINST*, 2016. CMS-JME-13-004.

[184] CMS Collaboration, "Pileup Jet Identification," Tech. Rep. CMS-PAS-JME-13-005, CERN, Geneva, 2013.

[185] S. Chatrchyan *et al.*, "Identification of b-quark jets with the CMS experiment," *JINST*, vol. 8, p. P04013, 2013.

[186] CMS Collaboration, "Performance of b tagging at $\sqrt{s}$=8 TeV in multijet, $t\bar{t}$ and boosted topology events," Tech. Rep. CMS-PAS-BTV-13-001, CERN, 2013.

[187] S. Chatrchyan *et al.*, "Missing transverse energy performance of the CMS detector," *JINST*, vol. 6, p. P09001, 2011.

[188] V. Khachatryan *et al.*, "Performance of the CMS missing transverse momentum reconstruction in pp data at $\sqrt{s}$ = 8 TeV," *JINST*, vol. 10, no. 02, p. P02006, 2015.

[189] S. Beranek, "Measurement of J/Ψ and Υ production in proton-proton collisions at $\sqrt{s}$ = 7 TeV with the CMS experiment," in *Proceedings, 30th International Conference on Physics in collision*, vol. C100901, (Karlsruhe, Germany), pp. 337–340, 2010.

[190] G. Antchev *et al.*, "First measurement of the total proton-proton cross section at the LHC energy of $\sqrt{s}$ =7 TeV," *Europhys. Lett.*, vol. 96, p. 21002, 2011.

[191] V. Khachatryan *et al.*, "First Measurement of the Cross Section for Top-Quark Pair Production in Proton-Proton Collisions at $\sqrt{s}$ = 7 TeV," *Phys. Lett.*, vol. B695, pp. 424–443, 2011.

[192] S. Chatrchyan *et al.*, "Measurement of the $t\bar{t}$ production cross section and the top quark mass in the dilepton channel in pp collisions at $\sqrt{s}$ = 7 TeV," *JHEP*, vol. 07, p. 049, 2011.

[193] S. Chatrchyan *et al.*, "Measurement of the $t\bar{t}$ production cross section in the dilepton channel in pp collisions at $\sqrt{s} = 7$ TeV," *JHEP*, vol. 11, p. 067, 2012.

[194] S. Chatrchyan *et al.*, "Measurement of the $t\bar{t}$ production cross section in the dilepton channel in pp collisions at $\sqrt{s} = 8$ TeV," *JHEP*, vol. 02, p. 024, 2014. [Erratum: JHEP02,102(2014)].

[195] G. Anagnostou, "Model Independent Search in 2-Dimensional Mass Space," *EPJ Web Conf.*, vol. 71, p. 00006, 2014.

[196] L. Sonnenschein, "Algebraic approach to solve $t\bar{t}$ dilepton equations," *Phys. Rev.*, vol. D72, p. 095020, 2005.

[197] L. Sonnenschein, "Analytical solution of ttbar dilepton equations," *Phys. Rev.*, vol. D73, p. 054015, 2006. [Erratum: Phys. Rev.D78,079902(2008)].

[198] V. Khachatryan *et al.*, "Measurement of the differential cross section for top quark pair production in pp collisions at $\sqrt{s} = 8$ TeV," *Eur. Phys. J.*, vol. C75, no. 11, p. 542, 2015.

[199] CMS Collaboration, "Search for ttbar resonances in dilepton+jets final states in pp collisions at 8 TeV," Tech. Rep. CMS-PAS-B2G-12-007, CERN, Geneva, 2014.

[200] LHC Higgs Combination Group. ATLAS & CMS Collaboration, "Procedure for the LHC Higgs boson search combination in Summer 2011," Tech. Rep. CMS-NOTE-2011-005. ATL-PHYS-PUB-2011-11, CERN, Geneva, Aug 2011.

[201] A. L. Read, "Modified frequentist analysis of search results (The CL_s method)," in *Workshop on confidence limits, 17-18 Jan 2000*, (CERN, Geneva, Switzerland), 2000.

[202] A. L. Read, "Presentation of search results: the cl_s technique," *J Phys G Nucl Part Phys*, vol. 28, p. 2693, Sep 2002.

[203] G. Cowan *et al.*, "Asymptotic formulae for likelihood-based tests of new physics," *Eur. Phys. J.*, vol. C71, p. 1554, 2011. [Erratum: Eur. Phys. J.C73,2501(2013)].

[204] S. Chatrchyan *et al.*, "Inclusive search for a vector-like T quark with charge $\frac{2}{3}$ in pp collisions at $\sqrt{s} = 8$ TeV," *Phys. Lett.*, vol. B729, pp. 149–171, 2014.

[205] M. Aliev *et al.*, "HATHOR: HAdronic Top and Heavy quarks crOss section calculatoR," *Comput. Phys. Commun.*, vol. 182, pp. 1034–1046, 2011.

Acknowledgements

This dissertation would not have been possible without the support and encouragement of a number of remarkable people. I would like to embrace the opportunity to express my deep gratitude.

First of all, I would like to thank my supervisor, Prof. Dr. Stefan Schael who offered me the doctoral position and made my long-term research stay at CERN possible. I am sincerely thankful for his continuous support and encouragements in my decisions throughout the thesis. His enthusiasm for particle physics is truly inspiring.
Furthermore, I thankfully acknowledge Prof. Dr. Thomas Hebbeker who kindly agreed to be my second supervisor.

My deep gratitude goes to Dr. Georgios Anagnostou, with whom I closely worked on the mass reconstruction method throughout all the years of my dissertation. Almost no week went by where we did not have long phone conversations, arguments and discussions about the analysis. His optimism was truly helpful especially while trying to publish our new model-independent search method in a large collaboration. His thorough and never hasty approach showed me a healthy way of life. I also would like to thank Dr. Andreas Psallidas, who joined Georgios and me in the second half of my thesis and was especially helpful by generating the simulations for the simplified signal models. My gratitude also goes to Dr. Bruno Wittmer who helped me get started with the software of the mass reconstruction method in the first months of my dissertation.

My special thanks goes to my colleagues and friends from the CMS Aachen group with whom I had many fruitful discussions and who always supported me and my work: Dr. Natalie Heracleous, Dr. Otto Hindrichs, Dr. Andrei Ostapchuk, Dr. Demetrios Pandoulas, Dr. Adrian Perieanu, Prof. Dr. Frank Raupach, Dr. Tobias Verlage and Dr. Hendrik Weber, the last two being such great office colleagues as well.

I would like to express my deep gratitude to the conveners of the B2G (Beyond 2nd Generation) Group of the CMS Collaboration who supported our analysis through out the long process of the PAS-publication - I would like to mention Dr. Patrizia Azzi, Prof. Dr. Freya Blekman, Dr. Roman Kogler, Dr. Justin Pilot, Prof. Dr. Salvatore Rappoccio and Dr. Alexander Schmidt in particular.

I would also like to thank the DESY theory group, especially Prof. Dr. Jürgen Reuter and Dr. Marco Tonini, who helped and guided us in the choice of the little higgs model and the corresponding parameters. They also implemented the required vertices in the Whizard generator.

Dr. Georgios Anagnostou, Bastian Beischer, Dr. Leila Cavasonza, Dr. Otto Hindrichs and Dr. Demetrios Pandoulas carefully proof-read parts of my dissertation for which I am very grateful.

I am gratefully acknowledging the financial support by the Graduiertenkolleg 1675 “Teilchen- und Astroteilchenphysik im Lichte von LHC”, of which I was fortunate to be a part of and which provided lots of opportunities to broaden the horizon within the field of particle physics and to exchange ideas with other doctoral candidates from the Graduiertenkolleg.

I also would like to thank my former school teacher Michael Große. His enthusiasm for physics paved the way for me to study physics in the first place, a decision I have never regretted.

My long-time friends from school and university have accompanied me through all highs and lows of the dissertation and I am very thankful for their continuous friendship and love. There are no words to thank Bastian enough for his constant encouragement and backing in any situation and for always being at my side.

Finally and most of all, I would like to sincerely thank my parents, Hans and Monika, my sister Anja and the rest of my family for always believing in me, supporting and loving me.